ANALYSIS, DESIGN AND IMPLEMENTATION OF HIGH PERFORMANCE CONTROL SCHEMES FOR THREE PHASE PWM AC-DC VOLTAGE SOURCE CONVERTER

XINHUI WU

NATIONAL UNIVERSITY OF SINGAPORE

2008

ANALYSIS, DESIGN AND IMPLEMENTATION OF HIGH PERFORMANCE CONTROL SCHEMES FOR THREE PHASE PWM AC-DC VOLTAGE SOURCE CONVERTER

XINHUI WU
(B.Eng(Hons.), SJTU, Shanghai, China)

A THESIS SUBMITTED

FOR THE DEGREE OF DOCTOR OF PHILOSOPHY

DEPARTMENT OF ELECTRICAL AND COMPUTER ENGINEERING
NATIONAL UNIVERSITY OF SINGAPORE
2008

Acknowledgments

I would like to express my deepest gratitude to my supervisor Prof. Sanjib Kumar Panda, for his persistent help, advice and encouragement. I learned not only from his academic knowledge in the area of power electronics and drives but also from his sincere and humble attitude toward science and engineering. I am extremely grateful and obliged to my co-supervisor Prof. Jian-Xin Xu for his intellectual innovative and highly investigative guidance to me for my project. Without his critical questions based on the sharp insight in the area of control theory and applications, this work would not have gotten so far. I would also like to thank Prof. Y. C. Liang and Prof. A. A. Mamun for their guidance as PhD Thesis Committee Members. I appreciate other Professors in the Drives, Power and Control Systems Group at ECE Department in NUS, for their help and guidance in various ways.

I wish to express my warm and sincere thanks to the laboratory officers, Mr. Y. C. Woo, and Mr. M. Chandra of Electrical Machines and Drives Lab, for their readiness to help on any matter. Also, I am grateful for the timely assistance from Mr. Seow from Power Systems Lab, Mr. Chang in Engineering Workshop and Mr. Jalil in PCB fabrication Lab.

The four and half years in NUS is surely a valuable experience. My warmest

thanks go to my fellow research scholars in Electrical Machines and Drives Lab for all the help to make my stay more enjoyable and beneficial. My heartfelt gratitude goes to Mr. Laurent Jolly for the happy time he brought to me. His remarkable persistence and curiosity displays me a new angle of life and arouse my desire of exploration. I am also very fortunate to know Ms. Zhou Haihua as a lab-mate and a good friend. Her immense enthusiasm leads me to come out of my black depression period. I am deeply indebted to Dr. S.K. Sahoo and Mr. Krishna Mainali for the valuable discussions on the design and development of my project and their constant help and suggestions in many aspects during these years.

I owe so much appreciation for many warm-hearted, and wonderful friends inside and outside of the NUS campus. Thanks to my old flatmates, Shen Yan, Hadja and my present flatmate Li Jie for their encouragement and help. I am truely grateful to Cao Xiao, Huang Zhihong and Shao Lichun for their advices on the hardware design of my project. Also, I will cherish the friendship with Weizhe, Carol, Weixian, Thomson, Yang Yuming, Yan Junhua and all the friends who take care of me and support me. I treasured all precious moments we shared and would really like to thank them.

I have been deeply touched by endless love and boundless support by my parents. Thank you for your always being on my side and keeping a sweetie home for me no matter what happens. I wish to dedicate what I have accomplished today to them.

Contents

Summary

Recently, three phase PWM AC-DC voltage source converters have been increasingly used for high-performance applications such as uninterruptible power supply (UPS) systems and industrial ac and dc drive systems, due to their attractive features such as providing high quality dc output voltage with a small filter dc-link capacitor, sinusoidal input current at unity power factor and bidirectional power flow. However, all these advantages are valid so long as the grid supply voltages are balanced. With the unbalanced and distorted supply voltages, the oscillation in the input instantaneous active power causes the even-order harmonics to appear at the output dc link voltage and odd-order harmonics in the ac line side currents. One way to eliminate or minimize the even-order harmonics at the dc output voltage and odd-order harmonics in the ac line side currents is to make use of bulky filters. However, the bulky filters would not only slow down the dynamic response of the PWM rectifier but also increase the size of the converter. The alternative is to make use of *active control methods* with a small size filter to either eliminate or minimize the voltage and current harmonics. The second alternative has the advantage of providing high dynamic performance. Hence, this thesis is aimed at developing active control solutions to achieve high performance for three phase PWM AC-DC voltage source converters under the distorted and unbalanced supply voltage operating conditions. By using these active control solutions, the even-order harmonics

at the dc link voltage of the converter can be minimized, while the input ac supply currents are kept sinusoidal and power factor is maintained at close to unity.

This thesis analyzes the mathematical model and instantaneous power flow of the three phase PWM AC-DC voltage source converter in the positive and negative synchronous rotating frames under the generalized supply voltage operating conditions. Based on this proposed model, the explanations of the appearance of the even-order harmonics at the dc output voltage and the low frequency odd-order harmonics in the input ac currents under the unbalanced and distorted supply voltage conditions are provided. Moreover, the power flow analysis not only provides direct insight into the relationship between the dc link voltage ripples and the harmonic components in the output instantaneous power, but also shows the inner link between the odd-order harmonics in the ac line side currents and the even-order harmonics at the dc output voltage. Hence, the performance of three phase PWM AC-DC voltage source converter under the generalized supply voltage conditions can be improved either by voltage harmonics control or by power regulation.

In order to eliminate the even-order harmonics at the dc link voltage and the odd-order harmonics in the ac line side currents, the proposed control scheme can be highlighted as two parts, (1) *DC link voltage harmonics control* scheme to eliminate the even-order harmonics at the dc link voltage and (2) *AC line side current harmonics control* scheme to eliminate the odd-order harmonics in the line side currents. Accordingly, the control signals S_d^p, S_q^p, S_d^n and S_q^n in the positive and negative sequence in the rotating synchronous *d-q* frame can be divided into two parts, (1) *voltage harmonics control signals*, S_{dv}^p, S_{qv}^p, S_{dv}^n and S_{qv}^n, those are used to take care of the even-order harmonics at the dc link voltage, and (2) *current*

harmonics control signals, S_{di}^{p}, S_{qi}^{p}, S_{di}^{n} and S_{qi}^{n}, those are supposed to eliminate the odd-order harmonics in the ac line side currents. These two parts of the proposed control scheme can be implemented by the cascaded dual frame current regulator with a voltage regulator to ensure high-performance of the three phase PWM AC-DC voltage source converter.

The *DC link voltage harmonics control* scheme is employed to provide four current reference commands of the cascaded current controllers in the positive and negative sequence *d-q* frame from the output of the voltage PI controller. Conventionally, the traditional method employed for this cascaded PI controllers design is depended on a locally linearized plant model, it cannot ensure the performance under the global operating conditions. Therefore, either an adaptive gain scheduling controller has to be designed or a fixed-gain PI controller would be used with degraded performance. Hence, the singular perturbation method has been proposed to design the cascaded PI controllers in the rotating *d-q* dual frame for three phase PWM AC-DC voltage source converter. The analysis of this method shows that it is insensitive to the nonlinearities of the system and the variations in the plant parameters. By using this singular perturbation method, two-time-scale motions, namely, *fast motion* sub-system and *slow motion* sub-system, are induced in the closed-loop system. Finally, the closed-loop system can achieve the desired output transient performance by ensuring the stability conditions and properly selecting the time constants for the fast and slow modes of the voltage and current loop, respectively.

Based on the analysis of the distorted supply voltages, the predominant voltage harmonics, 5^{th}, 7^{th} and 11^{th}, 13^{th} order harmonics result in the same frequency

harmonics on the line side currents, which appear as the 6^{th}, 12^{th} order harmonics in the rotating synchronous *d-q* frame. Therefore, *current harmonics control* is mainly used to eliminate the 6^{th} and 12^{th} order harmonics in the *d-q* frame for the line side currents. A plug-in time domain based repetitive controller (TDRC) scheme is developed and employed to achieve low THD line side currents of the three phase PWM AC-DC voltage source converter. The proposed plug-in digital repetitive control scheme can minimize the harmonics in the line side currents while maintaining the dc link voltage constant. Since harmonic components in the time domain are described as functions of time, the system response of the entire cycle will have to be stored for learning and updating. The controller design would be easier, provided the scheme is implemented in the frequency domain than in the time domain, because the repetitive controller in the frequency domain (FDRC) needs only to learn and update two parameters, namely, magnitude and phase. Because FDRC scheme can only learn the selected frequency, FDRC scheme performs like notch filter, which would avoid the integral operation for high band frequencies which are dominated by noise. Also, it is easier to calculate the appropriate phase angle compensation for the individual harmonic frequencies where the phase lag is inevitable from the plant and filters. Hence, FDRC scheme is introduced to replace TDRC scheme to enhance the robustness of the control system. The learning algorithm of FDRC scheme designed in the frequency domain by using Fourier series approximation (FSA) method gives the freedom of choosing different learning gains and phase angle delay compensations individually for each harmonic component, which leads to improved tracking performance for the supply side line currents.

In order to strengthen our research findings, all the proposed methods have been experimentally validated on a 1.6 kVA prototype PWM AC-DC voltage source

converter. With the proposed dual frame control schemes, the even-order harmonic components at the dc link voltage and the odd-order harmonic components in the supply ac line side currents can be minimized and the supply side power factor can be kept close to unity under the unbalanced and distorted supply voltage operating conditions. These findings should encourage the use of three phase PWM AC-DC voltage source converter in high-performance applications such as adjustable speed motor drives under the generalized supply voltage conditions.

Till this stage, the performance of three phase PWM AC-DC voltage source converter is investigated with a resistive load. However, in reality, this converter can be used as the front-end converter of the voltage source inverter (VSI) fed induction motor drive. Due to the time constraints, the performance of the proposed PWM AC-DC voltage source converter could not be examined for the dynamic load conditions and it is left as future work to be carried out.

List of Tables

List of Figures

Acronyms

2SN	Two Switch Network
3SN	Three Switch Network
AC	Alternating Current
ADC	Analog-to-Digital Conversion
ADS	Adjustable Speed Drives
AF	Active Filter
BESS	Battery Energy Storage System
CSR	Current Source Rectifier
DAC	Digital-to-Analog Conversion
DC	Direct Current
DPC	Direct Power Control
DSP	Digital Signal Processor
EMI	Electromagnetic Interference
FDRC	Frequency Domain Based Repetitive Control
FMS	Fast-Motion Sub-system
FSA	Fourier Series Approximation

GTO	Gate-Turn-Off Thyristors
IGBT	Insulated Gate Bipolar Transistor
ILC	Iterative Learning Control
HVDC	High Voltage Direct Current
MOSFET	Metal-Oxide-Semiconductor Field-Effect Transistor
PC	Personal Computer
PFC	Power Factor Corrector
PGA	Programmable Gain Amplifier
PI	Proportional-Integral
PF	Power Factor
PLL	Phase Locked Loop
PWM	Pulse-Width-Modulation
RC	Repetitive Control
SMS	Slow-Motion Sub-system
SMR	Switch-Mode Rectifier
SPLL	Software Phase Locked Loop
SPWM	Sinusoidal Pulse Width Modulation
SRF	Synchronous Reference Frame
SVPWM	Space Vector Pulse Width Modulation
TDRC	Time Domain Based Repetitive Control
THD	Total Harmonics Distortion
TTL	Transistor-Transistor Logic

UPS	Uninterruptible Power Supply
VOC	Voltage Orientated Control
VSI	Voltage Source Inverter
VSR	Voltage Source Rectifier
VCO	Voltage-Controlled Oscillator

Nomenclature

a	coefficient of PWM scheme
a_p	coefficient in the plant transfer function
A_1,A_2	coefficients in the k^{th}-order positive sequence current response
A_c,θ_c	magnitude and phase angle of the closed-loop system $C_{cl}(z)$
A_q,θ_q	magnitude and phase angle of the low-pass filter $Q(z)$
B_1,B_2	coefficients in the k^{th}-order negative sequence current response
C	DC link capacitor
$C_o(z)$	transfer function of the feedback controller
$C_{rc}(z)$	transfer function of the plug-in repetitive controller
$C_s(z)$	transfer function of symmetrical components calculator
C_{sm}	matrix of symmetrical components calculator
d_a, d_b, d_c	duty cycles for three phase
d_{ao}, d_{bo}, d_{co}	switching functions for three phase bottom switches
d_{ap}, d_{bp}, d_{cp}	switching functions for three phase top switches
$D(z)$	disturbance transfer function
e	tracking error

e_a, e_b, e_c	supply voltages in three phase *a*-*b*-*c* frame
e_{a1}, e_{b1}, e_{c1}	three phase fundamental frequency supply voltages
e_a^p,e_b^p,e_c^p	three phase positive sequence supply voltages
e_a^n,e_b^n,e_c^n	three phase negative sequence supply voltages
e_{ab}^p,e_{ab}^n,e_{bc}^p,e_{bc}^n	positive and negative sequence line voltage e_{ab} and e_{bc}
e_d^p,e_q^p,e_d^n,e_q^n	positive and negative sequence supply voltages in *d*-*q* frame
e_{dk}^p,e_{qk}^p,e_{dk}^n,e_{qk}^n	positive and negative sequence k^{th}-order supply voltage harmonics in *d*-*q* frame
e_i	tracking error for inner current loops
e_v	tracking error for outer voltage loop
e_α,e_β	three phase supply voltages in stationary α-β frame
e_α^p,e_β^p,e_α^n,e_β^n	positive and negative sequence supply voltages in α-β frame
$e_{\alpha k}^p$,$e_{\beta k}^p$,$e_{\alpha k}^n$,$e_{\beta k}^n$	positive and negative sequence k^{th}-order supply voltage harmonics in α-β frame
E_a,E_b,E_c	amplitude of three phase supply voltages
E_{a1}	amplitude of the fundamental supply voltage
E^p,E^n,E^o	amplitude of positive, negative and zero sequence voltages
E_k^p,θ_{ek}^p,E_k^n,θ_{ek}^n	amplitude and phase of positive and negative sequence k^{th}-order voltage harmonics
E_s^{in}	input voltage space vector
$E_s'^{in}$	quadrature input voltage space vector
$E(z)$	tracking error transfer function

$f(x)$, $b(x)$	nonlinear functions of the states
f_c	reference signal fundamental frequency
f_s	sampling frequency
F_m	matrix of low pass filter
$F(z)$	transfer function of the analog low-pass filter
$G(z)$	plant transfer function
$G_{current}$	open loop transfer function of inner current loops
G_{dual}	open loop transfer function in the dual frame
G_{open}	open loop transfer function of outer voltage loop
i	average current in positive and negative d-q frame
i^*	current reference in positive and negative d-q frame
i_a,i_b,i_c	input line side currents in three phase a-b-c frame
i_{a1}, i_{b1}, i_{c1}	fundamental frequency input line side currents
i'_a,i'_b,i'_c	three phase input line side currents after filter
i_{dc}	DC link current
i_d^p,i_q^p,i_d^n,i_q^n	input currents in positive and negative d-q frame
i_d^{p*},i_q^{p*},i_d^{n*},i_q^{n*}	currents reference in positive and negative d-q frame
i_α,i_β	line side currents in stationary α-β frame
i_α^p,i_β^p,i_α^n,i_β^n	input currents in positive and negative α-β frame
I_0	DC signal of DC link current
I_{a1},δ_i	amplitude and phase of fundamental line side current i_{a1}
I_{d0}^p,I_{q0}^p,I_{d0}^n,I_{q0}^n	DC signals in positive and negative d-q frame currents
I_{dh}^p,I_{qh}^p,I_{dh}^n,I_{qh}^n	h^{th}-order positive and negative d-q frame current harmonics

I_k^p,θ_{ik}^p,I_k^n,θ_{ik}^n	amplitude and phase of positive and negative sequence k^{th}-order current harmonics
I_{r2sin},I_{r2cos}	amplitude of the 2^{nd} order sin and cos terms in DC current harmonics
I_{r4sin},I_{r4cos}	amplitude of the 4^{th} order sin and cos terms in DC current harmonics
$I_{ra,h}$,$I_{rq,h}$	active and reactive components of the current I_{rh}
I_{rh},ϕ_{ih}	amplitude and phase of the h^{th}-order DC current harmonics
I_s^{in*}	conjugate of current space vector
I_C	IGBT maximum continuous collector current
$H_c(s)$	closed loop transfer function of phase locked loop
k	system gain of fast motion subsystem
k_1,k_2,k_3,k_4	coefficients for current reference calculation
k_a,k_b,k_c	modulation functions for three phase
k_{index}	modulation index
k_i	gain of fast motion subsystem for inner current loops
k_{pf}	ratio of input average reactive power to active power
k_v	gain of fast motion subsystem for outer voltage loop
K_6,K_{12}	learning gain K_{rc} for 6^{th} and 12^{th} order harmonics
K_{rc}	control gain for repetitive controller
K_{pl},K_{il}	proportional and integral gain in phase locked loop
K_{pc},K_{ic}	proportional gain and integral gain for inner current loops
K_{pv},K_{iv}	proportional gain and integral gain for outer voltage loop

l	gain of the fundamental supply voltage e_{d1}^{p}
L	line indctance
M_r,N_r	amplitude of the 2^{nd} order sin and cos terms in DC current harmonics
N	number of samples for each cycle
N_1	phase lag compensator for low-pass filter and plant
N_2	deduction from number N to number N_1
p_{in}	input instantaneous power
P_{loss}	estimated power loss
p_{out}	output instantaneous power
p_L	instantaneous power consumed by inductance L
p_R	instantaneous power consumed by parasitic resistance R
pf	power factor
P_{out}	output average active power
P_o^{in},P_{s2}^{in},P_{c2}^{in}	DC, sin and cos terms in 2^{nd} order harmonics in active input instantaneous power
P_o^{out},P_{s2}^{out},P_{c2}^{out}	DC, sin and cos terms in 2^{nd} order harmonics in active output instantaneous power
P_p,C_p	Park and Clark Transformation for positive sequence components
P_n,C_n	Park and Clark Transformation for negative sequence components

P_p^{-1},C_p^{-1}	Inverse Park and Clark Transformation for positive sequence components
P_n^{-1},C_n^{-1}	Inverse Park and Clark Transformation for negative sequence components
P_m	matrix of plant
$P(z)$	transfer function of plant
Q_{out}	output average reactive power
Q_o^{in},Q_{s2}^{in},Q_{c2}^{in}	DC, sin and cos terms in 2^{nd} order harmonics in reactive input instantaneous power
Q_o^{out},Q_{s2}^{out},Q_{c2}^{out}	DC, sin and cos terms in 2^{nd} order harmonics in reactive output instantaneous power
$Q(z)$	transfer function of low-pass filter in repetitive controller
R	parasitic resistance
R_{dc}	DC link resistive load
R_n,I_n	sin and cos coefficients in fourier series expansion
S	average value of switching function in d-q rotating frame
S_a,S_b,S_c	three phase averaging switching functions
S_α,S_β	three phase control signals in α-β frame
S_α^p,S_β^p,S_α^n,S_β^n	control signals in positive and negative α-β frame
S_d^p,S_q^p,S_d^n,S_q^n	control signals in positive and negative d-q frame
S_{di}^p,S_{qi}^p,S_{di}^n,S_{qi}^n	current harmonics control signals
S_{dv}^p,S_{qv}^p,S_{dv}^n,S_{qv}^n	voltage harmonics control signals

S_x	a x-degree phase-shift operator in the time domain
S^{in}	input complex power
S^{out}	output complex power
$T_e(\theta)$	rotating matrix
T_s	sampling time
$T_{SMS,i}$	time constant of slow motion sub-system for current loop
$T_{FMS,i}$	time constant of fast motion sub-system for current loop
$T_{SMS,v}$	time constant of slow motion sub-system for voltage loop
$T_{FMS,v}$	time constant of fast motion sub-system for voltage loop
T^{in}	quadrature input complex power
T^{out}	quadrature output complex power
u	control signal
u_{an1},u_{bn1},u_{cn1}	fundamental frequency terminal voltages
u_{ao},u_{bo},u_{co}	converter terminal voltages with respect to neutral point o
u_{an},u_{bn},u_{cn}	converter terminal voltages with respect to neutral point n
u_{on}	voltage difference between n and o
u^s	control signal in the quasi-steady state
U_{an1},δ_u	amplitude and phase of the fundamental converter voltage
U_{LL1}	line-to-line fundamental frequency terminal voltage (rms)
U_s^{in}	converter terminal voltage space vector
$U_s^{\prime in}$	quadrature converter terminal voltage space vector
v_{aL},v_{bL},v_{cL}	three phase voltage drop across the line inductance L

v_{aL1}	fundamental frequency voltage across the inductance
v_{dc}	DC link voltage
v_{dc}^{*}	reference value of DC link voltage
V_{rh},ϕ_{vh}	amplitude and phase of the h^{th}-order DC voltage harmonics
V_{CES}	IGBT maximum collector-emitter (direct) voltage
x	state variable in the system
$Y_d(z)$	transfer function of reference signal
$Y(z)$	transfer function of output
α_6,α_{12}	phase compensator for 6^{th} and 12^{th} order harmonics
α_v	phase angle delay compensation at v^{th} order frequency
ϵ	gain variation of the model caused by uncertainty
δ	error between the real and the estimated rotating angle
Δi_d^p,Δi_q^p	AC signal of positive sequence line side currents
Δi_d^n,Δi_q^n	AC signal of negative sequence line side currents
ΔS_d^p,ΔS_q^p	AC signal of positive sequence control signals
ΔS_d^n,ΔS_q^n	AC signal of negative sequence control signals
$\Delta\hat{\omega}$	change in supply voltage angular frequency
$\Delta\hat{\theta}$	increment of phase angle in one sampling time
η_i	degree of time-scale separation for current loop
η_v	degree of time-scale separation for voltage loop
$\gamma(w)$	phase delay in design of TDRC controller
$\gamma_f(w)$	phase delay in design of FDRC controller

$\hat{e}_d^p$	estimated d-axis positive sequence supply voltage
$\hat{\theta}$	estimated angle from phase locked loop
λ	time constant of tracking error
λ_i	time constant of tracking error for current loop
λ_v	time constant of tracking error for voltage loop
μ	small positive parameter for system dynamics
μ_i	small positive parameter for current loop dynamics
μ_v	small positive parameter for voltage loop dynamics
ω	the fundamental frequency (rad/sec)
ω_1	small variation in coefficient vector $\psi_{e,k}$ frequency
ω_c	cut-off frequency of analogy low pass filter
ω_l	learning frequency in repetitive controller
ω_n,ζ	coefficients in the 2^{nd}order system transfer function
ω^*	feedforward frequency command
$\Omega(f(k\Delta T))$	frequency component vector
ϕ_{dh}^p,ϕ_{qh}^p	phase of positive sequence h^{th}-order current harmonics
ϕ_{dh}^n,ϕ_{qh}^n	phase of negative sequence h^{th}-order current harmonics
$\psi_{e,k}$	coefficient vector of error signal
$\psi_{u,k}$	coefficient vector of control signal
$\Psi(f(k\Delta T))$	coefficient vector
ρ	factor in the output average reactive power
τ	complex phasor e^{-j120°

θ	rotating angle which is defined as ωt
θ_e^a,θ_e^b,θ_e^c	phase angle of three phase supply voltages
θ_e^p,θ_e^n,θ_e^o	phase angle of symmetrical sequence supply voltages
ς	small value caused by the variation in frequency
$\vec{e}_{a1}$	phasor of the fundamental supply voltage e_{a1}
$\vec{i}_{a1}$	phasor of the fundamental line side current i_{a1}
$\vec{u}_{an1}$	phasor of the fundamental converter voltage u_{a1}
$\vec{v}_{aL1}$	phasor of the fundamental voltage on inductance v_{aL1}
$\overline{i_{dc}}$,Δi_{dc}	DC signal and AC signal in DC link current
$\overline{i_d^p}$,$\overline{i_q^p}$,$\overline{i_d^n}$,$\overline{i_q^n}$	DC signals in positive and negative d-q frame currents
$\overline{v_{dc}}$,Δv_{dc}	DC signal and AC signal in DC link voltage
$\overline{S_d^p}$,$\overline{S_q^p}$,$\overline{S_d^n}$,$\overline{S_q^n}$	DC signals in positive and negative d-q frame control signals
$\overrightarrow{e_k^p}$, $\overrightarrow{e_k^n}$	space vectors of the k^{th}-order positive and negative sequence supply voltages
$\overrightarrow{i_k^p}$, $\overrightarrow{i_k^n}$	space vectors of the k^{th}-order positive and negative sequence line side currents
$\overrightarrow{u_k^p}$, $\overrightarrow{u_k^n}$	space vectors of the k^{th}-order positive and negative sequence converter voltages

Chapter 1

Introduction

Since power electronic systems provides high efficiency of energy conversion and being environmental friendly, they are used widely to process the available raw source power to meet the load demands of every electrical gadget and equipment. Three phase AC-DC conversion of electrical power is mostly required in adjustable speed drives (ASD), uninterruptible power supplies (UPS), HVDC systems, utility interfaces with non-conventional energy sources such as wind power systems, etc., battery energy storage systems (BESS) for intermittent resources and mobile devices such as electric vehicles, and power supplies for telecommunication systems [1]-[6]. Traditionally, AC-DC converters, known as rectifiers, can provide controlled and uncontrolled DC power by using diodes and thyristors. Those conventional converters have non-sinusoidal currents, poor power factor at input AC mains and low frequency ripples at the DC output voltage and they also need large size of AC and DC side filters. In order to achieve the stringent power quality requirements at the input ac main [7]-[10], a new breed of rectifiers has been developed, such as multilevel rectifiers, multipulse rectifiers, power factor correctors (PFC), etc. [11],[12].

Among all the improved power quality AC-DC converters, the pulsewidth-modulation (PWM) voltage source converter has been increasingly employed for high-performance applications in recent years, because it offers the possibility of bidirectional power flow, low line side current distortions with unity power factor operation and constant DC-link voltage with a small output filter capacitor. However, all the advantages of the PWM voltage source converter are valid only with the assumption of balanced input supply voltage conditions. Nevertheless, the distorted and unbalanced voltage conditions occur frequently in the input supply, particularly in a weak AC system [13]. The performance of the PWM rectifier deteriorates due to the presence of supply voltage harmonics and the negative sequence voltage component under the unbalanced input voltage conditions. Two approaches are feasible to eliminate the harmonics appearing at the output DC link voltage. One approach is to use bulky filters to remove the ripples in the input/output voltage, however, it would slow down the dynamic response of the PWM voltage source converter and cause the system oscillations due to the resonance [14], which might not be acceptable for high performance applications. The other alternative is to use *active control methods* to minimize the harmonics so that small size input/output filters can be used, which would improve the dynamic response of the PWM voltage source converter.

Therefore, the motivation behind this thesis is to model the three phase PWM voltage source converter under the general supply voltage conditions, and to make use of advanced control techniques to achieve ripple-free DC link voltage and sinusoidal ac input currents with a low total harmonic distortion (THD) level under the distorted and unbalanced operating conditions.

1.1 AC-DC Converter Topologies

As has been observed in recent decades, three phase AC-DC converters have been widely used in industrial and domestic applications, such as motor drives and power supplies etc. The AC to DC converters are of many types and can be classified as *uncontrolled* and *controlled* types [1]. Uncontrolled rectifiers are based on power diodes and provide a constant DC output voltage for a fixed ac input voltage. However, many applications such as DC drives require a variable DC output voltage which cannot be achieved with diode bridge rectifies. In order to alleviate this problem, phase-controlled AC-DC converters using the thyristors were introduced which can provide variable DC output voltage from a fixed AC voltage input using phase delay angle control. Both types of semiconductor devices have highly nonlinear characteristics, consequently, harmonic currents are generated on the AC line side. Thus, not only it causes voltage distortions and electromagnetic interferences (EMI) affecting other users of the power distribution system, but also decreases the power factor and increases volt-ampere rating of the power system equipment (generators, transformers, transmission lines, etc.). In particular, several standards [7]-[10] have introduced important and stringent limits on harmonics that can be injected into the power supply. One basic and typical method to reduce input current harmonics is the use of multipulse converters [15]-[19]. They either use a diode bridge or thyristor bridge with a special arrangement of magnetics through transformers and tapped inductors. Although the THD of the supply currents can be reduced to 5%, the converter becomes bulky and the cost of the converter increases.

With the development of new solid state self commutating devices such as

metal-oxide-semiconductor field-effect transistors (MOSFET), insulated gate bipolar transistors (IGBT), gate-turn-off thyristors (GTO), etc., many new switch-mode rectifier (SMR) topologies [20]-[23] have been developed to reduce the distortions in the input currents, so called power factor correction (PFC). In these converters, the controlled power switches are employed to change actively the input currents waveform and consequently the power factor is improved. Several PFC topologies like dual boost and *Vienna* rectifiers [22], [23], are only suitable for the application where power is transmitted from the ac source to the dc load. However, there are many applications that require bi-directional power flow during the operation. An additional improvement on the harmonics reduction is to use passive power filters, active filters (AF), and hybrid filters along with conventional rectifiers [24]-[28]. However, these filters are quite costly, bulky, and lossy, which reduce overall efficiency of the complete system.

Comparing with all these options for three phase improved power quality AC-DC converters, the simple PWM buck/boost rectifier topology as shown in Fig. 1.1 consists of the low-cost three-phase module with bidirectional energy flow capability and high quality input current waveforms. Therefore, it is still preferred to be used for high performance ASD, UPS, etc.

Buck/boost converters produce a regulated output voltage of either less than or greater than the input voltage. When the input voltage is higher than the output voltage, the rectifier is called as a buck converter. When the input voltage is lower than the output voltage, it is said to be a boost converter. In the buck type rectifiers, because of the inductance on the DC side in the circuit, it can provide extremely smooth DC currents to the load, so it is also called *current source*

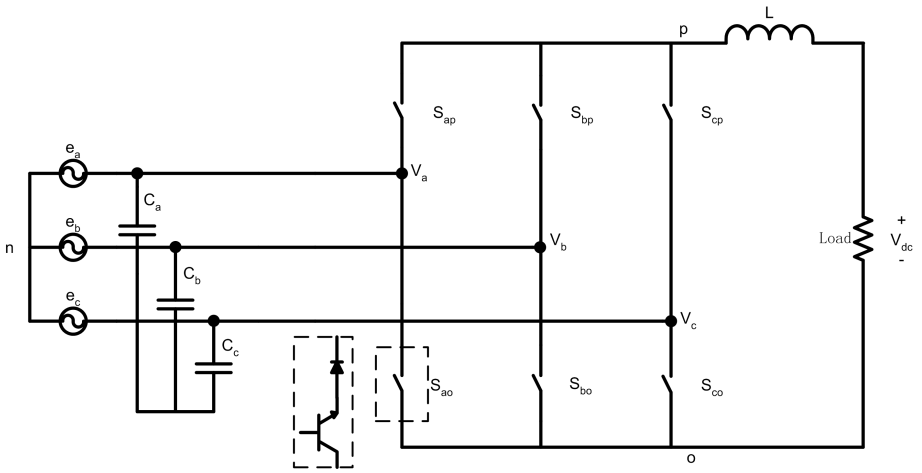

(a) Buck rectifier

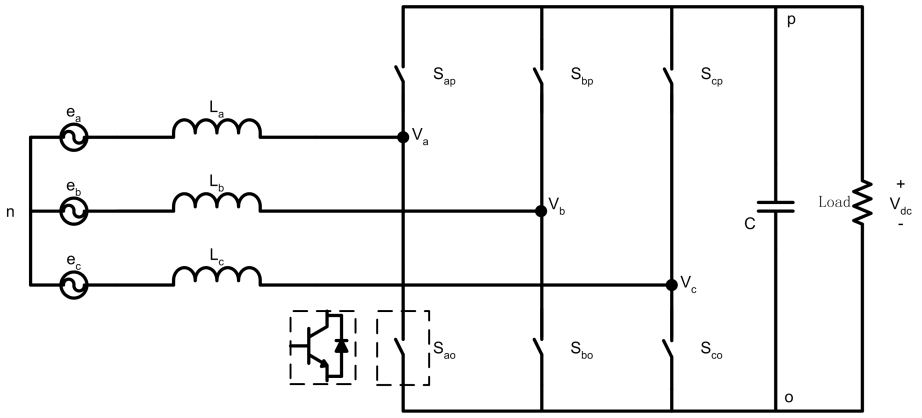

(b) Boost rectifier

Figure 1.1: Basic topologies of rectifiers (a) buck and (b) boost.

rectifiers (CSR). The output of the boost type rectifiers are connected with a DC capacitor, which can offer the stabilized DC link voltage, so it is called *voltage source rectifiers* (VSR). According to the switching network of the converter, the major difference between boost converter and buck converter is the switching structure [29]. Generally speaking, we can define the switching function d_{jk} of a switch jk as:

$$d_{jk} = \begin{cases} 1 & \text{switch } jk \text{ is on} \\ 0 & \text{switch } jk \text{ is off} \end{cases} \quad j = \{a, b, c\}, k = \{p, o\} \tag{1.1}$$

For buck rectifier, as shown in Fig. 1.1 (a), only one of three top switches

and one of three bottom switches can be turned on at the same time. So there are three possible switch states for top or bottom switches at one time. This kind of switching network is called as two single-pole triple-throw switches (Two Switch Network - 2SN) [29]. While boost rectifier in Fig. 1.1 (b) can only turn on one of two switches in each phase at the same time, so that there are two possible switch states for each phase switches at one time. It is called three single-pole double-throw switches (Three Switch Network - 3SN). But for any switching structure, it should be guaranteed that the terminal voltage sources are never shorted and there is always a source to provide the inductor current. Therefore, the switch function of buck rectifier can be expressed as

$$d_{ak} + d_{bk} + d_{ck} = 1, \quad k = \{p, o\} \tag{1.2}$$

And the switch function of boost rectifier can be written as

$$d_{jp} + d_{jo} = 1, \quad j = \{a, b, c\} \tag{1.3}$$

According to (1.2) and (1.3), the independent control of the three bridge legs in each phase is not allowed for Two Switch Network in the buck rectifier, whereas it is possible for Three Switch Network in the boost configuration. For this reason, it is easier to design control scheme for the boost rectifier to reduce the ripples at the output DC voltage. Moreover, the input currents of the buck rectifier are discontinuous, thus the very large filter capacitors should be put on the AC side in order to achieve the sinusoidal currents as shown in Fig. 1.1 (a). Those capacitors absorb the reactive power, as a result, the phase angle between converter input currents and supply voltages cannot be regulated. Therefore, in the area of the variable speed AC drives, it is believed that three-phase PWM AC-DC voltage source converter will replace the diode rectifier as the front-end converter in the near future. It is desirable to have the following characteristics for a three-phase

PWM AC-DC voltage source converter:

- Controlled ripple-free DC output voltage
- Close to sinusoidal input phase current
- Unity power factor
- Regenerative capability
- Load disturbance rejection
- High dynamic performance
- Small capacitor in the DC link

Besides that, three-phase PWM AC-DC voltage source converter has some other useful properties, such as the DC link voltage higher than the AC supply voltage amplitude and the possibility of being integrated into one module. On all accounts, the PWM voltage source converter is suitable to be employed not only in drive systems but also in reactive power compensators and power supply systems.

1.2 Operating Principle of PWM Voltage Source Converter

The power circuit configuration of a three-phase PWM AC-DC voltage source converter is shown in Fig. 1.2. The line inductance L is used to suppress the harmonics in the line side current supplies. The DC link voltage V_{dc} is established by charging the capacitor C through the switch-mode converter.

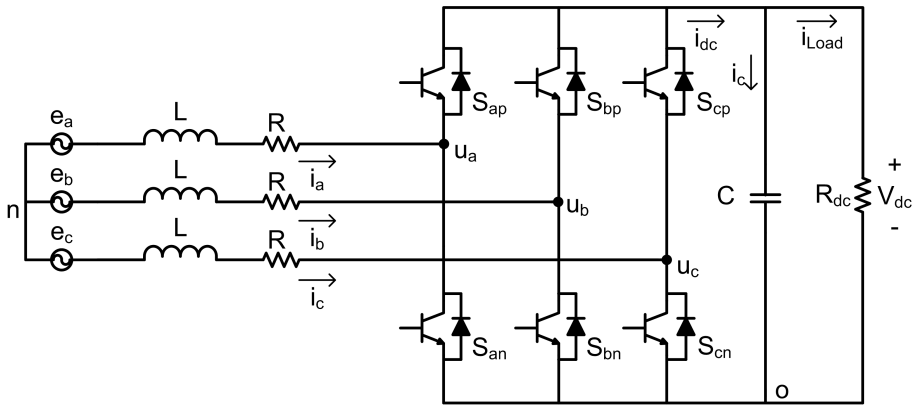

Figure 1.2: The three-phase PWM AC-DC voltage source converter circuit.

If all the parameters in the three phases are identical, we can use any one phase to represent the whole circuit. It is commonly known that the fundamental-frequency components of the three phase supply voltages $e_{a1}(t)$, $e_{b1}(t)$ and $e_{c1}(t)$ and the corresponding fundamental currents $i_{a1}(t)$, $i_{b1}(t)$ and $i_{c1}(t)$ are responsible for the useful power transfer. By ignoring the voltage drop across the parasitic resistance R, the basic circuit equation for the fundamental components in phase a can be expressed as,

$$e_{a1}(t) = u_{an1}(t) + v_{aL1}(t) \tag{1.4}$$

The phasor form of (1.4) can be expressed as (1.5), and the corresponding phasor diagram is shown in Fig. 1.3 (a).

$$\bar{e}_{a1} = \bar{u}_{an1} + \bar{v}_{aL1} \tag{1.5}$$

where $\bar{v}_{aL1}$ is the fundamental frequency component of voltage drop across the inductance, $\bar{v}_{aL1} = j\omega L\bar{i}_{a1}$.

Therefore, the fundamental component of the line side current can be written as,

$$\bar{i}_{a1} = \frac{\bar{e}_{a1} - \bar{u}_{an1}}{j\omega L} \tag{1.6}$$

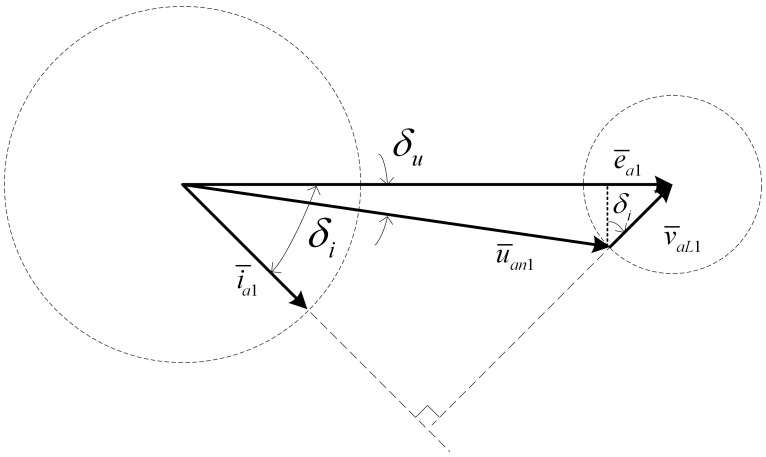

(a) Phasor diagram

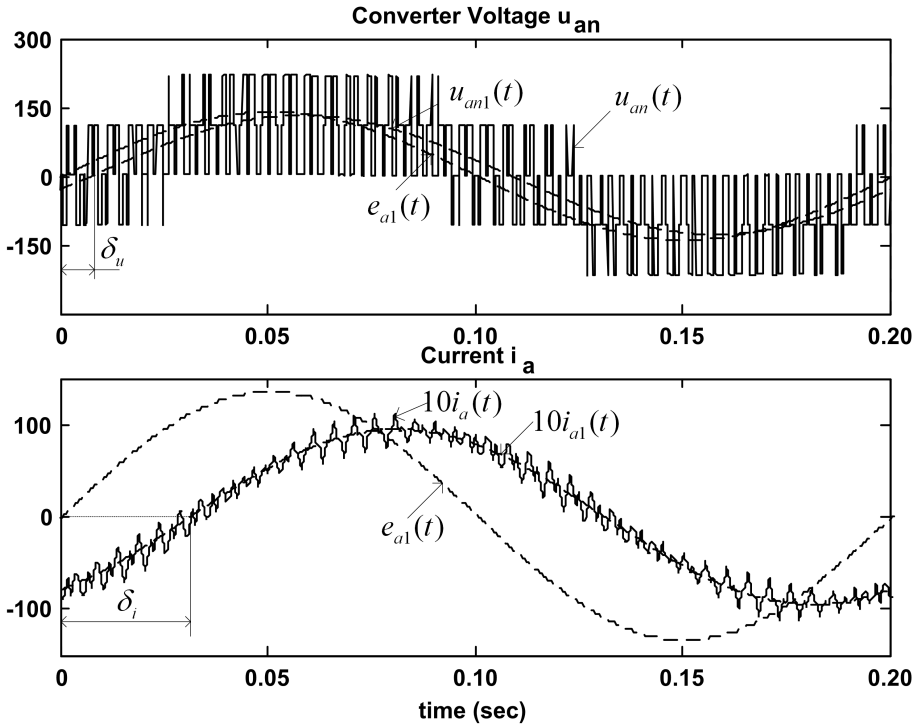

(b) Voltage and current waveforms

Figure 1.3: Waveforms of PWM converter in the rectifier mode.

The equation (1.6) shows that the phase angle δ_i and the magnitude I_{a1} of the fundamental line side current $\bar{i}_{a1}$ is decided indirectly by the angle δ_u and the amplitude U_{an1} of the fundamental converter voltage $\bar{u}_{an1}$.

From the phasor diagram in Fig. 1.3 (a), we can obtain the relations,

$$V_{aL1}\cos\delta_i = \omega L I_{a1}\cos\delta_i = U_{an1}\sin\delta_u \tag{1.7}$$

$$V_{aL1}\sin\delta_i = \omega L I_{a1}\sin\delta_i = E_{a1} - U_{an1}\cos\delta_u \tag{1.8}$$

Applying (1.7), the real power P_{in} supplied by the AC source to the converter is

$$P_{in} = E_{a1}I_{a1}\cos\delta_i = \frac{E_{a1}^2}{\omega L}\left(\frac{U_{an1}}{E_{a1}}\sin\delta_u\right) \tag{1.9}$$

The equation (1.9) shows that when the converter voltage $\bar{u}_{an1}$ applied to the load lags $\bar{e}_{a1}$ by the angle δ_u, that is, δ_u is positive value, so the real power is positive, and at that time, the converter is said to be operating in the *rectifier* mode where power flows from the ac supply side to the dc load side, while when the converter voltage $\bar{u}_{an1}$ leads $\bar{e}_{a1}$ by the angle δ_u is negative, so the real power is negative, the converter works as an *inverter* and the direction of power flow reverses. It also can be observed that the equation (1.9) is the same as a synchronous machine connected to utility where receiving end and sending end are separated by an inductance.

In the same way, the reactive power Q_{in} supplied by AC source can be expressed by using (1.8),

$$Q_{in} = E_{a1}I_{a1}\sin\delta_i = \frac{E_{a1}^2}{\omega L}\left(1 - \frac{U_{an1}}{E_{a1}}\cos\delta_u\right) \tag{1.10}$$

It is noted that Q_{in} is the sum of the reactive power absorbed by the converter and the reactive power consumed by the inductance L.

The steady state voltage and current waveforms for *rectifier* operation shown in Fig. 1.3 (b) matches the phasor diagram. It is clear that the power factor is determined by the phase delay δ_i between the supply voltage $\bar{e}_{a1}$ and the fundamental

line side current $\bar{i}_{a1}$. When $\bar{u}_{an1}$ is varied, the voltage drop across the inductance L can be adjusted, which leads to the desired line side current. Thus, for a given supply voltage and chosen inductance, the values of the active power P_{in} and the reactive power Q_{in} can be controlled by changing the magnitude U_{an1} and the phase δ_u of the converter voltage $\bar{u}_{an1}$ [30]. In this way, the component of $\bar{u}_{an1}$, which is perpendicular to supply voltage $\bar{e}_{a1}$, decides the active power proportionally. On the other hand, the reactive power can be controlled independently with the component of $\bar{u}_{an1}$ in phase with the supply voltage $\bar{e}_{a1}$.

Therefore, the key to provide the desired active output power and the controllable reactive power is to generate the proper switching signals for switches in the three legs of voltage source converter which decides the required fundamental converter voltage $\bar{u}_{an1}$. Changing the amplitude U_{an1} of this fundamental component and its phase shift δ_u with respect to the supply voltage e_{a1}, the three phase PWM voltage source converter can provide the regulated DC link voltage and low distorted line side currents with close to the unity power factor operation.

1.3 Problem Statement

Since the boost PWM rectifier offers several advanced features such as the sinusoidal input currents with unity power factor operation and simultaneous high quality dc output voltage with small size dc side filter, it has been increasingly used in the recent years. However, all the advantages for the PWM rectifier only work with the implicit assumption of the balanced supply voltage conditions. Nevertheless, evaluation of real operating conditions shows that this assumption is false

in nearly every case. The unbalance and distortion in the supply voltages occurs frequently, particularly in a weak ac system.

The major causes of the unbalanced voltage are that single phase loads in the system are not uniformly distributed among the three phases in some rural electric systems or that heavy single phase demands are imposed by some facilities in large urban power systems. Also, the the unbalanced condition can be caused by the load switching, a nonsymmetrical transformer winding or transmission impedances, open wye, open delta, etc. Both the power quality standards EN 50160 and IEEE Std.1159 define the normal operating range is typically from 90% to 110% of the nominal voltage [8],[9]. In addition, EN 50160 standard allows the duration of voltage sag to be less than 1 second and the voltage drops rarely below 40% [13].

In the power distribution networks, the voltage waveform is never exactly a perfect single frequency sine wave. The main contribution to harmonic voltage distortions is due to nonlinear loads. A growing part of the load is fed through power electronics converters, such as silicon controlled rectifiers and variable speed drives and etc., drawing nonsinusoidal currents. The harmonic current components cause harmonic voltage components, and thus a nonsinusoidal voltage, in the system. It is not uncommon to have current THD level as high as 25% within some industrial settings [13]. Standard EN 50160 gives limits for the harmonic voltages in grids that the 5^{th} order harmonics and the 7^{th} order harmonics should not exceed 6% and 5% of the nominal voltage, respectively [9].

Under the unbalanced and distorted input voltage conditions, the performance of three phase PWM AC-DC voltage source converter is deteriorated by

the negative sequence voltage and voltage harmonics. In [31] and [32], it has been shown that unbalanced supply voltage leads to the appearance of an abnormal second harmonic component at the converter dc output terminals. In turn, it reflects back to the input causing a third-order harmonic current to flow. Next, the third-order harmonic component causes a fourth-order harmonic voltage on the dc side. As a result, the unbalanced supply voltage conditions lead to even-order harmonics at the dc output voltage and low frequency odd-order harmonics in the input ac currents [33]. Also, the distorted supply voltages cause the harmonic component of the supply voltage harmonics frequency in the input line side currents [34]. Hence, the abnormal low frequency harmonics both on the ac and dc side under the unbalanced and distorted operating conditions completely offset several advantages of three phase PWM rectifiers.

However, most of the high performance industrial applications require that the DC output of the voltage supplies can be regulated to be within a specified tolerance band (e.g., $\pm 1\%$ around its nominal value) in response to changes in the output load and the input line voltages [1]. Besides, it is recommended that the THD of the harmonic currents injected into the utility system from power electronic equipment and other nonlinear loads should be less than 8% [10].

In order to guarantee that three phase PWM rectifiers are able to keep the DC link voltage constant and does not inject more harmonic currents into the distribution system under unbalanced and distorted supply voltage conditions, there are two possible approaches feasible. One approach is to use bulky filter circuits to remove the ripples in the output voltage and input currents [14], [35]. However, it would slow down the dynamic response of the PWM boost rectifier and cause the

system oscillations due to the resonance [14], also increase the size of the converter. The other alternative is to use active control schemes to minimize the harmonics so that small size input/output filters can be used and the dynamic response of the PWM rectifier can be ensured. Hence, this approach is more suitable for the high performance applications which require a ripple-free DC output voltage and low THD line side currents with close to unity power factor operation.

Therefore, the major focus of our study is to provide three phase PWM AC-DC voltage source converters under the unbalanced and distorted operating conditions with the active control solution to eliminate the even-order harmonics at the dc voltage, keep the input ac line currents sinusoidal and maintain close to unity power factor and low THD operation.

1.4 Literature Review

Over the past few years, there have been extensive studies on the control methods for three phase PWM AC-DC voltage source converters to eliminate the harmonics at the dc link voltage and keep the input ac line side current sinusoidal under the unbalanced input supplies [31]-[70]. Rioual et al. [36] have proven that there are the second-order harmonics in the instantaneous active and reactive power when three phase PWM AC-DC voltage source converter operates under the unbalanced operating conditions. Most of the control methods compensating for the unbalanced supply voltage in the preceding works can be classified depending on the method to regulate the active and reactive power.

As suggested in [37], we can establish an intimate relationship between con-

trol of PWM rectifier and control of an induction motor drive, as shown in Fig. 1.4. The speed control loop of the induction motor drive corresponds to dc link voltage control for PWM rectifier. The motor torque reference obtained from the speed control loop is analogous to the active power reference from the dc link voltage control. The motor torque and the active power reference are indirectly controlled by the q-axis current in both the systems, respectively. The flux control for induction motor drives can be considered similar to the reactive power control for PWM rectifiers, which both are related to the current in the d-axis in the each system.

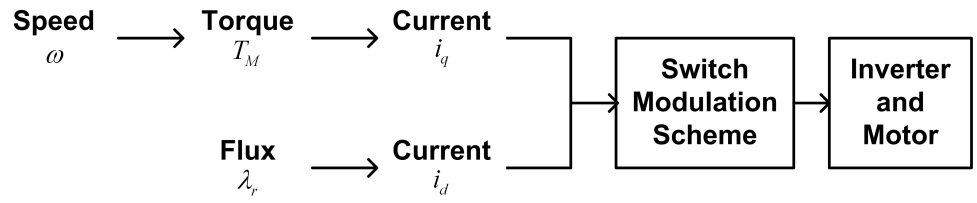

(a) Field oriented control of induction machine

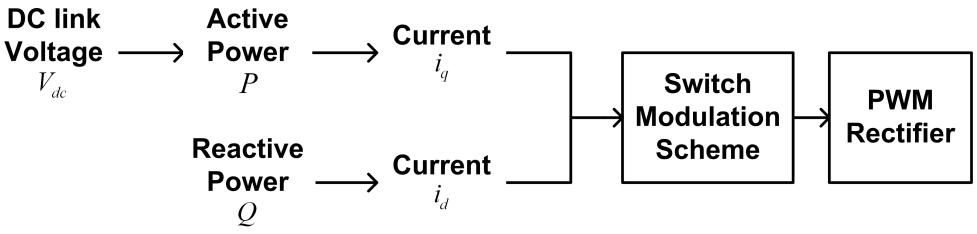

(b) Voltage oriented control of PWM rectifier

Figure 1.4: Control structure of induction machine and PWM rectifier.

As an analogous system with induction motor drives, the control strategies of three phase PWM rectifier can be divided into the two major categories. One strategy is *Voltage Oriented Control* (VOC), which is to regulate the active and reactive power indirectly by the respective currents, the other strategy is called *Direct Power Control* (DPC), which is to control the active and reactive power of the three phase PWM rectifier directly [38]. This idea is similar to the control strategy of *Direct Torque Control* (DTC) for the induction motor drives [39].

1.4.1 Voltage Oriented Control

In voltage oriented control (VOC) scheme, the DC voltage regulation is ensured by the outer voltage control loop and the unity power factor is met by controlling the inner current loops to make the current vector in phase with the supply voltage vector according to the operating principles discussed in Section 1.2. In VOC, the high dynamic and static performances are guaranteed via internal current control loops. Consequently, the final configuration and performance of the VOC system largely depends on the quality of the applied current control strategy [40].

Many researchers have analyzed the influences of the unbalanced supply voltage and provided the control schemes such as input power regulation method and output power regulation method, etc., as reported in [43]-[60]. In order to get rid of the additional hardware or corresponding software such as PLL circuit and make the implementation easier, the control schemes in [43], [44], [45] have been proposed in the *a*-*b*-*c* reference frame. However, because there is no direct relationship between the currents in the *a*-*b*-*c* reference frame and the instantaneous active and reactive power, the performance of the power regulation is degraded. To overcome this problem, Verdelho [46] has presented the the control schemes in the stationary α-β frame, the rotating synchronous *d*-*q* frame.

In the stationary α-β frame, the currents appear as sinusoidal even in the balanced operating condition, so simple linear controllers such as PI controller cannot handle this kind of tracking problem. While in the rotating synchronous *d*-*q* frame, the current signals are converted into the dc components i_d and i_q, hence, the controller is only required to deal with the regulation problem, which is

possible to handle by the simple PI controller. Therefore, the current controllers implemented in the rotating synchronous *d-q* frame are preferred, as shown in Fig. 1.5.

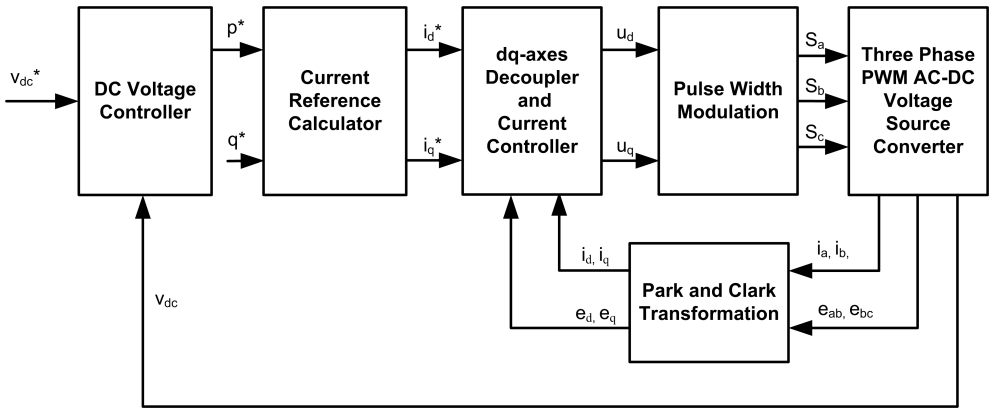

Figure 1.5: Simplified block diagram of the VOC scheme.

The reference active power is obtained from the output of the outer DC voltage controller. Then, together with the reference reactive power, the reference *d-q*-axes currents can be calculated. The inner current control loops are responsible to regulate the actual *d-q* currents at the reference level. As a result, the control objective to remove the harmonics at the dc link voltage is supposed to be achieved. However, under the unbalanced supply voltage conditions, the currents in the rotating synchronous *d-q* frame are not exactly constant because of the appearance of the negative sequence components in the currents and therefore, it poses problems for the current controllers.

In [47], the positive and negative sequence components of the input voltage are first considered in the control scheme. Rioual et al. [48] have proposed a generalized model of the PWM rectifier and determine the positive and negative sequence current commands in order to keep the dc link voltage constant and the average value of reactive power zero. In this scheme, the negative sequence command is

transformed into the positive synchronous reference frame (SRF), which appears as a second order harmonics. However, it is difficult to extend the control bandwidth wide enough to track this command.

To solve this problem, Song et al. [49], [50] and Suh et al. [51], [52] calculated the four reference currents based on the models built in the separated positive and negative SRFs and the current control is implemented with the four feedback PI controllers. However, these dual current regulators of positive and negative rotating synchronous frames in their works suffered from the limitation of current feedback loop bandwidth leading to the unsatisfactory transient responses. It is mainly due to the low pass filter and the notch filter employed in the functional block of extracting the positive and negative sequence components of the three phase line side currents.

In order to avoid the measurement delay or phase delay generated by the filters in the complicated calculation for separating the positive and negative sequence components, Ahn and Hyun [53] and Suh et al. [54] redefined the d-q components in the positive and negative rotating synchronous frame to simplify the calculation of the symmetrical components. Consequently, the d-q components in the dual frame are no longer constant, instead the second order harmonics were involved in the reference currents. Although this method relieves the stress on the limitation of the controller bandwidth, it brought the control problem back to the tracking task from regulation task.

From the power flow point of view, Rioual et al. [48] and Song et al. [49] had proposed the control scheme to regulate the instantaneous active power at the

input side of the voltage source converter under the unbalanced supply voltage conditions. However, under the unbalanced supply situations, even when the input power is maintained to be a constant, the output power of the rectifier is not constant due to nonzero instantaneous power on the line side inductances.

Stankovic and Lipo [55]-[57] addressed this problem and proposed a corresponding current reference calculation method based on the generalized converter model. However, the proposed control algorithm uses the definition of phasor notation that requires the calculation the phase amplitude and angle for a certain frequency. Moreover, this method utilizes the model to build the feed-forward compensations for the fundamental frequency rather than to regulate the instantaneous power explicitly so that it is not suitable for implementation with the feedback controller.

Chomat and Schreier [58], [59] also put forward a solution for the power regulation problem. Their proposed control scheme is to derive the control signals based on the DC link current regulation, which can maintain the output instantaneous output power directly. But this control signal derivation is model based, hence, the performance is sensitive to the circuit parameters and the measurement. This causes that the system can only work under the designed operating range.

Suh et al. [51]-[52], [54] and Yin et al. [60] proposed the mathematical model to regulate the instantaneous active power at the terminal of the converter, but the penalty is to increase the complexity of implementation significantly due to the requirement of solving a set of nonlinear equations in real-time.

1.4.2 Direct Power Control

Another control strategy, called direct power control (DPC), is based on the instantaneous active and reactive power control loops. In DPC, there are no internal current control loops and no PWM modulator block, because the converter switching states are appropriately selected by a switching table based on the instantaneous errors between the commanded and estimated values of active and reactive power. Therefore, the key point for implementation of the DPC system is a correct and fast estimation of the active and reactive line power [64].

In [64], the authors established the algorithm to calculate the instantaneous active and reactive power for the control purposes. This algorithm is based on the voltage source angular position and the derivative of the currents in the rotational reference frame. Although in the final expression of the controller only the active and reactive powers are involved, the nature of the controller is still related to the currents and the derivative of the currents make the system easily unstable. In addition, the method still needs a PWM block to generate the final control vector. Therefore, this technique cannot be considered as direct in the terminology that we use.

Noguchi [62] brought out the idea of DPC, which consists of selecting a control vector from a look-up table based on the error of active and reactive power as well as on the angular position of the estimated voltage source vector. This scheme is to regulate the dc link voltage by controlling the active power, while the unity power factor operation is achieved by controlling the reactive power to zero. In order to reduce the number of the voltage sensors and to simplify the implementation, the

authors proposed an estimation algorithm for the voltage vector. Unfortunately, this algorithm involves the computation of the derivative of the measured currents, so the computation may become noisy, especially at low currents, and it is strongly dependent on the plant parameters like the inductance.

Malinowski et al. [63] followed a similar control scheme as in [62], but they proposed to estimate a vector named virtual flux instead of the voltage source vector. Fig. 1.6 shows the block diagram of the most of the used DPC system. The instantaneous active and reactive power can be obtained from the estimated virtual flux and measured currents. The outputs of the power controller go through a switching table to decide the converter switching states appropriately. With this modification, Malinowski et al. [63] tried to reduce the extremely large sampling frequency required in the original DPC, as well as the inherent noise introduced in the computation of real and reactive power. The estimation algorithm is basically the integration of the injected voltage plus the voltage drop in the inductance. This technique, although inherently very practical, may be sensitive to inductance parameter variations and to initial conditions. Moreover, this algorithm requires a large value of the inductance and still needs a high sampling frequency, and results in variable switching frequency.

To alleviate the problem for the variable switching frequency, Malinowski et al. [65], [66] substituted the modulation strategy from a switching table method to the space vector modulation, which can guarantee a constant switching frequency. Also, Serpa et al. [67] tried to use the alternative method to solve this problem. In [67], the decoupling hysteresis controller was proposed to reduce the three phase current interaction, so that the switching frequency becoming more uniform and

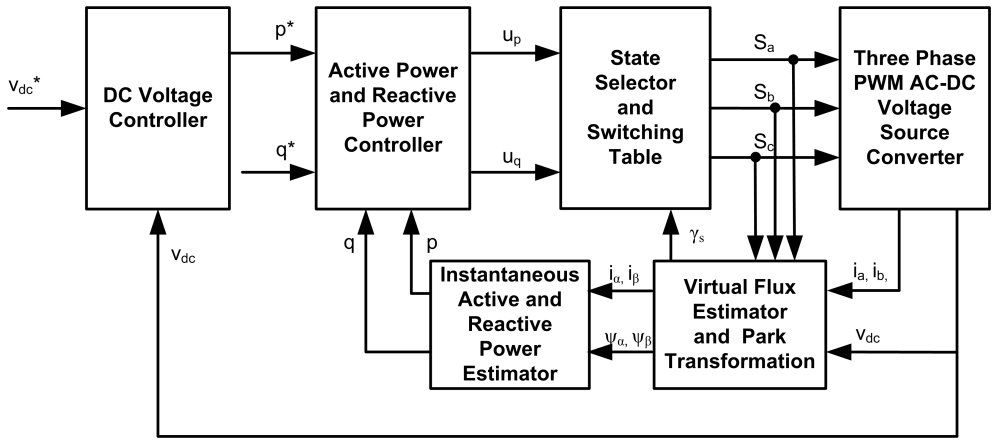

Figure 1.6: Simplified block diagram of the DPC scheme.

allows for a near constant switching frequency if a variable hysteresis band is implemented. However, all the works are based on the assumption of sinusoidal balanced supply voltage.

Komatsu and Kawabata [68] improved the algorithm for the instantaneous active and reactive power calculation to make it suitable for the unsymmetrical voltage system. But this method only can obtain the instantaneous active and reactive power in the input side of the voltage source converter, consequently, the output active and reactive power cannot be estimated accurately.

Escobar et al. [69] modified the original DPC algorithm by utilizing the concept of output regulation subspaces. Generally, this modified controller changes the origin of the space to make the selection of the control inputs more accurate, so that the voltage source converter can deal with unbalance and distortions in the supply voltage. The drawback of this method is that the complexity of computation increases significantly.

Cichowlas [70] improved the phase locked loop to synchronize the positive

sequence precisely and quickly under the unbalanced supply voltage conditions. But the controller in [70] only works on the positive sequence components, so the ripples in the dc link voltage under the unbalanced supply still cannot be eliminated properly.

The DPC system constitutes a viable alternative to the VOC of three phase PWM AC-DC voltage source converters, but this solution should have high sampling frequency, in response to obtain the estimated instantaneous active and reactive power accurately. As a result, the fast microprocessor and A/D converters are required. Due to the strict requirements of implementation, this method is not as popular as compared to VOC.

1.5 Contribution of this Thesis

As described in the literature survey on three phase PWM AC-DC voltage source converter, although most of the research works eliminate the harmonics at the dc link voltage under the unbalanced supply voltages by regulating the instantaneous power flow, there are no detailed investigations to explain the direct relationship between the instantaneous power and the ripples in the dc link voltage. Moreover, few control schemes have been considered to directly deal with the harmonics in the ac line side currents under the unbalanced supply voltages, which can hardly handle the supply current harmonics when the supply voltages are distorted. Hence, this thesis is aimed at developing an active control solution to eliminate the even-order harmonics at the dc voltage, to keep the input ac current sinusoidal and to maintain the unity power factor and low THD operation under the distorted and

unbalanced supply voltage conditions. The contributions of this thesis work are listed as following:

- A new mathematical model has been developed for the three phase PWM AC-DC voltage source converter in positive and negative synchronous rotating frames under the distorted and unbalanced operating conditions. Based on this mathematical model, a detailed explanation can be given on the appearance of the even-order harmonics at the dc link voltage and odd-order harmonics in the ac line side currents under the distorted and unbalanced supply voltages.

- The analytical expression of the instantaneous power flow has been obtained from the proposed mathematical model. This instantaneous power expression not only gives a clear picture about the link to the ripples in the dc link voltage, but also provides an insight into the way to improve the performance of three phase PWM AC-DC voltage source converter under the generalized supply voltages by power regulation.

- In order to eliminate the even-order harmonics at the dc link voltage and the odd-order harmonics in the ac line side currents, the control scheme can be divided into two parts, *DC link voltage harmonics control* scheme and *AC line side current harmonics control* scheme. For the purpose of *voltage harmonics control*, the cascaded PI dual rotating frame controller has been developed to make sure that the dc link voltage is maintained constant and the supply side power factor is kept close to unity. Unlink the conventional PI controller design relying on a locally linearized plant model, the nonlinear control approach, singular perturbation method has been adopted and two-time-scale motions are introduced to give a detailed dynamic analysis of the

whole control system.

- *Current harmonics control* is mainly to eliminate the 6^{th} and 12^{th} order harmonics in the *d-q* frame line side currents. A plug-in time domain based repetitive controller (TDRC) is developed and employed to achieve the low THD line side currents of the three phase PWM AC-DC voltage source converter. This scheme can improve the ac input currents and the dc output voltage tracking accuracy substantially under the distorted and unbalanced supply voltage conditions.

- The plug-in frequency domain based repetitive controller (FDRC) has been proposed to further minimize the odd-order harmonics in the line side currents. The repetitive control learning algorithm is designed in frequency domain, by using Fourier series approximation (FSA) method, provides the flexibility of choosing different learning gains and phase delay compensations individually for each harmonic component. This control scheme leads to the improved tracking performance for the ac line side currents.

1.6 Experimental Setup for the Thesis Work

To verify the feasibility of the proposed control scheme, the experiments for three phase PWM AC-DC voltage source converter were conducted to compare with the conventional controller, under the distorted and unbalanced operating conditions. The hardware prototype is described here.

Fig.1.7 shows a block diagram of our experimental setup. Here is a list of modules used in the experimental platform:

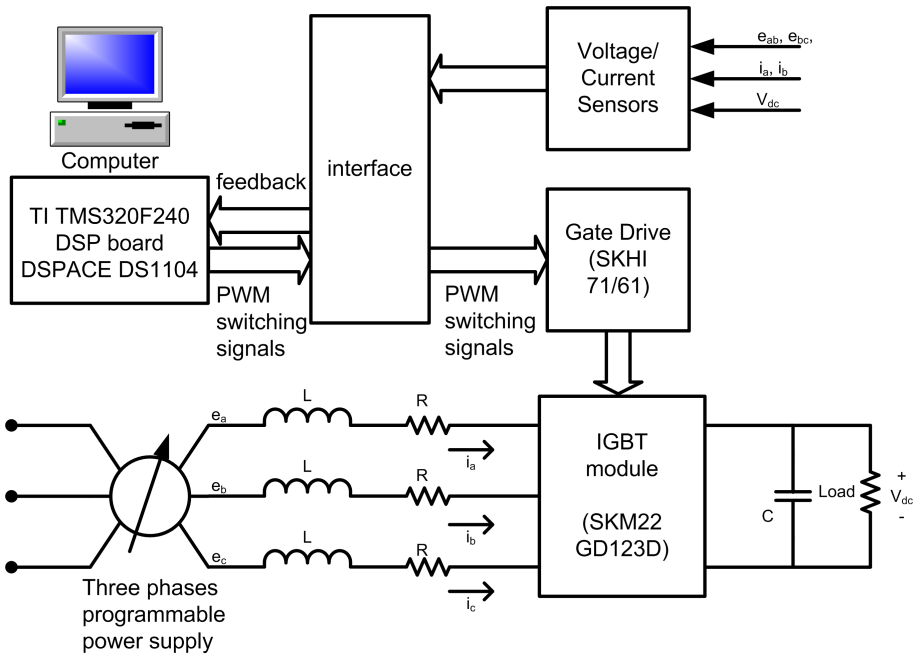

Figure 1.7: Experimental Setup.

- Three phase programmable power supply
- Digital controller for implementing the control algorithm
- Power converter and Driver
- Voltage sensors
- Current sensors
- Signal pre-processing boards

We will implement the proposed controller in our lab platform as shown in Fig. 1.7. The control development platform is DSPACE DSP system (DS1104), which uses a floating processor MPC8240 as the main processor, and a TMS320F240 motion control DSP. The PC interface of the DSP controller provides an easy development environment. The DSP controller has four A/D and D/A channels. The three phase supply voltage e_a, e_b and e_c, the dc link voltage v_{dc}, and the two line side

current i_a and i_b are measured. All the signals are scaled and filtered before fed back via the A/D channels. At the beginning, one 100Ω resistance is usd for loading the PWM boost rectifier. All the control algorithms developed are written in 'C' programming and downloaded in the DSP chip. The IGBT module adopted the symmetric PWM modulation at a 20 kHz switching frequency.

1.6.1 Programmable Power Supply

California Instruments 3000Lx has been used as the three phase programmable power supply for the prototype three phase PWM AC-DC voltage source converter. By combining a flexible AC power source with a high-end harmonic power analyzer, the power supply systems are capable of handling applications that would traditionally have required multiple instruments. With precise output regulation and accuracy, high load drive current, multi or single phase mode and built-in power analyzer measurement capabilities, this ac source address many application areas for AC power testing. Moreover, it provides sine and clipped sine waveforms in addition to user defined arbitrary waveforms. Harmonic waveforms can be used to test for harmonics susceptibility of a unit under test. To simulate common line disturbance occurrences, this supply offers a list of transient steps. All these setting can be programmed from the front panel or downloaded over the interface using the GUI program supplied. This supply equipped with IEEE-488 (GPIB) and RS232C remote control interfaces and support SCPI command language programming.

1.6.2 Digital Controller

The dSPACE R&D Controller Board (DS1104) has been used for testing the control algorithms. The DSP processor TI TMS320F240 was employed with 10 kHz sampling rate in the control board. Some of its special features are as follows:

1.6.2.1 Hardware Features

- It is plugged into a PCI slot of a PC.
- It is a complete real-time control system based on a 603 PowerPC floating-point processor running at 250 MHz
- Memory
  - Global memory: 32 MB SDRAM
  - Flash memory: 8 MB
- Timer
  - sample rate timer (decrementer): 32-bit down counter, reload by software, $40\,ns$ resolution
  - 4 general purpose timer: 32-bit down counter, reload by hardware, $80\,ns$ resolution
- Interrupt
  - 5 timer interrupts
  - 2 incremental encoder index line interrupts
- ADC

  - 4 multiplexed channels equipped with one 16-bit sample & hold ADC, 10 V input voltage range, 2 ms conversion time
  - 4 channels each equipped with one 12-bit sample & hold ADC, 10 V input voltage range, 800 ns conversion time

- DAC
  - Eight 16-bit resolution, 10 V output voltage range, 5 mA maximum output current Max. 10 ms settling time

- Digital I/O
  - 20-bit parallel I/O Single bit selectable for input or output 5 mA maximum output current TTL output/input levels

- PWM output Texas Instruments TMS320F240 DSP 16-bit fixed-point processor 20 MHz clock frequency slave DSP subsystem for timing signal generation
  - 3-phase PWM output
  - 14-bit digital I/O

1.6.2.2 Software Features

'ControlDesk' is dSPACE's software for carrying out experiments, a graphical user interface for managing the dSPACE boards. It provides all the functions to control, monitor and automate experiments and make the development of controllers more efficient. The dSPACE Real-Time Library, the real-time core software with a C programming interface is provided to help access the hardware I/O for implementation of the controller. Instrumentation offers a variety of virtual instruments

to build and configure virtual instrument panels according the one's needs. Input instruments allow to change parameter values online. Any set of instruments can be combined to produce a virtual instrument panel that is specific to the application. In addition, Instrumentation provides data acquisition instruments from the application running on the real-time platform.

The control algorithms developed as discussed in this thesis are written in 'C' programming language and have been verified on this experimental platform.

1.6.3 Power Converter and Drive

This power converter, three phase PWM AC-DC voltage source converter, comprises a three phase IGBT bridge with three 5.5 mH line side smooth inductances in series. The dc link of the three phase bridge is connected with a 200 μF capacitor and a resistive load. The driver signals to three phase voltage source converter are provided by the PWM output of the dSPACE R&D Controller Board via a shield flat-ribbon cable. The detail description of the power and drive modules are referred to Appendix E.

1.6.4 Voltage Sensor

Two voltage sensors are used for independent measurement of the two supply line voltages e_{ab} and e_{bc}. The multi-range (10-500V) LEM Module LV 25-P voltage transducers are employed. The conversion ratio is 2500:1000. The resistor on the primary side is $60\,k\Omega$ and the secondary $300\,\Omega$ resistor is connected to convert the

sensed current signal into an equivalent voltage signal. With the above setting, the calibrated voltage signal is given by $0.0125\,V/V$. Finally, the circuit board containing the two voltage sensors is put inside another shielding box to minimize the EMI effect.

1.6.5 Current Sensor

Two current sensors are used for independent measurement of the two line side currents. Here, multi-range (5-8-12-25A) LEM Module LA 25-NP current transducers are used. In this application, primary to secondary turns ratio is selected to be 1:1000 (thereby the current range becomes $25\,A$). Across the output, $300\,\Omega$ resistor is connected to convert the sensed current signal into an equivalent voltage signal. With the above turns ratio, the calibrated voltage signal is given by $0.3\,V/A$. Finally, the circuit board containing the two current sensors is put inside another shielding box to minimize the EMI effect.

1.6.6 Signal Pre-processing Boards

The DSP interfacing circuits consist of filters for line side current signals, supply side line voltage signals, and dc link voltage signal. Filters are required for the current and voltage signals since they generally come from noisy environment and it is necessary to minimize their noise content before feeding them into DSP for processing. They also act as anti-aliasing filters for the digital controller. According to 'Sharon's Sampling Theorem', the analog input to a digital system should not contain any frequency component beyond half the sampling frequency of the digital

system. The sensed signals from the line side currents and voltages contain the switching frequency 20 kHz, so that this switching frequency should be filtered out before the signals is fed back to digital controller. These two issues determine the cut-off frequencies for the filters. In the present implementation, second order low-pass Butterworth filters are used. The cut-off frequencies are chosen to be 1 kHz. Further, programmable gain amplifiers (PGAs) with a gain of 2 have been used in the filters to ensure the full load current spans the input range of the the ADC converters ($\pm 10\,V$). With this PGA gain, the current signals are calibrated as $1.6667\,A/V$. The outputs of the PGAs are connected to the ADC inputs of the DSP connector board.

1.7 Organization of This Report

Chapter 1 has introduced the background of the thesis work. Basic operation of three phase PWM AC-DC voltage source converter has been explained. The problem under the distorted and unbalanced operating conditions have been identified. Motivation for this research has been stated. A brief review of past work has been provided to show the state-of-the-art. Contributions of the thesis work have been listed. The prototype three phase PWM converter and the experimental setup are described.

Chapter 2 discusses issues of PWM voltage source converter modelling. The new mathematical model has been built for the three phase PWM AC-DC voltage source converter in the positive and negative synchronous rotating frames under the generalized operating conditions. From this mathematical model, a detailed

explanation can be given on the appearance of the even-order harmonics at the dc link voltage and odd-order harmonics in the ac line side currents under the distorted and unbalanced supply voltages. The analytical expression of the instantaneous power flow obtained from the proposed mathematical model shows the link between the ripples in the dc output voltage and the harmonics in the ac line side currents. The simulation results have been provided to verify the proposed analysis.

The issues of the implementation of control strategy are discussed in Chapter 3. In order to eliminate the even-order harmonics at the dc link voltage and the odd-order harmonics in the ac line side currents, the control scheme can be divided into two parts, *DC link voltage harmonics control* scheme and *AC line side current harmonics control* scheme. These two control schemes have been implemented by the cascaded dual frame current regulator with a voltage regulator. Moreover, the three independent blocks, namely, *PWM modulation scheme*, *software phase locked loop* and *symmetrical components calculator*, those are used in the control system of this thesis work, have been addressed. The influence of these blocks on the three phase PWM AC-DC voltage source converter have been explained from the analytical point of view.

Chapter 4 has discussed the issues of choosing the control parameters for the basic cascaded dual rotating frame controller. In *voltage harmonics control*, the dual frame controller has been developed to make sure that the dc link voltage is maintained constant and the supply side power factor is kept close to unity, so the control parameter should be properly designed for the generalized operating conditions according to some performance criteria. The nonlinear control approach, singular perturbation method has been introduced and two-time-scale motions are

used to give a detailed dynamic analysis of the whole control system. Detailed design steps are provided for obtaining various parameters of the cascaded dual frame controller used in this work.

Chapter 5 has proposed *current harmonics control* scheme for accurate tracking the ac line side currents. To eliminate the 6^{th} and 12^{th} order harmonics in the *d-q* frame line side current under the distorted and unbalanced supply voltages, a plug-in time domain based repetitive controller (TDRC) is developed and employed to achieve the low THD line side currents of the three phase PWM AC-DC voltage source converter. The experimental results verify that TDRC control scheme has improved the ac input currents and the dc output voltage tracking accuracy substantially under the distorted and unbalanced supply voltage conditions.

Chapter 6 introduces a plug-in frequency domain based repetitive controller (FDRC) for *current harmonics control* scheme for three phase PWM AC-DC voltage source converter. The frequency domain based repetitive controller (FDRC) has been proposed to further minimize the odd-order harmonics in the line side currents. The repetitive control learning algorithm is designed in frequency domain, by using Fourier series approximation (FSA) method, and provides the flexibility of choosing different learning gains and phase delay compensations individually for each harmonic component. The experimental results provided validate that FDRC control scheme leads to the improved tracking performance for the ac line side currents.

Chapter 7 concludes the thesis. It briefly states the focus areas and then discusses the proposed solutions. It also lists the possible future work in this line

of research.

In the first year of my PhD study, my research was focused on Cylindrical Ultrasonic Motors (CUSM) Control. This is a relatively new kind of piezoelectric actuators, having different characteristics from that of conventional electromagnetic motors. The aim of my research was to evaluate the dynamic and steady state performances of the CUSM drive system for speed/position control applications by using three different control variables, namely, the amplitude, frequency and phase difference of the excitation signals in the single mode control. Then, the dual mode control method was proposed to achieve fast and precise position control. This motor was specially designed by Prof. Lee Kwok Hong and his research team. However, because he expired, the project was not continued further and nor the similar type of motors were available in the market so that it can be bought off the shelf. Therefore, my research focus had been changed to high-performance control of power electronics converters instead. The earlier part of the research work has been reported in Appendix F as a part of my PhD Thesis work.

1.8 Summary

This chapter introduces the problem of the performance of three phase PWM AC-DC voltage source converter under the distorted and unbalanced operating conditions and explains the motivation for the thesis work. The principles of operation and the causes of the harmonic components at the dc link voltage and ac line side currents under the distorted and unbalanced operating conditions are described. A literature survey on the past work in this area is provided. The main contribu-

tion of this thesis are then listed. The structure of this thesis is provided along with the focus area of each chapter. The experimental platform used for validating the proposed control schemes is described. The next chapter elaborates on the mathematical model of three phase PWM AC-DC voltage source converter.

Chapter 2

Mathematical Model of Three Phase PWM AC-DC Voltage Source Converter

For designing a suitable controller for any plant, it is essential to have a good understanding of the detailed plant knowledge. Representation of the plant in a mathematical form leads to the convenience of analysis and controller design. In this chapter, the mathematical model for a three-phase PWM AC-DC voltage source converter is presented for the unbalanced and distorted operating conditions. In order to accurately describe the behavior of PWM rectifier under the unbalanced and distorted supply voltages, it is essential to deal with positive sequence input voltages as well as negative sequence input voltages, separately. Comparing with the conventional approaches to model PWM rectifier in [71], this chapter proposes a new mathematical model in the positive and negative rotating synchronous frames to illustrate the even-order harmonics at the DC link voltage and the odd-order harmonics in the line side currents under the unbalanced and distorted operating conditions from the analytical point of view. Since most of control schemes pro-

posed to eliminate the harmonics at the dc link voltage are based on the regulation of the instantaneous power flow of three phase PWM AC-DC voltage source converter, it is necessary to have a clear picture of the instantaneous power under the unbalanced and distorted supply voltages. This chapter investigates the direct relationship between the output instantaneous power and the ripples in the dc link voltage. Moreover, the analytical study of the instantaneous power flow provides an explanation of the occurrence of the odd-order harmonics in the line side currents of three phase PWM rectifier under unbalanced operating conditions.

2.1 Mathematical Model

Fig. 2.1 shows the power circuit configuration of a three phase PWM AC-DC voltage source converter. It is assumed that the converter is feeding a resistive load. The differential equations for the phase voltages in the AC line side can be expressed as,

$$\begin{aligned} e_a &= L\frac{di_a}{dt} + Ri_a + u_{an} \\ e_b &= L\frac{di_b}{dt} + Ri_b + u_{bn} \\ e_c &= L\frac{di_c}{dt} + Ri_c + u_{cn} \end{aligned} \tag{2.1}$$

Considering that the sum of the phase currents is equal to zero in the three phase system, $i_a + i_b + i_c = 0$, the group of equations (2.1) can be simplified into

two line voltage equations,

$$\begin{aligned} e_{ab} &= e_a - e_b = L\frac{di_a}{dt} - L\frac{di_b}{dt} + Ri_a - Ri_b + u_{an} - u_{bn} \\ e_{bc} &= e_b - e_c = L\frac{di_b}{dt} - L\frac{di_c}{dt} + Ri_b - Ri_c + u_{bn} - u_{cn} \\ &= L\frac{di_a}{dt} + 2L\frac{di_b}{dt} + Ri_a + 2Ri_b + u_{an} + 2u_{bn} \end{aligned} \tag{2.2}$$

According to the voltage source converter principles, the relationship between the

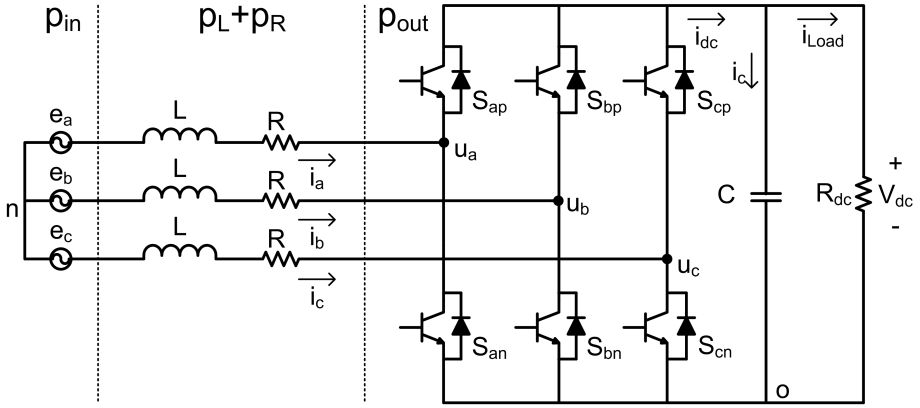

Figure 2.1: The three-phase PWM AC-DC voltage source converter circuit.

terminal voltages and the average switching signals can be expressed as,

$$\begin{aligned} u_{an} &= S_a v_{dc} \\ u_{bn} &= S_b v_{dc} \\ u_{cn} &= S_c v_{dc} \end{aligned} \tag{2.3}$$

Therefore, the equations in (2.2) can be summarized in matrix format as shown in (2.4),

$$\dot{\mathbf{x}} = \begin{bmatrix} -\frac{R}{L} & 0 \\ 0 & -\frac{R}{L} \end{bmatrix} \mathbf{x} + \begin{bmatrix} \frac{2}{3L} & \frac{1}{3L} \\ -\frac{1}{3L} & \frac{1}{3L} \end{bmatrix} \mathbf{e} + \begin{bmatrix} -\frac{v_{dc}}{L} & 0 \\ 0 & -\frac{v_{dc}}{L} \end{bmatrix} \mathbf{u} \tag{2.4}$$

where $\mathbf{x} = \begin{bmatrix} i_a & i_b \end{bmatrix}^T$, $\mathbf{e} = \begin{bmatrix} e_{ab} & e_{bc} \end{bmatrix}^T$ and $\mathbf{u} = \begin{bmatrix} S_a & S_b \end{bmatrix}^T$.

The line voltages e_{ab}, e_{bc}, the input currents i_a, i_b and the average switching functions S_a, S_b can be replaced by e_α, e_β, i_α, i_β and S_α, S_β respectively using the relevant forms of *Park Transformation* as given by (C.1) and (C.3) in Appendix C. Consequently, the model can be represented in the stationary reference α-β frame as,

$$\dot{\mathbf{x}} = \begin{bmatrix} -\frac{R}{L} & 0 \\ 0 & -\frac{R}{L} \end{bmatrix} \mathbf{x} + \begin{bmatrix} \frac{1}{L} & 0 \\ 0 & \frac{1}{L} \end{bmatrix} \mathbf{e} + \begin{bmatrix} -\frac{v_{dc}}{L} & 0 \\ 0 & -\frac{v_{dc}}{L} \end{bmatrix} \mathbf{u} \tag{2.5}$$

where $\mathbf{x} = \begin{bmatrix} i_\alpha & i_\beta \end{bmatrix}^T$, $\mathbf{e} = \begin{bmatrix} e_\alpha & e_\beta \end{bmatrix}^T$ and $\mathbf{u} = \begin{bmatrix} S_\alpha & S_\beta \end{bmatrix}^T$.

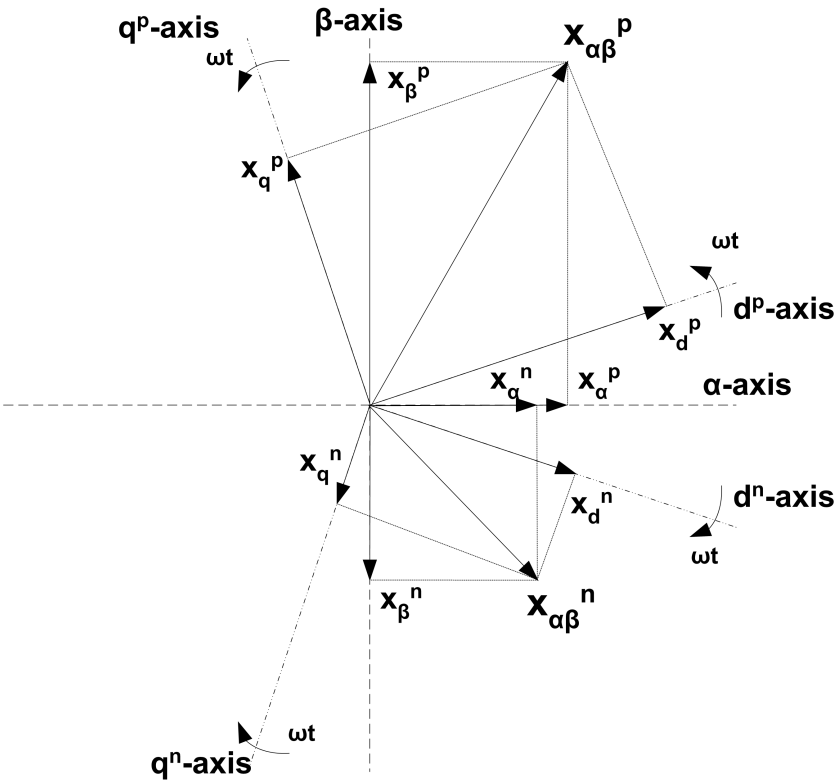

Figure 2.2: Phasor diagram of the unbalanced three-phase variables.

An unbalanced variable of a three-phase system can be resolved into the three variables in the three phase balanced systems [72], namely, positive-sequence component, negative-sequence component and zero-sequence components. Since the neutral point in Fig. 2.1 is not connected to the negative side of the dc bus

(point o), there is no zero-sequence component existing. Thus, the space vector of the unbalanced three-phase variables in the stationary α-β frame can be represented as the sum of the space vectors of the positive sequence component $\mathbf{x}^p_{\alpha\beta}$ and negative sequence component $\mathbf{x}^n_{\alpha\beta}$ as shown in Fig. 2.2. Therefore, the model of three phase PWM rectifier can be composed of one part in the positive stationary α-β frame and the other in the negative stationary α-β frame, (2.5),

$$\begin{bmatrix} \dot{i}^p_\alpha \\ \dot{i}^p_\beta \end{bmatrix} = \begin{bmatrix} -\frac{R}{L} & 0 \\ 0 & -\frac{R}{L} \end{bmatrix} \begin{bmatrix} i^p_\alpha \\ i^p_\beta \end{bmatrix} + \begin{bmatrix} \frac{1}{L} & 0 \\ 0 & \frac{1}{L} \end{bmatrix} \begin{bmatrix} e^p_\alpha \\ e^p_\beta \end{bmatrix} + \begin{bmatrix} -\frac{v_{dc}}{L} & 0 \\ 0 & -\frac{v_{dc}}{L} \end{bmatrix} \begin{bmatrix} S^p_\alpha \\ S^p_\beta \end{bmatrix} \quad (2.6)$$

$$\begin{bmatrix} \dot{i}^n_\alpha \\ \dot{i}^n_\beta \end{bmatrix} = \begin{bmatrix} -\frac{R}{L} & 0 \\ 0 & -\frac{R}{L} \end{bmatrix} \begin{bmatrix} i^n_\alpha \\ i^n_\beta \end{bmatrix} + \begin{bmatrix} \frac{1}{L} & 0 \\ 0 & \frac{1}{L} \end{bmatrix} \begin{bmatrix} e^n_\alpha \\ e^n_\beta \end{bmatrix} + \begin{bmatrix} -\frac{v_{dc}}{L} & 0 \\ 0 & -\frac{v_{dc}}{L} \end{bmatrix} \begin{bmatrix} S^n_\alpha \\ S^n_\beta \end{bmatrix} \quad (2.7)$$

Since the positive and negative sequence equations in PWM boost rectifiers constitute an orthogonal set of equations [49], these two sets of equations can be performed the transformation separately. As shown in Fig. 2.2, the space vectors $\mathbf{x}^p_{\alpha\beta}$ and $\mathbf{x}^n_{\alpha\beta}$ can be transformed into the positive and negative synchronous rotation d-q frame according to (C.5) and (C.7) in Appendix C, respectively. Therefore, the state-space model of positive sequence for three phase PWM rectifier in the positive rotating synchronous d-q frame can be obtained from (2.5),

$$\begin{bmatrix} \dot{i}^p_d \\ \dot{i}^p_q \end{bmatrix} = \begin{bmatrix} -\frac{R}{L} & \omega \\ -\omega & -\frac{R}{L} \end{bmatrix} \begin{bmatrix} i^p_d \\ i^p_q \end{bmatrix} + \begin{bmatrix} \frac{1}{L} & 0 \\ 0 & \frac{1}{L} \end{bmatrix} \begin{bmatrix} e^p_d \\ e^p_q \end{bmatrix} + \begin{bmatrix} -\frac{v_{dc}}{L} & 0 \\ 0 & -\frac{v_{dc}}{L} \end{bmatrix} \begin{bmatrix} S^p_d \\ S^p_q \end{bmatrix} \quad (2.8)$$

Similarly, the negative sequence equations can be derived in a negative rotating synchronous d-q frame,

$$\begin{bmatrix} \dot{i}^n_d \\ \dot{i}^n_q \end{bmatrix} = \begin{bmatrix} -\frac{R}{L} & -\omega \\ \omega & -\frac{R}{L} \end{bmatrix} \begin{bmatrix} i^n_d \\ i^n_q \end{bmatrix} + \begin{bmatrix} \frac{1}{L} & 0 \\ 0 & \frac{1}{L} \end{bmatrix} \begin{bmatrix} e^n_d \\ e^n_q \end{bmatrix} + \begin{bmatrix} -\frac{v_{dc}}{L} & 0 \\ 0 & -\frac{v_{dc}}{L} \end{bmatrix} \begin{bmatrix} S^n_d \\ S^n_q \end{bmatrix} \quad (2.9)$$

From Fig. 2.1, the state equation at the DC link side can be obtained and

written as follows,

$$C\frac{dv_{dc}}{dt} = i_{dc} - i_{load} = i_{dc} - \frac{v_{dc}}{R_{dc}} \tag{2.10}$$

The dc link current i_{dc} can be expressed in terms of input phase currents i_a, i_b, i_c and average switching functions S_a, S_b, S_c as [71],

$$i_{dc} = S_a i_a + S_b i_b + S_c i_c \tag{2.11}$$

After applying *Clark Transformation* as described in (C.3), the dc link current in (2.11) can be expressed in the stationary α-β frame as,

$$i_{dc} = S_\alpha i_\alpha + S_\beta i_\beta \tag{2.12}$$

Based on the phasor diagram in Fig. 2.2, we can express the current $\overrightarrow{i_s}$ in the space vector format, then transform to the rotating synchronous d-q frame, and define θ as ωt:

$$\begin{aligned}
\overrightarrow{i_s} = i_\alpha + j i_\beta &= (i_\alpha^p + j i_\beta^p) + (i_\alpha^n + j i_\beta^n) \\
&= e^{j\theta}(i_d^p + j i_q^p) + e^{-j\theta}(i_d^n + j i_q^n) \\
&= (\cos\theta i_d^p - \sin\theta i_q^p + \cos\theta i_d^n + \sin\theta i_q^n) \\
&\quad + j(\sin\theta i_d^p + \cos\theta i_q^p - \sin\theta i_d^n + \cos\theta i_q^n)
\end{aligned} \tag{2.13}$$

In the same way, the average switching functions S_α, S_β can be transformed into S_d^p, S_q^p, S_d^n and S_q^n as given by (2.14),

$$\begin{aligned}
S_\alpha + j S_\beta &= e^{j\theta}(S_d^p + j S_q^p) + e^{-j\theta}(S_d^n + j S_q^n) \\
&= (\cos\theta S_d^p - \sin\theta S_q^p + \cos\theta S_d^n + \sin\theta S_q^n) \\
&\quad + j(\sin\theta S_d^p + \cos\theta S_q^p - \sin\theta S_d^n + \cos\theta S_q^n)
\end{aligned} \tag{2.14}$$

The expressions of i_α, i_β, S_α and S_β can be derived from the real parts and

the imaginary parts of (2.13) and (2.14).

$$i_\alpha = \cos\theta i_d^p - \sin\theta i_q^p + \cos\theta i_d^n + \sin\theta i_q^n \tag{2.15}$$

$$i_\beta = \sin\theta i_d^p + \cos\theta i_q^p - \sin\theta i_d^n + \cos\theta i_q^n \tag{2.16}$$

$$S_\alpha = \cos\theta S_d^p - \sin\theta S_q^p + \cos\theta S_d^n + \sin\theta S_q^n \tag{2.17}$$

$$S_\beta = \sin\theta S_d^p + \cos\theta S_q^p - \sin\theta S_d^n + \cos\theta S_q^n \tag{2.18}$$

Substituting (2.15)-(2.18) into (2.12), the dc side current i_{dc} can be expressed as:

$$\begin{aligned} i_{dc} &= i_\alpha S_\alpha + i_\beta S_\beta \\ &= (i_d^n \cos 2\theta + i_q^n \sin 2\theta + i_d^p) S_d^p + (i_q^n \cos 2\theta - i_d^n \sin 2\theta + i_q^p) S_q^p \\ &+ (i_d^p \cos 2\theta - i_q^p \sin 2\theta + i_d^n) S_d^n + (i_d^p \sin 2\theta + i_q^p \cos 2\theta + i_q^n) S_q^n \end{aligned} \tag{2.19}$$

Finally, the dc link voltage can be presented as:

$$C\dot{v}_{dc} = -\frac{v_{dc}}{R_{dc}} + \begin{bmatrix} i_d^n \cos 2\theta + i_q^n \sin 2\theta + i_d^p \\ i_q^n \cos 2\theta - i_d^n \sin 2\theta + i_q^p \\ i_d^p \cos 2\theta - i_q^p \sin 2\theta + i_d^n \\ i_d^p \sin 2\theta + i_q^p \cos 2\theta + i_q^n \end{bmatrix}' \begin{bmatrix} S_d^p \\ S_q^p \\ S_d^n \\ S_q^n \end{bmatrix} \tag{2.20}$$

When the PWM rectifier works under the balanced condition, that is, all the variables in the negative sequence are equal to zero, (2.20) can be written as,

$$\dot{v}_{dc} = -\frac{1}{CR_{dc}} v_{dc} + \frac{1}{C}(i_d^p S_d^p + i_q^p S_q^p) \tag{2.21}$$

In the balanced condition, i_d^p and i_q^p only include the constant values in the steady state. Therefore, (2.21) indicates that v_{dc} only contains the dc quantity and this equation matches the conventional equation under the balanced operating

condition as shown in [73], which is rewritten as the equation (2.22) by using the definition in this thesis,

$$C\frac{dv_{dc}}{dt} = (i_d^p S_d^p + i_q^p S_q^p) - i_{dc} \tag{2.22}$$

Moreover, the equation (2.20) gives more details and clearer picture about the PWM rectifier model under the unbalanced operating condition as compared to the model derived in [71] and reproduced as follows,

$$C\frac{dv_{dc}}{dt} = (i_d^p S_d^p + i_q^p S_q^p + i_d^n S_d^n + i_q^n S_q^n) - \frac{v_{dc}}{R_{dc}} \tag{2.23}$$

The equation (2.20) shows the presence of the second-order harmonic component at the output of the rectifier due to the presence of the negative sequence components both in current as well as average switching function i_d^n, i_q^n, S_d^n and S_q^n such as the second term in (2.20).

2.2 Influence of Unbalanced Supply Voltages

In practice, the unbalanced supply conditions occur frequently in the grid, particularly in a weak ac system. It can be caused by single phase loads in the system which are not uniformly distributed among the three phases or a nonsymmetrical transformer winding or transmission impedances, open wye, open delta, etc. Regardless of the reasons, the performance of the three phase PWM rectifier is deteriorated by the appearance of the negative sequence voltage under the unbalanced input voltage conditions. In order to maintain all the advantages of the PWM rectifier under the unbalanced operating conditions, it is necessary to understand the way that the negative sequence components of the supply voltage generate the second order harmonics at the dc link voltage.

Generally, the supply voltages e_a, e_b and e_c from the grid can be separated as the positive-sequence components e_a^p, e_b^p and e_c^p, and negative-sequence components e_a^n, e_b^n and e_c^n. Correspondingly, the negative sequence components both in current as well as average switching function i_d^n, i_q^n, S_d^n and S_q^n would appear in the system. Considering that the average switching function S_d^p, S_q^p, S_d^n, and S_q^n are constant, the negative sequence currents and average switching function would cause the second-order harmonic component at the DC link voltage in (2.20). Correspondingly, the second order harmonic components in the DC link voltage would cause the second order harmonic in the ac line side currents i_d^p, i_q^p, i_d^n, and i_q^n in (2.8) and (2.9), which leads to higher even-order harmonics at the dc voltage. Consequently, the ac line side currents i_d^p, i_q^p, i_d^n and i_q^n in the positive and negative synchronous rotating frames will involve all the even-order harmonics, which can be written as,

$$\begin{aligned} i_d^p(t) &= I_{d0}^p + \sum_{h=2k,k=1} I_{dh}^p \sin(h\omega t + \phi_{dh}^p) \\ i_q^p(t) &= I_{q0}^p + \sum_{h=2k,k=1} I_{qh}^p \sin(h\omega t + \phi_{qh}^p) \\ i_d^n(t) &= I_{d0}^n + \sum_{h=2k,k=1} I_{dh}^n \sin(h\omega t + \phi_{dh}^n) \\ i_q^n(t) &= I_{q0}^n + \sum_{h=2k,k=1} I_{qh}^n \sin(h\omega t + \phi_{qh}^n) \end{aligned} \tag{2.24}$$

where the variables I_{d0}^p, I_{q0}^p, I_{d0}^n and I_{q0}^n represent the DC quantity of the AC side line side current. I_{dh}^p, I_{qh}^p, I_{dh}^n and I_{qh}^n are the amplitudes and ϕ_{dh}^p, ϕ_{qh}^p, ϕ_{dh}^n and ϕ_{qh}^n are the phase angles of the h^{th}-order harmonic components of the positive and negative sequence line side currents in the rotating d-q frame, respectively.

Therefore, the dc side current i_{dc} can be predicted to have the even-order harmonics from (2.19), which can be expressed as,

$$i_{dc}(t) = I_0 + \sum_{h=2k,k=1} I_{rh} \sin(h\omega t + \phi_{ih}) \tag{2.25}$$

where the variable I_0 represent the DC quantity, I_{rh} and ϕ_{ih} are the amplitudes and the phase angles of the h^{th}-order harmonic components in the DC link current.

In reality, the amplitude of the high order harmonic components of the ac line side current will be reduced with the increase of the harmonics order. Hence, to simplify the process of the derivation, only the second order harmonics are considered in the ac line side currents i_d^p, i_q^p, i_d^n, and i_q^n in (2.24). Accordingly, the DC side current i_{dc} in (2.19) will include the fourth order harmonic as written,

$$i_{dc}(t) = I_0 + I_{r2sin}\sin(2\omega t) + I_{r2cos}\cos(2\omega t) + I_{r4sin}\sin(4\omega t) + I_{r4cos}\sin(4\omega t) \quad (2.26)$$

where
$$I_{r2\sin} = I_{r2}\cos\phi_{i2}; \quad I_{r2\cos} = I_{r2}\sin\phi_{i2};$$
$$I_{r4\sin} = I_{r4}\cos\phi_{i4}; \quad I_{r4\cos} = I_{r4}\sin\phi_{i4}.$$

The dc quantity of the dc current I_0 can be written as,

$$\begin{aligned} I_0 &= S_d^p I_{d0}^p + S_q^p I_{q0}^p + S_d^n I_{d0}^n + S_q^n I_{q0}^n \\ &+\frac{1}{2}S_d^p(I_{d2}^n\sin\phi_{d2}^n + I_{q2}^n\cos\phi_{q2}^n) + \frac{1}{2}S_q^p(I_{q2}^n\sin\phi_{q2}^n - I_{d2}^n\cos\phi_{d2}^n) \quad (2.27) \\ &+\frac{1}{2}S_d^n(I_{d2}^p\sin\phi_{d2}^p - I_{q2}^p\cos\phi_{q2}^p) + \frac{1}{2}S_q^p(I_{q2}^p\sin\phi_{q2}^p + I_{d2}^p\cos\phi_{d2}^p) \end{aligned}$$

The amplitudes of the second and fourth order harmonic components for the sin and cos terms, I_{r2sin}, I_{r2cos}, I_{r4sin} and I_{r4cos} can be represented, respectively, as,

$$\begin{aligned} I_{r2\sin} &= S_d^p I_{q0}^n - S_q^p I_{d0}^n - S_d^n I_{q0}^p + S_q^n I_{d0}^p \quad (2.28) \\ &+S_d^p I_{d2}^p\cos\phi_{d2}^p + S_q^p I_{q2}^p\cos\phi_{q2}^p + S_d^n I_{d2}^n\cos\phi_{d2}^n + S_q^n I_{q2}^n\cos\phi_{q2}^n \\ I_{r2\cos} &= S_d^p I_{d0}^n + S_q^p I_{q0}^n + S_d^n I_{d0}^p + S_q^n I_{q0}^p \quad (2.29) \\ &+S_d^p I_{d2}^p\sin\phi_{d2}^p + S_q^p I_{q2}^p\sin\phi_{q2}^p + S_d^n I_{d2}^n\sin\phi_{d2}^n + S_q^n I_{q2}^n\sin\phi_{q2}^n \end{aligned}$$

$$I_{r4\sin} = \frac{1}{2}S_d^p(I_{d2}^n\cos\phi_{d2}^n + I_{q2}^n\sin\phi_{q2}^n) + \frac{1}{2}S_q^p(I_{q2}^n\cos\phi_{q2}^n - I_{d2}^n\sin\phi_{d2}^n) \quad (2.30)$$
$$+\frac{1}{2}S_d^n(I_{d2}^p\cos\phi_{d2}^p - I_{q2}^p\sin\phi_{q2}^p) + \frac{1}{2}S_q^n(I_{q2}^p\cos\phi_{q2}^p + I_{d2}^p\sin\phi_{d2}^p)$$
$$I_{r4\cos} = \frac{1}{2}S_d^p(I_{d2}^n\sin\phi_{d2}^n - I_{q2}^n\cos\phi_{q2}^n) + \frac{1}{2}S_q^p(I_{q2}^n\sin\phi_{q2}^n + I_{d2}^n\cos\phi_{d2}^n) \quad (2.31)$$
$$+\frac{1}{2}S_d^n(I_{d2}^p\sin\phi_{d2}^p + I_{q2}^p\cos\phi_{q2}^p) + \frac{1}{2}S_q^n(I_{q2}^p\sin\phi_{q2}^p - I_{d2}^p\cos\phi_{d2}^p)$$

In this case, the fourth order harmonic is coupled into the dc link voltage according to (2.20). Our ultimate control objective is to cancel the even-order harmonics voltage to generate a constant DC output voltage. In the steady state condition, the variables at the DC side can be replaced by the sum of the constant dc signal and the ripple component AC signal as,

$$v_{dc} = \overline{v_{dc}} + \Delta v_{dc} \quad (2.32)$$

$$i_{dc} = \overline{i_{dc}} + \Delta i_{dc} \quad (2.33)$$

Since the dc side current appears as periodic signal, the dc component $\overline{i_{dc}}$ can be obtained from the integral of i_{dc} over one cycle, which is the same as the equation (2.27),

$$\overline{i_{dc}} = \frac{\omega}{2\pi}\int_0^{\frac{2\pi}{\omega}} i_{dc}\,dt = I_0 \quad (2.34)$$

and Δi_{dc} can be derived by subtracting I_0 from the equation (2.26),

$$\Delta i_{dc} = I_{r2sin}\sin(2\omega t) + I_{r2cos}\cos(2\omega t) + I_{r4sin}\sin(4\omega t) + I_{r4cos}\sin(4\omega t) \quad (2.35)$$

Since the load is resistive, $\overline{v_{dc}}$ can be written as,

$$\overline{v_{dc}} = R_{dc}\overline{i_{dc}} = R_{dc}I_0 \quad (2.36)$$

Substituting (2.34) and (2.36) into (2.10) and cancelling the dc components in the equation, (2.10) can be written as,

$$\Delta\dot{v}_{dc} = -\frac{1}{CR_{dc}}\Delta v_{dc} + \frac{1}{C}\Delta i_{dc} \quad (2.37)$$

Based on (2.35), the differential equation (2.37) can be solved,

$$\Delta v_{dc} = Ke^{-\frac{t}{CR_{dc}}} + \frac{R_{dc}\sqrt{I_{r2sin}^2 + I_{r2cos}^2}}{\sqrt{1+4\omega^2C^2R_{dc}^2}}\sin(2\omega t + \phi_{v2}) + \frac{R_{dc}\sqrt{I_{r4sin}^2 + I_{r4cos}^2}}{\sqrt{1+16\omega^2C^2R_{dc}^2}}\sin(4\omega t + \phi_{v4}) \tag{2.38}$$

K is a constant value,

where $\cos\phi_{v2} = \frac{2\omega CR_{dc}I_{r2cos}+I_{r2sin}}{\sqrt{(I_{r2sin}^2+I_{r2cos}^2)(1+4\omega^2C^2R_{dc}^2)}}$,

$\cos\phi_{v4} = \frac{4\omega CR_{dc}I_{r4cos}+I_{r4sin}}{\sqrt{(I_{r4sin}^2+I_{r4cos}^2)(1+16\omega^2C^2R_{dc}^2)}}$

The equation (2.38) can be expressed as two parts: the first part of (2.38) is a decaying term. It will decay exponentially to zero in the steady state condition. When the values of the capacitor C is small, which means the system with a small capacitor, the response of the dc link voltage will be fast. And only the second part of (2.38) exists in the steady state condition. This term appears as a second order and a fourth order ripple components in the dc link voltage under the unbalanced supply conditions.

With the condition $4\omega^2C^2R_{dc}^2 \gg 1$ satisfied, (2.38) can be further simplified as during the steady state,

$$\Delta v_{dc} = \frac{\sqrt{I_{r2sin}^2 + I_{r2cos}^2}}{2\omega C}\sin(2\omega t + \phi_{v2}) + \frac{\sqrt{I_{r4sin}^2 + I_{r4cos}^2}}{4\omega C}\sin(4\omega t + \phi_{v4}) \tag{2.39}$$

For the specified values of I_{r2sin}, I_{r2cos}, I_{r4sin} and I_{r4cos} under the different operating conditions, (2.39) shows that the larger the capacitor value is, the smaller the ripple that appears in the dc link voltage, which can make the control problem easier to handle. However, using the large capacitor will slow down the response of the system according to the above analysis of the transient performance. Therefore, there is a trade-off between the fast dynamic performance and the small ripple

at the dc link voltage for the three phase PWM rectifier under the unbalanced operating conditions.

In order to minimize the second and fourth order harmonics in the DC link voltage with the small capacitor, to generate the proper control signals for the reduced values of I_{r2sin}, I_{r2cos}, I_{r4sin} and I_{r4cos} has become critical. From (2.39), we can see that only when the conditions, $I_{r2sin} = 0$, $I_{r2cos} = 0$, $I_{r4sin} = 0$ and $I_{r4cos} = 0$, are satisfied at the same time, the ripple of the dc voltage Δv_{dc} can be removed, so that a constant dc output voltage can be maintained.

From the above mentioned analysis and discussions, the physical control objective of ripple-free dc link voltage is successfully represented in terms of a mathematical expression, which can be understood more directly and therefore enhances the understanding of the appearance of harmonics in the ac line side current and the dc link voltage for the three phase PWM AC-DC voltage source converter under the unbalanced operating conditions.

2.3 Influence of Distorted Supply Voltages

In the power distribution networks, voltage distortions due to current harmonics is becoming a major issue because of the large numbers of nonlinear loads being connected to the utility grid. According to the standard [9], the maximum 5^{th} order harmonic voltage allowed is 6% and 7^{th} order harmonic voltage is 5% of the fundamental component. Hence, the performance of three phase PWM rectifier under distorted supply voltage conditions should be evaluated under these guidelines.

The unbalanced and distorted three phase voltages e_a, e_b and e_c are composed of the positive sequence components e_a^p, e_b^p, e_c^p and the negative sequence components e_a^n, e_b^n, e_c^n. According to the traditional method in [74] to extract the symmetrical components, the positive sequence components can be written as the sum of k^{th}-order harmonics with an amplitude E_k^p and angle offset θ_{ek}^p in the equation (2.40).

$$\begin{aligned} e_a^p &= \sum_{\substack{n=1 \\ k=1,6n-1,6n+1}}^{\infty} E_k^p \sin(k\omega t + \theta_{ek}^p) \\ e_b^p &= \sum_{\substack{n=1 \\ k=1,6n-1,6n+1}}^{\infty} E_k^p \sin(k\omega t - k \cdot \tfrac{2\pi}{3} + \theta_{ek}^p) \\ e_c^p &= \sum_{\substack{n=1 \\ k=1,6n-1,6n+1}}^{\infty} E_k^p \sin(k\omega t + k \cdot \tfrac{2\pi}{3} + \theta_{ek}^p) \end{aligned} \tag{2.40}$$

In a similar way, the negative sequence components can be expressed as the sum of k^{th}-order harmonics with an amplitude E_k^n and angle offset θ_{ek}^n,

$$\begin{aligned} e_a^n &= \sum_{\substack{n=1 \\ k=1,6n-1,6n+1}}^{\infty} E_k^n \sin(k\omega t + \theta_{ek}^n) \\ e_b^n &= \sum_{\substack{n=1 \\ k=1,6n-1,6n+1}}^{\infty} E_k^n \sin(k\omega t + k \cdot \tfrac{2\pi}{3} + \theta_{ek}^n) \\ e_c^n &= \sum_{\substack{n=1 \\ k=1,6n-1,6n+1}}^{\infty} E_k^n \sin(k\omega t - k \cdot \tfrac{2\pi}{3} + \theta_{ek}^n) \end{aligned} \tag{2.41}$$

By using the *Clark's transformation* in (C.3), the positive sequence components in the supply voltages e_a^p, e_b^p, e_c^p can be expressed as $e_{\alpha k}^p$ and $e_{\beta k}^p$ for the different k^{th}-order harmonics in the stationary reference α-β frame,

when $\mathbf{k = 6n\text{-}1}$,

$$e_{\alpha k}^p = \frac{\sqrt{6}E_k^p}{2} \sin(k\omega t + \theta_{ek}^p) \tag{2.42}$$

$$e_{\beta k}^p = \frac{\sqrt{6}E_k^p}{2} \cos(k\omega t + \theta_{ek}^p) \tag{2.43}$$

Similarly, when $\mathbf{k = 1}$ and $\mathbf{k = 6n+1}$,

$$e^p_{\alpha k} = \frac{\sqrt{6}E^p_k}{2}\sin(k\omega t + \theta^p_{ek}) \tag{2.44}$$

$$e^p_{\beta k} = -\frac{\sqrt{6}E^p_k}{2}\cos(k\omega t + \theta^p_{ek}) \tag{2.45}$$

It can be seen from (2.42)-(2.45) that the different voltage harmonics in the stationary *a-b-c* frame will cause the corresponding harmonics in the stationary α-β frame. Moreover, for $(6n-1)^{th}$ order harmonics such as 5^{th} and 11^{th} order harmonics, $e^p_{\alpha k}$ is lagging with $e^p_{\beta k}$ by 90°, while for $(6n+1)^{th}$ order harmonics such as 7^{th} and 13^{th}, $e^p_{\alpha k}$ is leading with $e^p_{\beta k}$ by 90°.

By using *Park's Transformation* in (C.5) and (C.7), the positive sequence components in the supply voltages can be resolved as e^p_{dk} and e^p_{qk}in the positive rotating *d-q* frame,

when $\mathbf{k = 1}$,

$$e^p_{d1} = \frac{\sqrt{6}E^p_1}{2}\sin\theta^p_{e1} \tag{2.46}$$

$$e^p_{q1} = \frac{\sqrt{6}E^p_1}{2}\cos\theta^p_{e1} \tag{2.47}$$

$\mathbf{k = 6n\text{-}1}$,

$$\begin{aligned} e^p_{dk} &= \frac{\sqrt{6}E^p_k}{2}\sin[(k+1)\omega t + \theta^p_{ek}] \\ &= \frac{\sqrt{6}E^p_k}{2}\sin(6n\omega t + \theta^p_{ek}) \end{aligned} \tag{2.48}$$

$$\begin{aligned} e^p_{qk} &= \frac{\sqrt{6}E^p_k}{2}\cos[(k+1)\omega t + \theta^p_{ek}] \\ &= \frac{\sqrt{6}E^p_k}{2}\cos(6n\omega t + \theta^p_{ek}) \end{aligned} \tag{2.49}$$

k = 6n+1,

$$\begin{aligned} e^p_{dk} &= \frac{\sqrt{6}E^p_k}{2}\sin[(k-1)\omega t + \theta^p_{ek}] \\ &= \frac{\sqrt{6}E^p_k}{2}\sin(6n\omega t + \theta^p_{ek}) \end{aligned} \tag{2.50}$$

$$\begin{aligned} e^p_{qk} &= -\frac{\sqrt{6}E^p_k}{2}\cos[(k-1)\omega t + \theta^p_{ek}] \\ &= -\frac{\sqrt{6}E^p_k}{2}\cos(6n\omega t + \theta^p_{ek}) \end{aligned} \tag{2.51}$$

The equations (2.46)-(2.51) show that the fundamental voltage would appear as a constant signal in the *d-q* frame, while the other voltage harmonics would result in the corresponding ac signals in the positive synchronous rotating *d-q* frame. For a specified n, the $(6n-1)^{th}$ and $(6n+1)^{th}$ order harmonics would produce the $6n^{th}$ order harmonics in the positive synchronous rotating *d-q* frame. For example, 5^{th} and 7^{th} order voltage harmonics in *a-b-c* frame appear as 6^{th} order harmonics in the positive synchronous rotating *d-q* frame, and similarly the 11^{th} and 13^{th} order voltage harmonics appear as 12^{th} order harmonics in the positive synchronous rotating *d-q* frame.

In the same manner, the negative sequence components in the supply voltages e^n_{dk} and e^n_{qk} in the negative rotating *d-q* frame can be obtained as,
when **k = 1**,

$$e^n_{d1} = \frac{\sqrt{6}E^n_1}{2}\sin\theta^n_{e1} \tag{2.52}$$

$$e^n_{q1} = -\frac{\sqrt{6}E^n_1}{2}\cos\theta^n_{e1} \tag{2.53}$$

k = 6n-1,

$$\begin{aligned} e_{dk}^{n} &= \frac{\sqrt{6}E_k^n}{2}\sin[(k+1)\omega t+\theta_{ek}^{n}] \\ &= \frac{\sqrt{6}E_k^n}{2}\sin(6n\omega t+\theta_{ek}^{n}) \qquad (2.54) \\ e_{qk}^{n} &= -\frac{\sqrt{6}E_k^n}{2}\cos[(k+1)\omega t+\theta_{ek}^{n}] \\ &= -\frac{\sqrt{6}E_k^n}{2}\cos(6n\omega t+\theta_{ek}^{n}) \qquad (2.55) \end{aligned}$$

k = 6n+1,

$$\begin{aligned} e_{dk}^{n} &= \frac{\sqrt{6}E_k^n}{2}\sin[(k-1)\omega t+\theta_{ek}^{n}] \\ &= \frac{\sqrt{6}E_k^n}{2}\sin(6n\omega t+\theta_{ek}^{n}) \qquad (2.56) \\ e_{qk}^{n} &= \frac{\sqrt{6}E_k^n}{2}\cos[(k-1)\omega t+\theta_{ek}^{n}] \\ &= \frac{\sqrt{6}E_k^n}{2}\cos(6n\omega t+\theta_{ek}^{n}) \qquad (2.57) \end{aligned}$$

The space vector of the positive and negative sequence supply voltages $\overrightarrow{e_k^p}$, $\overrightarrow{e_k^n}$ in the positive and negative rotating synchronous frames can be defined as, when **k = 1**,

$$\begin{aligned} \overrightarrow{e_1^p} &= e_{q1}^{p}+je_{d1}^{p}=E_1^p e^{j\theta_{e1}^{p}} \qquad (2.58) \\ \overrightarrow{e_1^n} &= e_{q1}^{n}+je_{d1}^{n}=E_1^n e^{j\theta_{e1}^{n}} \end{aligned}$$

k = 6n-1,

$$\begin{aligned} \overrightarrow{e_k^p} &= e_{qk}^{p}+je_{dk}^{p}=E_k^p e^{j(6n\omega t+\theta_{ek}^{p})} \qquad (2.59) \\ \overrightarrow{e_k^n} &= e_{qk}^{n}+je_{dk}^{n}=E_k^n e^{j(\pi-6n\omega t-\theta_{ek}^{n})} \end{aligned}$$

k = 6n+1,

$$\begin{aligned} \overrightarrow{e_k^p} &= e_{qk}^p + je_{dk}^p = E_k^p e^{j(\pi - 6n\omega t - \theta_{ek}^p)} \\ \overrightarrow{e_k^n} &= e_{qk}^n + je_{dk}^n = E_k^n e^{j(6n\omega t + \theta_{ek}^n)} \end{aligned} \tag{2.60}$$

Because of the linear characteristics of (2.8) and (2.9), the effect of each frequency component on the system can be considered separately. The fundamental components in the supply voltages appear as the dc quantity in the positive and negative synchronous rotating *d-q* frames. For k^{th}-order harmonics, the supply voltages in the frequency domain can be obtained from (2.59) and (2.60),

when **k = 6n-1**,

$$\begin{aligned} \overrightarrow{e_k^p} &= E_k^p e^{j\theta_{ek}^p} \frac{1}{s - j6n\omega} \\ \overrightarrow{e_k^n} &= E_k^n e^{j(\pi - \theta_{ek}^n)} \frac{1}{s + j6n\omega} \end{aligned} \tag{2.61}$$

k = 6n+1,

$$\begin{aligned} \overrightarrow{e_k^p} &= E_k^p e^{j(\pi - \theta_{ek}^p)} \frac{1}{s + j6n\omega} \\ \overrightarrow{e_k^n} &= E_k^n e^{j\theta_{ek}^n} \frac{1}{s - j6n\omega} \end{aligned} \tag{2.62}$$

Since the currents caused by the supply voltage harmonics are small in comparison with the fundamental line side currents, and also the operating value of the dc link voltage is relatively high, so the variation of the dc link voltage due to current harmonics can be neglected according to (2.20). The equations (2.8) and (2.9) in the positive and negative rotating synchronous *d-q* frame can be expressed

in the space vector format,

$$\begin{aligned} \dot{\overrightarrow{i_k^p}} &= (-\frac{R}{L} - j\omega)\overrightarrow{i_k^p} + \frac{1}{L}\overrightarrow{e_k^p} - \frac{1}{L}\overrightarrow{u_k^p} \\ \dot{\overrightarrow{i_k^n}} &= (-\frac{R}{L} + j\omega)\overrightarrow{i_k^n} + \frac{1}{L}\overrightarrow{e_k^n} - \frac{1}{L}\overrightarrow{u_k^n} \end{aligned} \tag{2.63}$$

where $\overrightarrow{i}$, $\overrightarrow{e}$, $\overrightarrow{u}$ represent the space vector of the input line side current, the supply voltage and the converter voltage, respectively. Superscript p and n designate the positive and negative sequence components in the positive and negative synchronous rotating d-q frames, respectively. And subscript k represents the k^{th} order component in the different variables.

Correspondingly, the response of the positive and negative sequence line side currents in the frequency domain can be derived as,

$$\begin{aligned} \overrightarrow{i_k^p}(s) &= \frac{1}{Ls - (-R - jL\omega)}(\overrightarrow{e_k^p}(s) - \overrightarrow{u_k^p}(s)) \\ \overrightarrow{i_k^n}(s) &= \frac{1}{Ls - (-R + jL\omega)}(\overrightarrow{e_k^n}(s) - \overrightarrow{u_k^n}(s)) \end{aligned} \tag{2.64}$$

The converter voltage $\overrightarrow{u_k^p}$ and $\overrightarrow{u_k^n}$ can be adjusted by designing the control signals S_d^p, S_q^p, S_d^n and S_q^n, so that the effect of supply voltage harmonic $\overrightarrow{e_k^p}$ can be compensated. When the system works in the open loop, there are only fundamental frequency and switching frequency included in the terminal voltage u_{an}, u_{bn} and u_{cn}, so $\overrightarrow{u_k^p} = 0$ and $\overrightarrow{u_k^n} = 0$. From (2.61), (2.62) and (2.64), the corresponding positive and negative sequence current response in the frequency domain are,

when $\mathbf{k = 6n\text{-}1}$,

$$\begin{aligned} \overrightarrow{i_k^p}(s) &= \frac{E_k^p e^{\theta_{ek}^p} s}{s(Ls + R + jL\omega)(s - j6n\omega)} \\ \overrightarrow{i_k^n}(s) &= \frac{E_k^n e^{\pi - \theta_{ek}^n} s}{s(Ls + R - jL\omega)(s + j6n\omega)} \end{aligned} \tag{2.65}$$

k = 6n+1,

$$\begin{aligned} \overrightarrow{i^p}(s) &= \frac{E_k^p e^{\pi-\theta_{ek}^p} s}{s(Ls+R+jL\omega)(s+j6n\omega)} \\ \overrightarrow{i^n}(s) &= \frac{E_k^n e^{\theta_{ek}^n} s}{s(Ls+R-jL\omega)(s-j6n\omega)} \end{aligned} \tag{2.66}$$

Consequently, the response of the positive and negative sequence line side currents in the time domain can be obtained from (2.65) and (2.66),

when **k = 6n-1**,

$$\begin{aligned} \overrightarrow{i_k^p}(t) &= A_1 e^{j6n\omega t} - A_1 e^{-\frac{R}{L}t-j\omega t} \\ \overrightarrow{i_k^n}(t) &= B_1 e^{-j6n\omega t} - B_1 e^{-\frac{R}{L}t+j\omega t} \end{aligned} \tag{2.67}$$

k = 6n+1,

$$\begin{aligned} \overrightarrow{i_k^p}(t) &= A_2 e^{-j6n\omega t} - A_2 e^{-\frac{R}{L}t-j\omega t} \\ \overrightarrow{i_k^n}(t) &= B_2 e^{j6n\omega t} - B_2 e^{-\frac{R}{L}t+j\omega t} \end{aligned} \tag{2.68}$$

where $A_1 = \frac{E_k^p e^{\theta_{ek}^p}}{R+j(6n+1)\omega L}$; $A_2 = \frac{E_k^p e^{\pi-\theta_{ek}^p}}{R+j(6n-1)\omega L}$;
$B_1 = \frac{E_k^n e^{\pi-\theta_{ek}^n}}{R-j(6n+1)\omega L}$; $B_2 = \frac{E_k^n e^{\theta_{ek}^n}}{R-j(6n-1)\omega L}$;

From (2.67) and (2.68), we can see that the second terms of (2.67) and (2.68) would decay exponentially to zero, and only the first terms of these two equations would remain at the steady state. The second term of (2.67) and (2.68) would substantially generate the $6n^{th}$ order harmonics in the positive and negative sequence currents of the positive and negative rotating synchronous *d-q* frame. These $6n^{th}$ order harmonic components in the positive and negative sequence line side currents will reflect as the k^{th} order harmonics in the *a-b-c* frame. Also, the amplitude of the positive and negative sequence currents are decided by the impedance of the line side. When the frequency of the supply voltage is higher, the amplitude of the

corresponding current is smaller. Therefore, the high frequency harmonics effect can be neglected because of high impedance, while the low frequency harmonics should be paid more attention, such as the 6^{th} and 12^{th} order harmonics in the line side currents of the positive and negative synchronous rotating *d-q* frames.

2.4 Instantaneous Power Flow Calculation

Over the past few years, extensive studies have been carried out to regulate the DC link voltage under the unbalanced operating conditions based on the instantaneous power flow of the system [47], [49], [51] and [57]. Therefore, the power flow is another concerned issue for the three phase PWM rectifier applications. The output instantaneous power is constant when the three phase PWM rectifier works under the balanced operating conditions. However, this output instantaneous power becomes oscillating when the converter operates under the unbalanced operating conditions. This oscillation of the instantaneous output power is the primitive cause of the harmonic generation both at the DC link output and AC input side currents of the three phase PWM AC-DC voltage source converter. In order to eliminate all these harmonics, the ultimate objective of the control strategy under the unbalanced supply voltages is to make the output instantaneous power constant at the desired frequency. To realize this objective, it is essential to understand the characteristics of the instantaneous power flow under unbalanced operating conditions.

Fig. 2.1 shows the instantaneous power flow of three phase PWM AC-DC voltage source converter. Let the supply voltages be $e_a(t)$, $e_b(t)$ and $e_c(t)$ and the

three phase currents be $i_a(t)$, $i_b(t)$ and $i_c(t)$. The three terminal voltage of the converter $u_{an}(t)$, $u_{bn}(t)$ and $u_{cn}(t)$ can be obtained from (2.1) according to Fig. 2.1. Therefore, the input instantaneous power $p_{in}(t)$ and $p_{out}(t)$ can be expressed as follows,

$$p_{in}(t) = e_a(t)i_a(t) + e_b(t)i_b(t) + e_c(t)i_c(t) \tag{2.69}$$

$$p_{out}(t) = u_{an}(t)i_a(t) + u_{bn}(t)i_b(t) + u_{cn}(t)i_c(t) \tag{2.70}$$

Assuming that the power transmission lines in the system is lossless, the instantaneous power between the input side and the output side should be balanced as,

$$p_{in}(t) = p_L(t) + p_R(t) + p_{out}(t) \tag{2.71}$$

where p_L and p_R denote the instantaneous power consumed by the inductance L and the parasitic resistance R, respectively.

The instantaneous output power can be obtained easily from the DC output current and voltage based on the mathematical model as described by (2.19) and (2.20). In addition, every term in the equation can be interpreted into the physical meaning by the standard definition of the instantaneous power in [75].

According to (2.34), (2.36) and (2.38), the instantaneous DC link voltage and current in the steady state can be simplified as,

$$\begin{aligned} v_{dc}(t) = {} & R_{dc}I_0 + \left[\frac{R_{dc}\sqrt{I_{r2sin}^2 + I_{r2cos}^2}}{\sqrt{1+4\omega^2C^2R_{dc}^2}}\right]\sin(2\omega t + \phi_{v2}) \\ & + \left[\frac{R_{dc}\sqrt{I_{r4sin}^2 + I_{r4cos}^2}}{\sqrt{1+16\omega^2C^2R_{dc}^2}}\right]\sin(4\omega t + \phi_{v4}) \end{aligned}$$

$$= R_{dc}I_0 + V_{r2}\sin(2\omega t + \phi_{v2}) + V_{r4}\sin(4\omega t + \phi_{v4}) \quad (2.72)$$

$$i_{dc}(t) = I_0 + \sqrt{I_{r2sin}^2 + I_{r2cos}^2}\sin(2\omega t + \phi_{i2}) + \sqrt{I_{r4sin}^2 + I_{r4cos}^2}\sin(4\omega t + \phi_{i4})$$

$$= I_0 + I_{r2}\sin(2\omega t + \phi_{i2}) + I_{r4}\sin(4\omega t + \phi_{i4}) \quad (2.73)$$

The output instantaneous power p_{out} is obtained by multiplying the instantaneous DC output voltage and the instantaneous DC output current,

$$\begin{aligned} p_{out}(t) &= v_{dc}(t) \times i_{dc}(t) \\ &= \left[R_{dc}I_0^2 + \frac{V_{r2}I_{r2}}{2}\cos(\phi_{v2} - \phi_{i2}) + \frac{V_{r4}I_{r4}}{2}\cos(\phi_{v4} - \phi_{i4})\right. \\ &\quad \left. + \frac{V_{r2}I_{r4}}{2}\cos(\phi_{v2} - \phi_{i4}) + \frac{V_{r4}I_{r2}}{2}\cos(\phi_{v4} - \phi_{i2})\right] \\ &\quad + \left[I_0V_{r2}\sin(2\omega t + \phi_{v2}) + R_{dc}I_0I_{r2}\sin(2\omega t + \phi_{i2})\right] \\ &\quad + \left[I_0V_{r4}\sin(4\omega t + \phi_{v4}) + R_{dc}I_0I_{r4}\sin(4\omega t + \phi_{i4})\right. \\ &\quad \left. - \frac{V_{r2}I_{r2}}{2}\cos(4\omega t + \phi_{v2} + \phi_{i2})\right] \\ &\quad - \left[\frac{V_{r2}I_{r4}}{2}\cos(6\omega t + \phi_{v2} + \phi_{i4}) - \frac{V_{r4}I_{r2}}{2}\cos(6\omega t + \phi_{v4} + \phi_{i2})\right] \\ &\quad - \frac{V_{r4}I_{r4}}{2}\cos(8\omega t + \phi_{v4} + \phi_{i4}) \end{aligned} \quad (2.74)$$

Based on the different components of the power flow, we can divide the instantaneous power p_{out} into two parts [8]. One part is produced by the active component $I_{ra,h}$ of the current I_{rh}, i.e., the component of the ripple part of the dc link current I_{rh} in phase with the dc voltage ripple V_{rh} as shown in Fig. 2.3, and is represented as the active instantaneous power p_a. The other is produced by the reactive component $I_{rq,h}$ of the current I_{rh}, i.e., the component in quadrature with the voltage V_{rh}, which is represented as the reactive instantaneous power p_q.

Therefore, it can be written as:

$$\begin{aligned}
p_a(t) &= \overline{v_{dc}} \times \overline{i_{dc}} + v_{r2}(t) \times i_{ra,2}(t) + v_{r4}(t) \times i_{ra,4}(t) \\
&= R_{dc} I_0 \times I_0 + \Big[V_{r2} \sin(2\omega t + \phi_{v2})\Big]\Big[I_{r2} \cos(\phi_{v2} - \phi_{i2}) \sin(2\omega t + \phi_{v2})\Big] \\
&\quad + \Big[V_{r4} \sin(4\omega t + \phi_{v4})\Big]\Big[I_{r4} \cos(\phi_{v4} - \phi_{i4}) \sin(4\omega t + \phi_{v4})\Big] \\
&= \left[R_{dc} I_0^2 + \frac{V_{r2} I_{r2}}{2} \cos(\phi_{v2} - \phi_{i2}) + \frac{V_{r4} I_{r4}}{2} \cos(\phi_{v4} - \phi_{i4})\right] \\
&\quad - \frac{V_{r2} I_{r2}}{2} \cos(\phi_{v2} - \phi_{i2}) \cos(4\omega t + 2\phi_{v2}) \\
&\quad - \frac{V_{r4} I_{r4}}{2} \cos(\phi_{v4} - \phi_{i4}) \cos(8\omega t + 2\phi_{v4})
\end{aligned} \tag{2.75}$$

$$\begin{aligned}
p_q(t) &= v_{r2}(t) \times i_{rq,2}(t) + v_{r4}(t) \times i_{rq,4}(t) \\
&\quad + \overline{v_{dc}} \times i_{r2}(t) + \overline{v_{dc}} \times i_{r4}(t) + \overline{i_{dc}} \times v_{r2}(t) + \overline{i_{dc}} \times v_{r4}(t) \\
&\quad + i_{r2}(t) \times v_{r4}(t) + v_{r2}(t) \times i_{r4}(t) \\
&= \Big[V_{r2} \sin(2\omega t + \phi_{v2})\Big]\Big[I_{r2} \sin(\phi_{v2} - \phi_{i2}) \sin(2\omega t + \phi_{v2} - 90^\circ)\Big] \\
&\quad + \Big[V_{r4} \sin(4\omega t + \phi_{v4})\Big]\Big[I_{r4} \sin(\phi_{v4} - \phi_{i4}) \sin(4\omega t + \phi_{v4} - 90^\circ)\Big] \\
&\quad + R_{dc} I_0 I_{r2} \sin(2\omega t + \phi_{i2}) + R_{dc} I_0 I_{r4} \sin(4\omega t + \phi_{i4}) \\
&\quad + I_0 V_{r2} \sin(2\omega t + \phi_{v2}) + I_0 V_{r4} \sin(4\omega t + \phi_{v4}) \\
&\quad + \Big[V_{r4} \sin(4\omega t + \phi_{v4})\Big]\Big[I_{r2} \sin(2\omega t + \phi_{i2})\Big] \\
&\quad + \Big[V_{r2} \sin(2\omega t + \phi_{v2})\Big]\Big[I_{r4} \sin(4\omega t + \phi_{i4})\Big] \\
&\approx R_{dc} I_0 I_{r2} \sin(2\omega t + \phi_{i2}) + I_0 V_{r2} \sin(2\omega t + \phi_{v2}) \\
&\quad + R_{dc} I_0 I_{r4} \sin(4\omega t + \phi_{i4}) + I_0 V_{r4} \sin(4\omega t + \phi_{v4})
\end{aligned} \tag{2.76}$$

The component p_a of the instantaneous output power p_{out} shows the rate

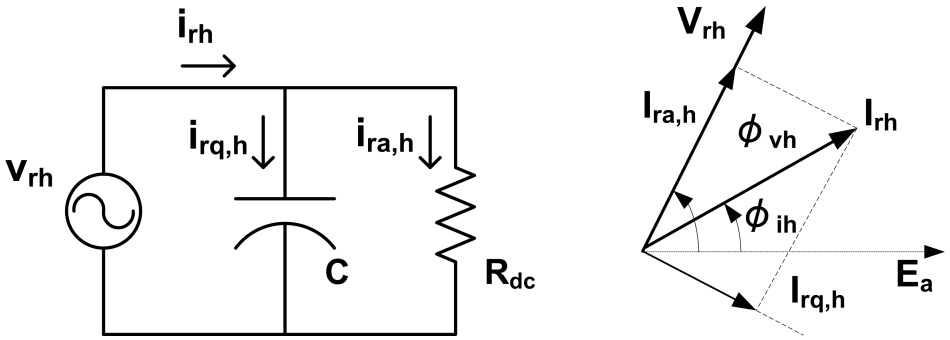

(a) Equivalent circuit (b) Phasor diagram

Figure 2.3: Equivalent circuit and phasor diagram of AC component of the current and voltage on the DC output side.

of flow of the energy from the source to the load. The mean value of p_a in (2.75) during one cycle is the average output active power P_{out}, which can be expressed as,

$$\begin{aligned} P_{out} &= R_{dc}I_0^2 + \frac{V_{r2}I_{r2}}{2}\cos(\phi_{v2}-\phi_{i2}) + \frac{V_{r4}I_{r4}}{2}\cos(\phi_{v4}-\phi_{i4}) \\ &= R_{dc}I_0^2 + \frac{R_{dc}(I_{r2sin}^2 + I_{r2cos}^2)}{2\sqrt{1+4\omega^2C^2R_{dc}^2}}\cos(\phi_{v2}-\phi_{i2}) \\ &\quad + \frac{R_{dc}(I_{r4sin}^2 + I_{r4cos}^2)}{2\sqrt{1+16\omega^2C^2R_{dc}^2}}\cos(\phi_{v4}-\phi_{i4}) \end{aligned} \tag{2.77}$$

From (2.77), we can see that the average active power absorbed by the load is also decided by the amplitude of the DC voltage ripple (i.e. I_{r2sin}, I_{r2cos}, I_{r4sin} and I_{r4cos}). Therefore, under the unbalanced operating conditions, the source has to provide more power if the ripples are not eliminated properly. Mostly, when v_{dc} is regulated, the second and fourth order harmonic components are not so obvious, which means the magnitude of Δv_{dc} is much smaller than $\overline{v_{dc}}$, so the factors $V_{r2}I_{r2}$ and $V_{r4}I_{r4}$ can be neglected, p_a will only have the first item $R_{dc}I_0^2$.

The component p_q shows the rate of the energy related with the reactive power, so the average value of this rate of energy flow is zero, and the net transfer

of energy to the load is zero. When the voltage regulation control is implemented, the second order and fourth order harmonic ripples on the DC link should be reduced to a small value. In this case, p_q will appear as a second order and a fourth order harmonic components, i.e. the approximated result in (2.76) by ignoring the factors $V_{r2}I_{r2}$, $V_{r2}I_{r4}$, $V_{r4}I_{r2}$ and $V_{r4}I_{r4}$, those are called the current distorted power and voltage distorted power [75]. The reactive power Q_{out} is the amplitude of the oscillating instantaneous power p_q, which can be represented as,

$$\begin{aligned} Q_{out} &= \sqrt{(R_{dc}I_0I_{r2}\cos\phi_{i2} + I_0V_{r2}\cos\phi_{v2})^2 + (R_{dc}I_0I_{r2}\sin\phi_{i2} + I_0V_{r2}\sin\phi_{v2})^2} \\ &\quad + \sqrt{(R_{dc}I_0I_{r4}\cos\phi_{i4} + I_0V_{r4}\cos\phi_{v4})^2 + (R_{dc}I_0I_{r4}\sin\phi_{i4} + I_0V_{r4}\sin\phi_{v4})^2} \\ &= \frac{2R_{dc}I_0}{\sqrt{1+4\rho^2}}\sqrt{(1+\rho^2)I_{r2\sin}^2 + 4\rho I_{r2\sin}I_{r2\cos} + \rho^2 I_{r2\cos}^2} \\ &\quad + \frac{4R_{dc}I_0}{\sqrt{1+16\rho^2}}\sqrt{(1+\rho^2)I_{r4\sin}^2 + 16\rho I_{r4\sin}I_{r4\cos} + \rho^2 I_{r4\cos}^2} \end{aligned} \tag{2.78}$$

where $\rho = \omega C R_{dc}$.

The equation (2.78) shows that the average reactive power is affected by the amplitude of the DC voltage ripple (i.e. I_{r2sin}, I_{r2cos}, I_{r4sin} and I_{r4cos}). Therefore, only when the DC link voltage is made ripple-free, the output average reactive power Q_{out} is close to zero.

According to (2.74), $p_{out}(t)$ contains not only the average value, but also the second order harmonics, the fourth order harmonics, the sixth order harmonics and the eighth order harmonics. According to [71], when the positive and negative sequence components of the input voltages and line side currents in rotating synchronous *d-q* frame are assumed to be constant, the input active instantaneous power $p_{in}(t)$ can be presented as the sum of a constant term P_o^{in} and two second order harmonic terms P_{s2}^{in} and P_{c2}^{in}. However, there are higher even-order harmonic

components, such as 4^{th}, 6^{th} and 8^{th} order harmonics, appearing in the output instantaneous power under the unbalanced operating conditions as shown in (2.74). The higher even-order harmonic components have not been discussed in [71].

Since the power flow should be balanced, the input instantaneous power p_{in} will also involve the fourth, sixth and eighth order harmonic components correspondingly. If the supply voltages (e_d^p, e_q^p, e_d^n and e_q^n) are still assumed to be constant without considering the distorted supply conditions, the d-q components of the ac currents (i_d^p, i_q^p, i_d^n and i_q^n) must have the second, fourth, sixth and eighth order harmonic components to provide the corresponding harmonic components in the input instantaneous power according to (D.4) in Appendix D. Those even-order harmonic components appear as the corresponding odd-order harmonics in the supply side line currents i_a, i_b, i_c based on the three phase a-b-c frame.

Since only the line frequency components of the input voltages contribute to supplying the system with the instantaneous power under the unbalanced and distorted conditions, it is considered that the three phase supply voltages can be decomposed into the fundamental positive and negative sequence components.

$$e_a(t) = E_1^p \sin(\omega t + \theta_{e1}^p) + E_1^n \sin(\omega t + \theta_{e1}^n) \tag{2.79}$$

$$e_b(t) = E_1^p \sin(\omega t - 120^\circ + \theta_{e1}^p) + E_1^n \sin(\omega t + 120^\circ + \theta_{e1}^n) \tag{2.80}$$

$$e_c(t) = E_1^p \sin(\omega t + 120^\circ + \theta_{e1}^p) + E_1^n \sin(\omega t - 120^\circ + \theta_{e1}^n) \tag{2.81}$$

where the variables E and θ_e represent the amplitude and the angle of the three phase voltages. Superscripts p and n designate the positive and negative sequence components, respectively, and subscript 1 represent the fundamental component.

To simplify the problem, we consider the corresponding currents only including the third order harmonics,

$$\begin{aligned} i_a(t) &= I_1^p \sin(\omega t + \theta_{i1}^p) + I_1^n \sin(\omega t + \theta_{i1}^n) \\ &\quad + I_3^p \sin(3\omega t + \theta_{i3}^p) + I_3^n \sin(3\omega t + \theta_{i3}^n) \end{aligned} \tag{2.82}$$

$$\begin{aligned} i_b(t) &= I_1^p \sin(\omega t - 120^\circ + \theta_{i1}^p) + I_1^n \sin(\omega t + 120^\circ + \theta_{i1}^n) \\ &\quad + I_3^p \sin(3\omega t - 120^\circ + \theta_{i3}^p) + I_3^n \sin(3\omega t + 120^\circ + \theta_{i3}^n) \end{aligned} \tag{2.83}$$

$$\begin{aligned} i_c(t) &= I_1^p \sin(\omega t + 120^\circ + \theta_{i1}^p) + I_1^n \sin(\omega t - 120^\circ + \theta_{i1}^n) \\ &\quad + I_3^p \sin(3\omega t + 120^\circ + \theta_{i3}^p) + I_3^n \sin(3\omega t - 120^\circ + \theta_{i3}^n) \end{aligned} \tag{2.84}$$

where the variables I and θ_i represent the amplitude and the angle of the three phase currents. Subscript 3 represent the third order of the harmonics.

According to the three phase currents in (2.82)-(2.84), the voltages across the inductance L can be determined as,

$$\begin{aligned} v_{aL}(t) &= L\frac{di_a}{dt} = L\omega I_1^p \cos(\omega t + \theta_{i1}^p) + L\omega I_1^n \cos(\omega t + \theta_{i1}^n) \\ &\quad + 3L\omega I_3^p \cos(3\omega t + \theta_{i3}^p) + 3L\omega I_3^n \cos(3\omega t + \theta_{i3}^n) \end{aligned} \tag{2.85}$$

$$\begin{aligned} v_{bL}(t) &= L\omega I_1^p \cos(\omega t - 120^\circ + \theta_{i1}^p) + L\omega I_1^n \cos(\omega t + 120^\circ + \theta_{i1}^n) \\ &\quad + 3L\omega I_3^p \cos(3\omega t - 120^\circ + \theta_{i3}^p) + 3L\omega I_3^n \cos(3\omega t + 120^\circ + \theta_{i3}^n) \end{aligned} \tag{2.86}$$

$$\begin{aligned} v_{cL}(t) &= L\omega I_1^p \cos(\omega t + 120^\circ + \theta_{i1}^p) + L\omega I_1^n \cos(\omega t - 120^\circ + \theta_{i1}^n) \\ &\quad + 3L\omega (I_3^p \cos(3\omega t + 120^\circ + \theta_{i3}^p) + 3L\omega I_{n3} \cos(3\omega t - 120^\circ + \theta_{i3}^n) \end{aligned} \tag{2.87}$$

Therefore, the instantaneous power consumed by the inductance L can be obtained by multiplying the currents in (2.82)-(2.84) and the voltages in (2.85)-

(2.87),

$$\begin{aligned} p_L(t) &= v_{aL}(t)i_a(t) + v_{bL}(t)i_b(t) + v_{cL}(t)i_c(t) \\ &= 3L\omega I_1^p I_1^n \sin(2\omega t + \theta_{i1}^p + \theta_{i1}^n) - 3L\omega I_1^p I_3^p \sin(2\omega t + \theta_{i1}^p - \theta_{i3}^p) \\ &\quad -3L\omega I_1^n I_3^n \sin(2\omega t - \theta_{i1}^n + \theta_3^n) + 6L\omega I_1^p I_3^n \sin(4\omega t + \theta_{i1}^p + \theta_{i3}^n) \\ &\quad +6L\omega I_1^n I_3^p \sin(4\omega t + \theta_{i3}^p + \theta_{i1}^n) + 9L\omega I_3^p I_3^n \sin(6\omega t + \theta_{i3}^p + \theta_{i3}^n) \end{aligned} \quad (2.88)$$

And the instantaneous power consumed by the resistance R can also be calculated by the currents in (2.82)-(2.84),

$$\begin{aligned} p_R(t) &= Ri_a^2(t) + Ri_b^2(t) + Ri_c(t)^2 \\ &= \frac{3RI_1^{p2}}{2} + \frac{3RI_1^{n2}}{2} + \frac{3RI_3^{p2}}{2} + \frac{3RI_3^{n2}}{2} \\ &\quad -3RI_1^p I_1^n \cos(2\omega t + \theta_{i1}^p + \theta_{i1}^n) + 3RI_1^p I_3^p \cos(2\omega t - \theta_{i1}^p + \theta_{i3}^p) \\ &\quad +3RI_1^n I_3^n \cos(2\omega t - \theta_{i1}^n + \theta_{i3}^n) - 3RI_1^p I_3^n \cos(4\omega t + \theta_{i1}^p + \theta_{i3}^n) \\ &\quad -3RI_1^n I_3^p \cos(4\omega t + \theta_{i3}^p + \theta_{i1}^n) - 3RI_3^p I_3^n \cos(6\omega t + \theta_{i3}^p + \theta_{i3}^n) \end{aligned} \quad (2.89)$$

The equations (2.88) and (2.89) provide a clear picture of the effect of the unbalanced supply voltages on the instantaneous power across L and R. In the balanced case, the negative sequence current is zero ($I_{n1} = 0, I_{n3} = 0$), and there are no third order harmonics in the ac line side currents ($I_{p3} = 0$), so that $p_L(t)$ is equal to zero, and $p_R(t)$ is constant but very small comparing with the output instantaneous power, whereas it is not so in the unbalanced case. The unbalanced supply voltages will cause the negative sequence components and thus the odd-order harmonics components appear in the ac line side currents. Consequently, p_L and p_R both consist of the second and the fourth order harmonics in (2.88) and (2.89).

The input instantaneous power can be obtained from (2.79) to (2.84) based on the expression of the input power in (2.69),

$$\begin{aligned} p_{in}(t) &= \frac{3}{2}E_1^p I_1^p \cos(\theta_{e1}^p - \theta_{i1}^p) + \frac{3}{2}E_1^n I_1^n \cos(\theta_{e1}^n - \theta_{i1}^n) \\ &\quad -\frac{3}{2}E_1^p I_1^n \cos(2\omega t + \theta_{e1}^p + \theta_{i1}^n) + \frac{3}{2}E_1^p I_3^p \cos(2\omega t - \theta_{e1}^p + \theta_{i3}^p) \\ &\quad -\frac{3}{2}E_1^n I_1^p \cos(2\omega t + \theta_{e1}^n + \theta_{i1}^p) + \frac{3}{2}E_1^n I_3^n \cos(2\omega t - \theta_{e1}^n + \theta_{i3}^n) \\ &\quad -\frac{3}{2}E_1^p I_3^n \cos(4\omega t + \theta_{e1}^p + \theta_{i3}^n) - \frac{3}{2}E_1^n I_3^p \cos(4\omega t + \theta_{e1}^n + \theta_{i3}^p) \quad (2.90) \end{aligned}$$

From the equation (2.90), we can see that when only the third order current harmonics is considered, there are the second and the fourth order harmonics appearing in the input instantaneous power. However, based on the calculation of the output instantaneous power p_{out} in (2.74) and the instantaneous power p_L and p_R in (2.88) and (2.89), the sixth and the eighth order harmonics also would be drawn from the input instantaneous power. Therefore, the higher order line side current harmonics must be involved in the system to provide the high order harmonics in the output instantaneous power. And the more the line side current harmonics occur, the more the non-active power should be provided from the supply voltage to compensate the oscillated instantaneous power to the load, the converter inductances and resistances.

2.5 Simulation Validation on Power Flow

Let us take an example to illustrate the proposed analysis of the output instantaneous power flow under the balanced and unbalanced supply voltage conditions. The three phase PWM AC-DC voltage source converter is considered to be working with the three balanced voltages of $80\sqrt{2}\sin(\omega t)$, $80\sqrt{2}\sin(\omega t - 120^\circ)$ and

$80\sqrt{2}\sin(\omega t + 120°)$ with open loop control. The desired dc link voltage is 400 V. The unbalanced supply voltages, which happens at $t = 0.05$ sec, are assumed to be $80\sqrt{2}\sin(\omega t)$, $80\sin(\omega t - 135°)$ and $80\sin(\omega t + 135°)$. Figs. 2.4-2.8 provide the performance of the system for this example by using Simulink toolbox in MATLAB software.

The system parameters used in the simulation studies as well as in the experiment tests are provided in Table 2.1.

Table 2.1: Circuit Parameters Used In the Simulation and the Experiment

Parameters	Value	Parameters	Value
R	2 Ω	R_{dc}	227 Ω
L	0.0055 H	C	250 μF

Fig. 2.4 shows the simulation results of the dc link voltage and the ac supply side currents i_d^p, i_q^p, i_d^n and i_q^n in the positive and negative synchronous rotating frames with the balanced and unbalanced supply voltages. The switching signals are kept unchanged as in the balanced case, $S_d^p = -0.02225$, $S_q^p = -0.34255$, $S_d^n = 0$ and $S_q^n = 0$. Under the balanced operating conditions, i_d^n and i_q^n would have been close to zero. Whereas under the unbalanced operating conditions, the negative sequence components appearing in the synchronous rotating currents, $i_d^n = -20.92A$ and $i_q^n = 5.0332A$ in the steady state. These negative sequence current components lead to the ripples in the dc link voltage as shown in Fig. 2.4. Also, the second order harmonics can be found in the positive sequence current components (I_d^p and I_q^p) as the zoomed view of Fig. 2.4. These second order harmonics provide the fourth order harmonic component in the dc link current and voltage in the equations (2.30), (2.31) and (2.38).

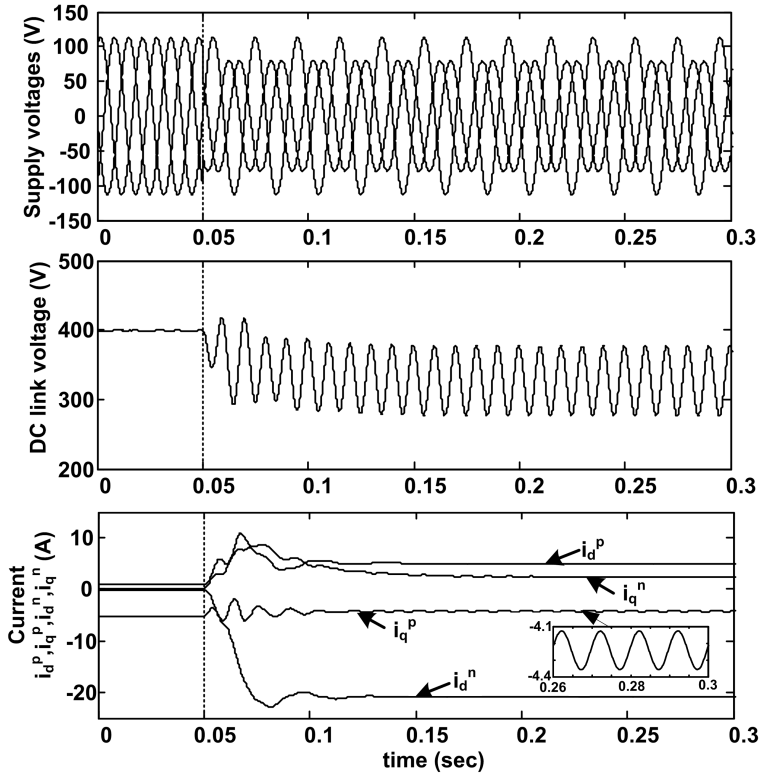

Figure 2.4: Simulation results of DC link output voltage and current when the rectifier starts to work under the unbalanced condition.

Fig. 2.5 shows the output dc link voltage and dc link current of the rectifier when the supply voltages are unbalanced. According to the observations from Fig. 2.4, the average value of i_d^p and i_q^p are $2.4287A$, $-4.243A$, respectively. The average dc constant $\overline{i_{dc}}$ can be calculated as $1.4A$ using (2.19). Similarly, I_{r2sin} and I_{r2cos} can be obtained from (2.38), $I_{r2sin} = 7.3$ and $I_{r2cos} = -1.3$. Consequently, the value of Δv_{dc} can be calculated from (2.39), $47.4V$. From Fig 2.5, it can be observed that there are the second order harmonic components in the output dc link voltage and current. The peak amplitude of the second order harmonic component of dc link voltage V_{r2} is around 50 V using (2.72) and that in the dc side current I_{r2} is around 7.8 A by (2.73), which almost match the theoretical results predicted.

The output instantaneous power is shown in Fig. 2.6, which can be calculated

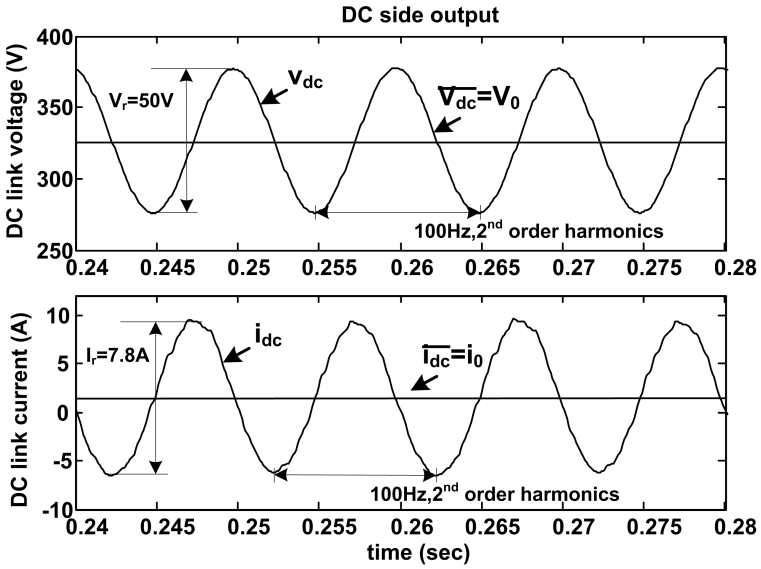

Figure 2.5: DC link output voltage and current under unbalanced condition with open loop control.

using (2.74). According to the different components of the power flow, the output instantaneous power can be expressed as the sum of two parts as the active instantaneous power p_a and the reactive instantaneous power p_q as shown in Fig. 2.7. Based on (2.75), the component p_a consists of not only the average value of the instantaneous output power, 471 W, but also the second and fourth order harmonic components as shown in the frequency spectra of the instantaneous output power (Fig. 2.6). The average value of p_q is almost around zero as can be seen in Fig. 2.7, but it has the ripple component which consists of the second order harmonic component as in (2.76).

From the equation (2.74), the output instantaneous power contains the average value, the second order, the fourth order, the sixth order and the eighth order harmonics. According to the result of the power spectra of the output instantaneous power in Fig. 2.6, the amplitude of the second order harmonic component is around 2560 VA and the fourth order harmonic 210 VA. In turn, the even-order harmonics

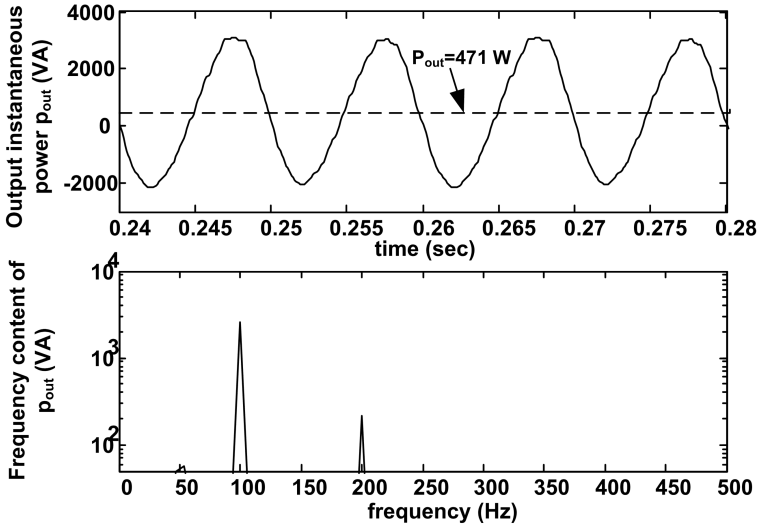

Figure 2.6: Simulation results of output instantaneous power and its frequency spectra.

would be generated in the input instantaneous power and the *d*-*q* component of the line side currents as discussed in Section 2.4. As a result, the odd-order harmonics appear in the ac side currents in *a*-*b*-*c* frame and the even-order harmonics on the dc link voltage. Therefore, the control objective is to cancel these even harmonic components in the output instantaneous power.

Fig. 2.8 shows the input instantaneous power p_{in}, the instantaneous power consumed by the inductance and resistance, p_L and p_R. Since the power flow of the whole system should be balanced as in (2.71), except to supply the instantaneous power to the output p_{out}, the remaining part of p_{in} provides the the instantaneous power consumed by the inductance and resistance, p_L and p_R. By analyzing the sequence components in the currents i_a, i_b and i_c, the amplitude of the positive and negative components can be found as $I_{p1} = 3.9621A$, $I_{n1} = 17.5018A$, $I_{p3} = 1.3669A$ and $I_{n3} = 0.1169A$. Those negative sequence and harmonic components in the ac line side currents will cause the second and fourth order harmonics in the input instantaneous power p_{in} as (2.90) and the second, fourth and sixth

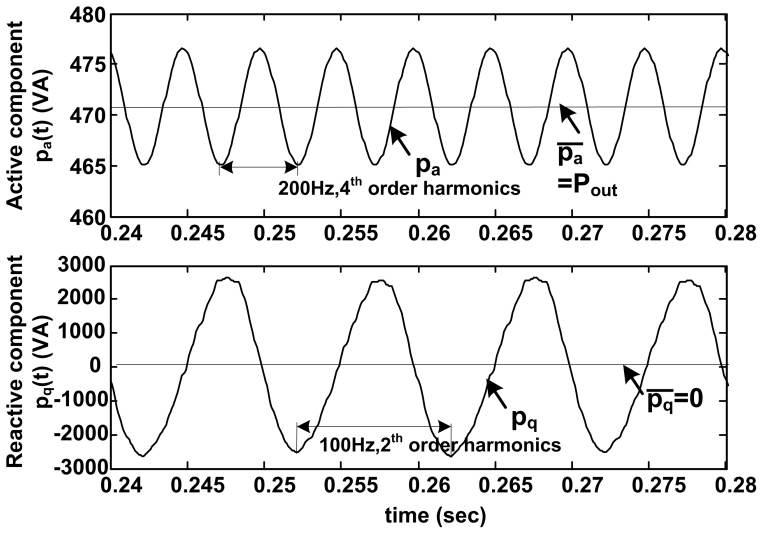

Figure 2.7: Simulation results of two components p_a and p_q calculated from DC link voltage and current.

order harmonics in the instantaneous power consumed by the inductances L and resistances R as (2.88) and (2.89). Based on (2.88) and (2.89), the average value of this part of the instantaneous power is 137 VA, which is decided by I_{p1}, I_{n1}, I_{p3} and I_{n3}. Moreover, from Fig. 2.8, we can see that the instantaneous power p_L and p_R also include the second order harmonic, whose peak value is 477 VA and the fourth order harmonic, 246 VA. All the results are close to the predicted result from (2.88) and (2.89).

From this example by using the simulation studies, it has been shown that the instantaneous power flow analysis presented in Section 2.4 and the presence of harmonics in the output and input side have been validated. According to the output instantaneous power calculated from the dc side in (2.74), the fourth order harmonic components in the dc link current and voltage can cause the even-order harmonics in the instantaneous power, such as 2^{nd}, 4^{th}, 6^{th} and 8^{th}. Also, the larger value of the negative sequence components and the more high frequency of the harmonics are in the DC link current and voltage, the more harmonics appear

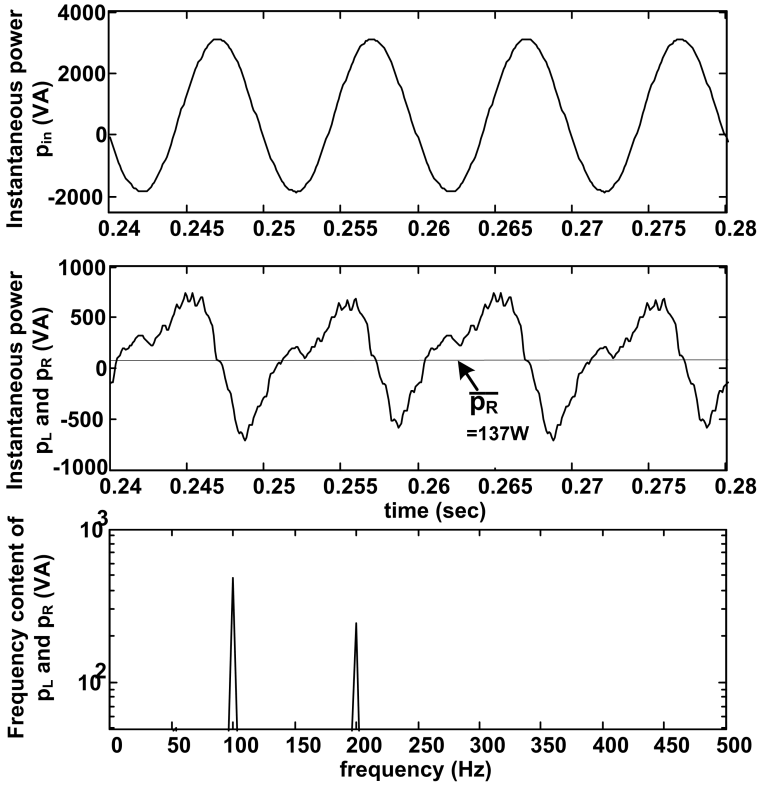

Figure 2.8: Simulation results of instantaneous power p_{in}, p_L and p_R and its frequency spectra.

in the instantaneous power and the more loss is generated. In order to meet the requirement of (2.71), the input current will involve a small amount of higher order harmonics accordingly. Therefore, to maintain a ripple-free dc output and sinusoidal input currents with the unity power factor of the three phase PWM AC/DC converter under the unbalanced supply voltages is to make the output instantaneous power constant at the interested frequency.

2.6 Summary

In this chapter, the model of three phase PWM AC-DC voltage source converter in the positive and negative synchronous rotating frames has been proposed. This

proposed model can be used to explain that the negative sequence components lead to the even-order harmonics at the dc output voltage and the low frequency odd-order harmonics in the input ac currents under the unbalanced supply voltage conditions. Also, this model gives the analytical explanation on the cause of the harmonic component of the supply voltage harmonics frequency in the ac line side currents under the distorted supply voltages. In order to give an insight of the power flow of the whole system, the instantaneous power flow based on the mathematical model in the positive and negative synchronous rotating frames is analyzed. This power flow analysis demonstrates the direct relationship between the dc link voltage ripple and the second harmonic terms in the instantaneous power and shows the inner link between the odd-order harmonics in the ac line side currents and the even-order harmonics at the dc output voltage. Finally, the simulation results are provided to validate the proposed model and analysis.

Chapter 3

Implementation of Control Strategy for Three Phase AC-DC PWM Voltage Source Converter

The PWM AC/DC boost converter system has some advanced features including providing loads with a suitable amount of average power at a specified level of output voltage and maintaining close to unity power factor for the utility interface perspective. However, all the advantages are valid only with the assumption of the balanced supply voltages. Under the distorted and unbalanced supply voltages, there would be the even-order harmonics at the dc link voltage and the odd-order harmonics in the ac line side currents. In order to eliminate all these harmonics, a proper control strategy should be implemented in the positive and negative sequence rotating synchronous frames as discussed in Chapter 2.

Based on the control objectives, the control signals are divided into two parts: *voltage harmonics control* and *current harmonics control* will be discussed in Section 3.1. Also, the control block diagram of the cascaded dual frame current regulator with a voltage regulator has been described.

Section 3.2 introduces the four control laws from which the references of the positive and negative sequence input currents are calculated.

Section 3.3 aims to investigate the direct effect of the different modulation schemes on the performance of voltage source converter based on the comparison of the two most popular PWM schemes (SPWM and SVPWM modulation schemes). The limitations on the steady state and dynamic performances with the SPWM scheme have been analyzed and compared with the SVPWM scheme.

In Section 3.4, the software phase locked loop (SPLL) has been introduced to provide a reference phase signal synchronized with the grid. To guarantee the stability and the performance of the SPLL system, the design procedures of SPLL have been provided.

Section 3.5 mainly focuses on the influence of the symmetrical components calculator on the performance of the three phase PWM AC-DC voltage source converter. First, the phase shifting method used to estimate the instantaneous symmetrical components online in our work has been introduced. Based on the dynamic analysis of the symmetrical components calculator, the difference of the three phase PWM AC-DC voltage source converter between the single frame controller and the dual frame controller has been elaborated.

3.1 Control Strategy

The control objective to operate the three phase PWM AC-DC voltage source converters under the distorted and unbalanced supply voltage conditions can be

highlighted as,

- to eliminate the even-order harmonics at the dc link voltage caused by negative sequence supply voltages; and
- to eliminate the odd-order harmonics in the supply side line currents because of the unbalanced and distorted supply voltages.

Accordingly, the control signals, S_d^p, S_q^p, S_d^n and S_q^n can be divided into two parts, 1) *voltage harmonics control signals*, S_{dv}^p, S_{qv}^p, S_{dv}^n and S_{qv}^n, those are used to take care of the even-order harmonics at the dc link voltage, and 2) *current harmonics control signals*, S_{di}^p, S_{qi}^p, S_{di}^n and S_{qi}^n, those are supposed to eliminate the odd-order harmonics in the line side currents.

Substituting the control signals in the PWM rectifier model as shown in the line side current equations (2.8), (2.9), under the distorted and unbalanced supply voltage conditions (2.40) and (2.41), the PWM rectifier model can be rewritten as,

$$\begin{aligned}\begin{bmatrix} \dot{i}_d^p \\ \dot{i}_q^p \end{bmatrix} &= \begin{bmatrix} -\frac{R}{L} & \omega \\ -\omega & -\frac{R}{L} \end{bmatrix} \begin{bmatrix} i_d^p \\ i_q^p \end{bmatrix} + \begin{bmatrix} \frac{1}{L} & 0 \\ 0 & \frac{1}{L} \end{bmatrix} \begin{bmatrix} e_{d1}^p \\ e_{q1}^p \end{bmatrix} + \begin{bmatrix} -\frac{v_{dc}}{L} & 0 \\ 0 & -\frac{v_{dc}}{L} \end{bmatrix} \begin{bmatrix} S_{dv}^p \\ S_{qv}^p \end{bmatrix} \\ &+ \begin{bmatrix} \frac{1}{L} & 0 \\ 0 & \frac{1}{L} \end{bmatrix} \begin{bmatrix} \sum_{k\neq 1} e_{dk}^p \\ \sum_{k\neq 1} e_{qk}^p \end{bmatrix} + \begin{bmatrix} -\frac{v_{dc}}{L} & 0 \\ 0 & -\frac{v_{dc}}{L} \end{bmatrix} \begin{bmatrix} S_{di}^p \\ S_{qi}^p \end{bmatrix} \end{aligned} \tag{3.1}$$

$$\begin{aligned}\begin{bmatrix} \dot{i}_d^n \\ \dot{i}_q^n \end{bmatrix} &= \begin{bmatrix} -\frac{R}{L} & -\omega \\ \omega & -\frac{R}{L} \end{bmatrix} \begin{bmatrix} i_d^n \\ i_q^n \end{bmatrix} + \begin{bmatrix} \frac{1}{L} & 0 \\ 0 & \frac{1}{L} \end{bmatrix} \begin{bmatrix} e_{d1}^n \\ e_{q1}^n \end{bmatrix} + \begin{bmatrix} -\frac{v_{dc}}{L} & 0 \\ 0 & -\frac{v_{dc}}{L} \end{bmatrix} \begin{bmatrix} S_{dv}^n \\ S_{qv}^n \end{bmatrix} \\ &+ \begin{bmatrix} \frac{1}{L} & 0 \\ 0 & \frac{1}{L} \end{bmatrix} \begin{bmatrix} \sum_{k\neq 1} e_{dk}^n \\ \sum_{k\neq 1} e_{qk}^n \end{bmatrix} + \begin{bmatrix} -\frac{v_{dc}}{L} & 0 \\ 0 & -\frac{v_{dc}}{L} \end{bmatrix} \begin{bmatrix} S_{di}^n \\ S_{qi}^n \end{bmatrix} \end{aligned} \tag{3.2}$$

In order to get rid of the odd-order harmonics and only keep the fundamental frequency component in the ac line side currents, the currents in the rotating synchronous frame, i_d^p, i_q^p, i_d^n, i_q^n should be regulated to a fixed and constant value depending on the load condition. Therefore, the effect from the supply voltage harmonics must be compensated by current harmonics control signals, S_{di}^p, S_{qi}^p, S_{di}^n and S_{qi}^n, as shown in the equations (3.1) and (3.2). The other parts of the control signals, S_{dv}^p, S_{qv}^p, S_{dv}^n and S_{qv}^n, are considered constant to ensure the required line side currents in this current model.

Similarly, the DC side model of the PWM rectifier can be obtained from the equation (2.20),

$$C\dot{v}_{dc} = -\frac{v_{dc}}{R_{dc}} + \begin{bmatrix} i_d^n \cos 2\theta + i_q^n \sin 2\theta + i_d^p \\ i_q^n \cos 2\theta - i_d^n \sin 2\theta + i_q^p \\ i_d^p \cos 2\theta - i_q^p \sin 2\theta + i_d^n \\ i_d^p \sin 2\theta + i_q^p \cos 2\theta + i_q^n \end{bmatrix}' \begin{bmatrix} S_{dv}^p + S_{di}^p \\ S_{qv}^p + S_{qi}^p \\ S_{dv}^n + S_{di}^n \\ S_{qv}^n + S_{qi}^n \end{bmatrix} \tag{3.3}$$

The voltage harmonic control signals are mainly to overcome the effects of unbalance in the supply voltages which deal with the fundamental voltage, while the current harmonic control signals are designed to take care of odd-order harmonics in supply side line currents due to the unbalanced and distorted supply voltages. However, the distortions in the supply voltage is the dominant contributor for the odd-order current harmonics. Since EN50160 standard [9] allows 6% low order supply voltage harmonics, the amplitude of *current harmonics control signals* are much smaller as compared to *voltage harmonics control signals*. Thus, in (3.3), the control signals S_{di}^p, S_{qi}^p, S_{di}^n and S_{qi}^n can be neglected and *voltage harmonics control signals*, S_{dv}^p, S_{qv}^p, S_{dv}^n and S_{qv}^n, are mainly responsible to eliminate the even-order harmonics at the dc link voltage. Therefore, these control signals are designed to

regulate the instantaneous output power and provide the required average output power demanded by the load.

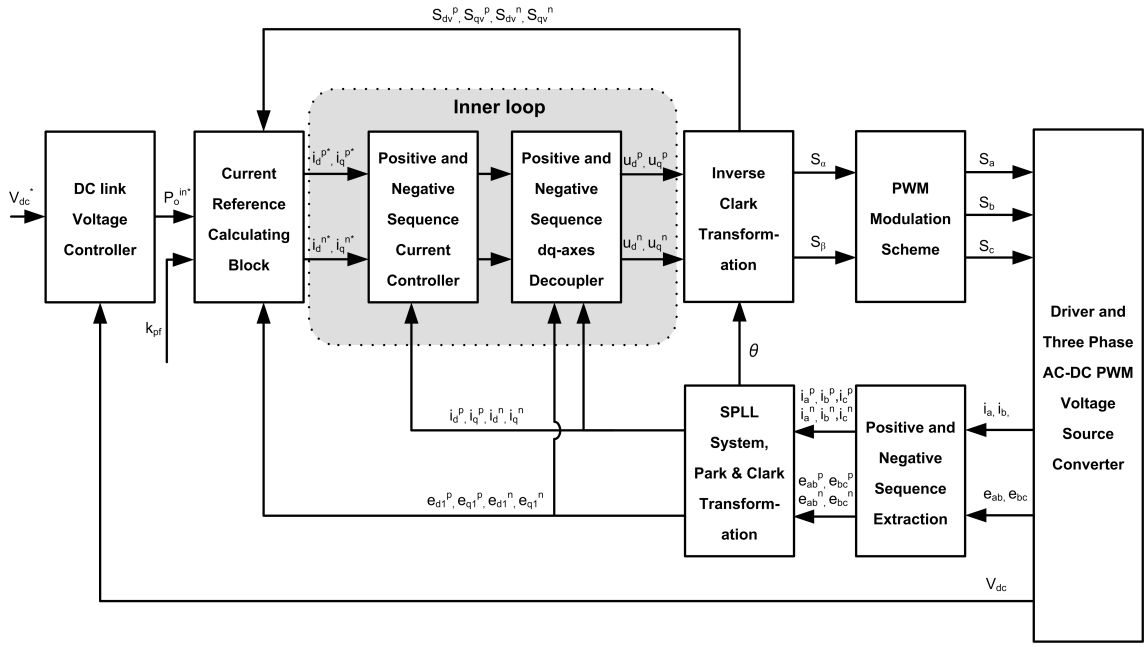

Figure 3.1: Cascaded control block diagram of three phase PWM AC-DC boost rectifier.

The complete control block diagram of the cascaded dual frame current regulator with a voltage regulator is shown in Fig. 3.1. Since the output average active power P_{out} is delivered from ac supply side and is decided by the dc link voltage level v_{dc}, the reference input average active power, P_o^{in} can be obtained from the error between the dc link reference voltage and the measured value. Then the estimated input average active power can be used in the reference current calculation block based on the *DC link voltage harmonics control* scheme. The current control calculation algorithm is implemented in the current reference calculating block of the control scheme to provide the four reference commands (i_d^{p*}, i_q^{p*}, i_n^{p*}, i_n^{p*}) for the inner current control loops. The inner loops are made up of two parallel positive and negative sequence *d-q* synchronous frame current regulators. The *AC line side current harmonics control* scheme can be implemented in this inner current con-

trollers to improve the performance of the ac line side current. The details about *AC line side current harmonics control* scheme would be discussed in Chapters 6 and 7.

3.2 Current Reference Calculation

Based on the analysis of the mathematical model in Chapter 2, the expression for the ripples on the dc link voltage under the unbalanced supply voltage conditions has been derived in (2.39), and is reproduced here for convenience.

$$\Delta v_{dc} = \frac{\sqrt{I_{r2sin}^2 + I_{r2cos}^2}}{2\omega C}\sin(2\omega t + \phi_{v2}) + \frac{\sqrt{I_{r4sin}^2 + I_{r4cos}^2}}{4\omega C}\sin(4\omega t + \phi_{v4}) \tag{3.4}$$

In order to improve the performance of the three phase PWM AC-DC voltage source converter under unbalanced supply voltage conditions, the ultimate goal of the control strategy is to cancel the second and fourth order harmonic components in Δv_{dc} to generate the required constant dc output voltage. The equation (3.4) shows that only when the conditions, $I_{r2sin} = 0$, $I_{r2cos} = 0$, $I_{r4sin} = 0$ and $I_{r4cos} = 0$, are satisfied at the same time, the ripples of the dc output voltage can be removed. Since in reality, the second order harmonics in the ac line side currents based on the d-q frame, I_{d2}^p, I_{q2}^p, I_{d2}^n and I_{q2}^n are relatively small as compared to the average value I_{d0}^p, I_{q0}^p, I_{d0}^n and I_{q0}^n, the equations (2.28)-(2.31) can be simplified as,

$$I_{r2\sin} \approx M_r = S_d^p I_{q0}^n - S_q^p I_{d0}^n - S_d^n I_{q0}^p + S_q^n I_{d0}^p \tag{3.5}$$

$$I_{r2\cos} \approx N_r = S_d^p I_{d0}^n + S_q^p I_{q0}^n + S_d^n I_{d0}^p + S_q^n I_{q0}^p \tag{3.6}$$

$$I_{r4\sin} \approx 0 \tag{3.7}$$

$$I_{r4\cos} \approx 0 \tag{3.8}$$

Since these equations are derived from the dc link voltage (2.20), the voltage harmonics control signals, S^p_{dv}, S^p_{qv}, S^n_{dv} and S^n_{qv} are dominant when compared with the current harmonics control signals as discussed in the preceding paragraph. The expressions of M_r and N_r can be further simplified as,

$$M_r = S^p_{dv} I^n_{q0} - S^p_{qv} I^n_{d0} - S^n_{dv} I^p_{q0} + S^n_{qv} I^p_{d0} \tag{3.9}$$

$$N_r = S^p_{dv} I^n_{d0} + S^p_{qv} I^n_{q0} + S^n_{dv} I^p_{d0} + S^n_{qv} I^p_{q0} \tag{3.10}$$

Therefore, only when the two conditions, $M_r = 0$ and $N_r = 0$ in (3.5) and (3.6), both are satisfied, a constant dc output voltage can be generated.

In the mean time, the output power should meet the load requirements and the power factor on the line side should be close to unity. The expression of the average input active power, P^{in}_o and the average input instantaneous reactive power, Q^{in}_o in terms of the *d-q* components of the positive and negative synchronous rotating frames have been given in Appendix D as,

$$P^{in}_o = e^p_d i^p_d + e^p_q i^p_q + e^n_d i^n_d + e^n_q i^n_q \tag{3.11}$$

$$Q^{in}_o = e^p_q i^p_d - e^p_d i^p_q - e^n_q i^n_d + e^n_d i^n_q \tag{3.12}$$

Since the useful input active and reactive power are only provided by the fundamental supply voltage e^p_{d1}, e^p_{q1}, e^p_{d1} and e^p_{q1}, and the second order harmonics in the ac line side currents based on the *d-q* frame can be ignored because of the small magnitude as compared to the average value I^p_{d0}, I^p_{q0}, I^n_{d0} and I^n_{q0}, so the equations (3.11) and (3.12) can be written as,

$$P^{in}_o = e^p_{d1} I^p_{d0} + e^p_{q1} I^p_{q0} + e^n_{d1} I^n_{d0} + e^n_{q1} I^n_{q0} \tag{3.13}$$

$$Q^{in}_o = e^p_{q1} I^p_{d0} - e^p_{d1} I^p_{q0} - e^n_{q1} I^n_{d0} + e^n_{d1} I^n_{q0} \tag{3.14}$$

This input average power, P_o^{in} is delivered to the DC link, so it should be matched not only to the load power P_o^{out} through DC link voltage but also to the power loss P_{loss} across AC filters and the power semiconductor devices within the converter. The average input reactive power Q_o^{in} exchanged between the utility source and voltage source converter determines the input power factor. We can define a parameter, k_{pf} as a ratio of Q_o^{in} to P_o^{in}. The relation between k_{pf} and power factor pf is shown in the following equation,

$$k_{pf} = \frac{Q_o^{in}}{P_o^{in}} = \frac{\sqrt{1 - pf^2}}{pf} \tag{3.15}$$

The power factor pf is defined as the ratio of the active power P to the apparent power S, and is a number between 0 and 1. According to the power definition in [75], for three phase system, the active power P and apparent power S can be defined as the sum of the active power and apparent power for each phase, respectively, i.e., $P = P_a + P_b + P_c$ and $S = S_a + S_b + S_c$. The power factor is desired to close to unity so that the maximum energy supplied by the source could be transferred to the load. This k_{pf} definition shows that during the unity power factor operation, k_{pf} is equal to zero.

To reject the harmonics on the DC link voltage and deliver the demanded power to the load under the unbalanced supply conditions, the control laws can be deduced from the following three points:

- the average input active power, P_o^{in} determines the output power to the load;
- the average input reactive power, Q_o^{in} exchanged between the utility source and the rectifier together with load determines the input power factor; and
- the conditions $M_r = 0$ and $N_r = 0$ decide that the output dc link voltage is

ripple-free.

Therefore, the control laws can be expressed by a set of four linear equations in a matrix form as the following,

$$\begin{bmatrix} P_o^{in} \\ Q_o^{in} \\ M_r \\ N_r \end{bmatrix} = \begin{bmatrix} P_o^{out} + P_{loss} \\ k_{pf} P_o^{in} \\ 0 \\ 0 \end{bmatrix} = \begin{bmatrix} e_{d1}^p & e_{q1}^p & e_{d1}^n & e_{q1}^n \\ e_{q1}^p & -e_{d1}^p & -e_{q1}^n & e_{d1}^n \\ S_{qv}^n & -S_{dv}^n & -S_{qv}^p & S_{dv}^p \\ S_{dv}^n & S_{qv}^n & S_{dv}^p & S_{qv}^p \end{bmatrix} \begin{bmatrix} I_{d0}^p \\ I_{q0}^p \\ I_{d0}^n \\ I_{q0}^n \end{bmatrix} \tag{3.16}$$

where the switching signals S_{dv}^p, S_{qv}^p,S_{dv}^n and S_{qv}^n used in this calculation are those obtained in the previous step.

The above matrix equation is solved to generate the four current reference values (i_d^{p*}, i_q^{p*}, i_d^{n*}, i_q^{n*}) as shown below,

$$\begin{aligned} i_d^{p*} &= I_{d0}^p = (k_1 P_o^{in} + k_{pf} k_2 P_o^{in})/dem \\ i_q^{p*} &= I_{q0}^p = (k_2 P_o^{in} - k_{pf} k_1 P_o^{in})/dem \\ i_d^{n*} &= I_{d0}^n = (k_3 P_o^{in} - k_{pf} k_4 P_o^{in})/dem \\ i_q^{n*} &= I_{q0}^n = (k_4 P_o^{in} + k_{pf} k_3 P_o^{in})/dem \end{aligned} \tag{3.17}$$

where k_1, k_2, k_3, k_4 and dem are defined as

$$\begin{aligned} k_1 &= e_{d1}^p (S_{dv}^{p2} + S_{qv}^{p2}) + e_{d1}^n (S_{qv}^p S_{qv}^n - S_{dv}^p S_{dv}^n) - e_{q1}^n (S_{dv}^p S_{qv}^n + S_{qv}^p S_{dv}^n) \\ k_2 &= e_{q1}^p (S_{dv}^{p2} + S_{qv}^{p2}) - e_{q1}^n (S_{qv}^p S_{qv}^n - S_{dv}^p S_{dv}^n) - e_{d1}^n (S_{dv}^p S_{qv}^n + S_{qv}^p S_{dv}^n) \\ k_3 &= e_{d1}^n (S_{dv}^{n2} + S_{qv}^{n2}) + e_{d1}^p (S_{qv}^p S_{qv}^n - S_{dv}^p S_{dv}^n) - e_{q1}^p (S_{dv}^p S_{qv}^n + S_{qv}^p S_{dv}^n) \\ k_4 &= e_{q1}^n (S_{dv}^{n2} + S_{qv}^{n2}) - e_{q1}^p (S_{qv}^p S_{qv}^n - S_{dv}^p S_{dv}^n) - e_{d1}^p (S_{dv}^p S_{qv}^n + S_{qv}^p S_{dv}^n) \\ dem &= k_1 e_{d1}^p + k_2 e_{q1}^p + k_3 e_{d1}^n + k_4 e_{q1}^n \end{aligned}$$

This algorithm is applied in the current reference calculating block of the control diagram as shown in Fig. 3.1. This current reference calculation algorithm connects the outer voltage loop and the inner current loops. It is based on the input active power P_o^{in} from the output of the voltage loop and estimates the average current reference command (i_d^{p*}, i_q^{p*}, i_n^{p*}, i_n^{p*}) which can ensure that the ripples in the dc link voltage are eliminated.

3.3 PWM Modulation Scheme

As shown in the control diagram in Fig. 3.1, the control outputs S_α and S_β can be obtained from the inner current loop controllers. To generate the gating switch signals for the PWM converter, these control signals should be converted to the switching signals by the Pulse-width modulation (PWM) scheme. Therefore, PWM scheme plays an important role in the performance of the voltage source converter. During the past decades, various types of PWM schemes have been studied extensively for inverters to achieve the following objectives: wide linear modulation range; less switching loss; less total harmonic distortion (THD); easy implementation and less computational time requirements [76]. However, mostly the comparison between the different PWM schemes on the performance of the voltage source converter in detail has been overlooked.

The power circuit of a three phase PWM AC-DC boost rectifier with a neutral point of input supply at n and the ground point of the dc link voltage at o is shown in Fig. 1.2. According to the operating status of each phase top switch S_{ap}, S_{bp} and S_{cp}, the resulting terminal voltage u_{ao}, u_{bo} and u_{co} can be related to the dc

link voltage v_{dc},

$$\begin{aligned} u_{ao} &= d_a v_{dc} \\ u_{bo} &= d_b v_{dc} \\ u_{co} &= d_c v_{dc} \end{aligned} \tag{3.18}$$

And the dc current can be expressed by the ac line side currents i_a, i_b and i_c as,

$$i_{dc} = i_a d_a + i_b d_b + i_c d_c \tag{3.19}$$

where d_a, d_b and d_c are the duty cycles for each phase a, b and c, which vary from 0 to 1.

Since the neutral point is not connected to the ground in Fig. 1.2, there is no zero-sequence component appearing in the circuit, so we can assume,

$$u_{an} + u_{bn} + u_{cn} = 0 \tag{3.20}$$

The voltage difference between the neutral point n and the ground point o can be expressed as,

$$u_{on} = u_{an} - u_{ao} = u_{bn} - u_{bo} = u_{cn} - u_{co} \tag{3.21}$$

Adding these three equations together and applying the condition (3.20), the voltage difference u_{on} can be obtained as,

$$\begin{aligned} u_{on} &= \frac{1}{3}(u_{an} + u_{bn} + u_{cn}) - \frac{1}{3}(u_{ao} + u_{bo} + u_{co}) \\ &= -\frac{1}{3}(u_{ao} + u_{bo} + u_{co}) \end{aligned} \tag{3.22}$$

Thus, by using the equations (3.18) and (3.22), each phase terminal voltage

can be written as,

$$u_{an} = u_{ao} + u_{on} = \frac{2}{3}u_{ao} - \frac{1}{3}u_{bo} - \frac{1}{3}u_{co} = \frac{2d_a - d_b - d_c}{3}v_{dc} \tag{3.23}$$

$$u_{bn} = u_{bo} + u_{on} = \frac{2}{3}u_{bo} - \frac{1}{3}u_{co} - \frac{1}{3}u_{ao} = \frac{2d_b - d_c - d_a}{3}v_{dc} \tag{3.24}$$

$$u_{cn} = u_{co} + u_{on} = \frac{2}{3}u_{co} - \frac{1}{3}u_{ao} - \frac{1}{3}u_{bo} = \frac{2d_c - d_a - d_b}{3}v_{dc} \tag{3.25}$$

Defining the coefficients between u_{an}, u_{bn}, u_{cn} and v_{dc} as the control signals S_a, S_b and S_c in the equations (3.23)-(3.25), respectively, so we can get,

$$S_a = \frac{2d_a - d_b - d_c}{3} \tag{3.26}$$

$$S_b = \frac{2d_b - d_c - d_a}{3} \tag{3.27}$$

$$S_c = \frac{2d_c - d_a - d_b}{3} \tag{3.28}$$

Consequently, the basic model for the three phase PWM rectifier can be represented as the equation (3.29), which has the same format as the conventional definition in (2.1), (2.10) and (2.11),

$$\begin{aligned} e_a &= Ri_a + L\frac{di_a}{dt} + S_a v_{dc} \\ e_b &= Ri_b + L\frac{di_b}{dt} + S_b v_{dc} \\ e_c &= Ri_c + L\frac{di_c}{dt} + S_c v_{dc} \\ C\frac{dv_{dc}}{dt} &= \sum S_a i_a + S_b i_b + S_c i_c - \frac{v_{dc}}{R_{dc}} \end{aligned} \tag{3.29}$$

The variables S_a, S_b and S_c, which express the relationship between the converter terminal phase voltages and dc link voltage, can be defined by the three phase duty cycles d_a, d_b and d_c. With the same control signals for each phase, the different PWM modulation schemes generate the different duty cycles d_a, d_b and d_c for the three phase switches, which result in the performance of the three phase PWM voltage source converter.

For the SPWM scheme, the control signal sine wave is compared with a triangle carrier waveform of unity amplitude, so the relationship between the sine modulation function k_m and the duty cycle function d_m is given by,

$$d_m = \frac{k_m}{2} + \frac{1}{2} \tag{3.30}$$

where m represents the phases a, b and c.

Substituting the relationship (3.30) into the equations (3.26)-(3.28) and considering the condition $k_a + k_b + k_c = 0$, the direct link between the control signals S_m and the equivalent sine modulation functions k_m for the SPWM scheme can be found as,

$$S_m = \frac{k_m}{2} \tag{3.31}$$

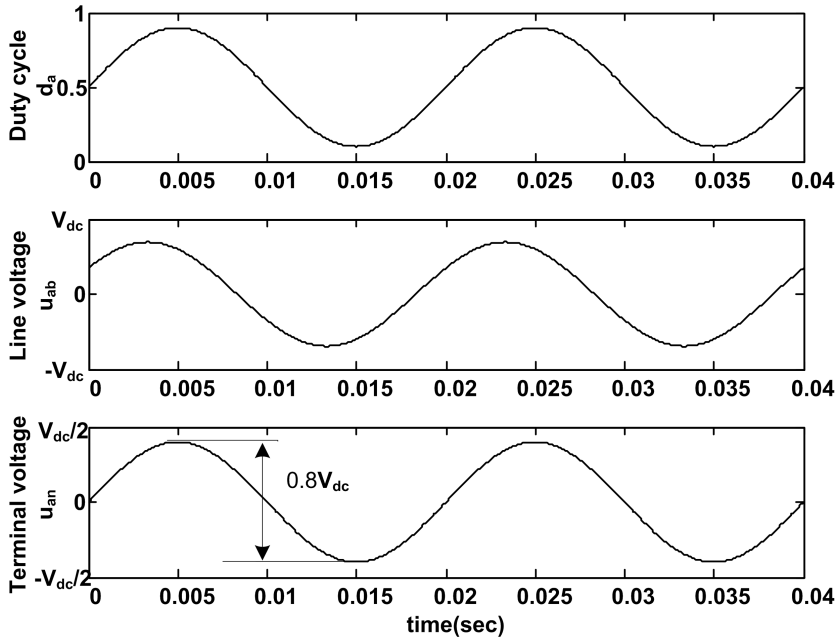

Figure 3.2: Duty cycle for phase a, line voltage u_{ab} and terminal voltage u_{an} by using SPWM modulation scheme.

The modulation functions k_a, k_b and k_c are assumed to be pure sinusoid

waveforms,

$$\begin{aligned} k_a &= k_{index}\sin(\omega t) \\ k_b &= k_{index}\sin(\omega t - 120^\circ) \\ k_c &= k_{index}\sin(\omega t + 120^\circ) \end{aligned} \tag{3.32}$$

where k_{index} is the modulation index, which varies from 0 to 1 for the linear operation region.

As an example, Fig. 3.2 shows the duty cycle and output voltage for phase a by using SPWM modulation scheme for k_{index} to be 0.8. V_{dc} is the average value of the DC link voltage. It can be seen from Fig. 3.2 that the peak-to-peak value of the terminal voltage is $k_{index}V_{dc}$ $(0.8V_{dc})$.

In the SVPWM scheme, the six switches' status are determined according to the position and the amplitude of the space vector [39]. The different combination of the switches will be applied based on the position of the voltage space vector in the different sectors. The relationship between the reference voltage and the base voltage will decide the switch on-time.

Fig. 3.3 shows the duty cycle and output voltage by using the SVPWM scheme for the same operating condition as in Fig. 3.2.

Although the function of the duty cycle for the SVPWM scheme is not continuous, the line to line voltage and the terminal voltage are still sinusoidal. For

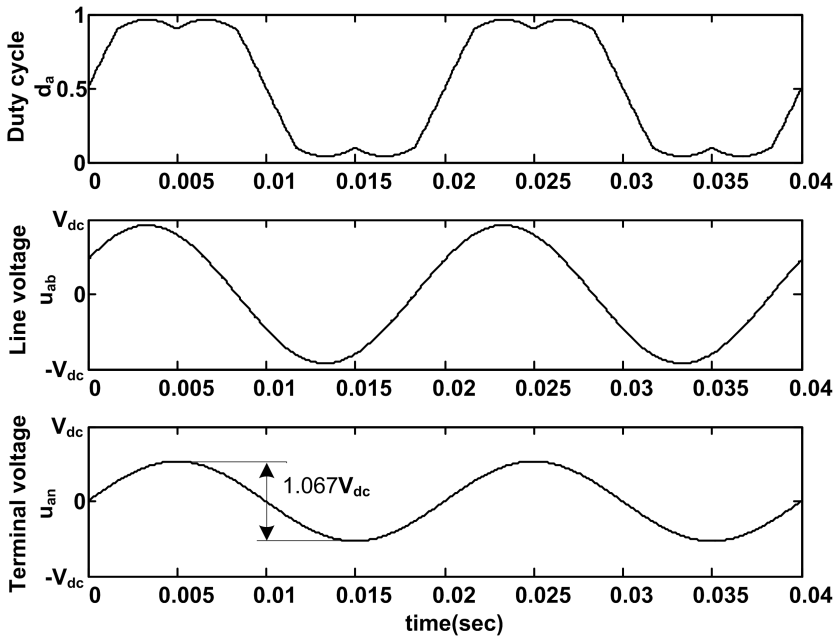

Figure 3.3: Duty cycle for phase a, line voltage u_{ab} and terminal voltage u_{an} by using SVPWM modulation scheme.

example,

$$u_{ab} = u_{ao} - u_{bo} = \frac{2}{\sqrt{3}} k_{index} \sin(\omega t + 30°) V_{dc} \tag{3.33}$$

$$\begin{aligned} u_{an} &= \frac{2}{3}u_{ao} - \frac{1}{3}u_{bo} - \frac{1}{3}u_{co} = \frac{2}{3}u_{ab} - \frac{1}{3}u_{bc} \\ &= \frac{2}{3} k_{index} \sin \omega t V_{dc} = \frac{2k_a}{3} V_{dc} \end{aligned} \tag{3.34}$$

It is noted that in order to make the space vector modulation operate in the linear region, the modulation index k_{index} should be limited within the range 0 to $\sqrt{3}/2$ [39].

Therefore, the relationship between the control signals S_m and the equivalent sine modulation functions k_m for the SVPWM scheme can be concluded as,

$$S_m = \frac{2k_m}{3} \tag{3.35}$$

The peak-to-peak terminal voltage u_{an} in Fig. 3.3 is $1.067V_{dc}$, which matches the expectation from the relationship in (3.35). And this peak-to-peak voltage is

33.3% higher than the one as shown and obtained using the SPWM scheme in Fig. 3.2. Thus, from the equations (3.31) and (3.35), we can conclude that for a specified operating condition, using the SPWM or SVPWM modulation scheme results in the different models for the PWM rectifier, and the gain of the voltage source converter with the SVPWM scheme is 33.3% higher than that with the SPWM scheme.

We can combine the two equations (3.31) and (3.35)in one,

$$S_m = ak_m \tag{3.36}$$

when using the SPWM scheme, $a = 1/2$, and when using the SVPWM scheme, $a = 2/3$.

Substituting this relationship into (3.29), we can obtain the model with SPWM or SVPWM modulation scheme as,

$$\begin{aligned} e_a &= Ri_a + L\frac{di_a}{dt} + ak_a v_{dc} \\ e_b &= Ri_b + L\frac{di_b}{dt} + ak_b v_{dc} \\ e_c &= Ri_c + L\frac{di_c}{dt} + ak_c v_{dc} \\ C\frac{dv_{dc}}{dt} &= \sum ak_a i_a + ak_b i_b + ak_c i_c - \frac{v_{dc}}{R_{dc}} \end{aligned} \tag{3.37}$$

The line-to-line rms terminal voltage at the fundamental frequency, U_{LL1}, can be written as [1],

$$U_{LL1} = \frac{\sqrt{3}}{\sqrt{2}}(U_{an1(peak)}) = \frac{\sqrt{3}}{\sqrt{2}} ak_{index} V_{dc} \tag{3.38}$$

Based on the equations (3.31) and (3.35), a will have different gain by using different PWM modulation schemes. In order to keep the PWM modulation

scheme of the converters to work in the linear region, for the SPWM scheme, the modulation ratio k_{index} is varied from 0 to 1, while the modulation ratio of the SVPWM scheme is limited in the range from 0 to $\sqrt{3}/2$. Assuming the voltage drop across L is small and $U_{an1} \approx E_a$, the relationship between the dc output voltage V_{dc} and the input line voltage U_{LL1} has to meet the requirements as laid out in Table 3.1.

Table 3.1: Operating Range of the Three Phase PWM Rectifier With Different Modulation Schemes

Schemes	Operating Range
SPWM	$V_{dc} > 1.634U_{LL1}$
SVPWM	$V_{dc} > 1.415U_{LL1}$

From Table 3.1, we can see that PWM rectifier can work over a wider range with the SVPWM scheme. For example, when the phase supply voltage is 80 V_{rms} value, so the dc output voltage must operate at more than 226.41 V with SPWM modulation scheme and more than 196.07 V with the SVPWM scheme. Hence, the PWM voltage source converter with SVPWM scheme can provide 13.4% lower output voltage than SPWM for the same ac input voltage.

Overall, by using the SVPWM scheme, the voltage source converter can operate over a wider range and the system loop gain is higher as compared to the SPWM scheme. Therefore, the SVPWM scheme should be preferred over the SPWM scheme.

3.4 Software Phase Locked Loop

Since the phase angle of the utility voltage vector is a basic information for the grid-connected power conditioning equipment such as AC-DC converters and uninterruptible power system (UPS), in these applications, an accurate and fast detection of the phase angle of the utility voltage is essential to assure the correct generation of the reference signals. Thus, the block of phase locked loop (PLL) [77],[78] with three phase PWM AC-DC voltage source converter takes an important role in providing a reference phase signal synchronized with the grid.

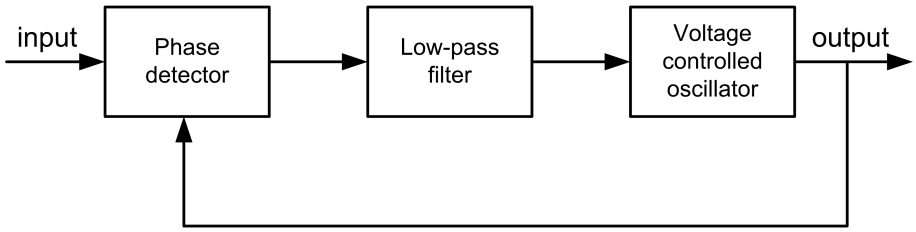

Figure 3.4: Basic topology of PLL.

Usually, three main blocks constitute the basic PLL system: phase detector, low pass filter and voltage-controlled oscillator (VCO) as shown in Fig. 3.4. Normally, the phase detector provides the output which consists of a dc term that has phase information of the input signal and an ac term. The ac term of the output signal from the phase detector should be filtered by the low pass filter. After the filter, the dc signal corresponding to the phase error between the estimated and actual signals is considered as the input to the VCO. With the advanced technology of microcontrollers and digital signal processors (DSPs), all of these functions of the classical PLL have been implemented by software. Since the software PLL (SPLL) can be tailored to perform any function, it has become a competitive alternative to the hardware PLL.

The SPLL technique has been adopted in the electric motor control and utility interface operation of power electronic systems [77]-[85]. A simple method of obtaining the phase information is to detect the zero crossing point of the utility voltages [77]. However, since the zero crossing point can be detected only at every half cycle of the utility frequency, the phase tracking action cannot handle measurement noise between the detecting points so that the system can suffer from poor performance or even instability. In order to obtain the fast dynamic performance, the synchronization must be updated not just at zero voltage crossing points, but continuously under the whole period. An improved method is to regulate the dc quantity, which is phase information obtained from the input waveform and the quadrature of the input waveform [77]. The *d*-*q* transform in the three phase system has the same behavior with this technique, so the SPLL can be implemented by using the *d*-*q* transform and the performance of the SPLL is controlled by a properly designed loop filter.

In a weak AC system, the synchronization algorithm must cope with the existing electrical environment such as harmonics, voltage sags and commutation notches [9]. The voltage unbalance generates a negative sequence voltage, which would induce an oscillating error in the measurement of the phase angle. If there is an error in the phase angle estimation then it may directly affect the compensation voltage and thus deteriorate the performance. Since the positive sequence voltage is the dominant part in the supply voltage, mostly the system requires to extract the positive and the negative sequence voltages instantaneously and synchronize the phase angle with the positive sequence voltage [82].

The block diagram of the three phase PLL system used in our system can be

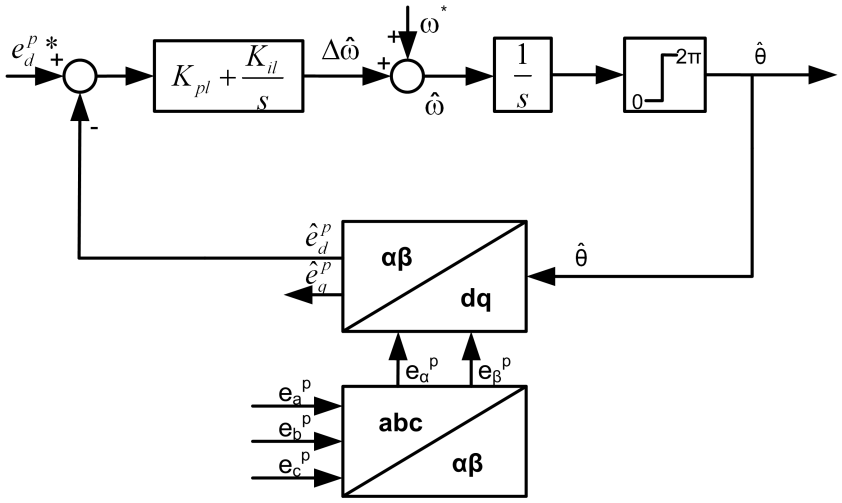

Figure 3.5: Block diagram of three phase phase-locked loop system.

described as shown in Fig. 3.5. It is assumed that the three phase utility voltages have been separated into the positive and negative sequence components as (2.40) and (2.41) in Chapter 2. The input three phase voltages e_a^p, e_b^p and e_c^p in Fig. 3.5 can represented as,

$$\begin{aligned} e_a^p &= \sum_{\substack{n=1 \\ k=1,6n-1,6n+1}}^{\infty} E_k^p \sin(k\omega t + \theta_{ek}^p) \\ e_b^p &= \sum_{\substack{n=1 \\ k=1,6n-1,6n+1}}^{\infty} E_k^p \sin(k\omega t - k \cdot \tfrac{2\pi}{3} + \theta_{ek}^p) \\ e_c^p &= \sum_{\substack{n=1 \\ k=1,6n-1,6n+1}}^{\infty} E_k^p \sin(k\omega t + k \cdot \tfrac{2\pi}{3} + \theta_{ek}^p) \end{aligned} \tag{3.39}$$

By using the *Clark's transformation* as (C.3), the input voltages e_a^p, e_b^p, e_c^p can be converted as $e_{\alpha k}^p$ and $e_{\beta k}^p$ for the different k^{th}-order harmonics in the stationary reference α-β frame. For the convenience of the analysis, we use the fundamental component as an example to explain, so e_α^p and e_β^p can be expressed as,

$$e_\alpha^p = \frac{\sqrt{6}E_1^p}{2} \sin(\omega t + \theta_{e1}^p) \tag{3.40}$$

$$e_\beta^p = -\frac{\sqrt{6}E_1^p}{2} \cos(\omega t + \theta_{e1}^p) \tag{3.41}$$

Ideally, the input voltage e_α^p and e_β^p can be transformed into the dc quantity e_d^p

and e_q^p in the rotating synchronous d-q frame by *Park's transformation*. However, the phase angle θ defined as ωt in the transform matrix (C.5) cannot be measured, so the estimated angle $\hat{\theta}$ from the PLL output is used instead. Hence, the rotating matrix $T_e(\theta)$ can be replaced by,

$$T_e(\hat{\theta}) = \begin{bmatrix} \cos\hat{\theta} & -\sin\hat{\theta} \\ \sin\hat{\theta} & \cos\hat{\theta} \end{bmatrix} \tag{3.42}$$

The voltage of interest is the d-axis component e_d^p and derived as,

$$\begin{aligned} \hat{e}_d^p &= \frac{\sqrt{6}E_1^p}{2}(\sin\theta\cos\hat{\theta} - \cos\theta\sin\hat{\theta}) \\ &= \frac{\sqrt{6}E_1^p}{2}\sin(\theta - \hat{\theta}) \\ &\approx \frac{\sqrt{6}E_1^p}{2}(\theta - \hat{\theta}) \\ &= \frac{\sqrt{6}E_1^p}{2}\delta \end{aligned} \tag{3.43}$$

where δ is the error between the real angle θ and the estimated angle $\hat{\theta}$. If it is assumed that the phase difference δ is very small, the relationship between d-axis component $\hat{e}_d^p$ and the phase difference δ is linear as shown in the approximation format of the equation (3.43). Therefore, the output phase angle $\hat{\theta}$ of the SPLL system can track the utility phase angle θ by regulating the voltage component $\hat{e}_d^p$ in the d axis to the reference value zero.

There are various methods in designing the loop filter. The second order loop is commonly used as a good trade-off of the filter performance and system stability [77]. As shown in Fig. 3.5, the proportional-integral (PI) type filter for the second order loop is used and the change in the angular frequency of the supply voltage $\Delta\hat{\omega}$ can be obtained. K_{pl} and K_{il} are the proportional gain and integral gain for the PI filter. The feedforward frequency command (ω^*) is introduced to

improve the overall tracking performance of the SPLL. Next, the estimated phase angle $\hat{\theta}$ can be derived by integrating the increment of the phase angle $\Delta\hat{\theta}$ in one sampling time T_s. Finally, the estimated angle $\hat{\theta}$ is used to obtain the voltage component $\hat{e}_d^p$ by *Park Transformation*.

According to Fig. 3.5 and the equation (3.43), the closed loop transfer function can be derived as,

$$H_c(s) = \frac{\hat{\theta}}{e_d^p} = \frac{K_{pl}s + K_{il}}{s^2 - lK_{pl}s - lK_{il}} \tag{3.44}$$

where $l = \sqrt{6}E_1^p/2$.

The closed loop transfer function $H_c(s)$ can be rewritten in the general form of the second order loop as,

$$H_c(s) = \frac{2\zeta\omega_n s + \omega_n^2}{s^2 + 2\zeta\omega_n s + \omega_n^2} \tag{3.45}$$

where $\omega_n = \sqrt{-lK_{il}}$; $\quad \zeta = -\frac{lK_{pl}}{2\sqrt{-lK_{il}}}$.

In the design of the SPLL system, it is desirable that the dynamic performance should satisfy the fast tracking and good filtering characteristics. However, both requirements cannot be satisfied simultaneously because the two conditions are inconsistent. Therefore, a trade-off is required in the design. Following the conventional method, the damping ratio can be derived as $\zeta = 0.707$. The closed loop bandwidth of the SPLL can be determined by the natural frequency ω [86]. In practice, the 5^{th} and 7^{th} order harmonics are involved in the supply voltages, and they appear as the sixth order harmonics (300Hz) in the rotating synchronous *d-q* frame as discussed in Chapter 2. Therefore, the system bandwidth is designed at 150Hz so that the 300Hz harmonics can be filtered and the dc signal for the phase detecting can be kept. The operating supply voltage E_1^p in the experiment is 113V,

so $l = 138$. Thus, K_{pl} is -9.6 and K_{il} is -6403.

During the operation of the three phase PWM AC-DC voltage source converter, the SPLL system is not a stand-alone system. The controller of the converter and the SPLL system will affect each other as shown in Fig. 3.6.

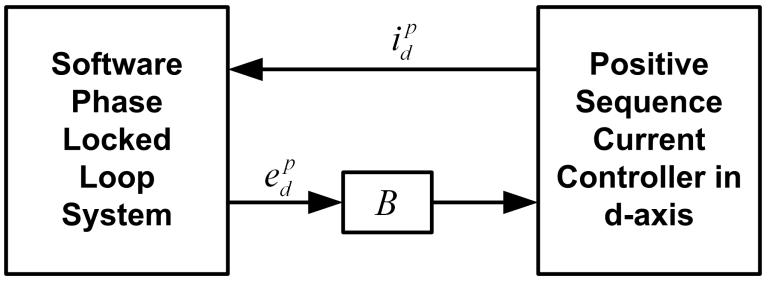

Figure 3.6: Block diagram of the current controller of three phase PWM AC-DC voltage source converter with SPLL.

When there are any impedances between the voltage source and the measurement point, this impedance would cause the measured voltage change because of the ac line side currents. From the other side, the decoupling term e_d^p in the positive sequence current controller in d-axis usually comes from the output of the SPLL system ($B = 1$). Therefore, the current controller and the SPLL system interact each other and the performance can not be ensured by designing these two loops separately. Whereas, since it is considered that the decoupling term e_d^p can be regulated at zero after properly designing the phase locked loop, the direct feedback from SPLL to the current controller can be cut off ($B = 0$). In this way, the SPLL system and the current controller can be designed independently.

3.5 Positive and Negative Sequence Extraction

In Chapter 2, it was explained that an unbalanced input supply has a negative sequence voltage component as well as a positive sequence voltage component. The negative sequence components of the control signals were introduced in order to adequately compensate for the unbalanced operating condition so that the output dc link voltage is kept constant without oscillating components. The symmetrical components calculator to extract the positive and negative sequence components from three phase instantaneous quantities such as voltages and currents is regarded as an important functional part of the entire unbalance compensation control system.

The symmetrical components [87],[88] have been conventionally used to analyze the unbalanced faults and systems. The traditional definition of the symmetrical components based on the concept of phasors in the frequency domain is suitable for steady state analysis, so it is called steady state symmetrical components. Various methods for the estimation of the steady state symmetrical components of a three phase system are available in the literature [89]-[95]. In order to accommodate dynamic and transient conditions, the concept of symmetrical components in the time domain which is also referred to as instantaneous symmetrical components is proposed in [96]-[101]. The instantaneous symmetrical components are used for the dynamic control and compensation of the unbalanced systems mostly by forced-commutated power electronic converters [96].

Traditionally, the unbalanced three phase voltages e_a, e_b and e_c are converted into the positive and negative synchronous rotating frames by using *Clark Transfor-*

mation and *Park Transformation* as highlighted in Appendix C. Since the positive and negative sequence components appear as 100Hz ac in the opposite rotating synchronous frame, the symmetrical components from three phase instantaneous variables can be obtained by the low pass filter or the notch filter [57]. However, the low pass filter and notch filter with low Q-factor lead to some measurement delay or phase delay, which results in sluggish system response. Comparing with the traditional method, the phase shifting method does not employ any low pass filter nor notch filter so that it would not introduce the phase delay problem in the system. Therefore, the phase shifting method is preferred to calculate the symmetrical components under the unbalanced supply conditions.

The phase shifting method basically replaces the complex phasor τ with a 120° phase-shift operator in the time domain. The detailed derivation and definitions of symmetrical components are discussed in Appendix B. Thus, the positive, negative and zero sequence can be expressed as,

$$\begin{bmatrix} e_a^p(t) \\ e_a^n(t) \\ e_a^o(t) \end{bmatrix} = \frac{1}{3} \begin{bmatrix} e_a(t) + S_{120}\left[e_b(t)\right] + S_{240}\left[e_c(t)\right] \\ e_a(t) + S_{240}\left[e_b(t)\right] + S_{120}\left[e_c(t)\right] \\ e_a(t) + e_b(t) + e_c(t) \end{bmatrix} \tag{3.46}$$

where S_x stands for a x-degree phase-shift operator in the time domain.

If the complex phasor τ can be written as,

$$\tau = e^{-j120^\circ} = -\frac{1}{2} - \frac{\sqrt{3}}{2} e^{j90^\circ} \tag{3.47}$$

and

$$\tau^2 = e^{j120^\circ} = -\frac{1}{2} + \frac{\sqrt{3}}{2} e^{j90^\circ} \tag{3.48}$$

So the equation (3.46) can be derived based on a 90° phase-shift operator

which is easier to implement, as shown in (3.49),

$$\begin{bmatrix} e_a^p(t) \\ e_a^n(t) \\ e_a^o(t) \end{bmatrix} = \frac{1}{3} \begin{bmatrix} e_a(t) - \frac{1}{2}\left(e_b(t) + e_c(t)\right) + \frac{\sqrt{3}}{2} S_{90}\left[e_b(t) - e_c(t)\right] \\ e_a(t) - \frac{1}{2}\left(e_b(t) + e_c(t)\right) - \frac{\sqrt{3}}{2} S_{90}\left[e_b(t) - e_c(t)\right] \\ e_a(t) + e_b(t) + e_c(t) \end{bmatrix} \tag{3.49}$$

The equations (3.46) and (3.49) show that the phase shifting method does not require any predetermined values of the amplitudes (E_a, E_b, E_c) and the phase angles (θ_e^a, θ_e^b, θ_e^c) of each phase voltage, so this method to calculate the instantaneous symmetrical components are suitable to use for dynamic compensation and control of power systems. The concepts of (3.46) and (3.49) are valid for all the frequency signals, but it only works for a single frequency component once the degree of the phase-shift is converted in the corresponding time scale. Hence, this phase-shift angle is usually designed for a specific frequency component. Since the fundamental component carries the most significant piece of information among the constituting components of a signal, the derivations in our work are applied to the fundamental component. It can be shown that (3.46) and (3.49) are equivalent with respect to the fundamental component.

Since the line voltages e_{ab} and e_{bc} measured in the circuit do not include the zero sequence components, the positive and negative sequence components e_{ab}^p, e_{bc}^p, e_{ab}^n and e_{bc}^n can be expressed by using the equation (3.49),

$$e_{ab}^p(t) = \frac{1}{3}\left[e_{ab}(t) - \frac{1}{2}\left(e_{bc}(t) + e_{ca}(t)\right) + \frac{\sqrt{3}}{2} S_{90}\left[e_{bc}(t) - e_{ca}(t)\right]\right] \tag{3.50}$$

$$e_{ab}^n(t) = \frac{1}{3}\left[e_{ab}(t) - \frac{1}{2}\left(e_{bc}(t) + e_{ca}(t)\right) - \frac{\sqrt{3}}{2} S_{90}\left[e_{bc}(t) - e_{ca}(t)\right]\right] \tag{3.51}$$

$$e^p_{bc}(t) = \frac{1}{3}\left[e_{bc}(t) - \frac{1}{2}\left(e_{ca}(t) + e_{ab}(t)\right) + \frac{\sqrt{3}}{2}S_{90}\left[e_{ca}(t) - e_{ab}(t)\right]\right] \tag{3.52}$$

$$e^n_{bc}(t) = \frac{1}{3}\left[e_{bc}(t) - \frac{1}{2}\left(e_{ca}(t) + e_{ab}(t)\right) - \frac{\sqrt{3}}{2}S_{90}\left[e_{ca}(t) - e_{ab}(t)\right]\right] \tag{3.53}$$

By utilizing the information that the sum of e_{ab}, e_{bc} and e_{ca} is zero, e_{ca} can be cancelled from (3.50)-(3.53) as shown in the following equations,

$$e^p_{ab}(t) = \frac{1}{2}e_{ab}(t) + \frac{\sqrt{3}}{6}S_{90}\left[e_{ab}(t) + 2e_{bc}(t)\right] \tag{3.54}$$

$$e^n_{ab}(t) = \frac{1}{2}e_{ab}(t) - \frac{\sqrt{3}}{6}S_{90}\left[e_{ab}(t) + 2e_{bc}(t)\right] \tag{3.55}$$

$$e^p_{bc}(t) = \frac{1}{2}e_{bc}(t) - \frac{\sqrt{3}}{6}S_{90}\left[2e_{ab}(t) + e_{bc}(t)\right] \tag{3.56}$$

$$e^n_{bc}(t) = \frac{1}{2}e_{bc}(t) + \frac{\sqrt{3}}{6}S_{90}\left[2e_{ab}(t) + e_{bc}(t)\right] \tag{3.57}$$

The phase shifting method explained in the expressions of (3.54)-(3.57) requires delay time of one-fourth of the period which is equal to 5 ms in the case of the input voltage being 50 Hz. According to [13], the short interruptions, such as voltage sag and swell, happen frequently in the supply voltages, whose duration is from 0.1 s to 3 mins. Although this 5 ms time delay in the positive and negative sequence extraction block causes the system response lagging behind, it can still help to improve the performance of three phase PWM voltage source converter under this type of grid faults, let alone the other long interruptions.

The detailed implementation diagram of the phase shifting method is shown in Fig. 3.7. The symmetrical components e^p_{ab}, e^p_{bc}, e^n_{ab} and e^n_{bc} obtained through this method would be used to calculate the components e^p_d, e^p_p, e^n_d and e^n_p in the positive and negative synchronous rotating *d-q* frames for the control purpose.

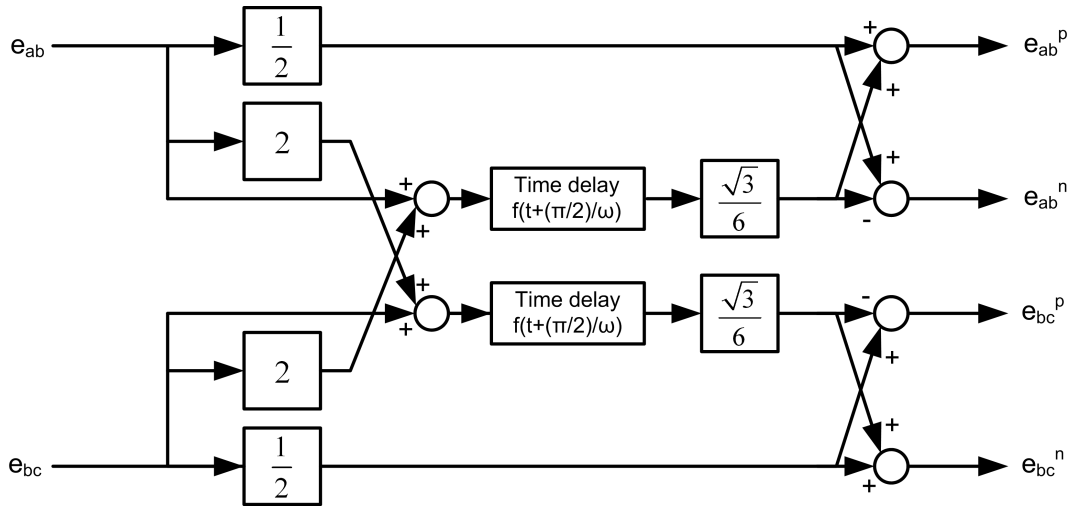

Figure 3.7: Block diagram of phase shifting method to calculate symmetrical components in the positive and negative synchronous rotating frames.

Similarly, the phase shifting method would be performed on the line side currents i_a, i_b, i_c to acquire the positive and negative sequence components i_a^p, i_a^n, i_b^p, i_b^n as shown in (3.58)-(3.61). Then, the components i_d^p, i_p^p, i_d^n and i_p^n can be derived by using *Clark Transformation* and *Park Transformation*.

$$i_a^p(t) = \frac{1}{2} i_a(t) + \frac{\sqrt{3}}{6} S_{90} \left[i_a(t) + 2 i_b(t) \right] \tag{3.58}$$

$$i_a^n(t) = \frac{1}{2} i_a(t) - \frac{\sqrt{3}}{6} S_{90} \left[i_a(t) + 2 i_b(t) \right] \tag{3.59}$$

$$i_b^p(t) = \frac{1}{2} i_b(t) - \frac{\sqrt{3}}{6} S_{90} \left[2 i_a(t) + i_b(t) \right] \tag{3.60}$$

$$i_b^n(t) = \frac{1}{2} i_b(t) + \frac{\sqrt{3}}{6} S_{90} \left[2 i_a(t) + i_b(t) \right] \tag{3.61}$$

Considering that the coupling terms in the current model of (2.8) and (2.9) have been compensated completely, the block diagram of dual frame current controller in the positive and negative synchronous rotating frames can be described in Fig. 3.8.

As shown in Fig. 3.8, the terminal voltages of power converter u_d^p, u_q^p, u_d^n and

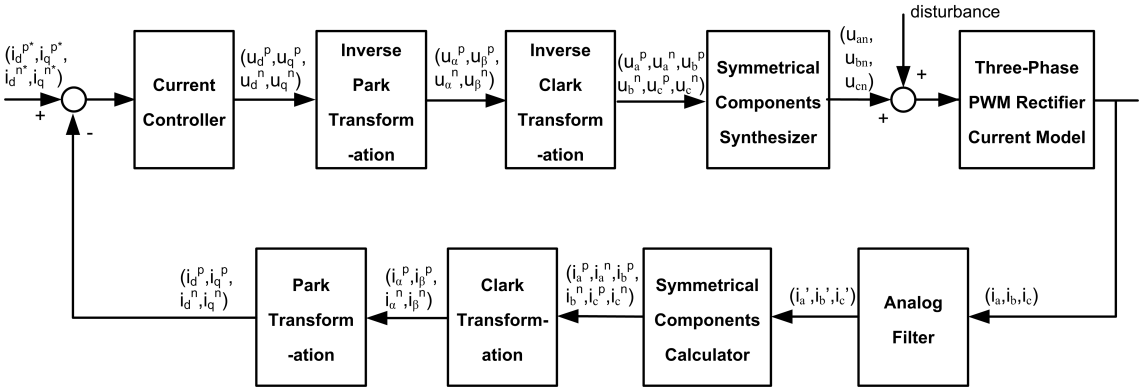

Figure 3.8: Block diagram of current control loop in the positive and negative synchronous rotating *d-q* frames.

u_q^n controlled by the current controllers, would be converted into the signals u_a^p, u_b^p, u_c^p, u_a^n, u_b^n and u_c^n by using *Inverse Clark Transformation* and *Inverse Park Transformation*. The symmetrical components synthesizer can yield the terminal voltages u_{an}, u_{bn}, u_{cn} in the *a-b-c* frame by simply adding the positive and negative sequence components together. These terminal voltages work on the three phase PWM AC-DC voltage source convert to provide the desired the dc link voltage and ac line side currents i_a, i_b and i_c. After passing the analog filter to remove the high frequency noise, the measured currents i'_a, i'_b and i'_c would go through the symmetrical components calculator. The symmetrical components calculator can separate the positive sequence components i_a^p, i_b^p, i_c^p and the negative sequence components i_a^n, i_b^n, i_c^n from the total signals. Then the currents i_d^p, i_q^p, i_d^n and i_q^n in the positive and negative synchronous rotating frames calculated by *Clark Transformation* and *Park Transformation* in Appendix C would be used as a feedback to the current controllers.

Therefore, the supply side current model in the positive and negative synchronous rotating *d-q* frames can be illustrated in Fig. 3.9. In this figure, P_p^{-1}, C_p^{-1}, P_p, C_p, C_n^{-1}, P_n^{-1}, P_n, C_n are *Inverse Park Transformation*, *Inverse Clark*

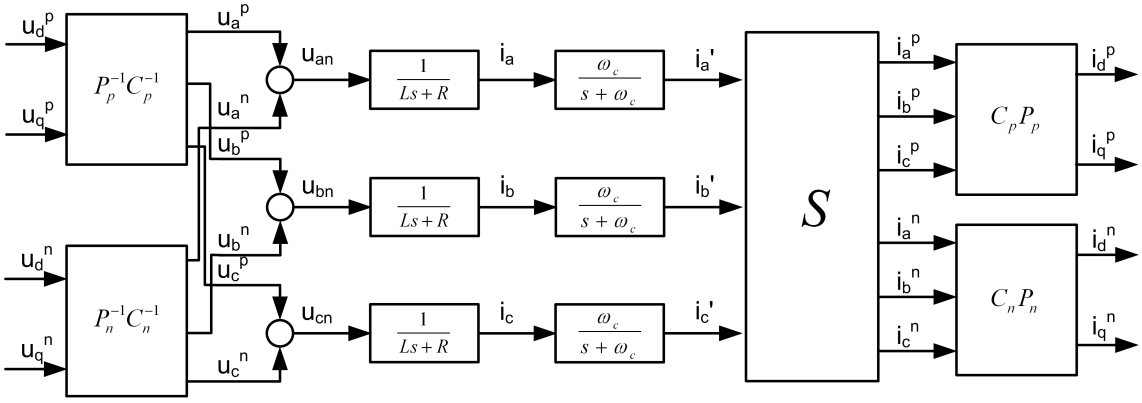

Figure 3.9: Current model in the positive and negative synchronous rotating *d-q* frames.

Transformation and *Park Transformation*, *Clark Transformation* for the matrix format of the positive and negative sequence components, respectively. ω_c is the cut-off frequency of the low pass filter. The symmetrical components calculator C_s is the transfer function based on (3.58)-(3.61). In order to utilize the symmetrical characteristics for the three phases to simplify the analysis, the original 120° degree phase shifting method has been adopted here. The symmetrical components calculator C_s is shown as,

$$i_a^p(s) = \left(i'_a(s) + e^{-\frac{2\pi s}{3\omega}} i'_b(s) + e^{-\frac{4\pi s}{3\omega}} i'_c(s)\right)/3 \tag{3.62}$$

$$i_b^p(s) = \left(i'_b(s) + e^{-\frac{2\pi s}{3\omega}} i'_c(s) + e^{-\frac{4\pi s}{3\omega}} i'_a(s)\right)/3 \tag{3.63}$$

$$i_c^p(s) = \left(i'_c(s) + e^{-\frac{2\pi s}{3\omega}} i'_a(s) + e^{-\frac{4\pi s}{3\omega}} i'_b(s)\right)/3 \tag{3.64}$$

$$i_a^n(t) = \left(i'_a(s) + e^{-\frac{4\pi s}{3\omega}} i'_b(s) + e^{-\frac{2\pi s}{3\omega}} i'_c(s)\right)/3 \tag{3.65}$$

$$i_b^n(s) = \left(i'_b(s) + e^{-\frac{4\pi s}{3\omega}} i'_c(s) + e^{-\frac{2\pi s}{3\omega}} i'_a(s)\right)/3 \tag{3.66}$$

$$i_c^n(s) = \left(i'_c(s) + e^{-\frac{4\pi s}{3\omega}} i'_a(s) + e^{-\frac{2\pi s}{3\omega}} i'_b(s)\right)/3 \tag{3.67}$$

Since the positive and negative sequence components of the input voltages and currents would not affect each other in three phase PWM boost rectifier according to [49], the positive and negative sequence equations can be analyzed separately.

The following discussions are focused on the analysis of the positive sequence of the current and voltage signals. The same way can be applied to the explanation of the negative sequence signals as well.

In order to simplify the derivation, $i_a(t)$, $i_b(t)$ and $i_c(t)$ are assumed to be a three phase balanced current. Hence, $i_b(t)$ is $i_a(t)$ with 120° phase delay and $i_c(t)$ is $i_a(t)$ with 120° phase lead. Thus, the positive sequence equations (3.62)-(3.64) can be converted as,

$$i_a^p(s) = \frac{1 + e^{-\frac{2\pi s}{3\omega}} + e^{-\frac{4\pi s}{3\omega}}}{3} i'_a(s) \tag{3.68}$$

$$i_b^p(s) = \frac{1 + e^{-\frac{2\pi s}{3\omega}} + e^{-\frac{4\pi s}{3\omega}}}{3} i'_b(s) \tag{3.69}$$

$$i_c^p(s) = \frac{1 + e^{-\frac{2\pi s}{3\omega}} + e^{-\frac{4\pi s}{3\omega}}}{3} i'_c(s) \tag{3.70}$$

As $\omega = 100\pi$, these continuous time domain based equations (3.68)-(3.70) can be transformed into the discrete time domain by z-transform, which can be defined as $z = e^{-T_s s}$. The sampling time T_s is 100 μs in the proposed control system. The transfer function of the symmetrical components calculator for each phase can be shown as,

$$\frac{i_a^p(z)}{i'_a(z)} = \frac{1 + z^{-\frac{200}{3}} + z^{-\frac{400}{3}}}{3} \tag{3.71}$$

$$\frac{i_b^p(z)}{i'_b(z)} = \frac{1 + z^{-\frac{200}{3}} + z^{-\frac{400}{3}}}{3} \tag{3.72}$$

$$\frac{i_c^p(z)}{i'_c(z)} = \frac{1 + z^{-\frac{200}{3}} + z^{-\frac{400}{3}}}{3} \tag{3.73}$$

From the equations (3.71)-(3.73), we can see that the symmetrical components calculator C_s for each phase can be decoupled under the balance supply conditions. The relationship between $\begin{bmatrix} u_d^p(z) & u_q^p(z) \end{bmatrix}^T$ and $\begin{bmatrix} i_d^p(z) & i_q^p(z) \end{bmatrix}^T$ can

be written in this way,

$$\begin{aligned}
\begin{bmatrix} u_d^p(z) \\ u_q^p(z) \end{bmatrix}^T &= C_p^{-1}(z)P_p^{-1}(z)P_m(z)F_m(z)C_{sm}(z)P_p(z)C_p(z)\begin{bmatrix} i_d^p(z) \\ i_q^p(z) \end{bmatrix}^T \\
&= P(z)F(z)C_s(z)C_p^{-1}(z)P_p^{-1}(z)P_p(z)C_p(z)\begin{bmatrix} i_d^p(z) \\ i_q^p(z) \end{bmatrix}^T \\
&= P(z)F(z)C_s(z)\begin{bmatrix} i_d^p(z) \\ i_q^p(z) \end{bmatrix}^T \qquad (3.74)
\end{aligned}$$

where $P_m(z)$, $F_m(z)$ and $C_{sm}(z)$ are the matrix format of the plant, the low pass filter and the symmetrical components calculator, respectively. And $P(z)$, $F(z)$ and $C_s(z)$ are the transfer function of the plant, the low pass filter and symmetrical components calculator for the single phase in the discrete time domain, which can be expressed as follows,

$$P(z) = \frac{1 - e^{-\frac{R}{L}T_s}}{R\left(z - e^{-\frac{R}{L}T_s}\right)} \qquad (3.75)$$

$$F(z) = \frac{1 - e^{-\omega_c T_s}}{z - e^{-\omega_c T_s}} \qquad (3.76)$$

$$C_s(z) = \frac{1 + z^{-\frac{200}{3}} + z^{-\frac{400}{3}}}{3} \qquad (3.77)$$

The open loop transfer function G_{dual} in the dual rotating *d-q* frame can be obtained from the equation (3.74) as,

$$G_{dual} = P(z)F(z)C_s(z) \qquad (3.78)$$

This transfer function shows that the transfer function of the symmetrical components calculator is a factor in open loop transfer function of the system designed in the dual rotating *d-q* frame, while this calculator is not required in the single frame control scheme. Therefore, the symmetrical calculator makes the

difference on the performance of the three phase PWM AC-DC voltage source converter between the single frame controller and the dual frame controller.

Fig. 3.10 and Fig. 3.11 show the bode plot of the open loop transfer function in the single and dual rotating *d-q* frame by using the system parameters as shown in Table 2.1 of Chapter 2.

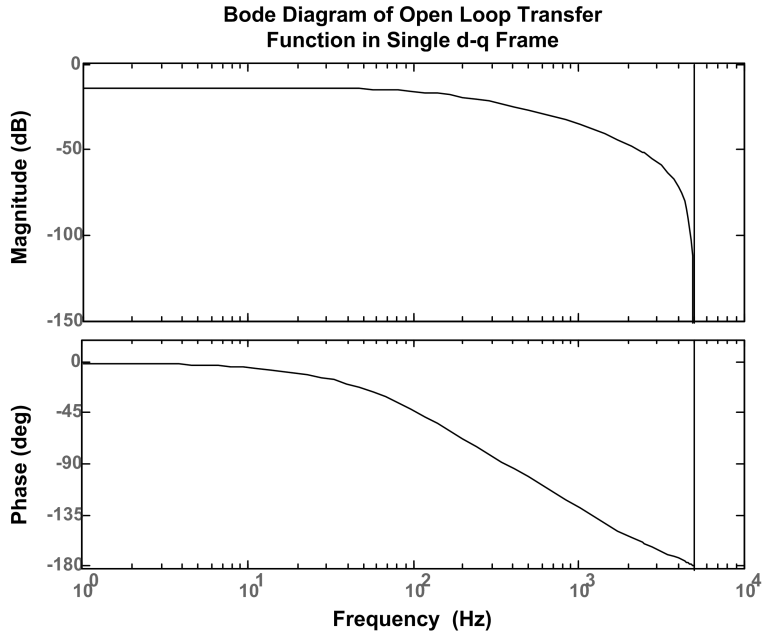

Figure 3.10: Bode plot of the open loop transfer function in the single rotating *d-q* frame.

In the single frame, the model performs as a second-order pass filter as shown in Fig. 3.10. In the high frequency region, the open loop gain would be reduced and the phase angle would change from 0° to −180°. When the system works in the dual rotating *d-q* frame, the controller would deal with the positive and negative sequence components separately. However, the symmetrical components calculator causes the notches at the certain frequencies such as 50Hz, 100Hz, 200Hz, 250Hz, 350Hz and so on, whereas the magnitude curve of bode plot in Fig. 3.11 still keeps the same shape approximately. Moreover, the symmetrical components calculator

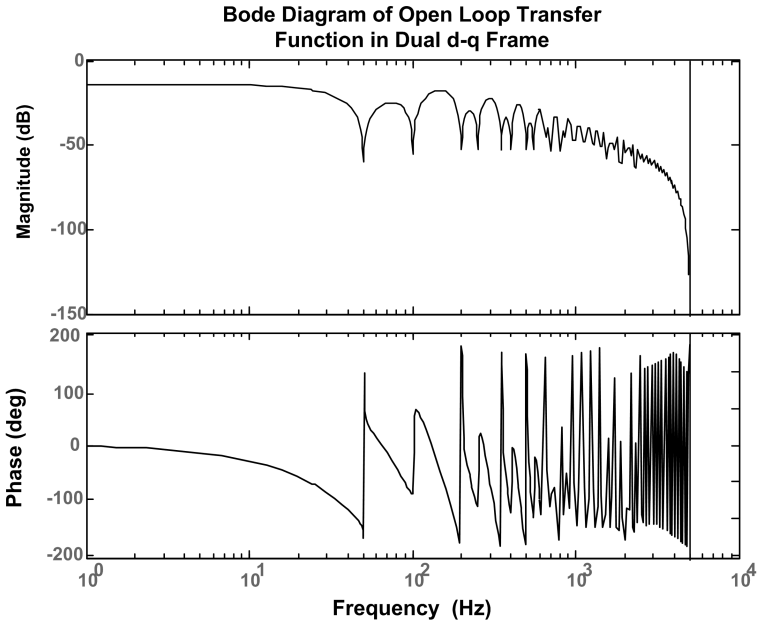

Figure 3.11: Bode plot of the open loop transfer function in the dual rotating *d-q* frame.

introduces the sudden phase changing at each notch frequencies as shown in the phase bode plot of Fig. 3.11. These phase changing is a serious drawback of the phase shifting method to calculate the symmetrical components since the phase changing would make the system easy to be unstable. However, the frequency of the phase changing is the same as the notch frequency, so that the gain of the transfer function G_{dual} would be very small which cannot make a big effect on the whole system. Therefore, we still can design the current controller by ignoring the influence from these phase changing.

3.6 Summary

In this chapter, the whole control strategy has been described in the positive and negative sequence rotating synchronous *d-q* frames. In order to eliminate the even-order harmonics at the dc link voltage and the odd-order harmonics in the ac line

side currents, the control scheme can be divided into two parts, *DC link voltage harmonics control* scheme and *AC line side current harmonics control* scheme. These two parts of control scheme can be implemented by the cascaded dual frame current regulators with a voltage regulator to ensure the performance of the three phase PWM AC-DC voltage source converter. Based on the control objectives in *DC link voltage harmonics control* scheme, the four control laws can be summarized to provide loads with a suitable amount of average power, maintain unity power factor for the utility interface and keep the dc link voltage ripple-free. The algorithm in the current reference calculating block is generated by solving the set of equations from these four control laws.

Moreover, the three independent blocks, *PWM modulation scheme*, *software phase locked loop* and *symmetrical components calculator*, have been discussed and this influences on the performance of the whole control scheme have been highlighted. It has been shown analytically that SVPWM scheme provides a 33.3% higher gain than SPWM scheme which would lead to a better dynamic performance. Also, by using the SVPWM scheme, the voltage source converter can operate at 13.4% lower output voltage than SPWM scheme for the same ac input voltage. Therefore, the SVPWM scheme is preferred over the SPWM scheme. In order to ensure the correct generation of the reference signals, software phase locked loop (SPLL) has been designed to synchronize the phase angle with the positive sequence voltage fast and accurately. The modified scheme has been proposed to decouple the SPLL system and the current controllers so that the stability and the desired performance for the whole system can be guaranteed. As the symmetrical components calculator, the phase shifting method is used to online estimate the instantaneous symmetrical components. Although the symmetrical components

calculator extracts the positive and negative sequence components effectively, it introduces the sudden phase changing at certain frequencies such as 50Hz, 100Hz, 200Hz, 250Hz, 350Hz and so on. These phase changing would cause the instability of the whole system easily. However, the gain at these frequencies is very small, as a result, the current controller design can neglect the effect of the symmetrical components calculator.

The details of the *DC link voltage harmonics control* scheme and *AC line side current harmonics control* scheme adopted in this work will provided in the next three chapters.

Chapter 4

Cascaded Dual Frame Controller Design

Since the negative sequence components would cause the ripples at the dc link voltage of the three phase PWM AC-DC voltage source converter under the unbalanced supply voltage conditions, the cascaded dual rotating frame controller is employed for regulating the positive sequence and negative sequence component independently to fulfil the control task. Based on the mathematical model of the three-phase PWM boost rectifier under the generalized supply voltage conditions, the control task is divided into: (a) *DC link voltage harmonics control* and (b) *AC line side current harmonics control*. For the purpose of *voltage harmonics control*, the basic cascaded dual rotating frame controller is regarded as an important functional part to make sure that the dc link voltage is maintained constant and the supply side power factor is kept close to unity. Therefor, the proper dynamic analysis of this cascaded control scheme is essential to ensure the performance of the PWM rectifier under the distorted and unbalanced supply voltages.

This chapter provides the detailed dynamic analysis of the cascaded dual ro-

tating frame controller for the three phase PWM AC-DC voltage source converter under the generalized supply voltage conditions. First, the analysis of the control system is based on the conventional PI controller design as reported in [71]. However, the linear controller is designed relying on a locally linearized plant model so that it only can guarantee the performance within the limited operating range. In order to design the controller to operate the system with the nonlinear characteristics in nature such as PWM AC-DC voltage source converter, the nonlinear control approach is preferred to analyze the dynamic performance of the whole system. In Section 4.2, the singular perturbation method has been applied and two-time-scale motions are introduced to the dynamic analysis. Finally, the experimental results provided in Section 4.3 have been compared with regards to the performance of the dc link voltage, the ac line side currents and the output instantaneous power between the dual frame controller and the single frame controller.

4.1 PI Controller Design Based on Traditional Method

The inner loop is made up of two parallel positive and negative sequence *d-q* synchronous frame current regulators. The positive sequence *d-q* components (i_d^p, i_q^p) are controlled in the positive synchronous rotating frame as shown in Fig. 4.1, on the other hand, the negative sequence *d-q* components (i_d^n, i_q^n) are controlled in the negative synchronous rotating frame. The structure of the negative sequence current controller is similar to that of the positive sequence current controller.

The voltages e_d^p, e_q^p, e_d^n, e_q^n obtained from the supply voltages are used as the signals in the current decoupling terms to compensate some part of the effect from

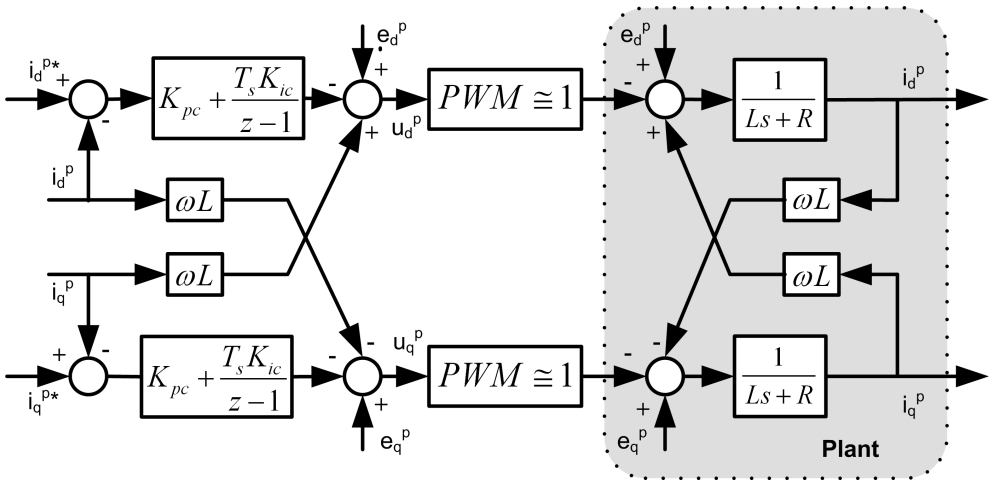

Figure 4.1: Block diagram of inner current loop and dq-axes decoupler for the positive sequence.

the supply voltage harmonics. The effective gain of the PWM stage should be compensated to approximately unity in the frequency range of interest for the current regulators. Ideally, after decoupling all the nonlinear terms and the components in the other axis, the current model can be simplified as Fig. 4.2.

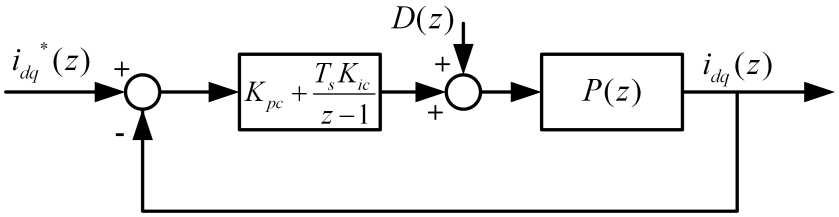

Figure 4.2: Simple model of inner current loop and dq-axes decoupler for the positive sequence.

The discretized plant transfer function $P(z)$ is,

$$P(z) = \frac{1-a}{R(z-a_p)} \tag{4.1}$$

where $a_p = e^{-\frac{R}{L}T_s}$.

Therefore, if the circuit parameter $L = 0.0055$ H and $R = 0.3\ \Omega$, the open

loop current loop transfer function $G_{current}(z)$ can be written as,

$$\begin{aligned} G_{current}(z) &= \left[K_{pc} + \frac{T_s K_{ic}}{z-1}\right] P(z) \\ &= \frac{0.01813(K_{pc}z - K_{pc} + 0.0001K_{ic})}{(z-0.9946)(z-1)} \end{aligned} \tag{4.2}$$

where K_{pc}, K_{ic} are the proportional gain and the integral gain for the current loops, respectively.

For each synchronous rotating frame, it is critical to have a high bandwidth for the inner current regulators so that the outer voltage loop and the inner current loops can be designed separately. However, since there is limitation on the overall bandwidth of the control loop from the switching frequency and the block of extracting positive and negative sequence components, it is necessary to design the controller properly so that the system performance can be optimized.

According to the transfer function (4.2), one pole can be designed to cancel the zero, so the relationship between K_{pc} and K_{ic} can be obtained ($K_{pc} = 0.01852K_{ic}$). Correspondingly, the root locus of the open loop transfer function for the current regulator are shown in Fig. 4.3. The roots of the close loop can move on the solid line according to the different K_{pc} value. To comprise the fast response and the immunity to the noise, the bandwidth of the current loop is set at around 1 kHz. This bandwidth is much smaller than the switching frequency at 20 kHz, so that the impact from the switches can be ignored in the controller design. Since the overshoot is not desired, the damping ratio is set to about 1. Based on the requirement of the bandwidth and the damping ratio, the closed loop poles should be placed on the marker near 0.8 on the real axis. ($K_{pc} = 3.7$ and $K_{ic} = 200$)

In order to analyze the dynamic performance of the outer voltage loop, the

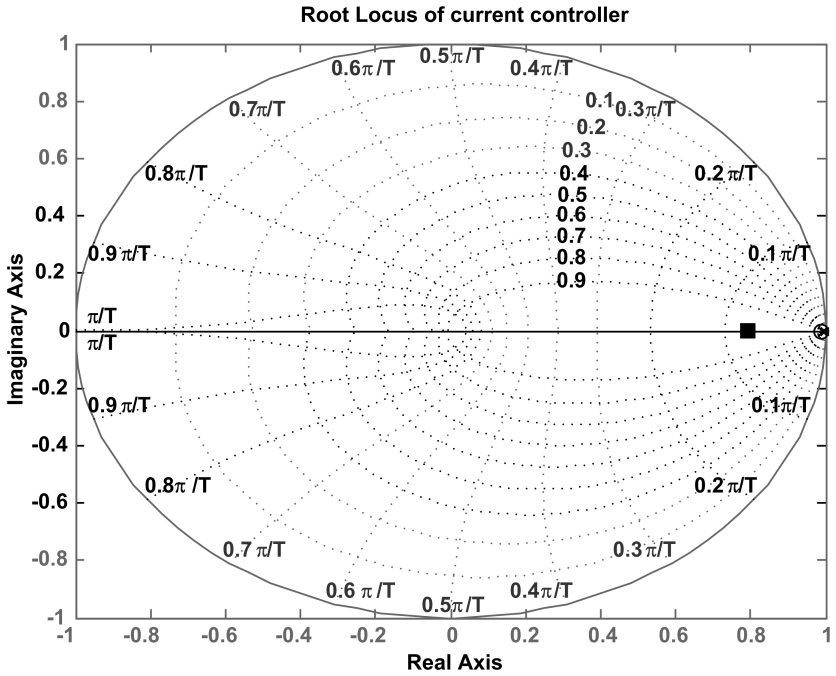

Figure 4.3: Root locus of the open loop transfer function for current controller.

transfer function from four current variables to dc link voltage should be derived. Since the model of the three phase PWM rectifier is highly nonlinear, the small signal perturbation is suggested to linearize the model at the steady state operating point. By replacing all the variables x in (2.8) and (2.9) as a small ac signal and a dc quantity $\Delta x + \overline{x}$ and neglecting the Δ^2 terms,

$$\begin{aligned}
\Delta\dot{i}_d^p &= -\frac{R}{L}\Delta i_d^p + \omega\Delta i_q^p - \frac{\overline{S_d^p}}{L}\Delta v_{dc} - \frac{\overline{v_{dc}}}{L}\Delta S_d^p \\
\Delta\dot{i}_q^p &= -\omega\Delta i_d^p - \frac{R}{L}\Delta i_q^p - \frac{\overline{S_q^p}}{L}\Delta v_{dc} - \frac{\overline{v_{dc}}}{L}\Delta S_q^p \\
\Delta\dot{i}_d^n &= -\frac{R}{L}\Delta i_d^n - \omega\Delta i_q^n - \frac{\overline{S_d^n}}{L}\Delta v_{dc} - \frac{\overline{v_{dc}}}{L}\Delta S_d^n \\
\Delta\dot{i}_q^n &= \omega\Delta i_d^n - \frac{R}{L}\Delta i_q^n - \frac{\overline{S_q^n}}{L}\Delta v_{dc} - \frac{\overline{v_{dc}}}{L}\Delta S_q^n
\end{aligned} \tag{4.3}$$

At the equilibrium point, the expression of the small signal of the control

signals ΔS_d^p, ΔS_q^p, ΔS_d^n and ΔS_q^n can be obtained,

$$\begin{aligned}
\Delta S_d^p &= \frac{1}{\overline{v_{dc}}}(-R\Delta i_d^p + \omega L\Delta i_q^p - \overline{S_d^p}\Delta v_{dc}) \\
\Delta S_q^p &= \frac{1}{\overline{v_{dc}}}(-\omega L\Delta i_d^p - R\Delta i_q^p - \overline{S_q^p}\Delta v_{dc}) \\
\Delta S_d^n &= \frac{1}{\overline{v_{dc}}}(-R\Delta i_d^n - \omega L\Delta i_q^n - \overline{S_d^n}\Delta v_{dc}) \\
\Delta S_q^n &= \frac{1}{\overline{v_{dc}}}(\omega L\Delta i_d^n - R\Delta i_q^n - \overline{S_q^n}\Delta v_{dc})
\end{aligned} \tag{4.4}$$

Assuming the control objective will be achieved in the steady state, there is no second order harmonic in the dc link voltage (2.20). The small signal equation can be derived as,

$$\begin{aligned}
\Delta\dot{v}_{dc} &= -\frac{1}{CR_{dc}}\Delta v_{dc} + \frac{1}{C}\overline{S_d^p}\Delta i_d^p + \frac{1}{C}\overline{S_q^p}\Delta i_q^p + \frac{1}{C}\overline{S_d^n}\Delta i_d^n + \frac{1}{C}\overline{S_q^n}\Delta i_q^n \\
&\quad + \frac{1}{C}\Delta S_d^p\overline{i_d^p} + \frac{1}{C}\Delta S_q^p\overline{i_q^p} + \frac{1}{C}\Delta S_d^n\overline{i_d^n} + \frac{1}{C}\Delta S_q^n\overline{i_q^n}
\end{aligned} \tag{4.5}$$

Substituting (4.4) into (4.5), the transfer function between Δv_{dc} and Δi_d^p, Δi_q^p, Δi_d^n and Δi_q^n can be obtained,

$$\Delta v_{dc}(s) = \frac{a_1\Delta i_d^p + a_2\Delta i_q^p + a_3\Delta i_d^n + a_4\Delta i_q^n}{s + a_5} \tag{4.6}$$

where
$$\begin{aligned}
a_1 &= \frac{\overline{S_d^p}}{C} - \frac{R\overline{i_d^p}}{C\overline{v_{dc}}} - \frac{\omega L\overline{i_q^p}}{C\overline{v_{dc}}} \\
a_2 &= \frac{\overline{S_q^p}}{C} - \frac{R\overline{i_q^p}}{C\overline{v_{dc}}} + \frac{\omega L\overline{i_d^p}}{C\overline{v_{dc}}} \\
a_3 &= \frac{\overline{S_d^n}}{C} - \frac{R\overline{i_d^n}}{C\overline{v_{dc}}} + \frac{\omega L\overline{i_q^n}}{C\overline{v_{dc}}} \\
a_4 &= \frac{\overline{S_q^n}}{C} - \frac{R\overline{i_q^n}}{C\overline{v_{dc}}} - \frac{\omega L\overline{i_d^n}}{C\overline{v_{dc}}} \\
a_5 &= -\frac{1}{CR_{dc}} - \frac{\overline{S_d^p}\cdot\overline{i_d^p}}{C\overline{v_{dc}}} - \frac{\overline{S_q^p}\cdot\overline{i_q^p}}{C\overline{v_{dc}}} - \frac{\overline{S_d^n}\cdot\overline{i_d^n}}{C\overline{v_{dc}}} - \frac{\overline{S_q^n}\cdot\overline{i_q^n}}{C\overline{v_{dc}}}
\end{aligned}$$

The equation (4.6) gives a link between four current variables in positive and negative synchronous rotating frame (i_d^p, i_q^p, i_d^n, i_q^n) and the dc link voltage output. The coefficients from P_o^{in} to i_d^p, i_q^p, i_d^n, i_q^n can be obtained according to the algorithm of the current reference calculation block under the different unbalanced

supply voltages. The bandwidth of the current controller is designed to be much higher than that of voltage controller so that the dynamics of the current controller can be ignored when designing the voltage loop. Hence, the total transfer function of the current controllers in the positive and negative rotating synchronous frame can be assumed to be unity,

$$\frac{\Delta i_d^p}{\Delta i_d^{p*}}, \frac{\Delta i_q^p}{\Delta i_q^{p*}}, \frac{\Delta i_d^n}{\Delta i_d^{n*}}, \frac{\Delta i_q^n}{\Delta i_q^{n*}} \approx 1 \tag{4.7}$$

Therefore, we can get the overall system model by putting all the blocks together as shown in Fig. 4.4.

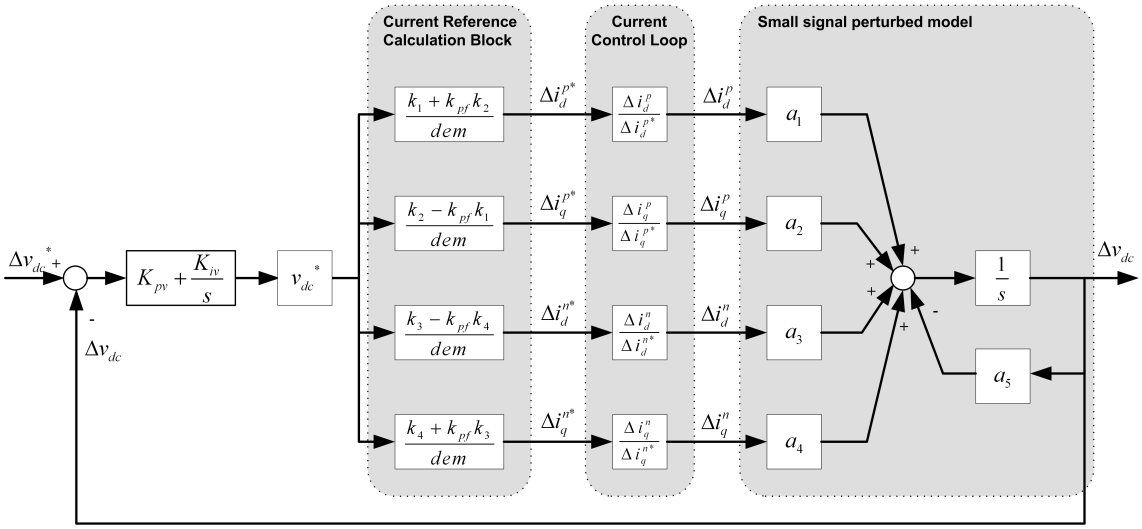

Figure 4.4: Voltage regulator with small signal perturbed model of voltage source converter at dc side.

In order to choose the initial K_{pv} and K_{iv} suitable for all the different unbalanced operating conditions, the controller design is based on the open loop transfer function $G_{open}(s)$ under the normal operating condition first,

$$G_{open}(s) = \frac{v_{dc}^*(a_1 e_{d1}^p + a_2 e_{q1}^p)}{(e_{d1}^{p2} + e_{q1}^{p2})(s + a_5)}(K_{pv} + \frac{K_{iv}}{s}) \tag{4.8}$$

where v_{dc}^* is the reference value of the DC link voltage, and K_{pc}, K_{ic} are the proportional gain and the integral gain for the current loop, respectively.

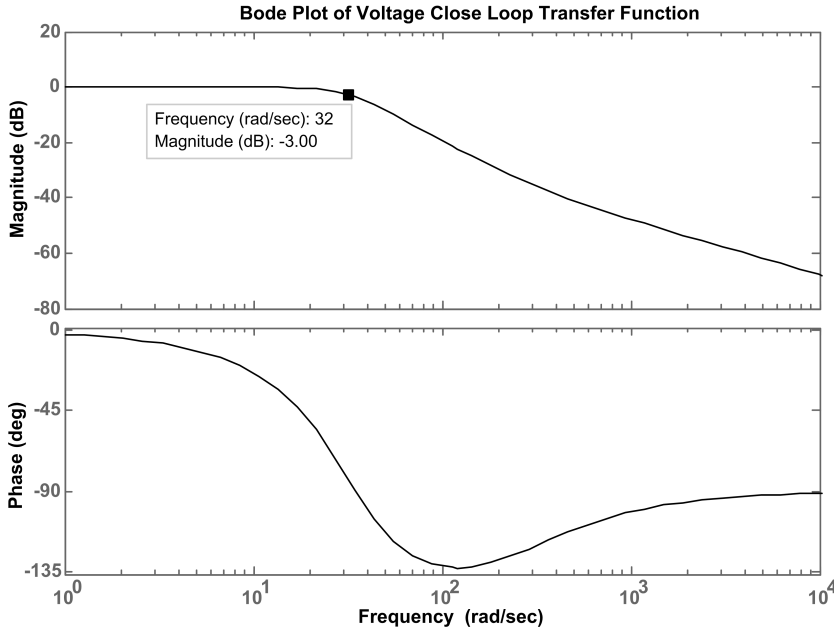

Figure 4.5: Bode plot of the close loop transfer function for voltage controller.

When the supply is three phase balanced voltages with the amplitude of $80V_{rms}$, the bode plot of the close loop for the voltage controller, with the parameter values in Table 2.1 and $K_{pv} = 0.03$, $K_{iv} = 4.59$, is shown in Fig. 4.5. It can be seen that the bandwidth of the voltage controller is 32 rad/sec (5.93 Hz). Considering that the bandwidth of the current regulators was obtained to be 254 Hz, and that of the voltage regulator was obtained to be 5.93 Hz, it ensures that these two cascaded regulating loops can be designed independently as they are in the different frequency range. Since the command of the voltage loop is constant, the system can work with this bandwidth of the voltage regulator.

4.2 PI Controller Design Based on Singular Perturbations Method

Conventionally, PI gain selection for the cascaded control loop is based on the linearized model at a fixed operating point as discussed in Section 4.1. However, due to the complexity of three phase PWM AC-DC voltage source converter, it is difficult to obtain the plant transfer function and to utilize the traditional method to derive the gains from the analytical point of view. This section has developed the cascaded PI control scheme by using the singular perturbation method [102], which deliberately induces the two-time-scale motions in the closed-loop system and ensures stability conditions for the fast-motion sub-system (FMS) and slow-motion sub-system (SMS), respectively.

In the system, the tracking error can be defined as $e = x^* - x$, where the variable x represents the positive and negative sequence currents in the d-q rotating frame or the output dc link voltage and x^* is the corresponding desired reference signal. The desired tracking error behavior is given by,

$$\dot{e} = -\lambda e \tag{4.9}$$

In accordance with the singular perturbation design methodology in [102], the controller can be designed as,

$$\mu \dot{u} = k(\lambda e + \dot{e}) \tag{4.10}$$

where μ is a small positive parameter, λ is the time constant of the tracking error ($\lambda > 0$) and k is a gain selected to ensure the fast motions stability condition. This control law (4.10) can be expressed in terms of transfer functions of a conventional

PI controller,

$$u(s) = \left[\frac{k\lambda}{\mu s} + \frac{k}{\mu}\right] e(s) \tag{4.11}$$

Considering that the system can be described as,

$$\dot{x} = f(x) + b(x)u \tag{4.12}$$

where $f(x)$ and $b(x)$ are the nonlinear functions of the states.

Substituting the equation (4.12) into (4.10), the closed-loop system can be written as,

$$\dot{e} = \dot{x}^* - f(x) - b(x)u \tag{4.13}$$

$$\mu\dot{u} = k(\lambda e + \dot{x}^* - f(x) - b(x)u) \tag{4.14}$$

Since μ is the small positive parameter, the closed-loop system equations (4.13) and (4.14) have the standard singular perturbation form. Hence the singular perturbation method [103]-[105] may be used to analyze the closed-loop system properties. Correspondingly, we obtain the fast-motion subsystem (FMS) from (4.14),

$$\mu\dot{u} = -kb(x)u + k[\lambda e + \dot{x}^* - f(x)] \tag{4.15}$$

where e, $f(x)$, $b(x)$ and x^* are treated as the frozen variables during the transients in (4.15). This assumption is valid when $\mu \to 0$, which leads to increase of time-scale separation degree between fast and slow modes in the closed-loop system.

In order to make FMS stable, the gain k is selected such that $kb > 0$. Then, after the rapid decay of transients in (4.15), we have the steady state (more precisely, quasi-steady state) for the FMS, where $u(t) = u^s(t)$ and,

$$u^s = b^{-1}(x)[\lambda e + \dot{x}^* - f(x)] \tag{4.16}$$

where u^s is the nonlinear inverse dynamics solution. Substitution of (4.16) into (4.13) yields the slow-motion subsystem (SMS) equation in the form of (4.9). Hence, after the damping of the fast transients, the desired tracking error can converge to zero despite that $f(x)$ and $b(x)$ are unknown.

It should be noted that the control parameters μ, λ and k should be selected in this controller design such that the closed-loop system would provide (1) the FMS and SMS stability; (2) the desired degree of time-scale separation between fast and slow motions. Correspondingly, PI controller gains would be determined by the relationship (4.11).

4.2.1 Inner Current Loop

The structure of the positive and negative sequence current controller is described in Section 4.1, as shown in Fig. 4.1. Ideally, after decoupling all the nonlinear items and the components in the other axis, the dynamics of the positive and negative sequence currents i_d^p, i_q^p, i_d^n and i_q^n can be simplified as (4.17),

$$\dot{i} = -\frac{R}{L}i + \frac{v_{dc}}{L}S \tag{4.17}$$

where the variables i and S represent the positive and negative sequence component of the average current and the average value of switching function in the d-q rotating frame for each switching cycle, respectively.

Substituting the equation (4.17) into (4.13) and (4.14), the equations of the

closed-loop system can be given by,

$$\dot{e}_i = \dot{i}^* + \frac{R}{L}\dot{i} - \frac{v_{dc}}{L}S \tag{4.18}$$

$$\mu_i \dot{S} = k_i(\lambda_i e_i + \dot{i}^* + \frac{R}{L}i - \frac{v_{dc}}{L}S) \tag{4.19}$$

where the subscript i represents the variables or the parameters used in the inner current loops.

From the standard singular perturbation form in (4.18) and (4.19), the two-time-scale motions are induced as $\mu_i \to 0$. Hence, the FMS can be obtained as,

$$\mu_i \dot{S} = -\frac{k_i v_{dc}}{L}S + k_i(\lambda_i e_i + \dot{i}^* + \frac{R}{L}i) \tag{4.20}$$

Since the variables i, i^* and v_{dc} are used to describe the SMS in the current loop, they can be treated as the frozen variables during the transients in (4.20) and $T_{FMS,i} = \frac{\mu_i L}{k_i v_{dc}}$ is the time constant of the fast motion subsystem of the inner current loops.

Assume that the control gain k_i has been selected such that the FMS (4.20) is stable as well as time-scale decomposition is maintained in the closed-loop system. Hence, after the rapid decay of transients in (4.20), we have the steady state (more precisely, quasi-steady state) of the FMS (4.20), where $u(t) = u^s(t)$ and

$$u^s = \overline{S} = \frac{L\lambda_i e_i + L\dot{i}^* + Ri}{v_{dc}} \tag{4.21}$$

where $\overline{S}$ is the nonlinear inverse dynamics solution for the switching function.

Substitution of (4.21) into (4.18) yields the slow-motion subsystem (SMS) equation in the form (4.9). Hence, after the damping of fast transients, the desired tracking error behavior is fulfilled despite of the different value of system parameters

R and L. The time constant of the slow motion subsystem $T_{SMS,i}$ is $1/\lambda_i$. Note that the degree of time-scale separation η_i can be estimated by the ratio of SMS time constant to the FMS time constant, that is $\eta_i = \frac{k_i v_{dc}}{L\mu_i\lambda_i}$.

In order to get the fast current performance in response to the switching change, the time constant $T_{FMS,i}$ of the current controller should be be very small, 2.5×10^{-6} s. Taking the system parameters of the circuit as $R = 0.3$ Ω, $R_{dc} = 225$ Ω, $L = 0.005$ H and $C = 200$ μF, and the positive parameter $\mu_i = 0.001$, the control parameter k_i is $\frac{L\mu_i}{T_{FMS,i}v_{dc}}$, that is $\frac{2}{v_{dc}}$. The SMS decide the response of the positive and negative sequence current. Because the response of the electrical variable is around 0.01 sec, the time constant of the SMS is limited. Hence, the desired degree of time-scale separation is designed as $\eta_i = 500$. Then, from the above, the time constant of SMS $T_{SMS,i}$ is $0.01s$ and corresponding value of λ_i is 100.

4.2.2 Outer Voltage Loop

The complete control system in Fig. 3.1 can be simplified into two cascaded control blocks, namely, the inner loop current controller and the outer loop voltage controller, as shown in Fig. 4.6. The desired dc link output voltage is v_{dc}^*. The output of the voltage controller provides the desired current reference i_{dc}^*, which would be used to decide the current reference i^* for each inner positive and negative sequence current controller. The load change of the PWM rectifier can be represented by varying the resistance R_{dc} as the external disturbance.

Assuming that the current $i_{dc} = i_{dc}^*$ in the average sense for the stationary

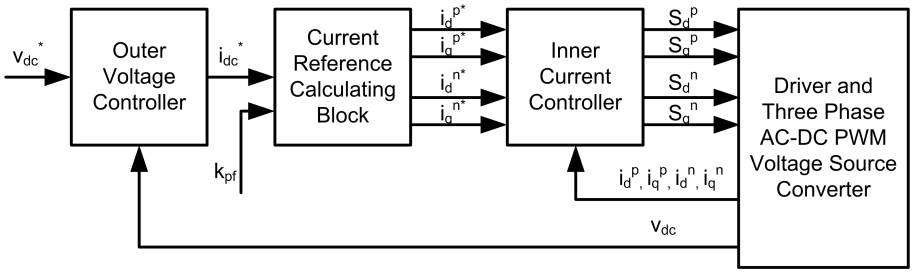

Figure 4.6: Block diagram of the closed-loop system with the inner current loops and outer voltage loop.

oscillations in the FMS, the behavior of v_{dc} can be approximately described by the simple format of the dc link voltage as (4.22), where i_{dc} is the new control variable, v_{dc} is the new output variable.

$$\dot{v}_{dc} = -\frac{1}{CR_{dc}} v_{dc} + \frac{1}{C} i_{dc} \tag{4.22}$$

Therefore, the equation of the outer voltage loop can be summarized as,

$$\dot{e}_v = \dot{v}_{dc}^* + \frac{1}{CR_{dc}} v_{dc} - \frac{1}{C} i_{dc} \tag{4.23}$$

$$\mu_v \dot{i}_{dc} = k_v(\lambda_v e_v + \dot{v}_{dc}^* + \frac{1}{CR_{dc}} v_{dc} - \frac{1}{C} i_{dc}) \tag{4.24}$$

This standard singular perturbation form in (4.23) and (4.24) would induce the two-time-scale motions when $\mu_v \to 0$. Correspondingly, the equation for the FMS can be written as,

$$\mu_v \dot{i}_{dc} = -\frac{k_v}{C} i_{dc} + k_v(\lambda_v e_v + \dot{v}_{dc}^* + \frac{1}{CR_{dc}} v_{dc}) \tag{4.25}$$

where the subscript v represents the variables or the parameters for the outer voltage loop. The variables v_{dc} and v_{dc}^* are treated as the frozen variables during the transients in (4.25) and $T_{FMS,v} = \mu_v C/k_v$ is the time constant of the FMS of the outer voltage loop.

By using the similar design procedures for the current controller, the corre-

sponding SMS can be obtained as,

$$\dot{e}_v = -\lambda_v e_v \tag{4.26}$$

and

$$\dot{v}_{dc} = \lambda_v (v^*_{dc} - v_{dc}) \tag{4.27}$$

where $v^*_{dc} = const.$ The time constant of the SMS $T_{SMS,v}$ is $1/\lambda_v$. The degree of time-scale separation η_v can be estimated as $\frac{k_v}{C\mu_v\lambda_v}$.

For the outer loop, the output of the controller is the reference current. It is not desirable to have a high inrush current when the step change is required, so the time constant of the reference current cannot be very fast. Hence, the time constant $T_{FMS,v}$ of the voltage controller can be set as 5×10^{-3} s. Taking the positive parameter as $\mu_v = 0.001$, the control parameter k_v is $\frac{C\mu_v}{T_{FMS,i}}$, that is 4×10^{-5}. In the mean time, we want the voltage response as fast as possible, so the time constant of voltage (SMS) is set around 0.02 sec. According to the desired degree of time-scale separation $\eta_v = 4$, the time constant of SMS, $T_{SMS,v}$ is 0.02 s and the control parameter λ_v is 50.

The singular perturbation method imposes the system into the fast-motion subsystem and the slow-motion subsystem and link the control parameters with the response of current and voltage waveform. Comparing with the traditional method to obtain the PI gain, this method not only provides the direct insight into the relationship between the PI parameters and the performance of the system, but also designs the controller based on the global operating conditions instead of the linearized model for a fixed operating point. The detailed performance of the whole control scheme will be examined in Section 4.3.

4.3 Experimental Validation of Proposed Dual Frame Controller

To verify the feasibility of the proposed dual frame control scheme, the experiments were conducted to compare with the conventional single frame controller, under the unbalanced operating conditions. The system parameters and the control parameters in the experiment platform are using the same values as shown in Table 2.1 and Table 4.1.

Table 4.1: Controller Parameters Used In the Experiment

Parameters	Value	Parameters	Value	Parameters	Value
μ_v	0.001	k_v	4×10^{-5}	λ_v	50
μ_i	0.001	k_i	$2/v_{dc}$	λ_i	100

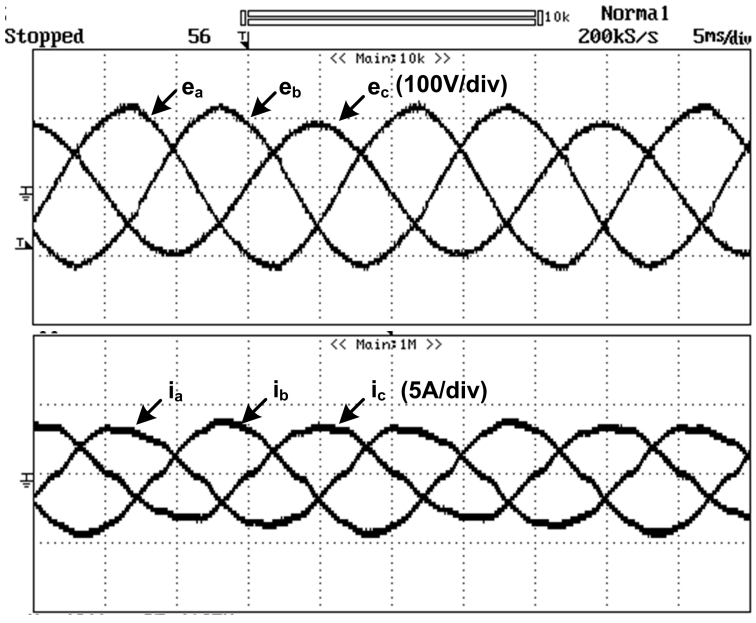

Figure 4.7: Experimental result of input voltage and input current by using a single frame controller.

Figs. 4.7-4.10 provide the performance of the single frame controller and the

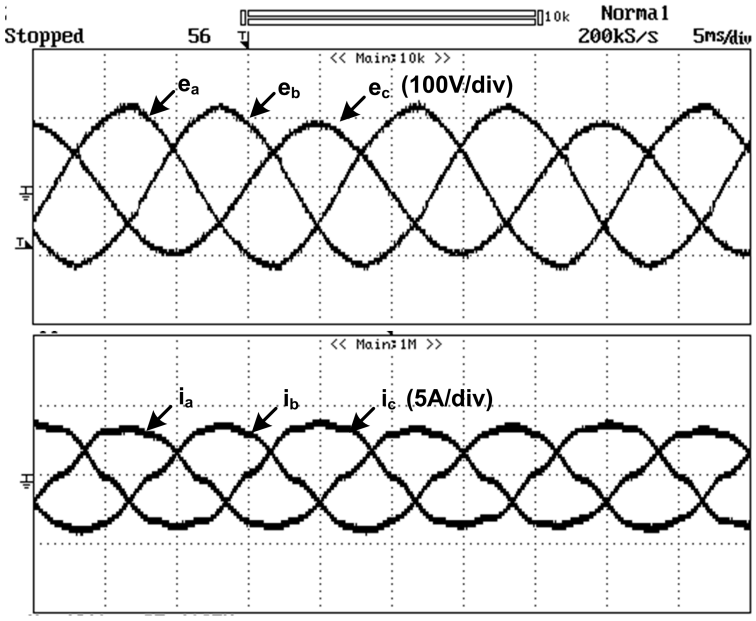

Figure 4.8: Experimental result of input voltage and input current by using a dual rotating *d-q* frame controller.

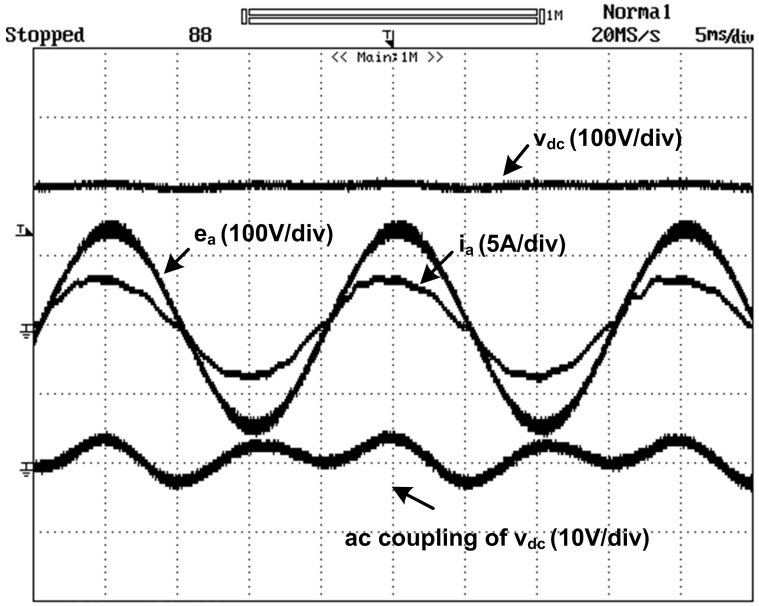

Figure 4.9: Experimental result of dc link voltage, phase *a* input voltage and current by using a single frame controller.

dual rotating *d-q* frame controller when the supply voltages was 80 V_{rms} and the amplitude of phase *c* drops from 113 V by 20 V.

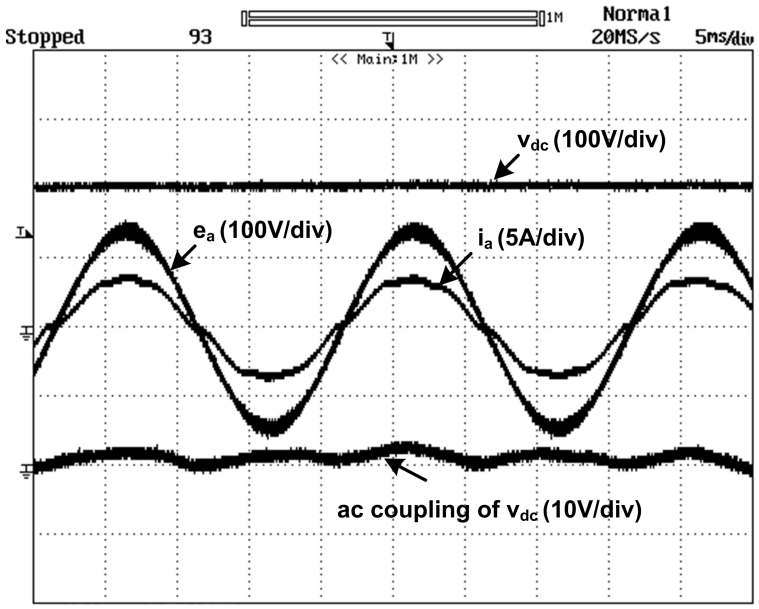

Figure 4.10: Experimental result of dc link voltage, phase *a* input voltage and current by using a dual rotating *d-q* frame controller.

The waveforms of experimental results for the single frame controller are shown in Fig. 4.7 and Fig. 4.9. We can see that when the amplitude of one phase voltage drops, the three phase input currents are not symmetrical any more. In addition, the dc output voltage has the second harmonic component with a ripple of 2.2% and the input current are no longer sinusoidal as shown in Fig. 4.9.

Fig. 4.8 and Fig. 4.10 show the waveforms of experimental results for the dual rotating *d-q* frame controller under the same unbalanced operating condition. It is noted that by employing the dual frame controller the three phase current waveforms are almost symmetrical and the dc link voltage v_{dc} is almost flat. The ripple component in v_{dc} has been reduced from 17% in the open-loop control to 0.78% with the proposed closed-loop control.

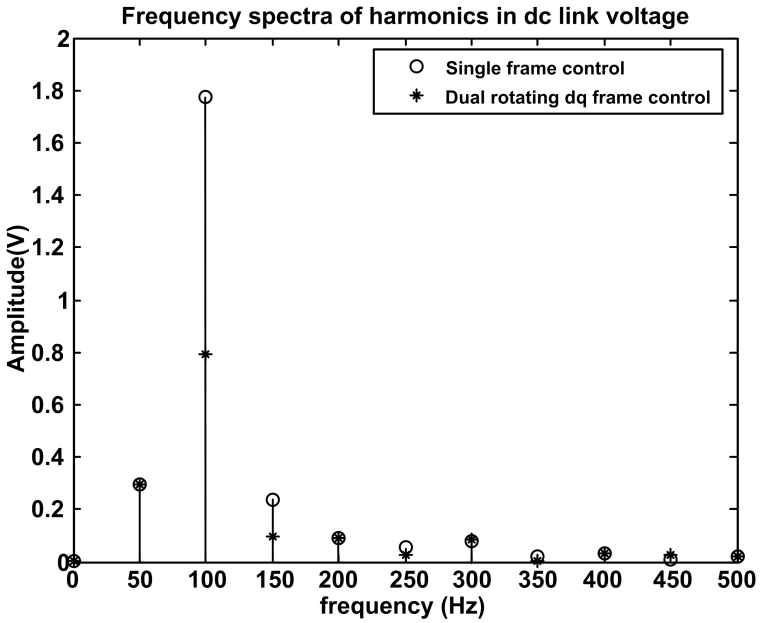

Figure 4.11: FFT analysis for the dc link voltage v_{dc} for the both single frame and dual frame controller under unbalanced condition.

In order to get a detailed picture of the system performance, the FFT analysis has been performed for the dc link voltages v_{dc} in Fig. 4.9 and Fig. 4.10 and the results are shown in Fig. 4.11. The frequency spectra of the dc link voltage clearly indicate that the second-order harmonic component at 100 Hz is reduced by using the dual rotating *d-q* frame controller is applied under the unbalanced condition.

Correspondingly, the total harmonic distortion (THD) of the dc link voltage is shown in Table 4.2. From the table, we can see that by adopting the dual rotating *d-q* frame controller, the THD of the dc link voltage V_{dc} is improved from 1.94% to 1.02%. In addition, the power factor is increased from 0.987 to 0.994 by employing the dual rotating *d-q* frame controller.

From the above results, it can be concluded that the proposed dual rotating *d-q* frame controller can minimize the second order harmonic component at the dc link voltage and the third order harmonic in the ac input current, in the mean time

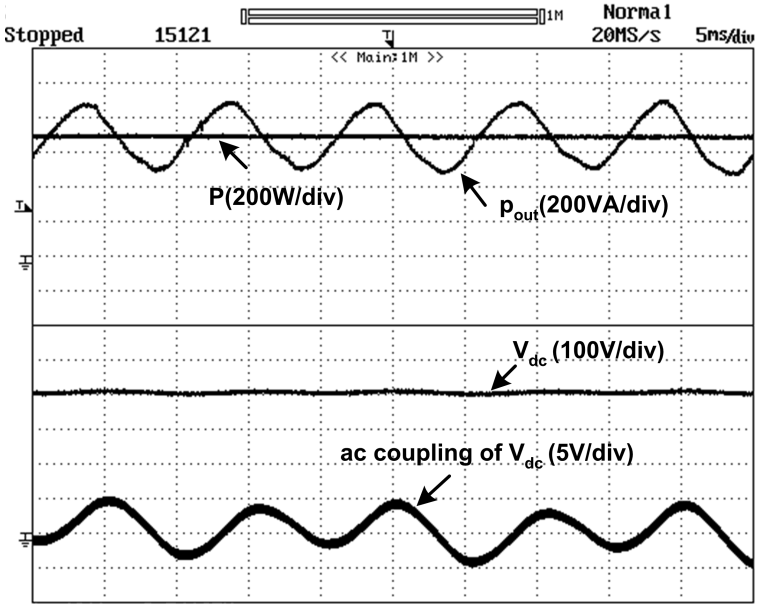

Figure 4.12: Experiment results of output instantaneous power, average active power and dc link voltage by using a conventional single frame controller.

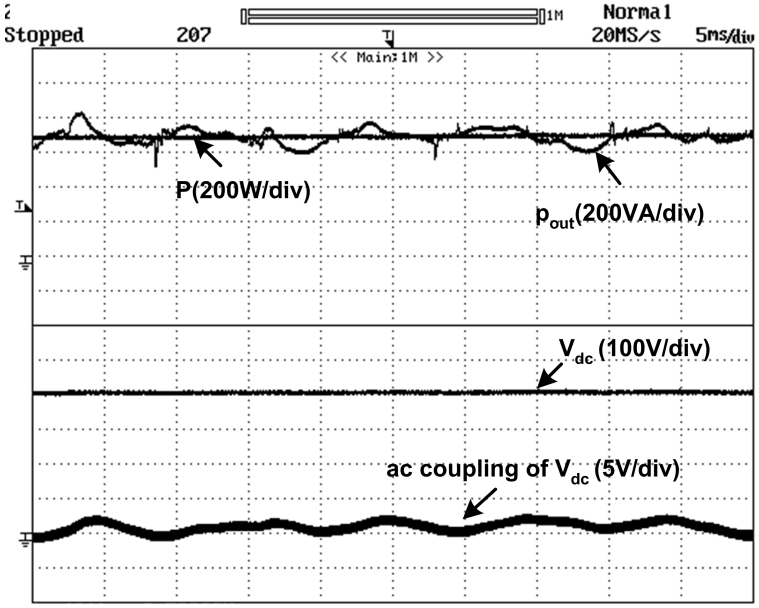

Figure 4.13: Experiment results of output instantaneous power, average active power and dc link voltage by using a dual rotating *d-q* frame controller.

Table 4.2: Total Harmonic Distortion (THD) of Output DC Link Voltage v_{dc}, Input AC Current i_a and Power Factor (PF)

	Single frame controller	Dual rotating frame controller
THD (v_{dc})	1.94%	1.02%
PF	0.987	0.994

the power factor can be maintained close to unity.

According to the discussions in Section 2.4, the variation of the output instantaneous power should be related to the output dc link voltage. Since the proposed control scheme tries to eliminate the dc link voltage ripple, the output average active power should be regulated and input average reactive power should go to zero. Fig. 4.12 and Fig. 4.13 provide the waveforms of the instantaneous power and average active power for the experimental results by using the conventional single frame controller and the proposed dual frame controller under the unbalanced supply voltage conditions. It can be observed from the figures that the dc voltage ripple, as shown in Fig. 4.10 with dual frame control, is quite small, 0.78%, in comparison with the dc link voltage ripple obtained with the single frame control, 2.2%. The average active power P_{out} in (2.77) is only decided by the load, which can be maintained at 700 W in the both methods. The ripple part of p_{out} is determined by the reactive power i.e. p_q in (2.76). This item is proportional to the dc voltage ripple based on the analysis in the model. Correspondingly, when the single frame control scheme is applied, the ripple in the dc link voltage is around 5 V, so there is an obvious second harmonic component in the instantaneous power, while by using the proposed control scheme method, the dc voltage ripple is less than 2 V, so the second harmonics in the instantaneous power is reduced significantly. The

results in Fig. 4.13 and Fig. 4.12 show regulating the dc link voltage and regulating the output instantaneous active power can be achieved simultaneously.

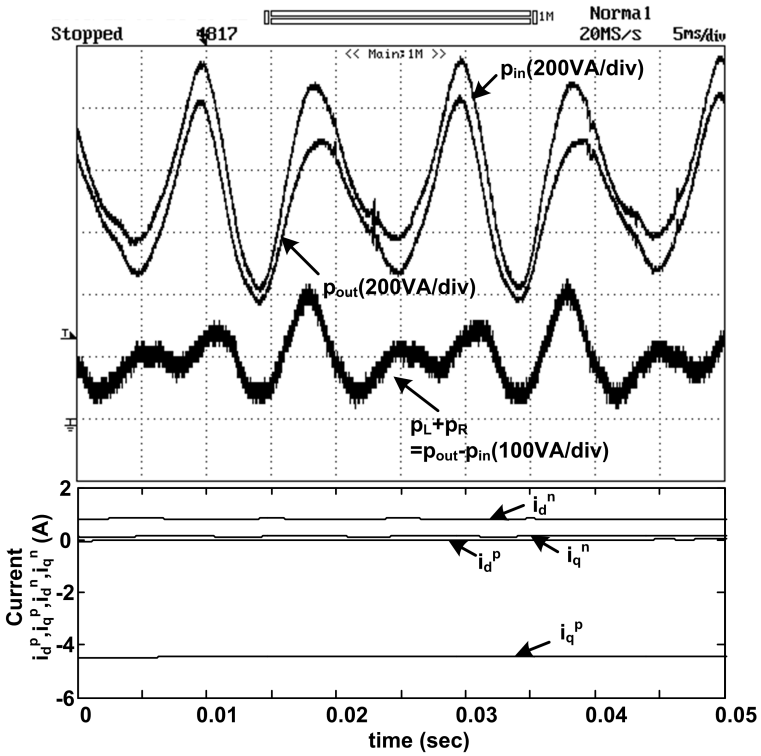

Figure 4.14: Experiment results of input and output instantaneous power and the currents in the rotating synchronous frame by using a conventional single frame controller.

Fig. 4.14 and Fig. 4.15 show the instantaneous power flow in the PWM rectifier by applying the different control scheme. The difference between the input instantaneous power p_{in} and the output instantaneous power p_{out} is equal to the instantaneous power consumed by the inductance and resistance, p_L and p_R. According to the analysis of the two terms in (2.88) and (2.89), p_L and p_R should be related to the positive and negative current components and the harmonics. Since the second order harmonics in I_d^p, I_q^p, I_n^p, I_n^p are pretty small, that means the third order harmonics in the ac current can be neglected in these two cases. Therefore, the magnitude of the oscillation for p_L and p_R can be considered to be proportional to the amplitude of the positive sequence current component I_{p1} and the nega-

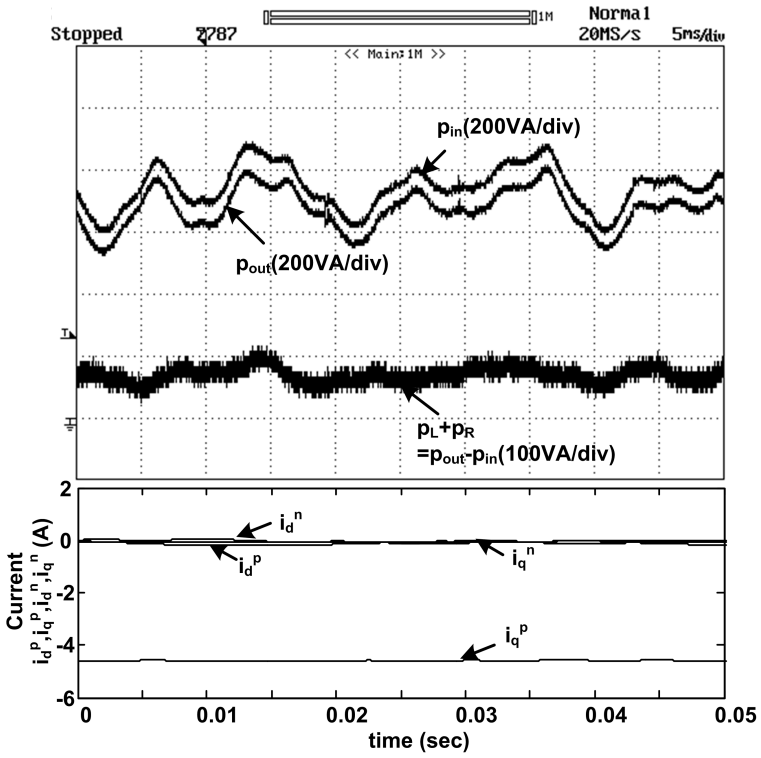

Figure 4.15: Experiment results of input and output instantaneous power and the currents in the rotating synchronous frame by using a dual rotating *d-q* frame controller.

tive sequence current component I_{n1}. Consequently, when the single frame control scheme is implemented, i_d^n is around 0.8 A, the amplitude of the negative sequence current is dominantly decided by this value, so the maximum amplitude of $p_L + p_R$ can reach 100 VA, while when using the proposed control scheme, i_d^n is around 0 A, the amplitude of the negative sequence current is correspondingly reduced, so $p_L + p_R$ is almost flat. The average of $p_L + p_R$ is the loss on the resistance, which is also determined by the amplitude of the positive and negative sequence components. Hence, eliminating the negative sequence current can reduce the loss and improve the efficiency of the system.

In order to validate the improved transient performance of the proposed dual frame control scheme designed by the singular perturbation method, the experi-

mental results for the step change under the unbalanced operating conditions were compared with those by using the traditional PI gain. The traditional designed control parameters which are used in the experiment platform are shown in Table 4.3.

Table 4.3: Controller Parameters Used In the Traditional Method

Parameters	Value	Parameters	Value
K_{pv}	0.03	K_{iv}	4.59
K_{pc}	3.7	K_{ic}	200

When the three phase supply voltages are unbalanced, two phase voltages are 80 V_{rms} and the amplitude of phase c drops to 65 V_{rms}, the dc reference voltage is a step-change from 250 V to 300 V, Figs. 4.16-4.17 compare the dynamic performances of PWM rectifier with a dual rotating frame controller designed by two different methods such as (1) tradition PI controller design method, (2) singular perturbation method.

The two methods as shown in the both figures can ensure the constant dc link voltage under the unbalanced supply voltage operating conditions. Fig. 4.16 show the response of the dc link output voltage and the line side current i_q^p by using the traditional cascaded dual frame controller. We can see that the settling time of the step change is around 100ms and the overshoot is around 45%. While by using the singular perturbation method to design the dual frame cascaded controller parameters as shown in Fig. 4.17, the settling time is shorten to 30ms and the overshoot can be minimized with the same rise time as in Fig. 4.16. Moveover, when the step-change in the reference occurs, the rush current i_q^p can be controlled by using the singular perturbation method.

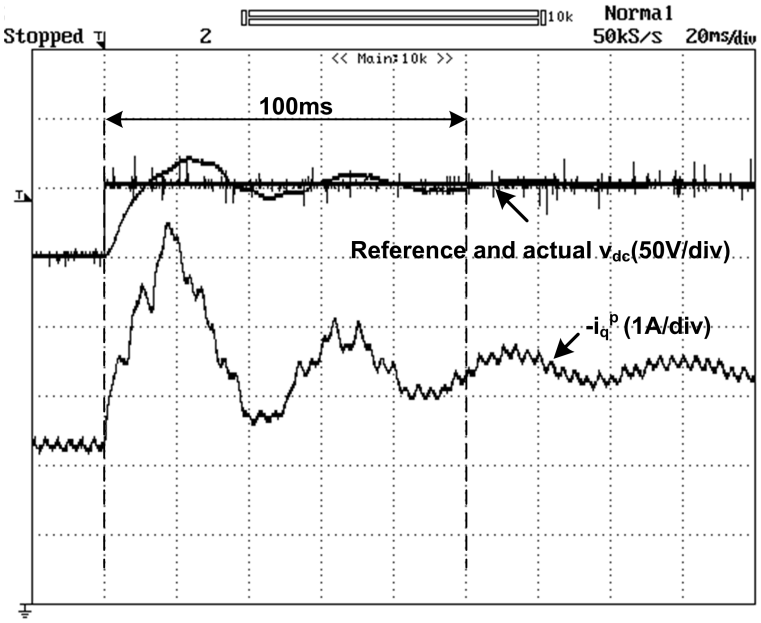

Figure 4.16: Experimental results of dynamic performance of PWM rectifier with a dual rotating *d-q* frame PI controller designed by the traditional method.

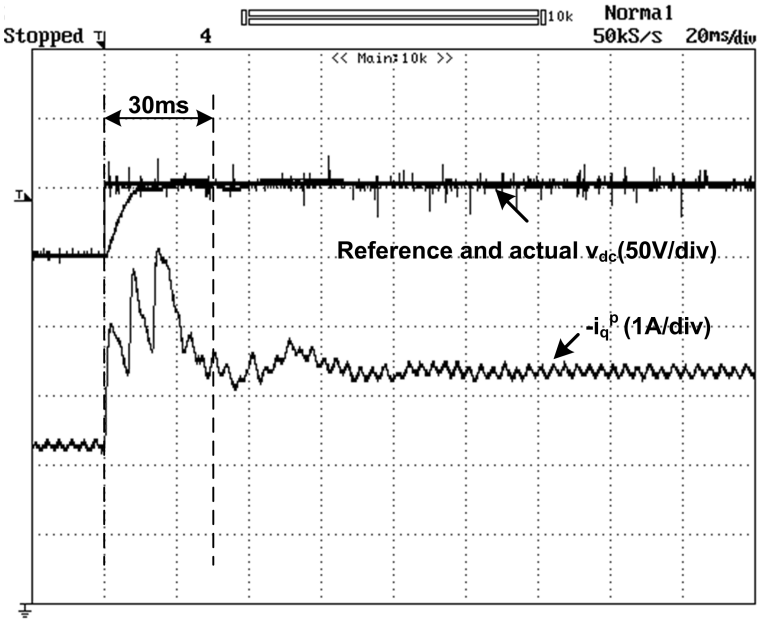

Figure 4.17: Experimental results of dynamic performance of PWM rectifier with a dual rotating *d-q* frame controller designed by the singular perturbation method.

Therefor, by properly designing the time constant for the FMS and SMS of the voltage and current loops, the singular perturbation method provide improved dynamic response of the PWM rectifier under unbalanced supply voltage condition.

4.4 Summary

In this chapter, the detailed dynamic analysis and design procedures of the cascaded dual rotating frame controller for the three phase PWM AC-DC voltage source converter have been presented under the generalized supply voltage conditions. In Section 4.1, the analysis of the control system are based on the conventional PI controller design. However, the traditional design methodology is dependent on a locally linearized plant model so that it cannot ensure the performance under the global operating conditions. Therefore, the nonlinear control approach is preferred to analyze the dynamic performance of three phase PWM AC-DC voltage source converter. In Section 4.2, the singular perturbation method has been used to develop the cascaded rotating d-q dual frame control scheme for PWM rectifier. By using this method, two-time-scale motions, namely, fast motion sub-system and slow motion sub-system, are induced in the closed-loop system. To ensure the stability conditions imposed on the fast and slow modes, sufficiently large mode separation rate by selecting the control law parameters, the closed-loop system can achieve the desired output transient performances and it is also insensitive to the nonlinearities of the system and the variations in the parameters.

In Section 4.3, the experimental test results provided on a 1.6 kVA laboratory based PWM AC-DC voltage source converter validate the performance of the pro-

posed cascaded rotating dual frame controller. The results prove that the proposed dual rotating *d-q* frame controller can minimize the even-order harmonic component at the dc link voltage and the odd-order harmonics in the ac line side currents under the unbalanced supply operating conditions. Also, the proposed dual frame control scheme can keep the supply side power factor closer to unity under the unbalanced operating conditions comparing with the single frame controller. Moreover, the validity of the analysis of the instantaneous power flow in Chapter 2 has been supported with the experimental test results in this section. Finally, the experimental results show that the singular perturbation method provides the improved dynamic response of the PWM rectifier under unbalanced supply voltage conditions by properly designing the time constants for the FMS and SMS of the voltage and current loop.

Chapter 5

Time Domain Based Repetitive Controller

In reality, the unbalanced and distorted input supply voltage conditions occur frequently, particularly in a weak ac system. Since EN 50160 [9] standard allows 6% low order supply voltage harmonics, and supply voltage sags/swells within ±10%. The unbalanced and distorted input supply voltages lead to the appearance of even-order harmonics at the dc output and odd-order harmonics in the input line side currents [34]. It is essential to ensure the supply side currents with low THD under such varying and unbalanced supply voltage conditions.

In practice, 5^{th}, 7^{th}, 11^{th} and 13^{th} order voltage harmonics are dominant in the power distribution networks. The analysis in Chapter 2 indicates that under the generalized supply voltage conditions, the currents in the positive and negative rotating synchronous *d-q* frame consist of a dc component together with the 6^{th} and 12^{th} order harmonic components. In order to obtain sinusoidal current waveforms in the *a-b-c* frame, these 6^{th} and 12^{th} order harmonics in the *d-q* frame supply side line currents should be eliminated.

Most of the proposed controllers in the literature [36]-[45] have tried to eliminate the harmonics in the supply side line currents as a side effect. Only few control schemes [61] have been considered to directly deal with the harmonics in the line side currents under the unbalanced input supply voltage conditions. Therefore, when the supply voltages are distorted, those control schemes can hardly handle the current harmonics on the supply side.

Repetitive control (RC) is specially designed for minimizing these periodic errors to improve the tracking performance, i.e., to suppress the harmonic components of a certain frequency in the currents i_d^p, i_q^p, i_d^n and i_q^n by generating a compensation control signals S_d^p, S_q^p, S_d^n and S_q^n. Repetitive control (RC) [107], originated from the internal model principle [106], can be employed to eliminate periodic errors in a nonlinear dynamical system to achieve high accuracy in the presence of periodic uncertainties. There are also many reports about the applications of repetitive control or iterative learning control (ILC) for power electronics converters [108], [109] as well as motor drives [110], [111]. In [108], a repetitive controller for the three phase PWM rectifier was implemented in *a*-*b*-*c* frame with the balanced supply voltage conditions. However, in reality, the supply voltages are distorted and unbalanced. According to the model in Chapter 2, the controller is preferred to be designed in the positive and negative synchronous rotating frames to take care of the low order frequency harmonics due to the negative sequence components.

In this chapter, a hybrid digital repetitive control scheme is proposed to effectively minimize the supply side line current harmonics under the distorted and unbalanced operating conditions. This repetitive controller, as *current harmonics*

control scheme, is used to achieve low THD line side currents of the three phase PWM boost rectifier under distorted supply voltage conditions. A plug-in repetitive controller is systematically developed with complete stability analysis. The experimental test results are provided to validate the effectiveness of the proposed control scheme on a 1.6 kVA laboratory based three phase PWM rectifier.

5.1 Design of a Plug-in Time Domain Based Repetitive Controller

Repetitive control is specially designed to remove the periodic errors generated due to the disturbances in inputs. The idea of repetitive control, which is based on the internal model principle, is to use the information of the preceding cycle to improve the control performance in the present cycle. The plug-in digital repetitive controller can be designed in the closed-loop as shown in Fig. 5.1. In this figure, $Y_d(z)$ is the reference signal, $Y(z)$ is the output, $E(z)$ is the tracking error, $D(z)$ is the disturbance, $G(z)$ is the plant transfer function, $C_o(z)$ is the transfer function of the feedback controller, $C_{rc}(z)$ is the transfer function of the plug-in repetitive controller and $F(z)$ is the transfer function of the analog filter to remove the high frequency noises at the interface between the system output and the digital controller. Hence, the total effect of the plug-in repetitive controller with the conventional feedback controller can be defined as $C(z) = C_o(z) + C_{rc}(z)$. $Q(z)$ is the low-pass filter to reject the noise and keep the system stable. It should be noted that it is crucial to keep the internal model accurate, so $Q(z)$ cannot be put inside the loop for high frequency application.

Usually, $C_o(z)$ is the basic feedback controller such as P controller or PI

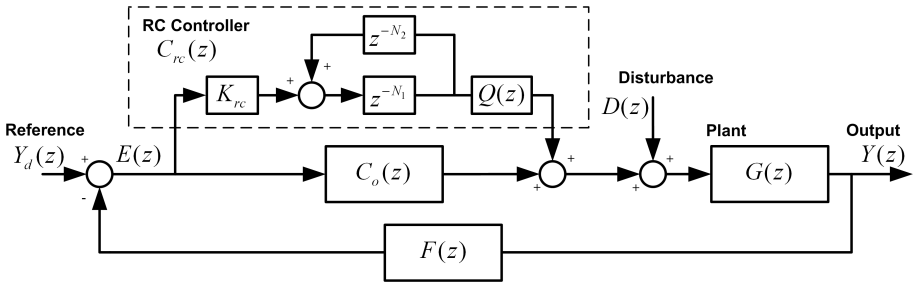

Figure 5.1: Implementation of a plug-in repetitive controller.

controller. $C_o(z)$ is chosen to ensure that the characteristic polynomial of the closed-loop system, $1 + C_o(z)G(z)F(z)$, meets the stability conditions.

According to Fig. 5.1, the transfer function of the repetitive controller $C_{rc}(z)$ is,

$$C_{rc}(z) = Q(z)\frac{K_{rc}z^{-N_1}}{1 - z^{-N}} \tag{5.1}$$

where $N = f_s/f_c$ is the number of samples for each cycle, which is equal to $N_1 + N_2$, with f_c being the reference signal fundamental frequency and f_s being the sampling frequency. N_1 is used to compensate the phase lag caused by the low-pass filter and signal transmission.

From Fig. 5.1, the output $Y(z)$ can be expressed by the reference $Y_d(z)$ and the disturbance $D(z)$,

$$Y(z) = \frac{C(z)G(z)}{1 + C(z)G(z)F(z)}Y_d(z) + \frac{G(z)}{1 + C(z)G(z)F(z)}D(z).$$

The tracking error $E(z)$ can be derived by,

$$E(z) = Y_d(z) - Y(z) = \frac{Y_d(z) + C(z)G(z)F(z)Y_d(z) - C(z)G(z)Y_d(z) - G(z)D(z)}{1 + C(z)G(z)F(z)}. \tag{5.2}$$

From the equation (5.2), the characteristic polynomial of the overall repetitive

control system can be written as,

$$\begin{aligned} 1 + C(z)G(z)F(z) &= 1 + C_o(z)G(z)F(z) + C_{rc}(z)G(z)F(z) \\ &= [1 + C_o(z)G(z)F(z)] \left[1 + \frac{C_{rc}(z)G(z)F(z)}{1 + C_o(z)G(z)F(z)}\right] \\ &= [1 + C_o(z)G(z)F(z)] [1 + C_{rc}(z)C_{cl}(z)], \end{aligned} \tag{5.3}$$

where $C_{cl}(z) = \frac{G(z)F(z)}{1+C_o(z)G(z)F(z)}$ is the transfer function from $D(z)$ to $Y(z)$ without the plug-in repetitive controller.

From the equation (5.3), we can conclude that one possible way to ensure the stability of the overall repetitive control system is that the roots of the polynomial $1 + C_o(z)G(z)F(z) = 0$ are inside the unit circle with the following condition,

$$|1 + C_{rc}(z)C_{cl}(z)| \neq 0. \tag{5.4}$$

The requirement of the roots of $1 + C_o(z)G(z)F(z) = 0$ can be met by choosing the controller transfer function $C_o(z)$ properly. Therefore, the design of the repetitive controller must guarantee that the stability condition (5.4) is satisfied.

By substituting the equation (5.1), the condition (5.4) yields,

$$\left|1 - z^{-N} + K_{rc}z^{-N_1}Q(z)C_{cl}(z)\right| \neq 0 \tag{5.5}$$

The equation (5.5) can be guaranteed, if the following condition is satisfied,

$$\left|z^{-N} - K_{rc}z^{-N_1}Q(z)C_{cl}(z)\right| < 1 \tag{5.6}$$

By realizing $z = e^{j\omega}$, ($\omega = 2\pi f/f_s$, which is a normalized frequency with π being the Nyquist frequency $f = f_s/2$ [107],) it can be easily shown that $|z^N| = 1$. Then, the condition (5.6) can be simplified as,

$$\left|1 - K_{rc}z^{N_2}Q(z)C_{cl}(z)\right| < 1 \tag{5.7}$$

Suppose the closed-loop system $C_{cl}(z)$ has frequency characteristics $C_{cl}(e^{j\omega}) = A_c(e^{j\omega})exp(j\theta_c(e^{j\omega}))$ with $A_c(e^{j\omega})$ being its magnitude and $\theta_c(e^{j\omega})$ being its phase. Similarly, the low pass filter $Q(z)$ can be defined as $Q(e^{j\omega}) = A_q(e^{j\omega})exp(j\theta_q(e^{j\omega}))$ with $A_q(e^{j\omega})$ being its magnitude and $\theta_q(e^{j\omega})$ being its phase. Then, the equation (5.7) has the form of,

$$\left|1 - K_{rc}A_c(e^{j\omega})A_q(e^{j\omega})e^{j\gamma(\omega)}\right| < 1 \tag{5.8}$$

where $\gamma(\omega) = \theta_c(e^{j\omega}) + \theta_q(e^{j\omega}) + N_2\omega$.

The equation (5.8) can be expanded as,

$$\left|1 - K_{rc}A_c(e^{j\omega})A_q(e^{j\omega})\cos\gamma(\omega) - jK_{rc}A_c(e^{j\omega})A_q(e^{j\omega})\sin\gamma(\omega)\right| < 1 \tag{5.9}$$

Taking square on the both sides of this inequality (5.9), we have,

$$K_{rc}^2A_c^2(e^{j\omega})A_q^2(e^{j\omega}) < 2K_{rc}A_c(e^{j\omega})A_q(e^{j\omega})\cos\gamma(\omega) \tag{5.10}$$

Since the repetitive control gain $K_{rc} > 0$ and the system gain $A_c(e^{j\omega}) > 0$, $A_q(e^{j\omega}) > 0$, the equation (5.10) yields,

$$K_{rc}A_c(e^{j\omega})A_q(e^{j\omega}) < 2\cos\gamma(\omega) \tag{5.11}$$

If K_{rc} is chosen as in the equation (5.12), the stability of the closed-loop system would be guaranteed.

$$K_{rc} < \frac{2\min\left[\cos\gamma(\omega)\right]}{\max\left[A_c(e^{j\omega})A_q(e^{j\omega})\right]} \tag{5.12}$$

Since $K_{rc} > 0$ and $A_c(e^{j\omega})$, $A_q(e^{j\omega})$ are both positive, the equation (5.11) implies,

$$\cos\gamma(\omega) > 0 \tag{5.13}$$

Therefore, the range of the phase angle $\gamma(\omega)$ can be obtained as,

$$|\gamma(\omega)| = \left|\theta_c(e^{j\omega}) + \theta_q(e^{j\omega}) + N_2\omega\right| < 90^\circ \tag{5.14}$$

From this condition, the phase angle compensator N_2 can be selected so that (5.14) can be satisfied in the frequency band of interest.

The equations (5.12) and (5.14) are the extended format for (5.11), which provide the stability conditions on the controller gain K_{rc} and phase angle compensator N_2 for the closed-loop system. We can see that the low pass filter $Q(z)$ plays an important role in the selection of control parameters K_{rc} and N_2. The low cut-off frequency for low pass filter $Q(z)$ would give the wider range of the controller gain K_{rc}, but it requires more phase angle compensation to ensure the validation of (5.14) in the low frequency range. As a result, the phase angle requirement (5.14) may not be met for high frequency signals. In practice, it is often difficult to hold the condition (5.14) valid for all frequencies. Since the cut-off frequency of the analog filter is designed at 1kHz, the model uncertainty and the system noise above this frequency would not affect the converter operation. Therefore, the mismatch of the requirement of phase angle can be ignored when the frequency is greater than 1kHz.

To enhance the robustness of the overall system, in the presence of the model uncertainty $\Delta(z)$, a gain variation of ϵ is introduced such that the condition (5.12) is written as,

$$K_{rc} < \frac{2 \min\left[\cos\gamma(\omega)\right]}{\max\left[A_c(e^{j\omega})A_q(e^{j\omega})\right] + \epsilon} \tag{5.15}$$

From this condition, the repetitive control gain can be determined with the approximated knowledge of $A_c(e^{j\omega})$, $A_q(e^{j\omega})$ and $\gamma(\omega)$.

In addition, the tracking error in the equation (5.16) can be expanded as,

$$E(z) = \frac{\left(1 - z^{-N}\right)\left(Y_d(z) + C(z)G(z)F(z)Y_d(z) - C(z)G(z)Y_d(z) - G(z)D(z)\right)}{\left(1 + C_o(z)G(z)F(z)\right)\left(1 - z^{-N} + K_{rc}z^{-N_1}Q(z)C_{cl}(z)\right)} \tag{5.16}$$

It is clear that when ω approaches $\omega_l = 2\pi l/N$ with $l = 0, 1, 2, ..., L$ ($L = N/2$ for even N and $L = (N-1)/2$ for odd N), $z^{-N} = 1$. Under the condition (5.5), we can design PI controller to avoid the roots of the characteristic polynomial $1 + C_o(z)G(z)F(z)$ at the frequency ω_l. Therefore, for all ω_l, we have,

$$E(e^{j\omega_l}) = 0 \tag{5.17}$$

The equation (5.17) indicates that if the frequency of the reference input or disturbance is multiple of the frequency designed to be eliminated and less than half of the sampling frequency, zero steady state tracking errors for the reference input are ensured using the plug-in repetitive controller, even in the presence of model uncertainty.

5.2 TDRC for Supply Current Harmonics Control

In practice, 5^{th} and 7^{th} order voltage harmonics are dominant in the power distribution networks. As analyzed in the PWM rectifier model in Chapter 2, 5^{th} and 7^{th} order voltage harmonics in *a-b-c* frame cause 6^{th} order current harmonics in the *d-q* frame. The input current harmonics control is mainly to eliminate the 6^{th} order harmonics in the *d-q* frame for the line side currents. Therefore, the time domain based repetitive control (TDRC) method can be employed to regulate the currents i_d^p, i_q^p, i_d^n and i_q^n and remove the periodic errors.

The proposed current control scheme consists of the conventional PI controller together with a plug-in type repetitive controller for PWM rectifier as shown in Fig. 5.2.

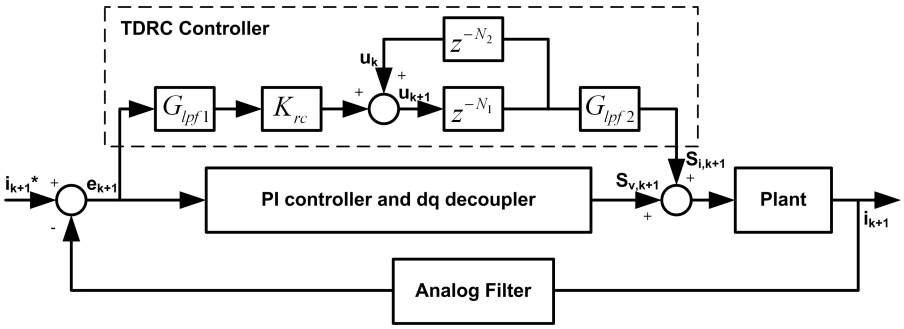

Figure 5.2: Block diagram of PI controller with a plug-in type repetitive controller.

The basic control law for the TDRC is given by,

$$u_{k+1}(z) = u_k(z) + K_{rc}e_{k+1}(z) \tag{5.18}$$

where $u_{k+1}(z)$ and $u_k(z)$ are the z-transforms of the control signals from the repetitive control during cycle $k+1$ and k, respectively. K_{rc} is the learning gain, and e_{k+1} is the tracking error during cycle $k+1$. $G_{lpf1}(z)$ and $G_{lpf2}(z)$ are the two low-pass filters to reject noise in the error signals and TDRC controller output, respectively.

The transfer function of the plug-in repetitive controller $C_{rc}(z)$ is

$$C_{rc}(z) = G_{lpf1}(z)G_{lpf2}(z)\frac{K_{rc}z^{-N_1}}{1-z^{-N}} \tag{5.19}$$

The feedback controller $C_o(z)$ uses the PI controller designed in Chapter 4. The Bode plot of the transfer function $C_{cl}(z)$ is shown in Fig. 5.3. The phase delay compensator N_2 is used to compensate the phase lag caused by the two low-pass filters and the plant, so that the phase angle $\gamma(\omega)$ possibly can be maintained

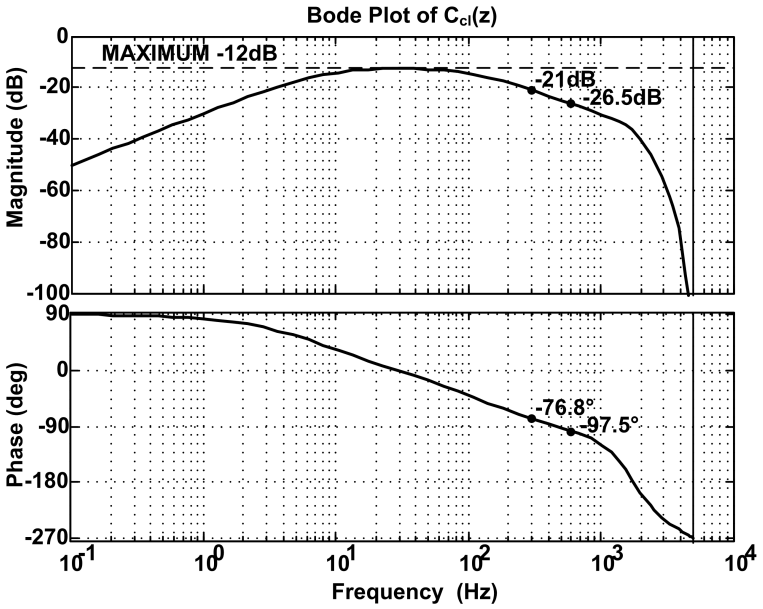

Figure 5.3: Bode plot of $C_{cl}(z)$ for three phase PWM rectifier.

within the region from $-90°$ to $90°$ as shown in the equation (5.14). Based on the phase angle of close loop transfer function $C_{cl}(z)$ and two low pass filters $G_{lpf1}(z)$ and $G_{lpf2}(z)$, the phase angle $\gamma(\omega)$ can be plotted as shown in Fig. 5.4. Fig. 5.4 shows the different curves of the phase angle $\gamma(\omega)$ for the different values of the phase angle compensator $N_2 = 6, 8, 11$. It is clear that $N_2 = 8$ provides the widest frequency band to meet the requirement of (5.14).

When $N_2 = 8$, the the phase angle $\gamma(\omega)$ varies from $-82.4°$ to $73.33°$, so $\min(cos\gamma(\omega)) = 0.13$. And the maximum gain of $C_{cl}(z)$ as shown in Fig. 5.3, -12dB ($\max(A_c(e^{j\omega})) = 0.25$). According to (5.15), the stable range for K_{rc} can be obtained,

$$K_{rc} < \frac{2 \times 0.13}{0.25 + \epsilon} \tag{5.20}$$

Ideally, when the value of K_{rc} is less than 1, the system should be stable. However, the gain variation of $C_{cl}(z)$ is from -12dB (0.25) to -33dB (0.02) until the operating frequency range of 1kHz. Since the variation of $A_c(e^{jw})$ is around 92%,

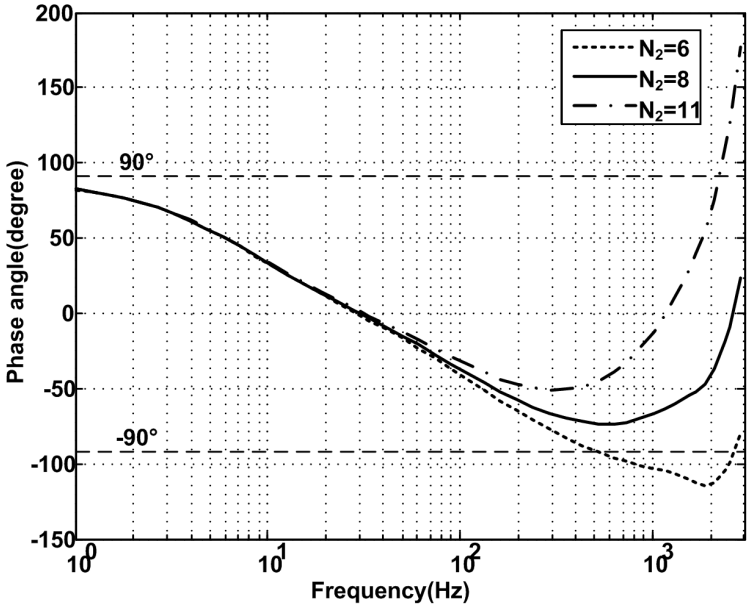

Figure 5.4: Plot of phase angle $\gamma(\omega)$ with the different the phase angle compensator N_2.

it is reasonable to make an assumption of 10% model uncertainties. Therefore, we can choose ϵ to be around 0.1 or so, leading to $K_{rc} < 0.74$, and the overall system would be stable.

In this hybrid control scheme, the linear PI controller provides majority of the control efforts during the transient stage. Once the system enters the steady state, the repetitive controller takes over the control effort and tries to reduce the steady state tracking error from cycle to cycle. Therefore, the 6^{th} order harmonics in the currents i_d^p, i_q^p, i_d^n and i_q^n can be removed.

5.3 Experimental Validation

To verify the feasibility of the proposed control scheme, the experiments were conducted under the distorted operating conditions. The complete control scheme was

implemented on a dSPACE platform (DS1104). The DSP processor TI TMS320F240 was employed with 10 kHz sampling rate in the control board. The IGBT module adopted the symmetric PWM modulation with 20 kHz switching frequency. The system parameters used in the experimental platform are summarized in Table 5.1.

Table 5.1: Control Parameters used in Time Domain Based Repetitive Controller

Parameters	Value	Parameters	Value
K_{rc}	0.3	N_2	8

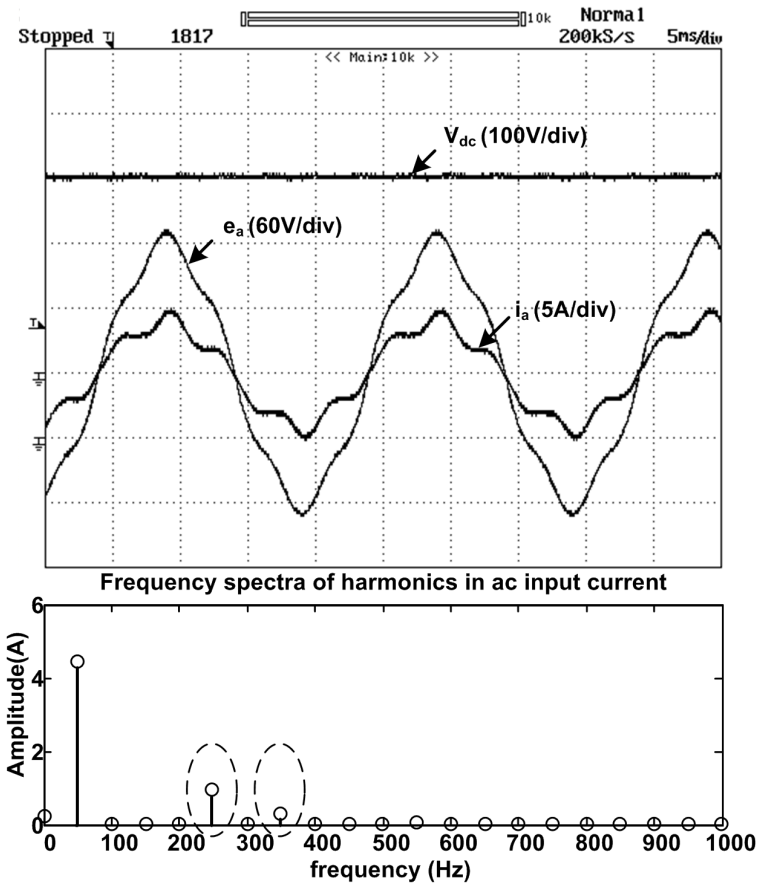

Figure 5.5: Experiment results of dc link voltage and ac line side current before using the repetitive controller when the supply voltage is distorted with 10% 5^{th} order harmonics.

Fig. 5.5 and Fig. 5.6 show the performance of the PWM rectifier without

and with the proposed hybrid TDRC control scheme when 10% of the 5^{th} order harmonic voltages are injected in the supply voltages.

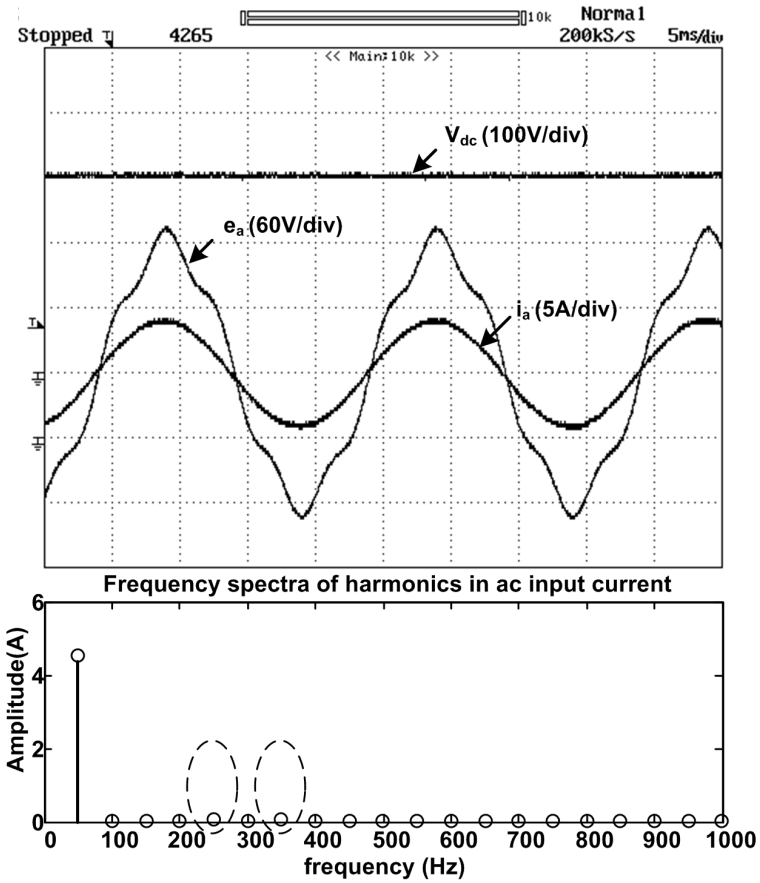

Figure 5.6: Experiment results of dc link voltage and ac line side current after using the repetitive controller when the supply voltage is distorted with 10% 5^{th} order harmonics.

Without using the repetitive control, Fig. 5.5 shows the dc link voltage, phase a supply voltage and current of the system. The distorted supply voltages cause 5^{th} and 7^{th} order harmonics in the ac line side currents to be 20.00% and 4.90%, respectively. The total harmonics distortion (THD) factor of the phase a input current is 21.09%. When the plug-in repetitive controller is activated, the current harmonics are reduced significantly as can be seen in Fig. 5.6. From the frequency spectra of the harmonics in the ac line side currents, we can see that the 5^{th} order harmonic component decreases from 20.00% to 2.82% and 7^{th} order harmonics is

from 4.95% to 1.41%, and the THD factor of the phase input current is reduced from 21.09% to 5.27%.

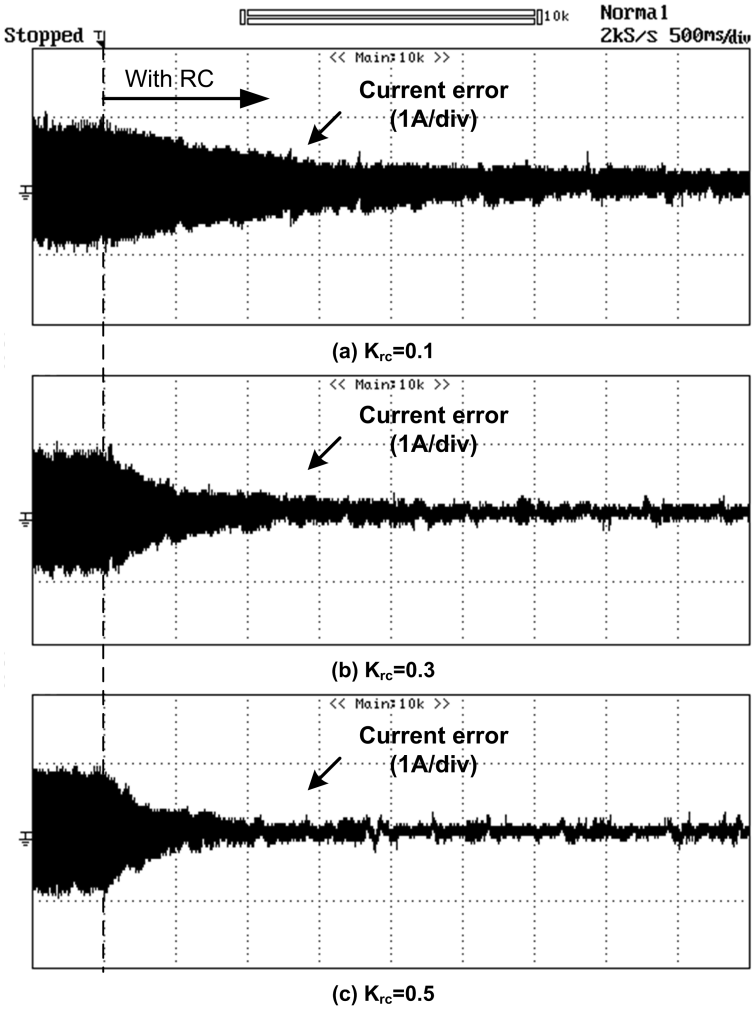

Figure 5.7: Experiment transient response of error convergence with the different K_{rc} values when the repetitive controller has been plugged in.

Fig. 5.7 shows the transient response of the error convergence for the i_q^p current control loop with the different K_{rc} values when the phase delay compensator N_2 is set to 8. For the different gain $K_{rc} = 0.1, 0.3$ and 0.5, the errors between the reference current and the actual current are all gradually reduced from 1.8 A to 0.2 A. Furthermore, the higher gain makes the error to converge faster as can be seen from Fig. 5.7. So when $K_{rc} = 0.5$, it provides the fastest response in these three cases. However, if K_{rc} is too high, the system becomes unstable. A conservative

value of 0.3 is recommended for our experimental platform.

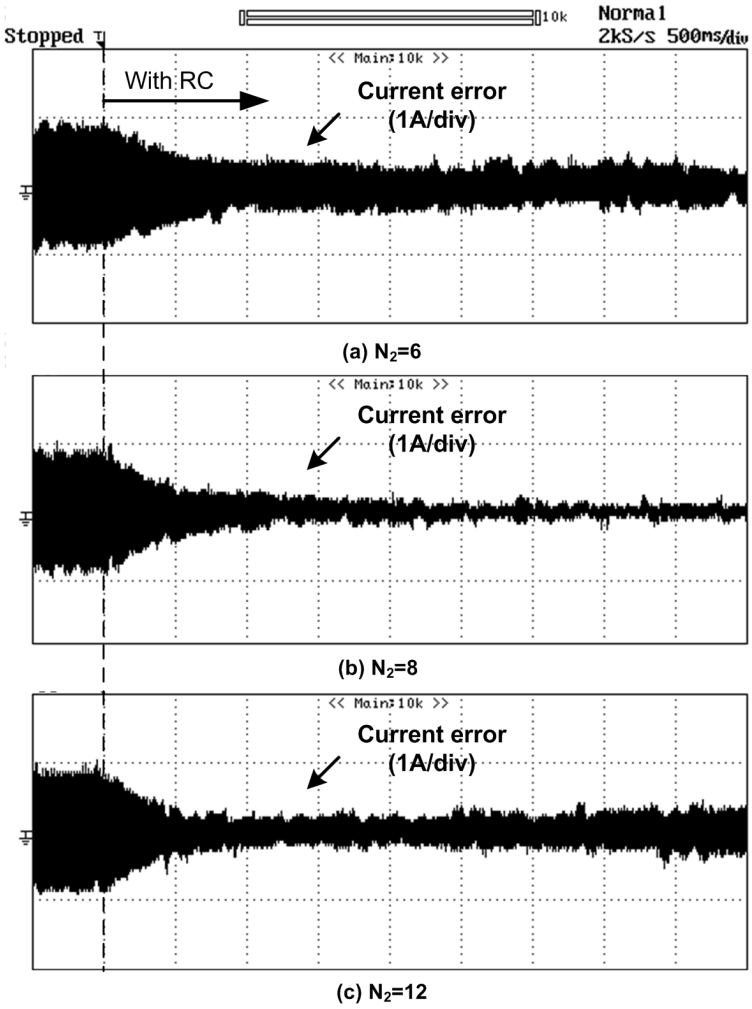

Figure 5.8: Experiment transient response of error convergence with the different phase delay N_2 when the repetitive controller has been plugged in.

Fig. 5.8 shows the transient response of the error convergence for the i_q^p current control loop with the different phase delay compensator N_2 when the gain K_{rc} is 0.3. When $N_2 = 6$, the amplitude of the steady state error is around 0.3 A, while when $N_2 = 8$, the steady state error can be reduced till 0.1 A. However, when N_2 is 12, the current error diverges again after some time as shown in Fig. 5.8 (c). Fig. 5.8 shows that it is important to choose the proper phase delay compensator for the repetitive controller. For this case, $N_2 = 8$ gives the best performance of the zero error tracking of the current control loop.

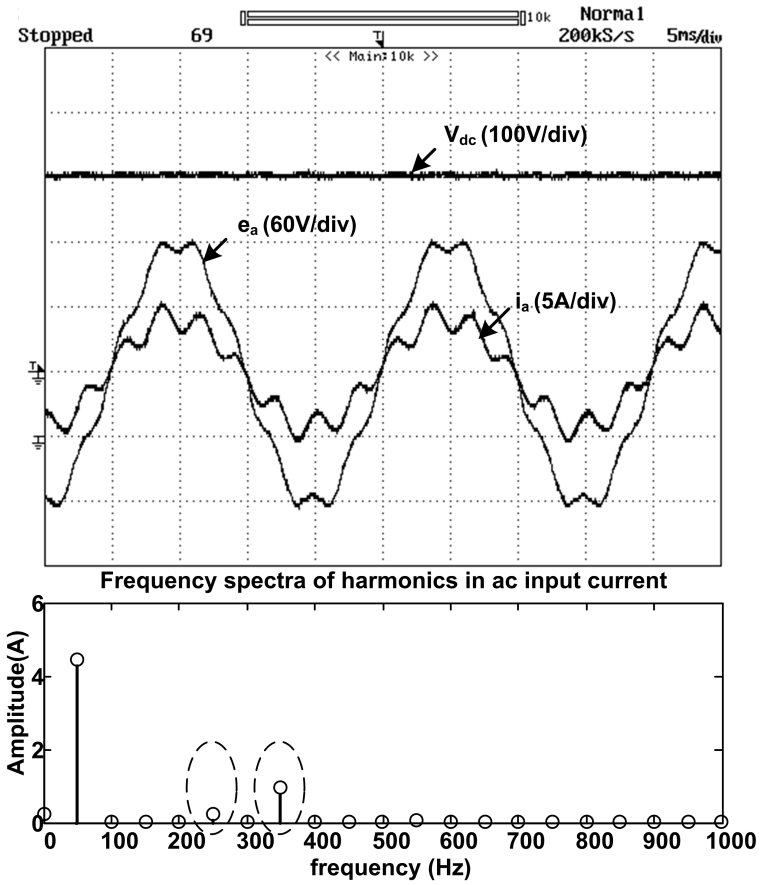

Figure 5.9: Experiment results of dc link voltage and ac line side current before using the repetitive controller when the supply voltage is distorted with 10% 7^{th} order harmonics.

The same control scheme has been used to test when 10% of the 7^{th} order harmonic voltages are injected in the supply voltages. Fig. 5.9 shows the dc link voltage, phase a ac supply voltage and current of the system without using the repetitive control. These distorted supply voltages cause 5^{th} and 7^{th} order harmonics in the ac line side currents to be 5.01% and 21.07%, respectively. The THD factor of the phase a input current is 22.68% as shown in Fig. 5.9.

Fig. 5.10 shows the results with TDRC scheme applied. From Fig. 5.10, the current harmonics are reduced significantly when the plug-in repetitive controller is used, the 5^{th} order harmonic component decreases from 5.01% to 1.02% and 7^{th}

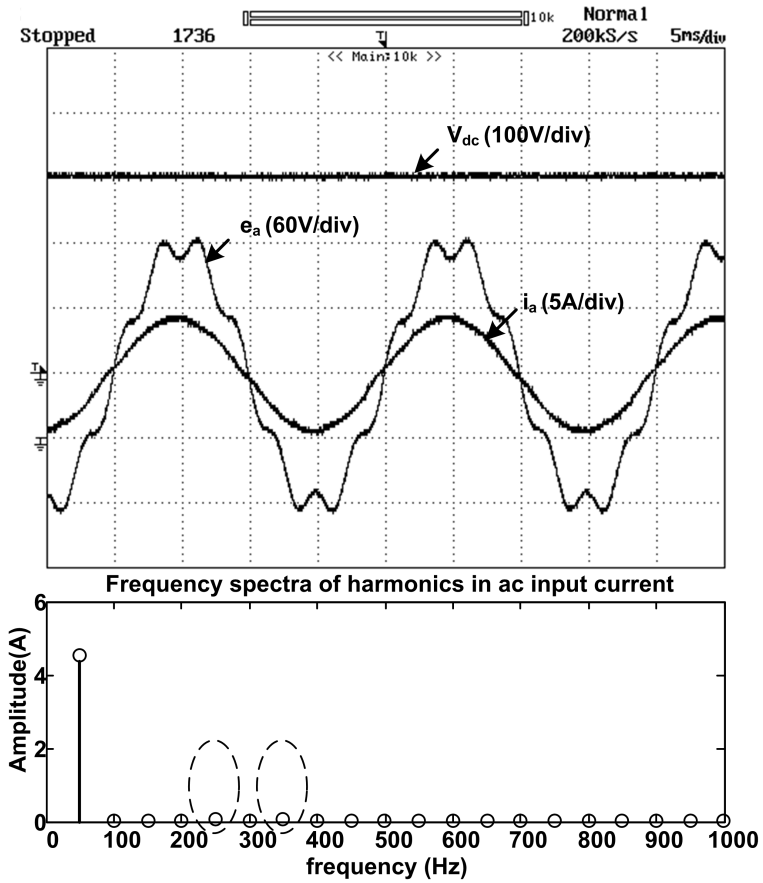

Figure 5.10: Experiment results of dc link voltage and ac line side current after using the repetitive controller when the supply voltage is distorted with 10% 7^{th} order harmonics.

order harmonics is from 21.07% to 2.13%. Also, the THD factor of the phase a input current is reduced from 22.68% to 5.53%.

In practice, the 5^{th} order and 7^{th} order harmonics are both involved in the supply voltages. Fig. 5.11 and Fig. 5.12 show the dc link voltage, phase a ac supply voltage and current of the system, and compare the performance of the PWM rectifier without and with the proposed hybrid control scheme when 5% of the 5^{th} order and 5% of the 7^{th} order harmonic voltages are injected in the supply voltages. Without using the repetitive control, the distorted supply voltages cause the 5^{th} and 7^{th} order harmonics in the ac line side currents to be 6.95% and 14.46%,

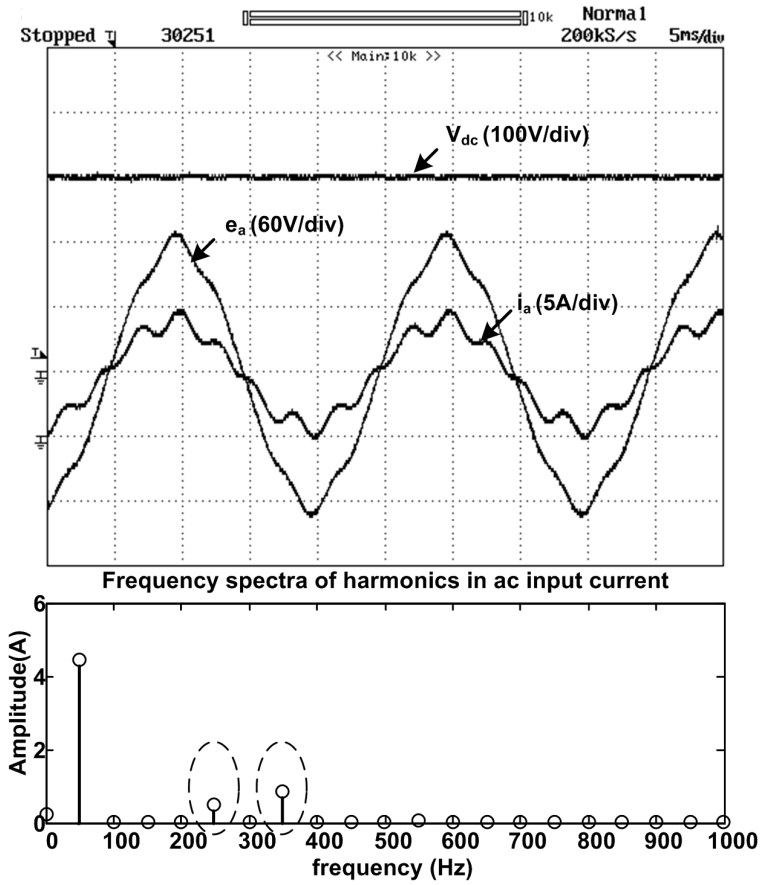

Figure 5.11: Experiment results of dc link voltage and ac line side current before using the repetitive controller when the supply voltage is distorted with 5% 5^{th} and 5% 7^{th} order harmonics.

respectively, which can be seen in Fig. 5.11. Fig. 5.12 shows that the current harmonics are decreased significantly when the repetitive controller is plugged in. From the frequency spectra of the harmonics in the ac line side currents, we can see that the 5^{th} order harmonic component decreases from 6.95% to 1.40% and 7^{th} order harmonics is from 14.46% to 2.09%. Moreover, the THD factor of the phase input current is reduced from 16.63% to 4.90%.

In the proposed hybrid control scheme, the plug-in repetitive controller can maintain the steady state error within 0.1A error band and the cascaded PI controller takes care of the dynamic performance. Fig. 5.13 shows the dc link voltage

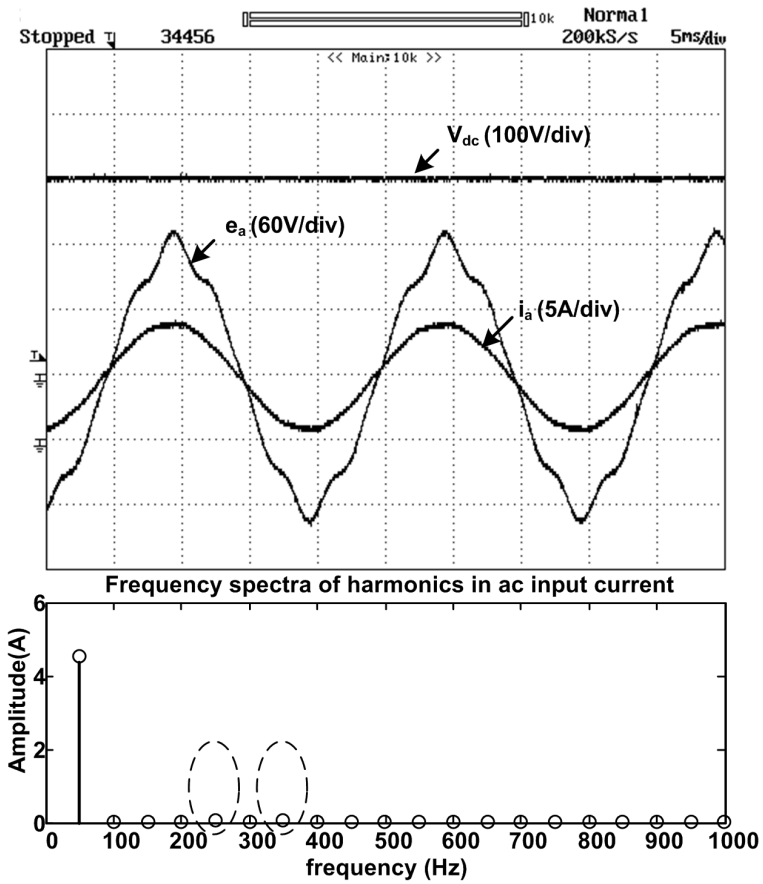

Figure 5.12: Experiment results of dc link voltage and ac line side current after using the repetitive controller when the supply voltage is distorted with 5% 5^{th} and 5% 7^{th} order harmonics.

and the ac line side current when the load is changed from 340Ω to 226Ω. We can see that the variation of the dc link voltage is within 0.5% and the line side current goes to the steady state in two cycles, around 40 ms. Hence, the proposed control scheme still can regulate the dc link voltage and keep the link current sinusoidal when the load disturbance occurs.

Therefore, it can be concluded that the plug-in repetitive controller can minimize the harmonics in the supply side currents and provide better steady state performance under the distorted supply voltage operating conditions as compared to the conventional controller.

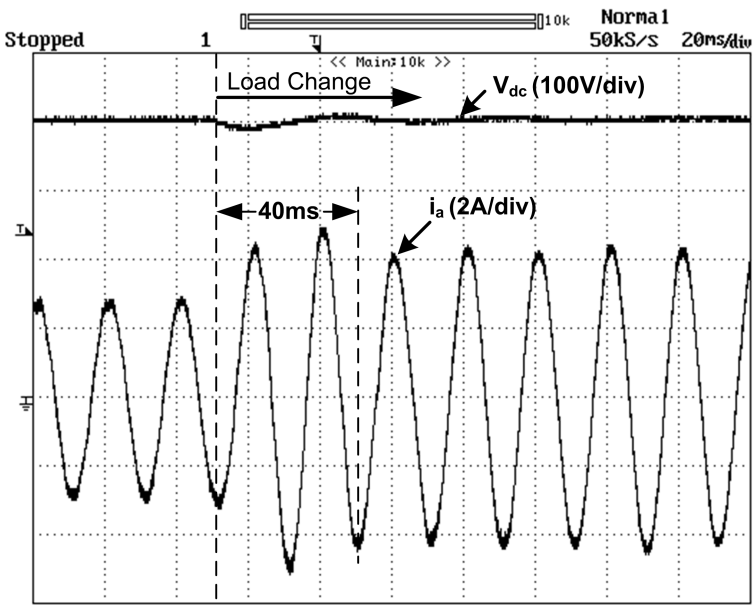

Figure 5.13: Experiment results of dc link voltage and ac line side current when the load increases.

5.4 Summary

In this chapter, a digital repetitive control scheme is proposed for the three phase PWM boost rectifiers to eliminate the supply side current harmonics under the generalized supply voltage conditions. Based on the analysis of the distorted supply voltages, the predominant voltage harmonics, 5^{th} and 7^{th} order harmonics result in the same frequency and 6^{th} order harmonics on the line side currents in the rotating synchronous *d-q* frame. Therefore, the control task is divided into *voltage harmonics control* and *current harmonics control*. The conventional PI controller is operating *voltage harmonics control* scheme to make sure that the dc link voltage is maintained constant and the supply side power factor is kept close to unity. A plug-in repetitive current controller (RC), as *current harmonics control* scheme, is designed and employed to improve the line side current waveforms of the three phase PWM boost rectifier under the distorted supply voltage conditions. The

choice of the repetitive control parameters such as gain K_{rc} and the phase delay compensator N_2 have been discussed. The experimental results verify that the proposed plug-in digital repetitive control scheme can minimize the harmonics in the ac line side currents while maintaining the dc link voltage constant.

Chapter 6

Frequency Domain Based Repetitive Controller

Since the repetitive controller (RC) [107] is suitable to eliminate periodic errors in a nonlinear dynamical system to achieve high accuracy in the presence of periodic uncertainties, it can be employed to remove the supply line side current harmonics of voltage source converter under the unbalanced and distorted supply voltage conditions. In this chapter, we focus on a new approach – repetitive controller designed in the frequency domain (FDRC) as has been explored partially in [110], [115].

The main advantage of designing a repetitive controller in the frequency domain is the simplicity in the control algorithm and the real-time implementation. Note that a harmonics is completely determined by two real numbers: magnitude and phase. By using the known sinusoidal feature of harmonics, the repetitive controller needs only to learn and update these two parameters. On the contrary, a harmonics in time domain is described as a function of time. Thus the system response of an entire cycle will have to be stored for learning and updating in a

pointwise manner. The controller design would be easier in the frequency domain than in the time domain. Moreover, FDRC scheme performs like notch filters and learns the selected harmonic frequencies only, so that it avoids the integral operation for high band frequencies which are dominated by noise. It is also easier to calculate the appropriate phase angle compensation for the individual harmonic frequencies where the phase lag is inevitable from the plant and filters. Hence, FDRC scheme is introduced to enhance the robustness of the control system.

In this chapter, a plug-in frequency domain based repetitive control (FDRC) scheme is proposed to effectively minimize the supply line side current harmonics and the dc link voltage harmonics under the distorted and unbalanced operating conditions. Based on the mathematical model of the three-phase PWM boost rectifier in the positive and negative synchronous rotating frames, the control objectives can be separated as *voltage harmonics control* and *current harmonics control*. A plug-in FDRC is designed and employed in *current harmonics control* scheme to eliminate the current harmonics in the line side. The learning algorithm in the FDRC scheme uses Fourier series analysis to obtain the magnitude and phase angle of each chosen frequency component, and utilize these information to reconstruct a signal for the learning process. As a result, low THD line side currents of the three phase PWM boost rectifier under the distorted supply voltage conditions can be achieved. The experimental test results provided validate the effectiveness of the proposed control scheme on a 1.6 kVA laboratory based three phase PWM rectifier.

6.1 Design of a Plug-in Digital Frequency Domain Based Repetitive Controller

The plug-in digital repetitive controller can be designed in the closed-loop as shown in Fig. 5.1 in Chapter 5. The transfer function of the plug-in repetitive controller $C_{rc}(z)$ is the frequency domain based repetitive controller. The basic idea of repetitive controller is to utilize the knowledge of previous cycle error and control effort for each frequency component to eliminate periodic error in the current cycle. According to the major difference of the implementation with and without Fourier series expansion (FSA) in the control scheme, the repetitive controller can be divided into two kinds, namely, the time domain based repetitive controller and the frequency domain based repetitive controller.

Similar to the analysis in Chapter 5, one possible way to ensure the stability of the overall repetitive control closed-loop system is that the roots of the polynomial $1 + C_o(z)G(z)F(z) = 0$ are inside the unit circle and the condition $|1 + C_{rc}(z)C_{cl}(z)| \neq 0$ can be hold as shown in the equation (5.4).

The learning algorithm of FDRC scheme is implemented in the frequency domain by using Fourier series approximation (FSA) method [114]. The principle idea of FDRC scheme is then to learn from the previous cycle data and update two coefficients, the magnitude and phase, for each harmonic to be compensated. In practice, system noise or other small non-repeatable factors always exist in the system. Accumulation of those components contained in u_{k+1} may degrade the approximation precision of the controller. Fourier series based learning mechanism, on the other hand, updates coefficients R_0 and R_n of the learned frequency compo-

nents over the entire learning period according to (6.1), which takes an averaging operation on output control signals and tracking error signals, and is able to remove the majority of noise and nonrepeatable factors. Therefore, Fourier series based learning method enhances the robustness property of repetitive learning control while improving the tracking performance.

The error signal e_{k+1} and control signal u_{k+1} can be presented by a continuous periodic signal $f(t)$, which is defined over the time interval $0 \leq t < T$ for one cycle and sampled with sampling time ΔT. This periodic signal $f(t)$ can be expressed in Fourier series approximation format [115],

$$f(k\Delta T) = R_0 + \sum_{n=1}^{v-1}(R_n \cos(n\omega k\Delta T) + I_n \sin(n\omega k\Delta T)) \tag{6.1}$$

where

$$\begin{aligned} R_0 &= \frac{\Delta T}{T}\sum_{k=0}^{N-1} f(k\Delta T) \\ R_n &= \frac{2\Delta T}{T}\sum_{k=0}^{N-1} f(k\Delta T)\cos(n\omega k\Delta T) \\ I_n &= \frac{2\Delta T}{T}\sum_{k=0}^{N-1} f(k\Delta T)\sin(n\omega k\Delta T) \end{aligned}$$

where $n = 1, 2, 3, ..., v-1$; $k = 0, 1, 2, ..., N-1$; N denotes sampling number in the interval $0 \leq t < T$; v is the number of harmonics; $\omega = 2\pi/T$.

The FSA calculation algorithm used in the controller can be simplified as the product of the frequency component vector $\Omega(f(k\Delta T))$ and the coefficient vector $\psi(f(k\Delta T))$. The frequency component vector of the signal $f(t)$ is given as,

$$\Omega(f(k\Delta T)) = \begin{matrix}[1 & \cos(\omega k\Delta T) & \cos(2\omega k\Delta T) & ... & \cos(v\omega k\Delta T) \\ & \sin(\omega k\Delta T) & \sin(2\omega k\Delta T) & ... & \sin(v\omega k\Delta T)].\end{matrix} \tag{6.2}$$

The coefficient vector of the signal $f(t)$ can be expressed as,

$$\psi\left(f(k\Delta T)\right) = \begin{matrix}[R_0 & R_1 & R_2 & ... & R_v \\ & I_1 & I_2 & ... & I_v]^T.\end{matrix} \tag{6.3}$$

At every sampling point, FDRC scheme updates its coefficient vector $\psi\left(f(k\Delta T)\right)$ based on previous cycle information and calculates its frequency component vector $\Omega\left(f(k\Delta T)\right)$. By using FSA, we can obtain,

$$FSA\left(f(k\Delta T)\right) = \Omega\left(f(k\Delta T)\right) \cdot \psi\left(f(k\Delta T)\right). \tag{6.4}$$

However, the analog anti-aliasing filter shown in Fig. 5.1 and the plant characteristics introduce the phase delays between the output control signals and the feedback signals in the system. Due to the presence of phase delays, the internal model of RC cannot be kept accurate. Hence, this phase delay problem which commonly exists in all control systems lead to an ineffective error minimization scheme. Additionally, the phase delay for each frequency component is not the same and differ from one to another. Mostly, the phase delay with the higher order harmonic components are much higher than that for the lower order harmonics, which leads to a positive feedback effect. Consequently, the inability of compensating the phase delay properly will cause the harmonics components to increase significantly instead. Wu et.al [34] show that TDRC scheme only can provide a fixed phase angle delay compensator for all the frequency components. In order to avoid the deterioration of the performance caused by the incomplete phase compensation in the high frequency range, the low pass filter is required to eliminate the high frequency harmonic. Unlike the TDRC, FDRC can extract the magnitude and phase angle information for each frequency component separately, and the phase delay compensation could be easily added in to (6.2), so that $\Omega\left(f(k\Delta T)\right)$ can be

modified as,

$$\Omega_\alpha\left(f(k\Delta T)\right) = \begin{bmatrix} 1 & \cos(\omega k\Delta T+\alpha_1) & \cos(2\omega k\Delta T+\alpha_2) & \ldots & \cos(v\omega k\Delta T+\alpha_v) \\ & \sin(\omega k\Delta T+\alpha_1) & \sin(2\omega k\Delta T+\alpha_2) & \ldots & \sin(v\omega k\Delta T+\alpha_v)\end{bmatrix},$$

where α_v are the value of the phase angle delay compensation and the subscript v shows which order harmonic components are supposed to be eliminated.

The FSA with the phase angle delay compensation can be expressed as,

$$FSA_\alpha\left(f(k\Delta T)\right) = \Omega_\alpha\left(f(k\Delta T)\right)\cdot\psi\left(f(k\Delta T)\right). \tag{6.5}$$

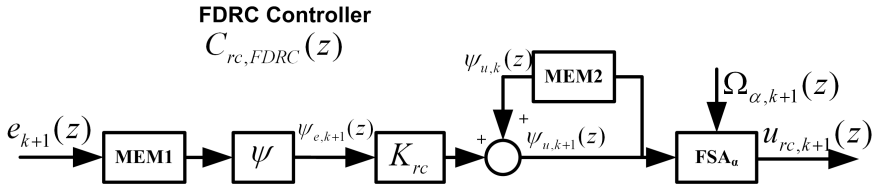

Figure 6.1: Block diagram of frequency domain based repetitive controller.

The FDRC control block diagram by means of Fourier series approximation method is shown in Fig. 6.1. In the figure, $MEM1$, $MEM2$ are the memories used to keep one cycle data. ψ is the calculator for the coefficient vector of the periodic signal $f(t)$ in Fourier series approximation format. FSA_α is the step to reconstruct the signal $f(t)$ by using modified Fourier series approximation in (6.5).

From Fig. 6.1, the corresponding control law for the FDRC scheme is given by,

$$\psi_{u,k+1}(z) = \psi_{u,k}(z) + K_{rc}\cdot\psi_{e,k+1}(z), \tag{6.6}$$

where k is the cycle number; K_{rc} is a vector for the learning gain; the subscripts u and e represent the control input and tracking error, respectively; the subscripts $k+1$ and k designate the present and previous cycles respectively.

Since there are N samples in one cycle, the transfer function between the coefficient vector of the error signal $\psi_{e,k}$ and the coefficient vector of the control signal $\psi_{u,k}$ can be expressed as,

$$\frac{\psi_{u,k}}{\psi_{e,k}} = \frac{K_{rc}}{1 - z^{-N}}. \tag{6.7}$$

The coefficient vector is the vector including the gain for each frequency component, so the variation of the coefficient vector would not be big during the steady state. Assuming the frequency of the $\psi_{e,k}$ variation is a small value ω_1, the equation (6.7) can be written by realizing $z = e^{j\omega}$, ($\omega = 2\pi f/f_s$, which is a normalized frequency with π being the Nyquist frequency $f = f_s/2$ [107], f_s is the sampling frequency),

$$\frac{\psi_{u,k}}{\psi_{e,k}} = \frac{K_{rc}}{1 - e^{-jN\omega_1}}. \tag{6.8}$$

The ratio between the magnitude of $\psi_{u,k}$ and $\psi_{e,k}$ can be obtained from (6.9),

$$\frac{|\psi_{u,k}|}{|\psi_{e,k}|} = \frac{K_{rc}}{2 - 2\cos N\omega_1} = \frac{K_{rc}}{\varsigma}, \tag{6.9}$$

when ω_1 is assumed to be a small and fixed value, ς is close to zero. Hence, the ratio between the magnitude of $\psi_{u,k}$ and $\psi_{e,k}$ would be very big and proportional to the gain vector K_{rc} for the different frequency components.

According to the modified FSA with the phase delay compensation in (6.5), the phase angle between the error signal e_k and the final output control signal $u_{rc,k}$ is decided by α_v for each v^{th} order harmonics. Therefore, the transfer function of the plug-in frequency domain based repetitive controller $C_{rc,FDRC}(z)$ is

$$C_{rc,FDRC}(\omega) = \frac{K_{rc}}{\varsigma} e^{j\alpha_v}. \tag{6.10}$$

By substituting the equation (6.10), the stability condition (5.4) yields,

$$\left| 1 + \frac{K_{rc} e^{j\alpha_v} C_{cl}(e^{j\omega})}{\varsigma} \right| \neq 0. \tag{6.11}$$

Using the closed loop frequency characteristics $C_{cl}(e^{j\omega}) = A_c(e^{j\omega})exp(j\theta_c(e^{j\omega}))$ with $A_c(e^{j\omega})$ being its magnitude and $\theta_c(e^{j\omega})$ being its phase, the equation (6.11) can be rewritten as,

$$\left|1 + \frac{K_{rc}A_c(e^{j\omega})e^{j\gamma_f(\omega)}}{\varsigma}\right| \neq 0 \tag{6.12}$$

where $\gamma_f(\omega) = \theta_c(e^{j\omega}) + \alpha_v$.

The equation (6.12) can be guaranteed, if the following condition is satisfied,

$$\left|\frac{K_{rc}A_c(e^{j\omega})e^{j\gamma_f(\omega)}}{\varsigma}\right| < 1 \tag{6.13}$$

Since $|e^{j\gamma_f(\omega)}| = 1$, the repetitive control gain $K_{rc} > 0$, $\varsigma > 0$ and the system gain $A_c(e^{j\omega}) > 0$, and some margin δ is kept for the model uncertainty, K_{rc} in the range (6.14) would grantee the stability of the closed loop system,

$$K_{rc} < \frac{\varsigma(1-\delta)}{A_c(e^{j\omega})} \tag{6.14}$$

From Fig. 5.1, we can see that the transfer function between the error signal e_k and the final output control signal of the FDRC controller $u_{rc,k}$ can be expressed as

$$\frac{E(z)}{U_{rc}(z)} = -\frac{G(z)F(z)}{1 + C_o(z)G(z)F(z)} = -C_{cl}(z) \tag{6.15}$$

The transfer function shows that phase delay between $U_{rc}(z)$ and $E(z)$ is caused by the filters, the plant and controller C_o. To achieve the good tracking performance by using the repetitive control, the key is to inject the control signal which can provide the feedback signal with the 180° phase angle shift to the error signal. As a result, the output signal generated by FDRC controller can reduce the original error signal. Accordingly, the phase angle delay compensation α_v should be added to match the following relationship,

$$\alpha_v + \left(-\theta_c(e^{j\omega})\right) = \pi \tag{6.16}$$

6.2 FDRC for Supply Current Harmonics Control

One of the control objective for the three phase PWM AC-DC voltage source converter under the generalized operating condition, as described in Chapter 3, is to eliminate the odd-order harmonics in the supply side line currents. In practice, 5^{th}, 7^{th}, 11^{th} and 13^{th} order voltage harmonics are dominant in the power distribution networks. As analyzed in the PWM rectifier model in Chapter 2, the corresponding 6^{th} and 12^{th} order harmonics are generated in the positive and negative rotating synchronous *d-q* frame supply side line currents. Therefore, the 300 Hz, 600 Hz frequency components are selected as the learning objectives to be eliminated. Accordingly, the learning gain and the phase angle delay compensation are designed for each frequency component.

The block diagram of the implemented current control scheme is shown in Fig. 6.2. The feedback controller $C_o(z)$ adopted the PI controller designed in Chapter 4. The frequency domain based repetitive controller for PWM rectifier is plugged in as an additional controller with the existing PI controller.

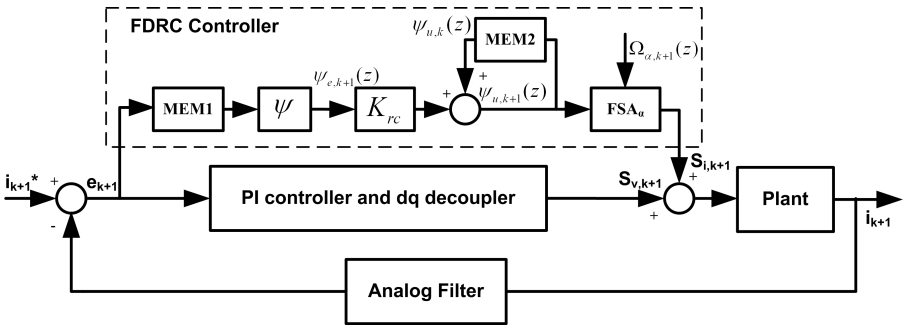

Figure 6.2: Block diagram of PI controller with a plug-in type frequency domain based repetitive controller.

The frequency component vector of the tracking error e_k and the control

signal u_k is given as,

$$\Omega\left(f(k\Delta T)\right) = \begin{bmatrix} 1 & \cos(6k\Delta T) & \cos(12k\Delta T) \\ & \sin(6k\Delta T) & \sin(12k\Delta T) \end{bmatrix}, \tag{6.17}$$

and the coefficient vector of the tracking error and control signal is written as,

$$\Psi\left(f(k\Delta T)\right) = \begin{bmatrix} R_0 & K_6R_6 & K_{12}R_{12} \\ & K_6I_6 & K_{12}I_{12} \end{bmatrix}^T. \tag{6.18}$$

The modified frequency component vector Ω_α can be obtained by adding the phase delay compensation into (6.17),

$$\Omega_\alpha\left(f(k\Delta T)\right) = \begin{bmatrix} 1 & \cos(6k\Delta T + \alpha_6) & \cos(12k\Delta T + \alpha_{12}) \\ & \sin(6k\Delta T + \alpha_6) & \sin(12k\Delta T + \alpha_{12}) \end{bmatrix} \tag{6.19}$$

where α_6, α_{12} are the phase angle delays caused by the filter and the plant for the 6^{th} and 12^{th} harmonic components, respectively.

Correspondingly, the vector of the learning gain K_{rc} for the 6^{th} and 12^{th} order harmonics is $\begin{bmatrix} K_6 & K_{12} \end{bmatrix}$.

The Bode plot of the close loop transfer function $C_{cl}(z)$ for the conventional PI controller is shown in Fig. 5.3. From the figure, we can see that the maximum system gain $A_c(e^{j\omega})$ is -21dB (0.089) and the phase angle $\theta_c(e^{j\omega})$ is -76.8° at the 6^{th} order harmonics frequency (300 Hz). Also, the system gain $A_c(e^{j\omega})$ is -26.5dB (0.047) and the phase angle $\theta_c(e^{j\omega})$ is -97.5° at the 12^{th} order harmonics frequency (600 Hz).

The advantage of the frequency domain based repetitive controller is to provide the flexibility of designing different learning gains and phase angle delay compensations individually for each harmonic component. Assuming the frequency of

the variation ω_1 in (6.9) is ten times smaller than the first learning frequency component f_c (300 Hz), so the parameter ς is 0.38. According to the stability condition (6.14) with the variation consideration ($\epsilon = 0.1$), the range of the learning gain K_6, K_{12} for 300 Hz and 600 Hz can be obtained,

$$K_6 < \frac{0.38 \times 0.9}{0.089} = 3.83; \tag{6.20}$$

$$K_{12} < \frac{0.38 \times 0.9}{0.047} = 7.27. \tag{6.21}$$

The phase angle delay compensations α_6 and α_{12} are used to compensate the phase lag caused by the low-pass filter and the plant system, so that the repetitive controller can provide the control signal $S_{i,k}$ with the proper phase shift to cancel the corresponding current error. Based on the equation (6.16), the phase angle delay compensations α_6 and α_{12} can be designed as 103.2° (1.80 rad) and 82.5° (1.43 rad), respectively.

In this hybrid control scheme, the linear PI controller provides majority of the control efforts during the transient stage. Once the system enters the steady state, the frequency domain based repetitive controller takes over the control effort and tries to reduce the steady state tracking error from cycle to cycle. Therefore, the 6^{th} and 12^{th} order harmonics in the currents i_d^p, i_q^p, i_d^n and i_q^n can be removed.

6.3 Experimental Validation

To verify the feasibility of the proposed control scheme, the experiments were conducted under the unbalanced and distorted supply voltage conditions. The complete control scheme was implemented on a dSPACE platform (DS1104) with

Table 6.1: Control Parameters used in Frequency Domain Based Repetitive Controller

Parameters	Value	Parameters	Value
K_6	3	K_{12}	6
α_6	1.8 *rad*	α_{12}	1.4 *rad*

10 kHz sampling rate. The switching frequency is 20 kHz. The system parameters used in the experimental platform are summarized in Table 6.1.

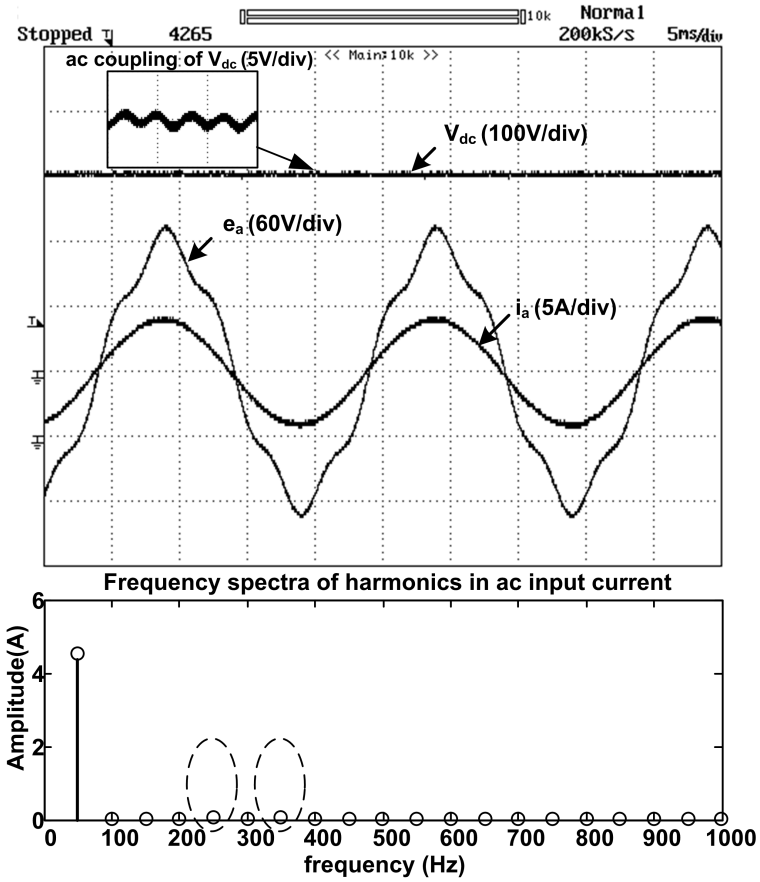

Figure 6.3: Experiment results of dc link voltage and ac line side current with FDRC controller when the supply voltage is distorted with 10% 5^{th} order harmonics.

Fig. 6.3 shows the performance of the PWM rectifier with the proposed hybrid frequency domain based repetitive control scheme when 10% of the 5^{th} order harmonic voltages are injected in the supply voltages. Without using FDRC scheme

as shown in Fig. 5.5 in Chapter 5, the distorted supply voltages cause 5^{th} and 7^{th} order harmonics in the supply side line currents to be 20.00% and 4.90%, respectively. The total harmonics distortion (THD) factor of the phase a input current is 21.09%. When the plug-in frequency domain based repetitive controller is activated, the current harmonics are reduced significantly as can be seen in Fig. 6.3. From the frequency spectra of the harmonics in the supply side line currents, we can see that the 5^{th} order harmonic component decreases from 20.00% to 0.96% and 7^{th} order harmonics is from 4.95% to 0.57%, and the THD factor of the supply line side current is reduced from 21.09% to 4.12%.

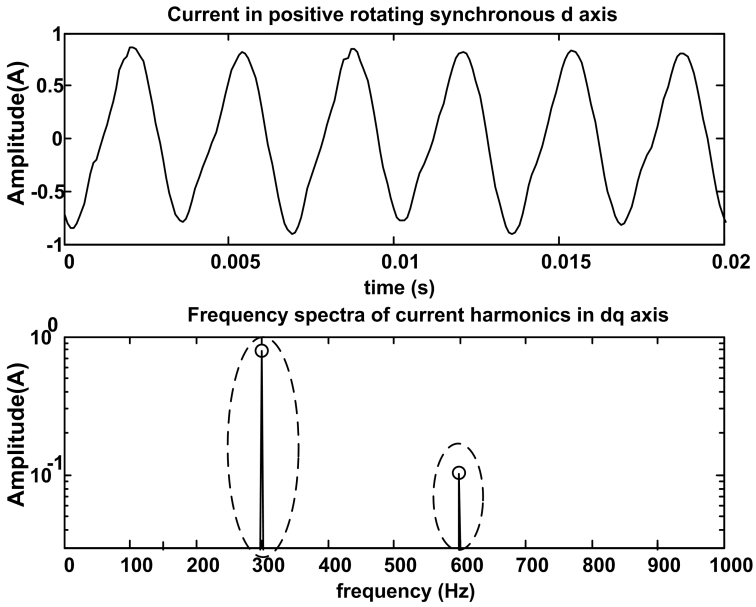

Figure 6.4: Experimental results of the current i_d^p and its frequency spectra without RC scheme.

Figs. 6.4-6.7 show experimental results of the steady state current i_d^p in the positive rotating synchronous d-q frame and the frequency spectra of this current without and with the repetitive controller. Before using any repetitive controller, there are obvious 6^{th} (300 Hz) and 12^{th} (600 Hz) order harmonics in the current i_d^p, that are caused by the distorted supply voltages. From Fig. 6.4, we can see that the amplitude of the 6^{th} and 12^{th} order harmonic components are 0.7891 A and 0.1025

A, respectively. By using TDRC scheme, the amplitude of the 6^{th} and 12^{th} order harmonic components have been significantly reduced, the 6^{th} order harmonics is reduced from 0.7891 A to 0.1253 A, and the 12^{th} order harmonics is reduced from 0.1025 A to 0.0315 A. The THD factor of the supply line side current for phase-a is decreased from 21.09% to 5.27%.

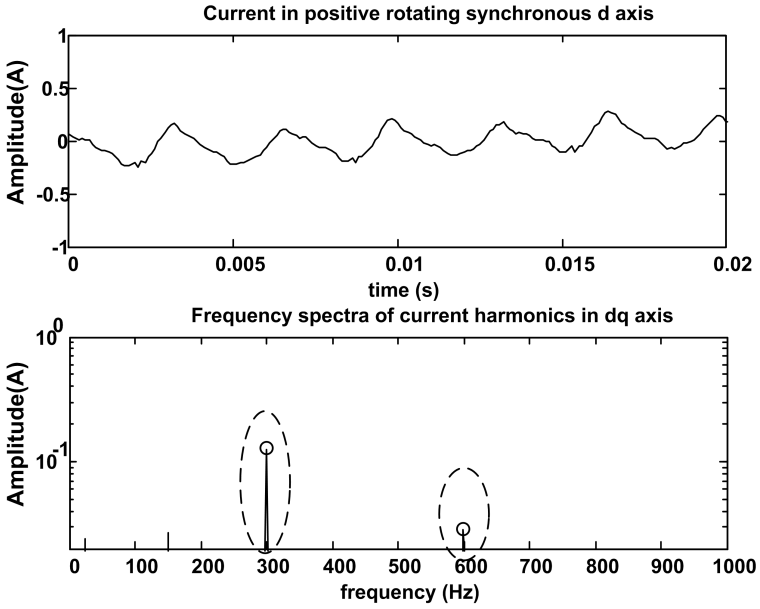

Figure 6.5: Experimental results of the current i_d^p and its frequency spectra with TDRC scheme.

Once FDRC scheme is applied to eliminate the 300 Hz and 600 Hz frequency components, the harmonics in the current i_d^p can be further trimmed down. Fig. 6.6 and Fig. 6.7 show the results by using FDRC scheme with the learning frequency at 300 Hz and at 300 Hz, 600 Hz, respectively. With only learning 300 Hz frequency component as shown in Fig. 6.6, FDRC scheme can suppress the 6^{th} order harmonic component from 0.789 A to 0.0501 A, but the amplitude of the 12^{th} order harmonic component is still quite high, 0.0788 A. In order to get the better tracking performance, both 300 Hz and 600 Hz should be learned in FDRC scheme. The results in Fig. 6.7 shows the 6^{th} order harmonics is 0.0434 A, much smaller as compared to that without RC scheme, 0.7891 A, and that with TDRC scheme, 0.1253 A, and

the 12^{th} order harmonics also can be reduced from 0.1025 A (without RC scheme) to 0.0311 A. The total harmonic distortion (THD) of the phase a supply line side current is decreased from 21.09% to 4.12% by using FDRC scheme.

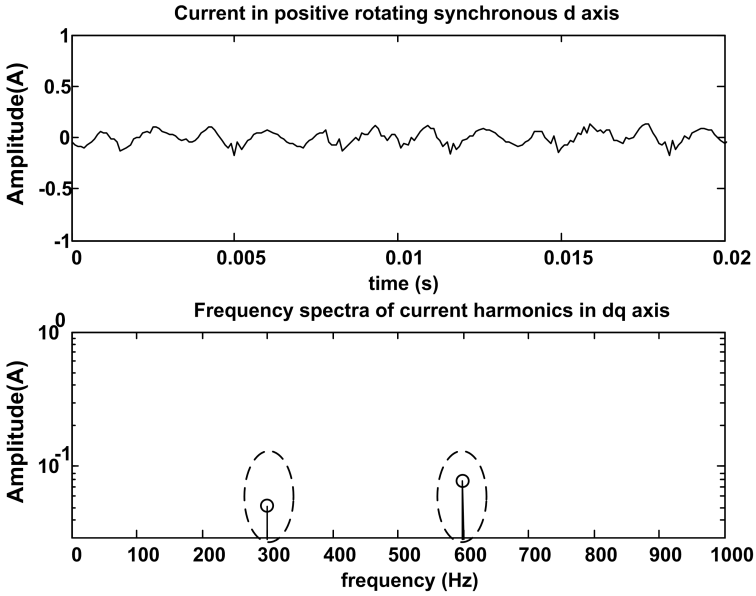

Figure 6.6: Experimental results of the current i_d^p and its frequency spectra with FDRC scheme to learn 300Hz component.

Fig. 6.8 shows the transient response of the error convergence for the i_q^p current control loop with the different repetitive control scheme plugged in. Due the limitation on the stability condition, the maximum safe value for the learning gain K_{rc} is around 0.5 by using TDRC scheme. While the learning gain for FDRC scheme can be chosen for the individual learning frequency component. Hence, the learning gain K_6 for 300 Hz frequency harmonics can be selected at 3, and the learning gain K_{12} can be 6 according to the condition (6.20). Fig 6.8 verifies that FDRC scheme provides much shorter convergence time, which only takes 100ms, as compared that the current error needs 800ms to converge with TDRC scheme plugged in.

In practice, the unbalanced and distorted supply voltages often occur. The

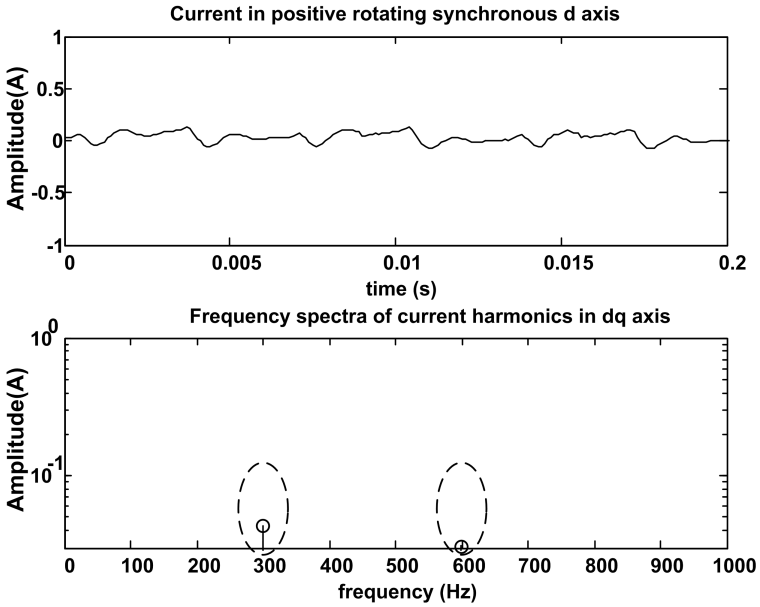

Figure 6.7: Experimental results of the current i_d^p and its frequency spectra with FDRC scheme to learn 300Hz and 600Hz component.

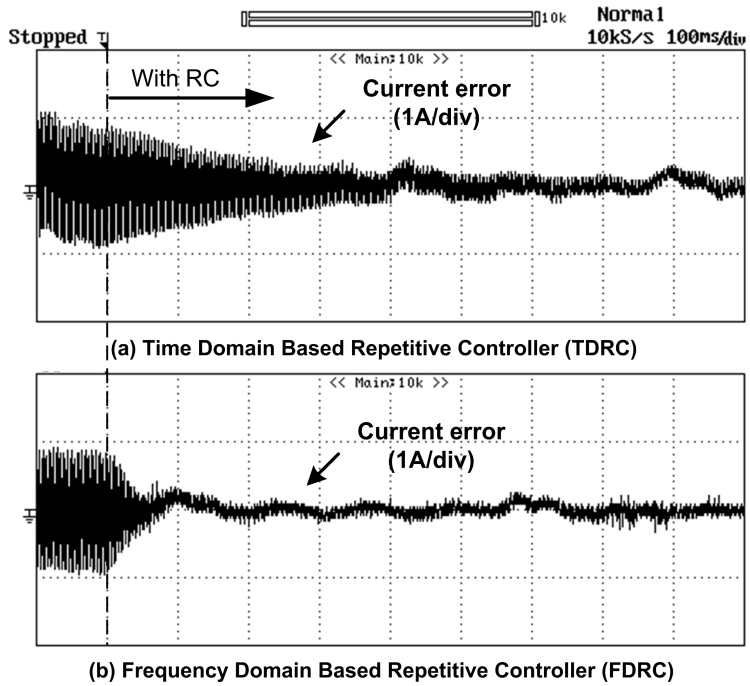

Figure 6.8: Experiment transient response of error convergence with TDRC scheme and FDRC scheme plugged in.

controller should be ensured to eliminate the even-order harmonics at the dc link voltage and the odd-order harmonics in the supply side line currents. The following experiments show the test results of three phase PWM AC-DC voltage source converter with the proposed hybrid control scheme under unbalanced and distorted supply conditions.

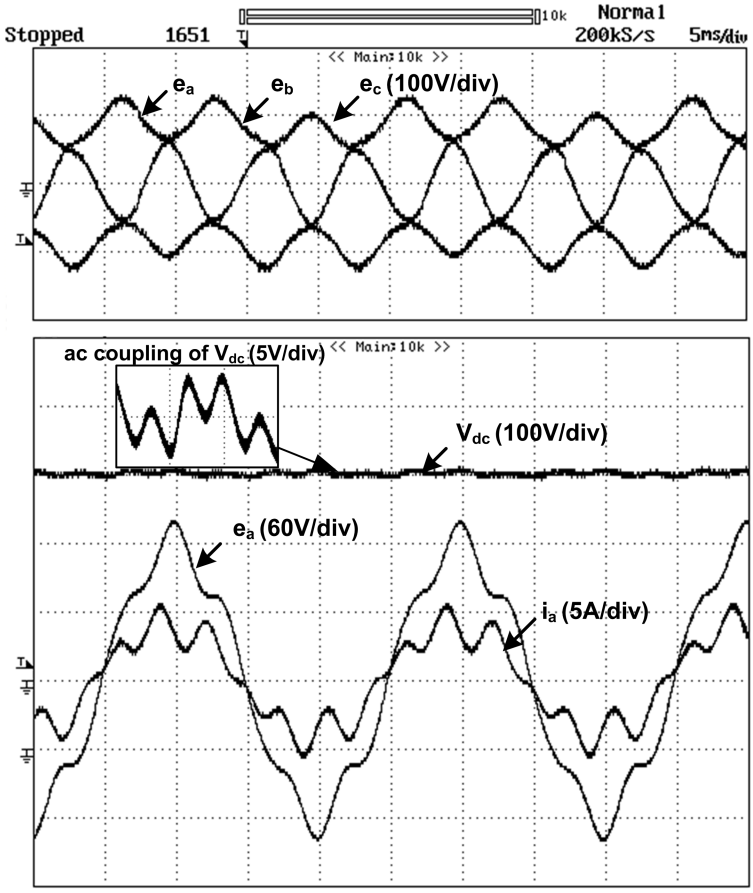

Figure 6.9: Experiment results of dc link voltage and ac line side current by using a conventional single frame controller.

Figs. 6.9-6.11 compare the performance of the PWM rectifier by using the conventional single frame, the dual rotating *d-q* frame without and with the hybrid frequency domain based repetitive control scheme when 10% of the 5^{th} order harmonic voltages are injected in the balanced supply voltages and the amplitude of phase *c* drops by 20 V from 113 V to 93 V. With the single frame controller,

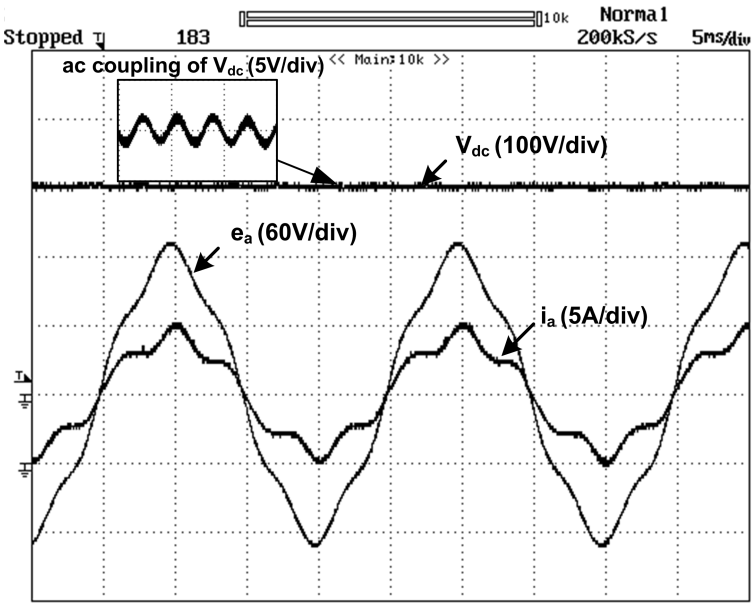

Figure 6.10: Experiment results of dc link voltage and ac line side current by using a dual rotating *d-q* frame controller.

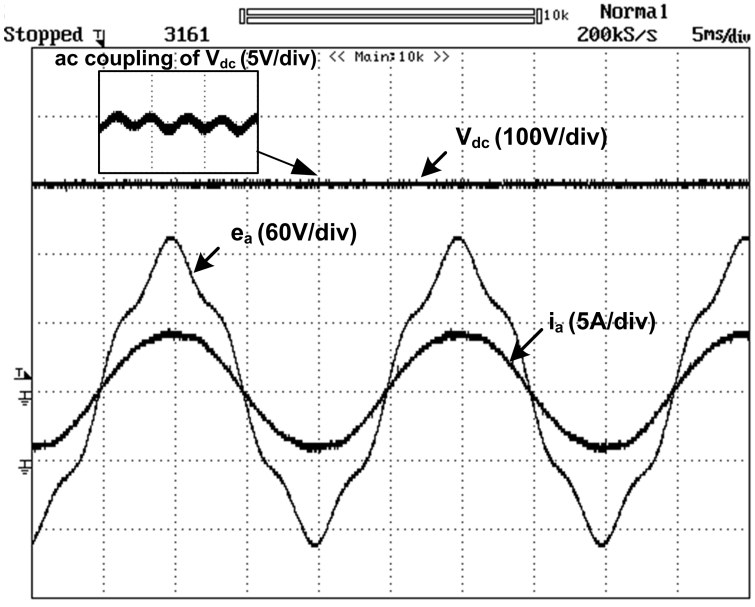

Figure 6.11: Experiment results of dc link voltage and ac line side current by using a dual rotating frame controller with FDRC scheme.

the ripple of the dc link voltage is 2.5% and THD factor of the ac line side current is 29.03% as shown in Fig. 6.9. When the dual rotating frame controller is implemented, we can see from Fig. 6.10 that the ripple component in v_{dc} is reduced from 2.5% to 1.0%. Although the ac line side currents are still distorted, the THD factor of the line side current is decreased from 29.03% to 16.68%. After using FDRC scheme in the dual frame controller as shown in Fig 6.11, the performance of three phase PWM rectifier has been improved further. The ripple at the dc link voltage has been reduced from 2.5% by using the single frame controller to 0.5% by using the dual frame controller with FDRC scheme. The ac line side current is almost sinusoidal and the THD factor of the line side current with FDRC scheme in the dual frame controller, is quite small, 5.93%, in comparison with the line side current THD with the single frame controller, 29.03%.

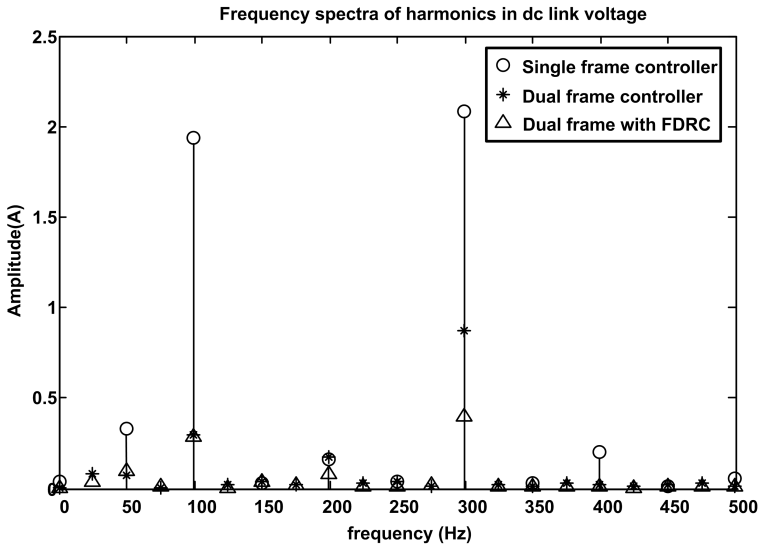

Figure 6.12: Frequency spectra of harmonics at dc link voltage by using the three different control schemes.

Figs. 6.12-6.13 show the frequency spectra of harmonics in dc link voltage and ac line side current by using the three different control schemes. As shown in Fig. 6.12, by using the dual frame controller, the even-order harmonics at dc link voltage which is caused by the unbalanced supply voltages have been significantly

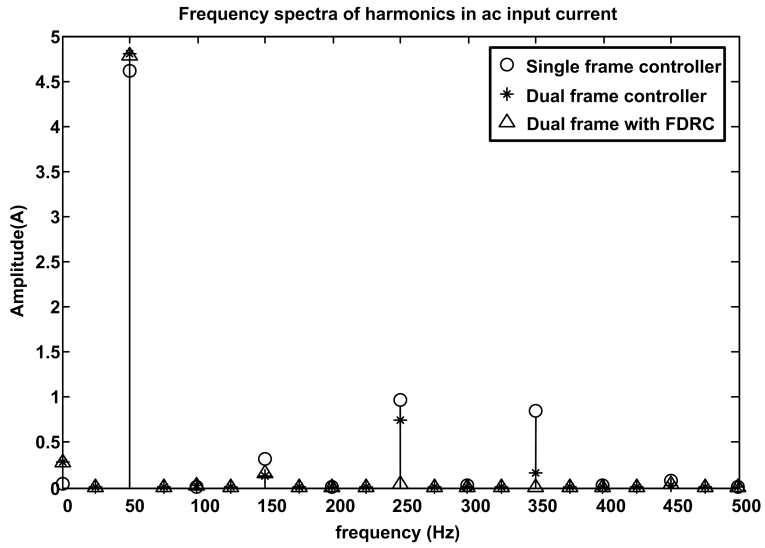

Figure 6.13: Frequency spectra of harmonics in ac line side current by using the three different control schemes.

reduced, 2^{nd} (100 Hz) order harmonics from 1.941V with the single frame controller to 0.3 V and 6^{th} (300 Hz) order harmonics from 2.08 V to 0.8714 V. When the FDRC scheme is plugged into the dual frame controller, the components of each frequency harmonics have been further reduced. From Fig. 6.13, we can see that the harmonics in the line side current have been decreased by using the dual frame controller with FDRC scheme. The amplitude of the 5^{th} and 7^{th} order harmonic components with FDRC scheme in the dual frame are much smaller, 0.04707 A and 0.0168 A, respectively, as compared to 0.9681 A and 0.8462 A obtained from the single frame controller.

Therefore, it can be concluded that the plug-in frequency domain based repetitive controller in the dual rotating frame can minimize the harmonics at the dc link voltage and in the supply side currents under the distorted and unbalanced supply voltage operating conditions as compared to the conventional controller.

6.4 Summary

In this chapter, a frequency domain based repetitive control scheme is proposed as a plug-in controller for the three phase PWM AC-DC voltage source converters to eliminate the dc link voltage ripples and the supply side current harmonics under the distorted and unbalanced supply voltage conditions. Since the control task of the three phase PWM boost rectifier has been divided into *voltage harmonics control* and *current harmonics control* under the generalized supply conditions, a plug-in frequency domain based repetitive current controller (FDRC) scheme, is employed as *current harmonics control* scheme by using Fourier series approximation (FSA) method. The learning algorithm of FDRC scheme designed in frequency domain gives the freedom of choosing different learning gains and phase angle delay compensation individually for each harmonic component, which leads to the improved tracking performance for the supply side line currents. The experimental results verify that the ripple at the dc link voltage can be reduced from 2.5% to 0.5% and the THD of the line side current can be improved from 29.03% to 5.93% with the insertion of the plug-in frequency domain based repetitive controller in the dual rotating frame.

Chapter 7

Conclusions and Future Works

This chapter concludes the thesis. It briefly restates the motivation of the thesis work, the identified problem areas and the various findings in each problem area. Finally, it shows the the direction of future research in this regard.

7.1 Conclusions

This thesis covers work done on development of a high-performance control scheme for three phase PWM AC-DC voltage source converter under the unbalanced and distorted supply voltage conditions. This AC-DC voltage source converter can offer several advanced features such as the sinusoidal input current with unity power factor and simultaneous high quality dc output voltage with small size dc side filter. However, all the advantages for the voltage source converter only work with the implicit assumption of the balanced input voltage conditions. Nevertheless, the unbalanced and distorted voltage conditions occur frequently in input supply, particularly in a weak ac system. Under the unbalanced and distorted input voltage

conditions, the performance of three phase PWM AC-DC voltage source converter is deteriorated by the presence of the negative sequence voltage and voltage harmonics. Hence, the even-order harmonics at the dc side voltage and the odd-order harmonics in the ac side currents under the unbalanced and distorted operating conditions would offset several advantages of three phase PWM AC-DC voltage source converters.

In order to guarantee the performance of three phase PWM AC-DC voltage source converters under unbalanced and distorted supply voltage conditions, there are two possible approaches feasible. One approach is to use bulky filters to remove the ripples in the output voltage and input currents. However, it would slow down the dynamic response of the PWM AC-DC voltage source converter and also increase the size of the converter. The other alternative is to use active control schemes to minimize the harmonics so that small size input/output filters can be used and the dynamic response of the PWM rectifier can be ensured. Hence, this approach is more suitable for the high performance application which requires a ripple-free DC output voltage and low THD line side currents with unity power factor operation. Therefore, the major focus of our study is to provide high performance of three phase PWM AC-DC voltage source converters under the unbalanced and distorted operating conditions with the active control solution.

In Chapter 1, a thorough literature review of various active control solution for three phase PWM AC-DC voltage source converter under the unbalanced and distorted operating conditions. Although most of the research works eliminate the harmonics at the dc link voltage under the unbalanced supply voltages by regulating the instantaneous power flow, there are no detailed investigations to explain the

direct relationship between the instantaneous power and the ripples in the dc link voltage. Moreover, few control schemes have been considered to directly deal with the harmonics in the ac line side currents under the unbalanced supply voltages, which can hardly handle the supply current harmonics when the supply voltages are distorted. Hence, this thesis is aimed at developing an active control solution to to eliminate the even-order harmonics at the dc voltage, keep the input ac supply current sinusoidal and maintain the unity power factor and low THD for three phase PWM AC-DC voltage source converter under the distorted and unbalanced supply voltage operating conditions.

It is essential to have a good understanding of the plant before designing a high-performance controller. Detailed modelling of three phase PWM AC-DC voltage source converter in the positive and negative synchronous rotating frames was carried out in Chapter 2. This proposed model can be used to explain that the negative sequence components lead to the even-order harmonics at the dc output voltage and the low frequency odd-order harmonics in the input ac currents under the unbalanced supply voltage conditions. Besides that, the explanations of the appearance of the harmonic component in the input line side currents are given based on the proposed mathematical model under the distorted supply voltages. Moreover, the instantaneous power flow of the complete system can be analyzed by using this mathematical model in the positive and negative synchronous rotating frames. The power flow analysis provides the direct insight into the relationship between the dc link voltage ripple and the second harmonic terms in the instantaneous power and shows the inner link between the odd-order harmonics in the ac line side currents and the even-order harmonics at the dc output voltage. Hence, the performance of three phase PWM AC-DC voltage source converter under the

generalized supply voltages can be improved by power regulation. Finally, the simulation results are provided to validate the proposed model and analysis.

In Chapter 3, the complete control strategy in the positive and negative sequence rotating synchronous *d-q* frames has been described . In order to eliminate the even-order harmonics at the dc link voltage and the odd-order harmonics in the ac line side currents, the control scheme can be divided into two parts, *DC link voltage harmonics control* scheme and *AC line side current harmonics control* scheme. These two parts of control scheme can be implemented by the cascaded dual frame current regulator with a voltage regulator to ensure the performance of the three phase PWM AC-DC voltage source converter. Based on the control objectives and power requirements, the four control laws can be summarized to provide loads with a suitable amount of average power, maintain unity power factor for the utility interface and keep the dc link voltage ripple-free in *DC link voltage harmonics control* scheme. The positive and negative sequence current references i_d^{p*}, i_q^{p*}, i_d^{n*} and i_q^{n*} are generated by solving the set of the equations from these four control laws.

Moreover, the influence on the performance of the whole control scheme of the three independent blocks, *PWM modulation scheme*, *software phase locked loop* and *symmetrical components calculator*, have been discussed. It has been shown analytically that SVPWM scheme provides a 33.3% higher gain than SPWM scheme which would lead to the better dynamic performance. Also, by using the SVPWM scheme, the voltage source converter can operate at 13.4% lower output voltage than SPWM scheme for the same ac input voltage. Therefore, by using the different PWM modulation scheme, the operating range and dynamic performance

of the converter would be different. According to the comparison between the SPWM scheme and the SVPWM scheme, the SVPWM scheme is preferred over the SPWM scheme for three phase PWM AC-DC voltage source converter. In order to assure the correct generation of the reference signals, *software phase locked loop* (SPLL) has been designed to synchronize the phase angle with the positive sequence voltage fast and accurately. The modified scheme has been proposed to decoupled the SPLL system and the current controller so that the stability for the closed-loop system can be guaranteed and the accurate phase angle information can be obtained. In *symmetrical components calculator*, the phase shifting method is used to extract the positive and negative sequence components effectively online. However, the frequency spectrum of the transfer function of this block shows that the phase shifting method introduces the sudden phase changing at at the certain frequencies such as 50Hz, 100Hz, 200Hz, 250Hz, 350Hz and so on, which may cause the instability of the system easily. Nevertheless, the gain at these frequencies of the block *symmetrical components calculator* is very low. Therefore, when we design the current controller, the effect of *symmetrical components calculator* can be neglected.

After introducing the complete control scheme and elaborating the auxiliary function blocks, the cascaded dual rotating frame controller for the three phase PWM AC-DC voltage source converter under the generalized supply voltage conditions has been developed for the purpose of *voltage harmonics control* in Chapter 4. The traditional method and the singular perturbation method have been employed for this cascaded PI controller design. Since the traditional design methodology is depended on a locally linearized plant model, it cannot ensure the performance under the global operating conditions. In addition, the linearized model usually is

very complex so that it is time-consuming task to obtain this model. Therefore, the nonlinear control approach is preferred to analyze the dynamic performance of the three phase PWM AC-DC voltage source converter. The singular perturbation method has been proposed to develop the cascaded rotating *d-q* dual frame control scheme for PWM rectifier. By using this method, two-time-scale motions, namely, fast motion sub-system and slow motion sub-system, are induced in the closed-loop system. To ensure the stability conditions imposed on the fast and slow modes, sufficiently large mode separation rate by selecting the control law parameters, the closed-loop system can achieve the desired output transient performances and it is also insensitive to the nonlinearities of the system and the variations in the parameters.

Also, the experimental test results provided on a 1.6 kVA laboratory based PWM AC-DC voltage source converter validate the performance of the proposed cascaded rotating dual frame controller in Chapter 4. By using the proposed dual rotating *d-q* frame controller, the even-order harmonic component at the dc link voltage and the odd-order harmonic in the supply ac line side currents can be minimized and the supply side power factor can be kept close to unity under the unbalanced supply operating conditions. Moreover, the experimental test results validate that the output instantaneous power directly links with the dc link output voltage. The proposed analysis of the instantaneous power flow of the complete system in Chapter 2 has also been supported with the experimental test results. Finally, the experimental results show that the singular perturbation method provides the improved dynamic response of three phase PWM AC-DC voltage source converter under unbalanced supply voltage conditions by properly designing the time constants for the FMS and SMS of the voltage and current loop.

Based on the analysis of the distorted supply voltages, the predominant voltage harmonics, 5^{th}, 7^{th} and 11^{th}, 13^{th} order harmonics result in the same frequency on the line side currents, which appear as the 6^{th}, 12^{th} order harmonics in the rotating synchronous *d-q* frame. Therefore, *current harmonics control* is mainly to eliminate the 6^{th} and 12^{th} order harmonics in the *d-q* frame line side current. A plug-in time domain based repetitive controller (TDRC) scheme is developed and employed to achieve the low THD line side currents of the three phase PWM AC-DC voltage source converter in Chapter 5. The choice of the repetitive control parameters such as gain K_{rc} and the phase delay compensator N_2 have been made according to the trade-off between the stability and the fast response. The experimental results verify that the proposed plug-in digital repetitive control scheme can minimize the harmonics in the ac line side currents while maintaining the dc link voltage constant.

Since harmonic components in time domain are described as functions of time, the controller learns and updates the system response of an entire cycle point by point. While a repetitive controller designed in the frequency domain needs only to learn and update these two parameters, magnitude and phase. Moreover, FDRC scheme performs like notch filters and learns the selected harmonic frequencies only, so that it avoids the integral operation for high band frequencies which are dominated by noise. It is also easier to calculate the appropriate phase angle compensation for the individual harmonic frequencies where the phase lag is inevitable from the plant and filters. Hence, FDRC scheme is introduced to enhance the robustness of the control system in Chapter 6. A plug-in frequency domain based repetitive current controller (FDRC) scheme, is employed as *current harmonics control* scheme by using Fourier series approximation (FSA) method.

The learning algorithm of FDRC scheme designed in frequency domain gives the freedom of choosing different learning gains and phase angle delay compensations individually for each harmonic component, which leads to the improved tracking performance for the supply side line currents. The experimental results verify that the ripple at the dc link voltage can be reduced from 2.5% to 0.5% and the THD of the line side current can be improved from 29.03% to 5.93% with the insertion of the plug-in frequency domain based repetitive controller in the dual rotating frame.

In all, the main objectives as laid out in Chapter 1 of this thesis have been achieved. The findings of this work have been published in international technical conferences and journals for benefit of the future researchers and users to study three phase PWM AC-DC voltage source converter under the generalized operating conditions. A list of the publications from this thesis work is provided.

7.2 Future Works

For three phase PWM AC-DC voltage source converter modelling, the effect of the unbalanced input impedances has been neglected. In reality, it is difficult to make three phase input impedances always equal. Hence, the model of three phase PWM AC-DC voltage source converter should include the effect of the unbalanced input impedances. Inclusion of the unbalance on the input impedances would require further work on the converter modelling and voltage and current harmonics control algorithm. This study would make the application more practical.

Since wind generation has competitive costs, requires short installation time

and causes low environment impact, the wind power has been chosen as an alternative resource for distributed generation. As the speed of wind is always changing, the output voltage and frequency of the wind turbines cannot remain constant. Generally AC-DC-AC technology is utilized to produce fixed voltage and fixed frequency electricity to the grid. Also, it should to be noted that the DC voltage is desired to boost to the requested value at low wind speeds. Therefore, three phase PWM AC-DC voltage source converter is an ideal solution to connect variable speed wind turbines and to provide the constant DC link voltage. Since the frequency variation may reach 1% [116], the block *software phase locked loop* would be crucial to synchronize the phase angle with the positive sequence supply voltage fast and accurately. Hence, the design of *software phase locked loop* should be improved and the further study would be done on this particular application.

The three phase PWM AC-DC voltage source converter is mostly used for the front-end converter of the VSI-fed induction motor drives. The nature of induction motor drives is a nonlinear load, unlike the resistance connected to the end of the PWM voltage source converter. Hence, the typical VSI-fed induction motor drive needs be connected with three phase PWM AC-DC voltage source converter and various dynamic studies would be conducted to demonstrate the effectiveness of the proposed control scheme.

In the proposed control scheme for three phase PWM AC-DC voltage source converter, three kinds of sensors, such as dc voltage sensor, ac line side current sensors and ac line voltage sensors, are applied to obtain the feedback signal. The possibility to reduce the expensive sensors have been studied especially in the field of motor drive application [117], but the research on the rectifier applications is

still limited. Hence, the investigation of sensorless technique using an observer to replace the input voltage sensors can be considered. This would provide technical and economical advantages to the system, such as simplification, isolation between the power circuit and controller, reliability and cost effectiveness.

All the proposed control algorithms have been tested on a rapid-prototyping system with a high-speed DSP. As it is commercially not feasible to use such an expensive controller for the actual drive system, investigations are necessary for commercially viable, cheaper controllers with similar high-performance. This step is necessary for commercialization of various findings of this thesis work.

Appendix A

Photo of Experimental Setup

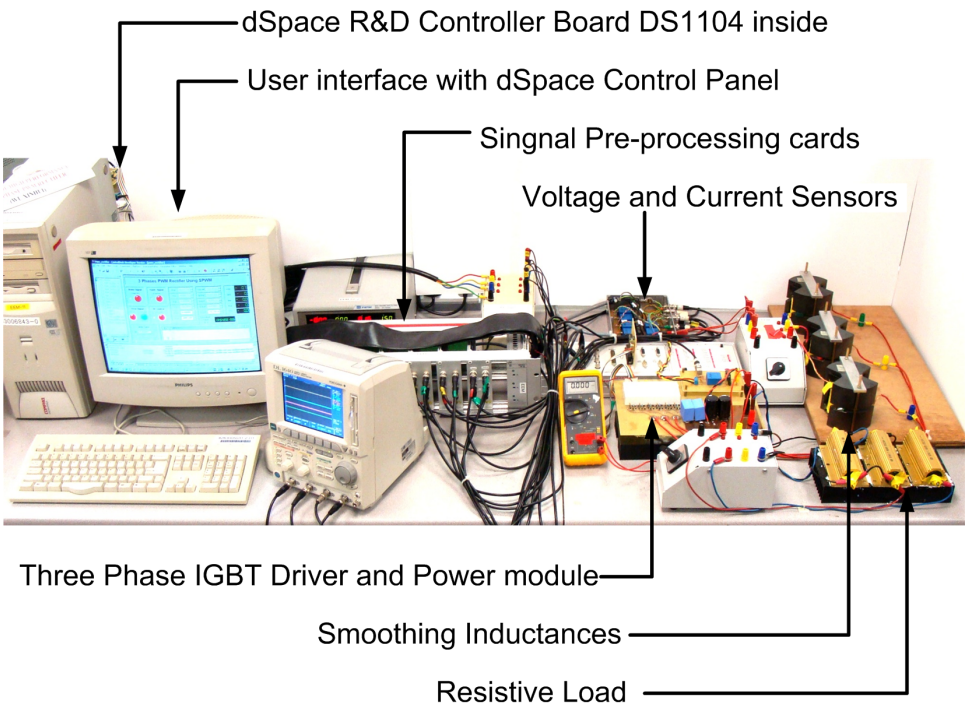

Photo of Experimental Setup

Appendix B

Definition of Symmetrical Components

B.1 Symmetrical Components in Phasors

Unbalanced three phase voltages of the fundamental frequency can be represented by a set of three phase voltages with arbitrary amplitude and phase angle for each phase as shown in the follows.

$$e_a(t) = E_a \sin(\omega t + \theta_e^a) \tag{B.1}$$

$$e_b(t) = E_b \sin(\omega t - 120^\circ + \theta_e^b) \tag{B.2}$$

$$e_c(t) = E_c \sin(\omega t + 120^\circ + \theta_e^c) \tag{B.3}$$

where E_a, E_b, E_c are the different magnitudes and θ_e^a, θ_e^b, θ_e^c are the different phase angles for each phase.

According to symmetrical component theory [87], unbalanced three phase voltages can be expressed as a sum of three sets of positive sequence, negative

sequence and zero sequence components, which are shown as,

$$\begin{aligned} e_a(t) &= e_a^p + e_a^n + e_a^o \qquad \text{(B.4)} \\ &= E^p \sin(\omega t + \theta_e^p) + E^n \sin(\omega t + \theta_e^n) + E^o \sin(\omega t + \theta_e^o) \\ e_b(t) &= e_b^p + e_b^n + e_b^o \qquad \text{(B.5)} \\ &= E^p \sin(\omega t - 120^\circ + \theta_e^p) + E^n \sin(\omega t + 120^\circ + \theta_e^n) + E^o \sin(\omega t + \theta_e^o) \\ e_c(t) &= e_c^p + e_c^n + e_c^o \qquad \text{(B.6)} \\ &= E^p \sin(\omega t + 120^\circ + \theta_e^p) + E^n \sin(\omega t - 120^\circ + \theta_e^n) + E^o \sin(\omega t + \theta_e^o) \end{aligned}$$

where E^p, E^n, E^o and θ_e^p, θ_e^n, θ_e^o are the different amplitudes and phase angles for the positive, negative and zero sequence components of the three phase system, respectively.

In order to derive the relationship between a set of unbalanced voltages in (B.1)-(B.3) and sequential components in (B.4)-(B.6), phase of *abc* voltages and sequential components are introduced and defined as the followings.

$$\begin{aligned} \bar{e}_a &= E_a \angle \theta_e^a \qquad \text{(B.7)} \\ \bar{e}_b &= E_b \angle \theta_e^b \qquad \text{(B.8)} \\ \bar{e}_c &= E_c \angle \theta_e^c \qquad \text{(B.9)} \\ \bar{e}_a^p &= E^p \angle \theta_e^p \qquad \text{(B.10)} \\ \bar{e}_a^n &= E^n \angle \theta_e^n \qquad \text{(B.11)} \\ \bar{e}_a^o &= E^o \angle \theta_e^o \qquad \text{(B.12)} \end{aligned}$$

In [87], the phasors of symmetrical components $\bar{e}_a^p$, $\bar{e}_a^n$, $\bar{e}_a^o$ are calculated from

the phasors of three phase supply voltages $\bar{e}_a$, $\bar{e}_b$, $\bar{e}_c$ using the relationship shown in (B.13).

$$\begin{bmatrix} \bar{e}_a^p \\ \bar{e}_a^n \\ \bar{e}_a^o \end{bmatrix} = \frac{1}{3} \begin{bmatrix} 1 & \tau & \tau^2 \\ 1 & \tau^2 & \tau \\ 1 & 1 & 1 \end{bmatrix} \begin{bmatrix} \bar{e}_a \\ \bar{e}_b \\ \bar{e}_c \end{bmatrix} \tag{B.13}$$

where the complex phasor $\tau = e^{-j120^\circ}$.

B.2 Symmetrical Components in Time Domain

A general asymmetrical three phase voltage (B.1)-(B.3) can be written as the sum of two complex conjugated terms,

$$e_a(t) = \bar{e}_a e^{j\omega t} + \bar{e}_a^* e^{-j\omega t} \tag{B.14}$$

$$e_b(t) = \bar{e}_b e^{j\omega t} + \bar{e}_b^* e^{-j\omega t} \tag{B.15}$$

$$e_c(t) = \bar{e}_c e^{j\omega t} + \bar{e}_c^* e^{-j\omega t} \tag{B.16}$$

This way to link the signals in the time domain to the corresponding phasors can be used in the symmetrical components,

$$e^p(t) = \bar{e}_a^p e^{j\omega t} + \bar{e}_a^{p*} e^{-j\omega t} \tag{B.17}$$

$$e^n(t) = \bar{e}_a^n e^{j\omega t} + \bar{e}_a^{n*} e^{-j\omega t} \tag{B.18}$$

$$e^o(t) = \bar{e}_a^o e^{j\omega t} + \bar{e}_a^{o*} e^{-j\omega t} \tag{B.19}$$

Replacing the relationship in (B.13), the equations (B.17)-(B.19) can be

rewritten as,

$$\begin{aligned} e^p(t) &= \frac{1}{3}(\bar{e}_a e^{j\omega t} + \bar{e}_a^* e^{-j\omega t}) + \frac{1}{3}\left(\alpha\bar{e}_b e^{j\omega t} + (\alpha\bar{e}e_b)^* e^{-j\omega t}\right) \\ &\quad + \frac{1}{3}\left(\alpha^2\bar{e}_c e^{j\omega t} + (\alpha^2\bar{e}_c)^* e^{-j\omega t}\right) \qquad \text{(B.20)} \\ e^n(t) &= \frac{1}{3}(\bar{e}_a e^{j\omega t} + \bar{e}_a^* e^{-j\omega t}) + \frac{1}{3}\left(\alpha^2\bar{e}_b e^{j\omega t} + (\alpha^2\bar{e}_b)^* e^{-j\omega t}\right) \\ &\quad + \frac{1}{3}\left(\alpha\bar{e}_c e^{j\omega t} + (\alpha\bar{e}_c)^* e^{-j\omega t}\right) \qquad \text{(B.21)} \\ e^o(t) &= \frac{1}{3}(\bar{e}_a e^{j\omega t} + \bar{e}_a^* e^{-j\omega t}) + \frac{1}{3}\left(\bar{e}_b e^{j\omega t} + (\bar{e}_b)^* e^{-j\omega t}\right) \\ &\quad + \frac{1}{3}\left(\bar{e}_c e^{j\omega t} + (\bar{e}_c)^* e^{-j\omega t}\right) \qquad \text{(B.22)} \end{aligned}$$

In the equation (B.20), the terms related to phase-b can be derived as,

$$\begin{aligned} \alpha\bar{e}_b e^{j\omega t} + (\alpha\bar{e}_b)^* e^{-j\omega t} &= \bar{e}_b e^{j\omega t - 120^\circ} + \bar{e}_b^* e^{-j\omega t + 120^\circ} \\ &= E_b \sin(\omega t - 120^\circ + \theta_e^b - 120^\circ) \\ &= S_{120}\left[e_b(t)\right] \end{aligned} \qquad \text{(B.23)}$$

where S_x stands for a x-degree phase-shift operator in the time domain.

Using the same method, the equations (B.20)-(B.22) can be revised as,

$$e_a^p(t) = e_a(t) + S_{120}\left[e_b(t)\right] + S_{240}\left[e_c(t)\right] \qquad \text{(B.24)}$$

$$e_a^n(t) = e_a(t) + S_{240}\left[e_b(t)\right] + S_{120}\left[e_c(t)\right] \qquad \text{(B.25)}$$

$$e_a^o(t) = e_a(t) + e_b(t) + e_c(t) \qquad \text{(B.26)}$$

Appendix C

Clark Transformation Matrix and Park Transformation Matrix

Clark Transformation matrix is used to convert the variables in the three phase *a-b-c* frame to the stationary *α-beta* frame.

Usually, line-to-line voltage is more preferred than a phase voltage to measure. *Clark Transformation* matrix for line-to-line voltages instead of phase voltages is shown as the following.

$$\begin{bmatrix} e_\alpha \\ e_\beta \end{bmatrix} = \sqrt{\frac{2}{3}} \begin{bmatrix} \frac{1}{2} & -\frac{1}{2} \\ -\frac{\sqrt{3}}{2} & -\frac{\sqrt{3}}{2} \end{bmatrix} \begin{bmatrix} e_{ab} \\ e_{bc} \end{bmatrix} \tag{C.1}$$

The inverse form becomes,

$$\begin{bmatrix} e_{ab} \\ e_{bc} \end{bmatrix} = \sqrt{\frac{2}{3}} \begin{bmatrix} \frac{3}{2} & -\frac{\sqrt{3}}{2} \\ -\frac{3}{2} & -\frac{\sqrt{3}}{2} \end{bmatrix} \begin{bmatrix} e_\alpha \\ e_\beta \end{bmatrix} \tag{C.2}$$

Using the assumption of zero neutral current, i.e., $i_a + i_b + i_c = 0$, *Clark Transformation matrix* for this case is found to be,

$$\begin{bmatrix} i_\alpha \\ i_\beta \end{bmatrix} = \sqrt{\frac{2}{3}} \begin{bmatrix} \frac{3}{2} & 0 \\ \frac{\sqrt{3}}{2} & \sqrt{3} \end{bmatrix} \begin{bmatrix} i_a \\ i_b \end{bmatrix} \tag{C.3}$$

And the inverse form is,

$$\begin{bmatrix} i_a \\ i_b \end{bmatrix} = \sqrt{\frac{2}{3}} \begin{bmatrix} 1 & 0 \\ -\frac{1}{2} & \frac{\sqrt{3}}{2} \end{bmatrix} \begin{bmatrix} i_\alpha \\ i_\beta \end{bmatrix} \tag{C.4}$$

Park Transformation matrix is used to obtain the variables in the synchronous rotating *d-q* frame from the stationary *α-beta* frame, so that the fixed frequency ω sinusoidal waveform in the time domain can be expressed as the constant value in the synchronous rotating *d-q* frame with the speed ω.

For the unbalanced three phase system, the phasor diagram is described in Fig. C.1. The phasors in the stationary *α-beta* frame can be separated into the positive sequence phasor and the negative sequence phasor. These two phasors can be converted into the positive and negative synchronous rotating *d-q* frame using *Park Transformation*, respectively, as shown in Fig. C.1.

To get the positive sequence components in the positive synchronous rotating *d-q* frame, *Park Transformation* matrix can be found as,

$$\begin{bmatrix} e_d^p \\ e_q^p \end{bmatrix} = \begin{bmatrix} \cos\omega t & \sin\omega t \\ -\sin\omega t & \cos\omega t \end{bmatrix} \begin{bmatrix} e_\alpha^p \\ e_\beta^p \end{bmatrix} \tag{C.5}$$

The inverse format is,

$$\begin{bmatrix} e_\alpha^p \\ e_\beta^p \end{bmatrix} = \begin{bmatrix} \cos\omega t & -\sin\omega t \\ \sin\omega t & \cos\omega t \end{bmatrix} \begin{bmatrix} e_d^p \\ e_q^p \end{bmatrix} \tag{C.6}$$

The negative sequence components in the negative synchronous rotating *d-q* frame can be obtained by using *Park Transformation* matrix shown as,

$$\begin{bmatrix} e_d^n \\ e_q^n \end{bmatrix} = \begin{bmatrix} \cos\omega t & -\sin\omega t \\ \sin\omega t & \cos\omega t \end{bmatrix} \begin{bmatrix} e_\alpha^n \\ e_\beta^n \end{bmatrix} \tag{C.7}$$

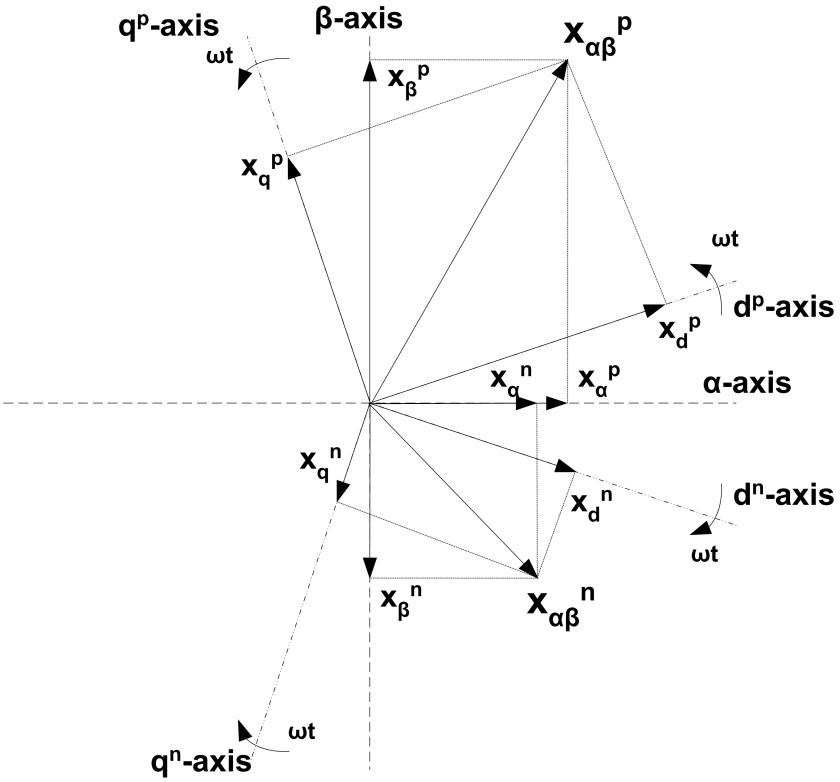

Figure C.1: Phasor diagram of the unbalanced three-phase variables.

The inverse format is,

$$\begin{bmatrix} e_\alpha^n \\ e_\beta^n \end{bmatrix} = \begin{bmatrix} \cos\omega t & \sin\omega t \\ -\sin\omega t & \cos\omega t \end{bmatrix} \begin{bmatrix} e_d^n \\ e_q^n \end{bmatrix} \tag{C.8}$$

Appendix D

Expressions of Average Active and Reactive Power with Symmetrical Components

Under balanced operating conditions, the sum of three-phase instantaneous active powers is constant having the value equal to the sum of average active power of each phase. However, when the converter operates under unbalanced operating conditions the sum of three-phase instantaneous active power becomes oscillatory. Finally, this oscillation of the instantaneous active power in the three-phase converter leads to the harmonic generation at the dc link output and ac input side. Therefore, it is extremely important to understand the characteristic of the instantaneous active power flow under unbalanced operating conditions, particularly in a synchronous frame because the control law is implemented in a synchronous frame.

In order to find the interpretation of the instantaneous active power in a synchronous frame, the concept of complex power is introduced, as defined to be the product of a input voltage space vector and the conjugate of current space

vector as shown in the equation (D.1).

$$S^{in} = E_s^{in} I_s^{in*} \tag{D.1}$$

E_s^{in} and I_s^{in} are the complex expressions of the input voltage and the input current in rotating synchronous *d-q* frame, by employing Clark Transformation and the positive and negative sequence Park Transformation,

$$E_s^{in} = e^{j\omega t}(e_d^p + je_q^p) + e^{-j\omega t}(e_d^n + je_q^n) \tag{D.2}$$

$$I_s^{in} = e^{j\omega t}(i_d^p + ji_q^p) + e^{-j\omega t}(i_d^n + ji_q^n) \tag{D.3}$$

After replacing E_s^{in} and I_s^{in}, the instantaneous active power is obtained to be identical to the real part of the complex power in the equation (D.1).

$$\begin{aligned} P^{in} &= Real\{S^{in}\} \\ &= P_o^{in} + P_{s2}^{in}\sin(2\omega t) + P_{c2}^{in}\cos(2\omega t) \\ &= e_d^p i_d^p + e_q^p i_q^p + e_d^n i_d^n + e_q^n i_q^n \\ &\quad +(e_d^p i_q^n - e_q^p i_d^n - e_d^n i_q^p + e_q^n i_d^p)\sin(2\omega t) \\ &\quad +(e_d^p i_d^n + e_q^p i_q^n + e_d^n i_d^p + e_q^n i_q^p)\cos(2\omega t) \end{aligned} \tag{D.4}$$

It can be seen from (D.4) that the real part of the complex power consists of three kinds of terms such as constant term, $\cos(2\omega t)$ term and $\sin(2\omega t)$ term. The constant terms P_o^{in} stands for the actual average power delivered to the dc link assuming that the power dissipation within a converter is modelled and effectively added to the values of ac side resistors. It is also noted that the negative sequence components of both input voltage and current contribute to useful constant terms of input power independently. The oscillating terms of $\cos(2\omega t)$ and $\sin(2\omega t)$ appear because the existence of the negative sequence, which is made of the product of

the negative sequence components and the positive sequence components. The input power is supplied from the unbalanced utility grid, so the resistors or the inductances have no effect on it.

Similarly, at the terminal of the ac side, the complex power can be defined as,

$$S^{out} = U_s^{in} I_s^{in*} \tag{D.5}$$

where

$$\begin{aligned} U^{in} &= e^{j\omega t} U_{dq}^{p} + e^{-j\omega t} U_{dq}^{n} \\ &= e^{j\omega t}(e_{dq}^{p} - Ri_{dq}^{p} - j\omega L i_{dq}^{p}) + e^{-j\omega t}(e_{dq}^{n} - Ri_{dq}^{n} - j\omega L i_{dq}^{n}) \end{aligned}$$

In the equation (D.5), all the variables are the expressions in the form of the space vector.

Replacing and expanding the output power equation (D.5) also yields constant terms P_o^{out}, $\sin(2\omega t)$ terms P_{s2}^{out} and $\cos(2\omega t)$ terms P_{c2}^{out}, as follows.

$$\begin{aligned} P^{out} &= Real\{S^{out}\} \\ &= P_o^{out} + P_{s2}^{out}\sin(2\omega t) + P_{c2}^{out}\cos(2\omega t) \\ &= [(e_d^p i_d^p + e_q^p i_q^p + e_d^n i_d^n + e_q^n i_q^n) \\ &\quad -(Ri_d^{p^2} + Ri_q^{p^2} + Ri_d^{n^2} + Ri_q^{n^2})] \\ &\quad +[(e_d^p i_q^n - e_q^p i_d^n - e_d^n i_q^p + e_q^n i_d^p) \\ &\quad +(2Ri_q^p i_d^n - 2Ri_d^p i_q^n + 2\omega L i_q^p i_q^n + 2\omega L i_d^p i_d^n)]\sin(2\omega t) \\ &\quad +[(e_d^p i_d^n + e_q^p i_q^n + e_d^n i_d^p + e_q^n i_q^p) \\ &\quad -(2Ri_q^p i_q^n + 2Ri_d^p i_d^n - 2\omega L i_q^p i_d^n + 2\omega L i_d^p i_q^n]\cos(2\omega t) \end{aligned} \tag{D.6}$$

Comparing with the equations (D.4) and (D.6), it shows that the constant terms only is consumed by the resistors, and the terms P_{s2}^{out} and P_{c2}^{out} are affected by the inductances and resistors. Since the oscillating components of the output instantaneous power are the dominating cause to generate harmonics, the instantaneous power consumed by inductance should be used to eliminate P_{s2}^{out} and P_{c2}^{out} by compensating the oscillating terms P_{s2}^{in} and P_{c2}^{in}.

It is natural to expect that the imaginary part of the complex power represents the instantaneous reactive power since the real part of the complex power has been proved to be the instantaneous active power. This argument is true as long as the three phase system is under balanced operating conditions. When operating condition becomes unbalanced, the imaginary part of the complex power doesn't represent the instantaneous reactive power any more [71]. To solve this problem, a new kind of complex power based on the quadrature voltage is introduced. T^{in} referred as a quadrature complex power is defined to be the product of a quadrature voltage space vector, which is the original voltage phase delayed by 90°, and the conjugate of current space vector as shown in the equation (D.7).

$$T^{in} = E_s'^{in} I_s^{in*} \tag{D.7}$$

where a quadrature voltage space vector $E_s'^{in}$ is defined as the following.

$$E_s'^{in} = -je^{j\omega t}(e_d^p + je_q^p) + je^{-j\omega t}(e_d^n + je_q^n) \tag{D.8}$$

Manipulating 90° phase-delay corresponds to a 90° backward rotation of space vector in its own rotating synchronous frame. Therefore, the positive sequence components are rotated 90° in a clockwise and the negative sequence components are rotated in a counter-clockwise.

Substituting $E_s'^{in}$ (D.8) and I_s^{in} (D.3) into T^{in} (D.7), the real part of the

quadrature complex power corresponds to the instantaneous reactive power.

$$\begin{aligned} Q^{in} &= Real\{T^{in}\} \\ &= Q_o^{in} + Q_{s2}^{in}\sin(2\omega t) + Q_{c2}^{in}\cos(2\omega t) \\ &= -e_d^p i_q^p + e_q^p i_d^p + e_d^n i_q^n - e_q^n i_d^n \\ &\quad +(e_d^p i_d^n + e_q^p i_q^n + e_d^n i_d^p + e_q^n i_q^p)\sin(2\omega t) \\ &\quad +(-e_d^p i_q^n + e_q^p i_d^n + e_d^n i_q^p - e_q^n i_d^p)\cos(2\omega t) \end{aligned} \tag{D.9}$$

It can be seen from (D.9) that the real part of the quadrature complex power T^{in} consists of three kinds of terms such as constant term, $\cos(2\omega t)$ term and $\sin(2\omega t)$ term. The average input reactive power Q_o^{in} exchanged between the utility source and the rectifier determines the input power factor. The oscillatory components of instantaneous reactive power, which constitute oscillatory components of twice input fundamental frequency, supplied from the unbalanced utility grid.

Similarly, at the terminal of the ac side, the quadrature complex power can be defined as,

$$T^{out} = U_s^{'in} I_s^{in*} \tag{D.10}$$

where

$$\begin{aligned} U_s^{'in} &= -je^{j\omega t}U_{dq}^p + je^{-j\omega t}U_{dq}^n \\ &= -je^{j\omega t}(e_{dq}^p - Ri_{dq}^p - j\omega L i_{dq}^p) + je^{-j\omega t}(e_{dq}^n - Ri_{dq}^n - j\omega L i_{dq}^n) \end{aligned}$$

In the equation (D.10), all the variables are the expressions in the form of the space vector.

Replacing and expanding the output power equation (D.10) also yields constant terms Q_o^{out}, $\sin(2\omega t)$ terms Q_{s2}^{out} and $\cos(2\omega t)$ terms Q_{c2}^{out}, as follows.

$$\begin{aligned}
Q^{out} &= Real\{T^{out}\} \\
&= Q_o^{out} + Q_{s2}^{out}\sin(2\omega t) + Q_{c2}^{out}\cos(2\omega t) \\
&= [(-e_d^p i_q^p + e_q^p i_d^p + e_d^n i_q^n - e_q^n i_d^n) \\
&\quad -(\omega L i_d^{p^2} + \omega L i_q^{p^2} + \omega L i_d^{n^2} + \omega L i_q^{n^2})] \\
&\quad +[(e_d^p i_d^n + e_q^p i_q^n + e_d^n i_d^p + e_q^n i_q^p) \\
&\quad -(2R i_q^p i_q^n + 2R i_d^p i_d^n + 2\omega L i_q^p i_d^n - 2\omega L i_d^p i_q^n)]\sin(2\omega t) \\
&\quad +[(-e_d^p i_q^n + e_q^p i_d^n + e_d^n i_q^p - e_q^n i_d^p) \\
&\quad -(2R i_q^p i_d^n - 2R i_d^p i_q^n + 2\omega L i_q^p i_q^n + 2\omega L i_d^p i_d^n)]\cos(2\omega t) \qquad \text{(D.11)}
\end{aligned}$$

The constant terms, from (D.9) to (D.11) show that the average reactive power loss is across input ac inductors. For the oscillating terms, it is noted from (D.6) and (D.11) that each term of Q_{s2}^{out} is equal to either positive or negative of the corresponding term of P_{c2}^{out}, while each term of Q_{c2}^{out} is equal to either positive or negative of the corresponding term of P_{s2}^{out}. These relationships suggest that the oscillating components of instantaneous active and reactive power have the same absolute magnitude. Once the oscillating component of the instantaneous active power is regulated to zero, then the instantaneous reactive power automatically becomes constant without any oscillating component of twice input frequency.

Appendix E

Hardware Components for Power Converter and Drive Module

E.1 Power Converter

SEMITRANS Standard IGBT modules SKM 22GD123D has been adopted as the three phase IGBT bridge. This IGBT module is suitable for switched mode power supplies, three phase inverters for AC motor speed control and general power switching applications. The pulse frequencies can reach above 15 kHz. The maximum voltage V_{CES} is 1200 V and the maximum collect current I_C is 25 A.

E.2 Driver Module

SEMIDRIVER SKHI 71 sevenpack IGBT and MOSFET driver module has been used as the three phase IGBT bridge drive. The driver module has hybrid components which may directly be mounted to the PCB. Devices for driving, voltage supply, error monitoring and potential separation are integrated in the driver. The

forward voltage of the IGBT is detected by an integrated short-circuit protection, which will turn off the module when a certain threshold voltage is exceeded. In case of short-circuit or too low supply voltage the integrated error memory is set and an error signal is generated. The driver is connected to a controlled +15V supply voltage. The input signal level is 0/5V. Additionally a digitally adjustable interlocking time is generated by the driver, which has to be longer than the turn-off delay time of the IGBT. The connections in between the driver board and the IGBT module are made by wires of twisted pairs.

Appendix F

Micro-Cylindrical Ultrasonic Motor (CUSM) Drive

Cylindrical Ultrasonic Motors (CUSM), is a relatively new kind of piezoelectric actuators, having different characteristics from that of conventional electromagnetic motors. In order to choose the most suitable control variable for speed/position control applications, this research work evaluates the dynamic and steady state performance of the CUSM drive system by using three different control variables, namely, the amplitude, the frequency and the phase difference of the excitation signals. In the single mode control, only one control variable is used while the other two variables are maintained constant. Among the three variables, amplitude control is found to be superior as compared to other control variables. Furthermore, to achieve quick and precise position control, the dual mode control method is proposed in which two control variables are used simultaneously while maintaining the third variable constant. Experiment test results obtained by using a 10mm diameter and 30 mm long CUSM verify that the dual mode control is superior to the single mode control and Amplitude and Frequency control is the best choice for position control application.

F.1 Introduction

The Cylindrical Ultrasonic Motor (CUSM) is a new type of ultrasonic motor (USM), whose stator is made of a monolithic PZT (Lead Zirconate Titanate) tube. Like other types of USM, CUSM has many useful features, such as high torque at low speed, quiet operation, high holding torque, quick response and no EMI problems as there is no magnetic field generation [119]. Moreover, because of its cylindrical construction, the size of CUSM can be reduced further, even to less than one millimeter in diameter.

Since USM has many special features, usually not available in normal electromagnetic type of motors, it has drawn particular attentions from the mechatronics field. Recently, the USMs have been applied for direct drive actuators in articulated robots and accurate position control of machine tools. All of these applications require quick response and precise position control. So far, there have been several attempts to control speed/position of ring-type USM refer to Izumi[120], Senjyu[121], [122], Lin[123]. However, since the motor is driven by ultrasonic vibration of piezoelectric elements, its mathematical model is difficult to obtain, therefore no accurate model of USM is available as of now. For this reason, it is difficult to design model based position controller. Alternatively, many position control schemes based on model free control, such as neural networks [122], and fuzzy logic [123] have been proposed for ring-type USM.

As one type of rotary USM, CUSM has almost the same operating characteristics as ring-type USM. However, due to the different construction of its stator, the motion in CUSM is generated by the bending vibration of its stator PZT tube

[124]. Wang et al. [125] presents the work on speed controller of CUSM, but the scope is limited to single mode control with amplitude as the control variable only. In this thesis, single and dual modes control are evaluated in order to find the control variable to get the best performance for every application.

First, because of CUSM's unique structure, Section F.2 shows its operating characteristics and driving circuit. Next, the single mode control with amplitude, frequency and phase difference as control variables are described in Section F.3. In this part, by changing one control variable at a time while keeping the other two variables fixed, the dynamic and steady state performances of CUSM are evaluated and compared, respectively, for speed regulation and speed tracking application. In order to achieve quick and precise position control, the dual mode control is proposed in Section F.4. Similarly, the performance of Amplitude and Frequency control and Amplitude and Phase difference control are evaluated for position regulation and tracking. Finally, the experimental results are presented and summarized in Section F.5.

F.2 Structure and Driving Circuit

A CUSM mainly consists of a PZT stator tube, which goes through the center of the shaft of the motor, as shown in Fig. F.1. One brass cap is fixed at each end of the PZT tube. As frictional force generation is the key criteria between the stator and rotor, the spring and nut are screwed onto the rotor to provide the pre-load.

The construction of the motor is almost similar to the one used in [124], except for the material of the stator tube. Monolithic PZT tube has been used in

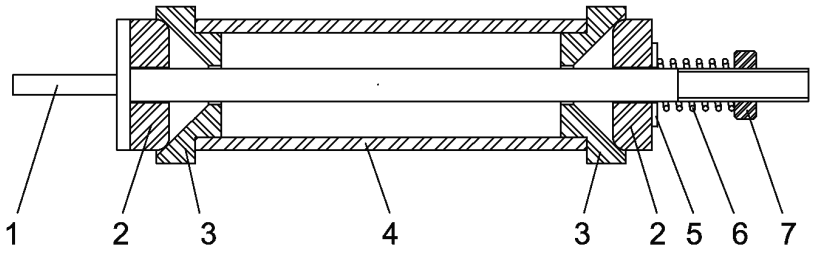

(1) Shaft (2) Rotors (3) Stator caps (4) PZT tube
(5) Washer (6) Spring (7) Nut

Figure F.1: Cross sectional view of CUSM.

our experimental setup instead of a titanium tube [124], in order to produce larger torque. Fig. F.2 shows the actual CUSM with 10mm diameter and 30 mm long. All experiments in this thesis are carried out using this CUSM.

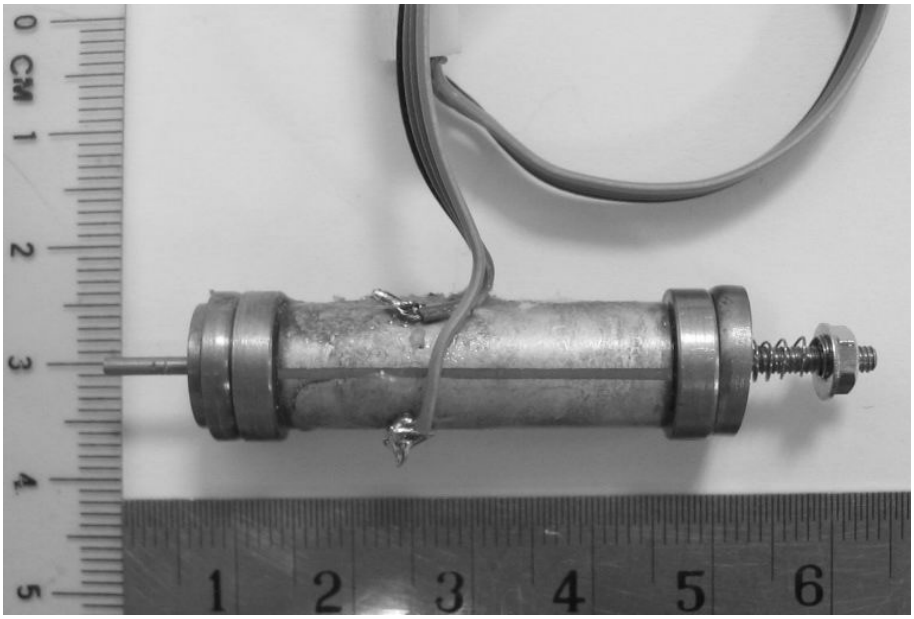

Figure F.2: CUSM for experiment.

The principle of CUSM is different from that of general electromagnetic motors. It is driven by the ultrasonic vibration of the piezoelectric elements on the stator. When the two sinusoid waveforms are applied to the piezoelectric thin film, the vibration is generated in the stator. Finally, the stator pushes against the rotor to start rotation by the frictional force.

Although the accurate model has not been developed yet, an approximated relationship between the angular speed of the motor and input voltage signal for one phase has been reported in [126]. When the phase difference between the two sinusoidal voltage supply is fixed at 90°, the relationship can be expressed as:

$$\omega_{rotor} = \alpha \frac{V_{rms}}{\sqrt{\left[1 - \left(\frac{f}{f_1}\right)^2\right]^2 + \left[2\zeta \frac{f}{f_1}\right]^2}} \tag{F.1}$$

where ω_{rotor} is the angular speed of the rotor in rad/sec, V_{rms} is rms value of the applied sinusoidal voltage in V, α is a constant depending on the inherent properties of the piezoelectric tube, f is the frequency of the applied sinusoidal voltage in Hz, f_1 is the resonant frequency of the stator tube in Hz and ζ is the damping factor within the CUSM system. The equation (F.1) shows that the motor speed can be controlled by the voltage amplitude and frequency of the excited control signal. Besides that, the speed can also be varied by changing the phase difference between two sinusoidal phase voltages.

In order to drive the two phase CUSM, two sinusoidal voltage excitation signals having some specific phase difference should be applied. These two driving voltage signals are generated by a two-phase full-bridge inverter. As every phase is based on a single-phase full-bridge series load resonant inverter, the driving circuits for phase A-A' is equal to for phase B-B'. Fig. F.3 shows the driving circuits for phase A-A' only.

This resonant inverter includes a rectifier and two-phase full bridge-type series load resonant high frequency inverter. The ultrasonic motor, being a capacitive load, is connected in series with the two inductors $L1$ and $L2$ to form a resonant tank. The large external capacitor C is used to cancel the amplitude fluctuation in

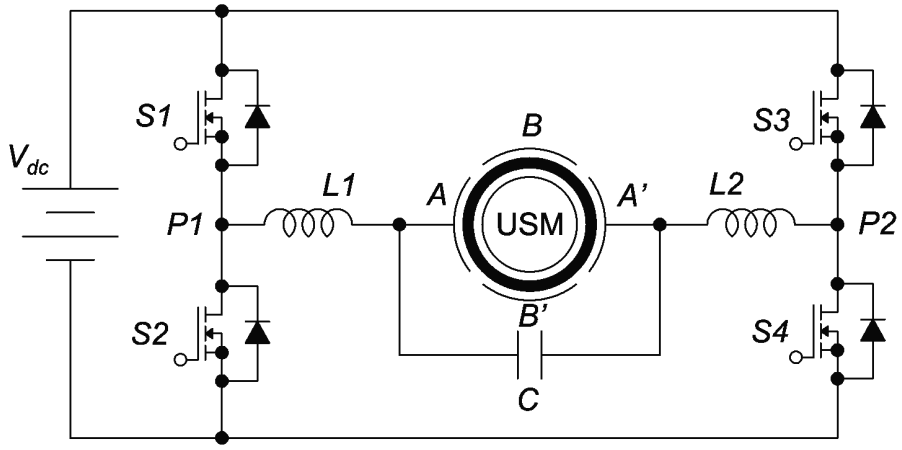

Figure F.3: Driving circuit for phase A-A'.

each phase, as the internal capacitance of the CUSM varies with different voltages. The phase A-A' becomes part of the resonant circuit, which works as a Low-Pass Filter (LPF) that filters out high frequency components and noise of the square voltage signal across $P1$ and $P2$. However, because of the effect of the LPF, the fundamental sinusoidal voltage amplitude is not proportional to the interval of the switching signal, which decides the duty cycle in the PWM scheme, so we can use an inverse sine function to make input-output relationship linear [125].

F.3 Single Mode Control

Due to the highly non-linear characteristics of the CUSM, it is difficult to obtain an accurate mathematical model of the motor. Therefore, in order to choose the most suitable control variable for speed/position control application, a simple Proportional-Integral-Derivative (PID) controller has been applied. Table F.1 gives the parameters for the CUSM drive system.

As described in Section F.2, we can adjust the voltage amplitude, driving

Table F.1: Experimental Parameters of CUSM Drive System

Parameters	Value
DC-Link Voltage	12 V
CUSM Resonant Frequency	44.6 kHz
Sampling Frequency	2,000 Hz
Encoder Resolution	5,000 pulses/rev.

frequency and phase difference of two sinusoidal voltage waveforms applied to the motor terminals to control its speed/position. Fig. F.4 gives the closed-loop speed/position control scheme to exert the three different strategies.

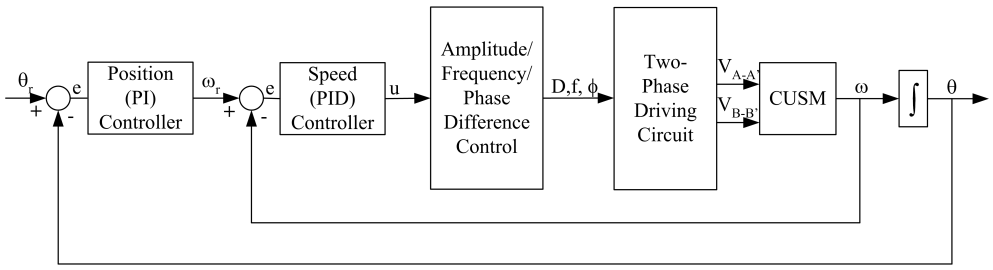

Figure F.4: Single mode speed/position control scheme.

Fig. F.4 shows a Proportional-Integral (PI) position controller with a PID speed controller used as the inner loop. The position output of the CUSM is measured by an incremental rotary encoder and the speed feedback signal is calculated by numerically differentiating the position readings. Then, the measured position signal is compared to a setpoint position reference value to generate the speed reference ω_r, as the input to the speed loop. The speed error e is used to compute the control output u. The digital speed/position controller takes PID discrete-time

form [118]:

$$u(k) = u(k-1) + K\Big[e(k) - e(k-1) + \tfrac{T}{T_I}e(k) + \tfrac{T_D}{T}(e(k) - 2e(k-1) + e(k-2))\Big] \tag{F.2}$$

where K is the proportional gain, T_I is the integral time constant, T_D is the derivative time constant and T is the sampling period. The parameters K, T_I and T_D are determined by trial-and-error method. In our case, K, T_I and T_D are fixed for a given reference signal.

For the single mode control, there are three possible strategies, Case I: Amplitude Control, Case II: Frequency Control, Case III: Phase Difference Control. In every strategy, only one variable is changed, while keeping the other two variables fixed. In Case I, the absolute value of u goes through the inverse sine function as described in Section F.2 to give the actual duty cycle D. In Case II, according to [127], there is hysteresis phenomenon observed at the vicinity of resonant frequency. Fig.F.5 shows the frequency hysteresis phenomenon of this cylindrical motor. The solid line denotes the relationship between speed and frequency when the frequency increase from 41kHz to 49kHz, in contrast, the dash line is obtained when the frequency is reduced from 49kHz to 41kHz. Therefore, it is better to limit the command of the motor for frequencies above the resonant frequency f_s (44.6 kHz) in order to avoid the aforementioned phenomenon. In Case III, the phase difference can be varied from $-90°$ to $90°$ according to the sinusoidal relationship between speed and phase difference [119].

Similarly, u can also be used to decide the direction of rotation by controlling the phase difference ϕ between the two driving voltage [125]. When u is positive,

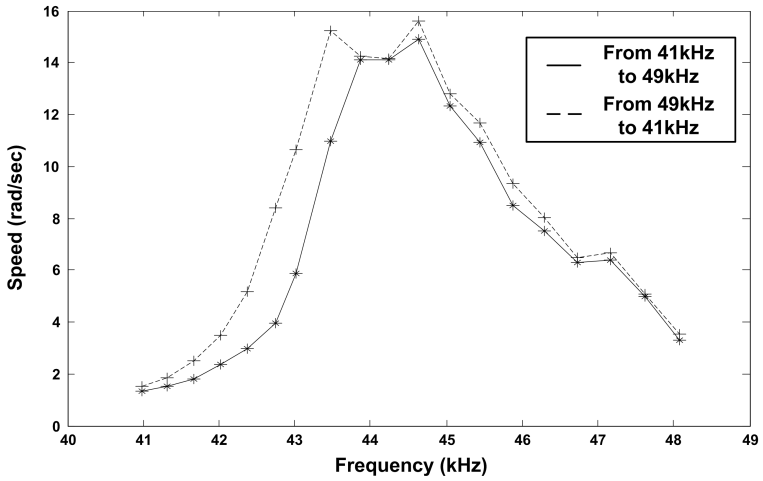

Figure F.5: Frequency hysteresis phenomenon.

ϕ varies from $0°$ to $90°$, the motor rotates clockwise; when u is negative, ϕ varies from $-90°$ to $0°$, the motor rotates anti-clockwise. Next, the comparison among the three strategies for speed regulation and speed tracking will be presented.

F.3.1 Speed Regulation

Fig. F.6 shows the speed response for a step-change in speed command of 10 rad/sec when the system is operated under closed-loop speed control using the three different control parameters individually. We can see that the actual speed is almost kept at the reference level. The rise times are about 0.06 seconds and the overshoot can be kept below 2% for the three cases. The zoomed steady state responses are also shown in Fig. F.6. Comparing with frequency control, the ripples using amplitude and phase difference control seem relatively smaller. However, it is noted that there is some obvious steady state error when phase difference control is applied.

When the speed command is varied over a wider range, the response of the system is different by applying different control inputs. Table F.2 shows that the

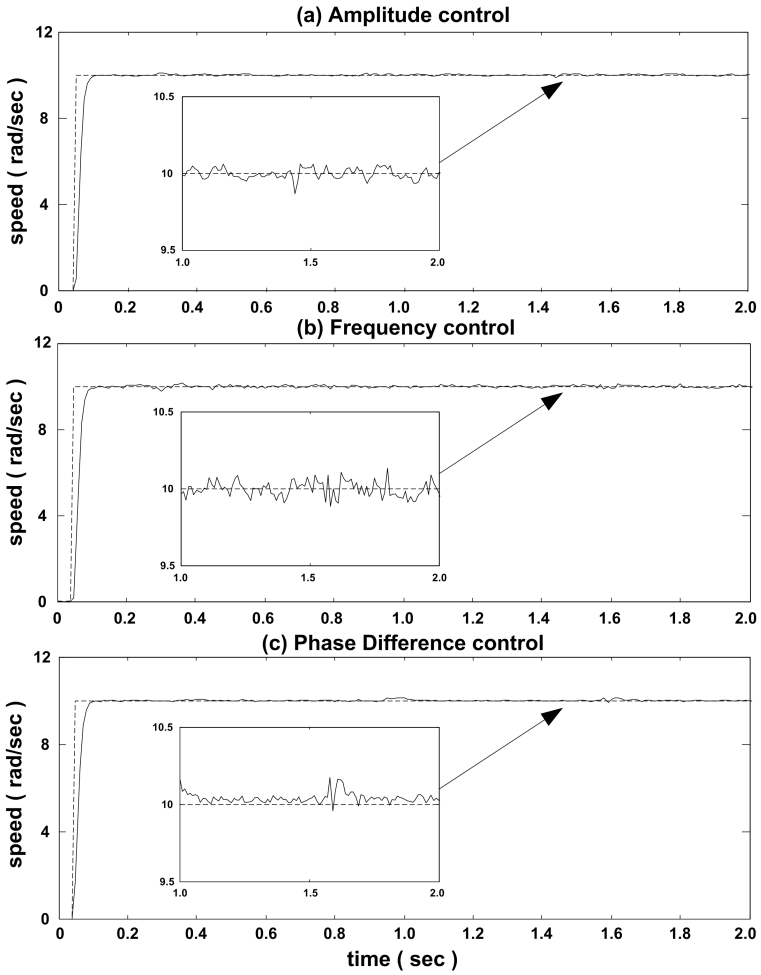

Figure F.6: Speed response at $\omega_r = 10 rad/sec$ by using different parameters (a) amplitude (b) frequency (c) phase difference.

CUSM's peak-to-peak speed ripples at different speeds.

From Table F.2, first, we can conclude that using amplitude and phase difference control, the minimum speed which can be reached is 0.5 rad/sec, but for the frequency control, the CUSM cannot rotate continuously below 1 rad/sec. Furthermore, the ripple using amplitude control is smaller while comparing with the response with the other two control parameters, except at very high speeds. However, when frequency and phase difference control are used at some specific speed, the ripple is small as well. It is also worth pointing that, even though using ampli-

Table F.2: Peak-to-peak Speed Ripple

ω_r(rad/sec)	Percentage of Speed Ripples		
	Amplitude(%)	Frequency(%)	Phase Difference(%)
10	1.10	1.90	1.70
8	1.50	2.50	0.50
4	1.25	1.50	3.75
2	1.50	3.00	5.00
1	2.50	6.00	8.00
0.5	6.00	--	16.00

tude control, the value of the ripples still increases when the CUSM is operating at a relatively low or high speed.

From the above analysis of test results, we can conclude that voltage amplitude is the most suitable control variable for the speed control for CUSM under single mode control.

F.3.2 Speed Tracking

In practice, the reference signal is more likely to change within some range as a function of time rather than being kept constant. In order to compare the tracking performance of the three different control strategies, a sinusoidal waveform is given as reference. We can find that when the controller is tracking a 0.1 Hz, peak value 2π sinusoidal speed reference, the speed error is almost same for the amplitude, frequency and phase difference control. It is basically limited from -1 rad/sec to 1 rad/sec.

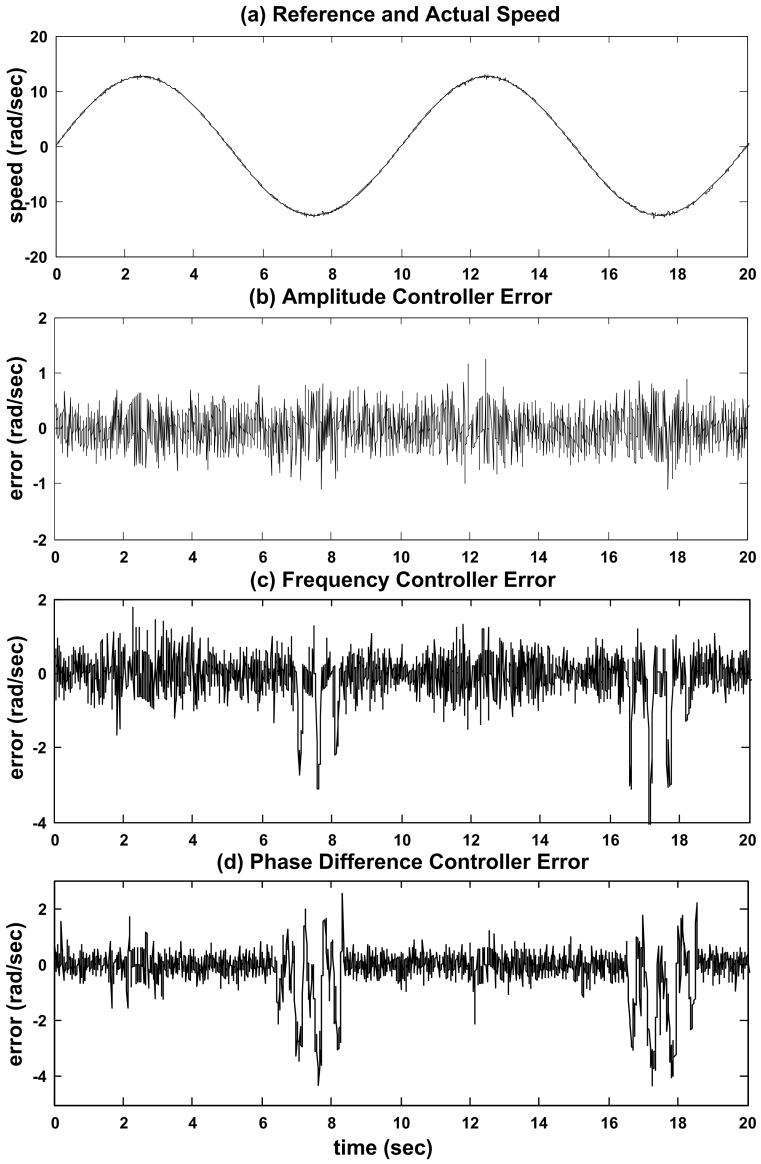

Figure F.7: Tracking speed and error when input is a 0.1 Hz, peak value 4π sinusoidal waveform (a) reference and actual speed (b) amplitude controller error (c) frequency controller error (d) phase difference controller error.

Fig. F.7 gives the speed response and error by controlling each parameter when a 0.1 Hz, peak value 4π sinusoidal speed signal is given as reference. It shows motor construction causes the difference between forward and reverse rotation performance. We can find that the error still can be limited from -1 rad/sec to 1 rad/sec when amplitude control is applied. However, for frequency and phase difference control, the system cannot track the signal very well and the error will become large

as the reference speed is increased to higher value. Therefore, amplitude control variable is preferred for the speed tracking application.

In summary, amplitude is the most suitable control variable for speed regulation/tracking application in the single mode control.

F.4 Dual Mode Control

In the light of the high holding torque characteristics and compactness, CUSM is expected to be used as a position control in industrial application. Therefore, usually we pay more attention to the accurate position control of the system. However, it is difficult to realize the quick and precise control if only amplitude control of applied voltages is used.

Looking at the improved speed control performance with amplitude control as in Section F.3, we apply this control strategy first. However, driving frequency and phase difference also can affect the result. For example, in Fig. F.8, we keep phase difference unchanged at 90°. We can see that when the driving frequency is higher than resonant frequency as Fig. F.8 (a), the system has low gain; the speed is relatively low; the precise position control can be expected, but it has a slow response. In contrast, Fig. F.8 (b) indicates that when the revolving speed is large as driving frequency is set at resonant frequency, the system has a high gain; quick position control can be expected, but it has poor steady state precision. If we keep frequency constant and change phase difference to adjust the speed, the result is the same. It is known that high gain helps the system achieve the commanded position quickly and it requires a low gain for stability purposes. Therefore, it is

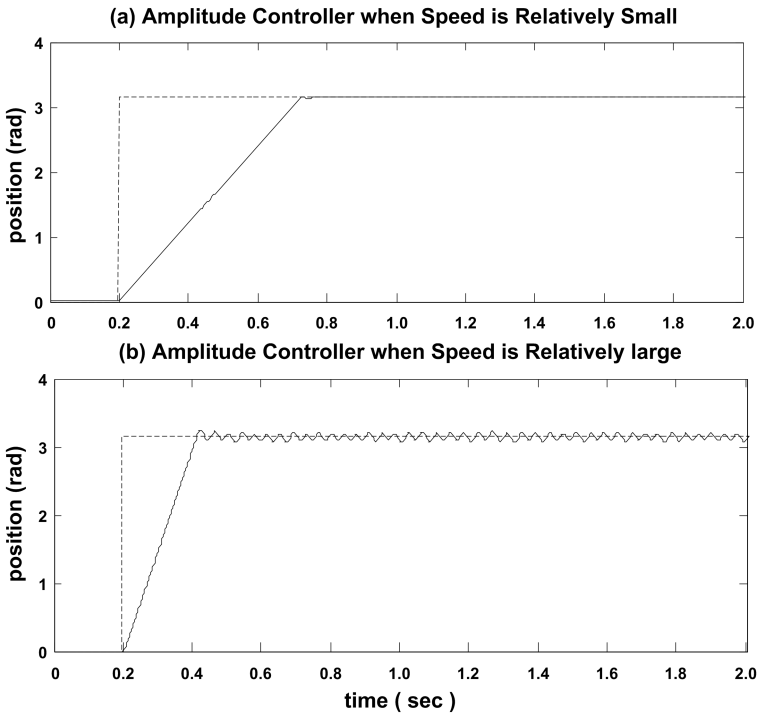

Figure F.8: Position response at difference speed (a) amplitude controller when frequency is higher than resonant value (b) amplitude controller when frequency is at resonant value.

necessary for quick and precision control to use dual mode control, Amplitude and Frequency control or Amplitude and Phase difference control.

Fig. F.9 shows the scheme of the dual mode position control for CUSM. We still adopt a PI controller in order to simplify the control system. The amplitude of applied voltage is based on the output of PI controller. Comparing with the scheme of single mode in Fig. F.4, the comparator is the extra part to decide driving frequency or phase difference. In the comparator, e_{th} is defined as the threshold of the control mode, which has responsibility to determine two values of control mode.

When Amplitude and Frequency control is applied, phase difference is fixed at $+90°$ or $-90°$ according to the direction of rotation of the motor. One control

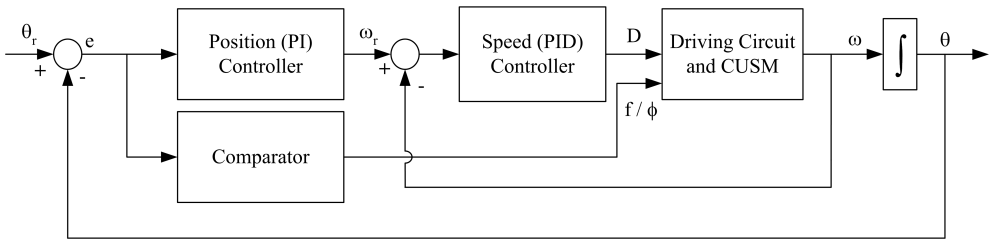

Figure F.9: Dual mode speed/position control scheme.

input, amplitude is determined by PI controller output. Since the motor provides high speed at $f = 44.64$ kHz, low speed at $f = 47.62$ kHz shown in Fig. F.5, the other control input, frequency follows the following rules:

$$\begin{aligned} f &= 44.64 \text{ kHz} \qquad \text{when } e \geq e_{th} \\ f &= 47.62 \text{ kHz} \qquad \text{when } e < e_{th} \end{aligned} \tag{F.3}$$

When Amplitude and Phase difference control is used, driving frequency is fixed at around resonant frequency, 44.64 kHz. The amplitude of applied voltage is decided by the same method. And according to different speed obtained from different phase angle, the control input D is changed as follows:

$$\begin{aligned} |D| &= 90^\circ \qquad \text{when } e \geq e_{th} \\ |D| &= 40^\circ \qquad \text{when } e < e_{th} \end{aligned} \tag{F.4}$$

where the comparator only decides the absolute value of phase difference, while the sign depends on which direction of rotation of the motor.

This system enables combining both the quick response at high speed during the transient period and the precise position control with low speed at steady state.

F.4.1 Position Regulation

Fig. F.10 gives the performance and input of the control system between Amplitude and Frequency control. First, the CUSM has the ability to rotate at high speed. Also, as soon as the position error is less than e_{th}, driving frequency will be adjusted to reduce the motor speed to make sure accurate position control is achieved. In this way, the quick and precise position control can be realized.

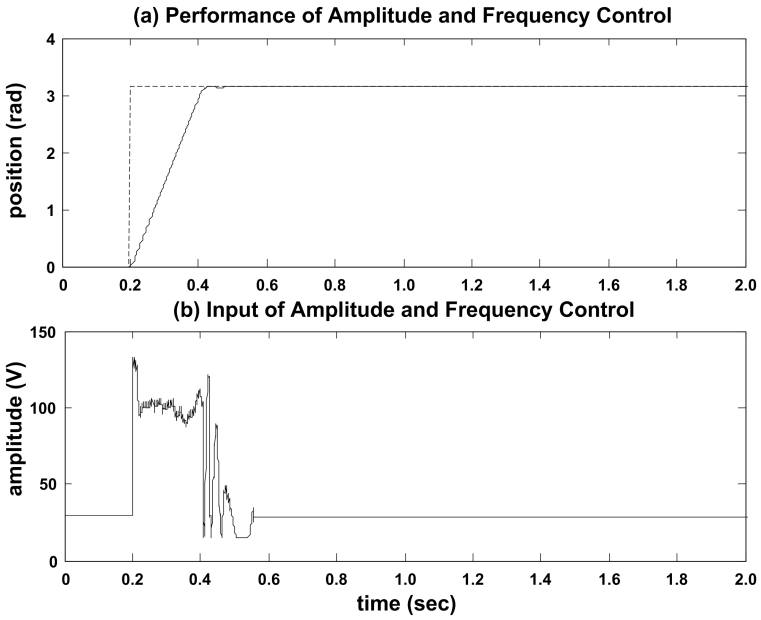

Figure F.10: Performance and input of dual mode control (a) performance of amplitude and frequency control (b) input of amplitude and frequency control.

If the single mode control is applied, if we choose the speed to be high; the rise time is small but the overshoot is a little larger and the rotor oscillates when the gain is high, on the other hand, if the speed is chosen to be low and the rise time increases. However, the dual mode control combines the quick position control at high speed during transient period and the precise position control at low speed during steady state. Comparing with amplitude and phase difference control, amplitude and frequency control has less oscillations. Additionally, the

speed ripple for phase difference control is larger than that for frequency. In other words, the dual mode is superior to the single input control and amplitude and in the dual mode control amplitude and frequency control is the best one in the position regulation application.

Table F.3 shows the details about the difference between Single Mode Control and Dual Mode Control.

Table F.3: Comparison Between Single Mode and Dual Mode

Control Mode		T_r (Sec)	Over-shoot(%)	T_s (Sec)	e_{ss} (10^{-4}%)
Single mode	A	0.214	3.25	3.037	2.87
	B	0.525	0.35	0.529	3.19
	C	0.631	0.43	0.635	0.96
Dual mode	D	0.225	0.50	0.230	2.23
	E	0.226	0.53	0.232	2.87

where T_r is the rise time; T_s is the settling time; e_{ss} is steady state error; A, B and C are single mode control; their driving frequency and phase difference are fixed at 44.64 kHz and 90° for A, 47.62 kHz and 90° for B and 44.64 kHz and 40° for C; D and E are dual mode control; D is Amplitude and Frequency Control and E is Amplitude and Phase Difference Control. It is noted that single mode control here adopts amplitude control.

From Table F.3, it can be seen that if the single input control is applied, when the CUSM runs at high speed such as in Case A, the rise time is much smaller than in Case B and C, but the overshoot is a lot larger and the rotor oscillates around the commanded position, it is not easy to be stabilized, thus, this causes the settling time to be long. On the contrary, the motor speed is low in Case B and C, so

the rise time increases but the overshoot decreases. Therefore, if only using single mode, it cannot achieve the quick and precise position control at the same time.

When the dual mode control is applied like Cases D and E, they seem to combine the quick position control at high speed and the precise position control at low speed, so the rising time in Cases D and E is less than the rising time in Cases B and C; the overshoot is smaller than that in Case A. Furthermore, as they have quick response and do not oscillate, the settling time is smaller than that of single mode, such as Case A, B and C. Comparing with Amplitude and Phase Difference Control, Amplitude and Frequency Control is more stable. Additionally, the speed ripple for phase difference control is larger than that for frequency according to Section F.3.2.

In other words, dual mode control is superior to single mode control. Moreover, in dual mode control, Amplitude and Frequency Control gives better performance in the position regulation application.

F.4.2 Position Tracking

Fig. F.11 shows the actual position response and error of tracking a 0.1 Hz, peak value 2π sinusoidal position reference when single mode control (amplitude control) at different frequency and dual mode control (Amplitude and Frequency Control) are applied, respectively.

According to Fig. F.11 (a), the output can track the reference position smoothly by either single mode control or dual mode control. As shown in Fig. F.11 (b),

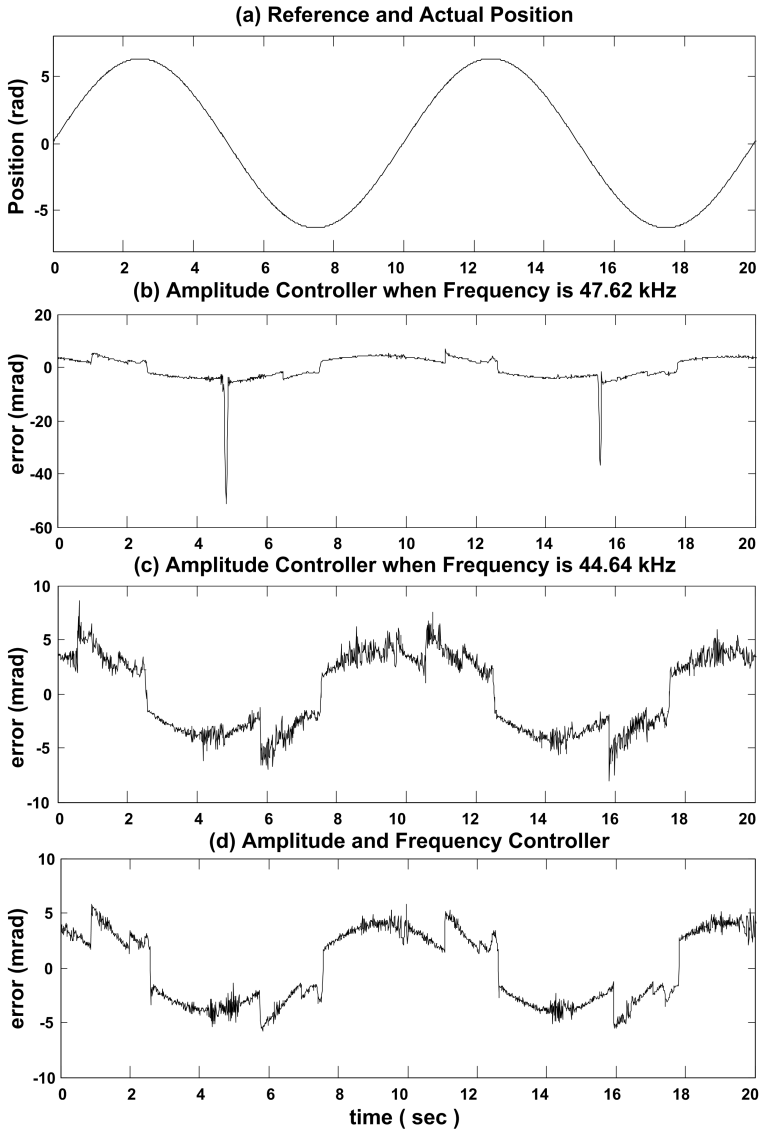

Figure F.11: Tracking position and error when input is a 0.1 Hz, peak value 2π sinusoidal waveform (a) reference and actual position (b) amplitude controller error when frequency is 44.64 kHz (c) amplitude controller error when frequency is 47.62 kHz (d) amplitude and frequency controller error.

we can know that if using amplitude control at high frequency such as 47.62 kHz, that is, the maximum speed is low, there is less oscillation in the system, but it cannot meet high speed requirement. If using amplitude control at low frequency, 44.62 kHz in Fig. F.11 (c), the maximum speed is high, but a lot of oscillation will happen. Conversely, dual mode control in Fig. F.11 (d) takes the advantage of Fig. F.11 (b) and Fig. F.11 (c)'s benefits, thus, the system can manage oper-

ate at high speed and there is not much oscillation with the system. Also, the peak-to-peak value of the error is slightly reduced.

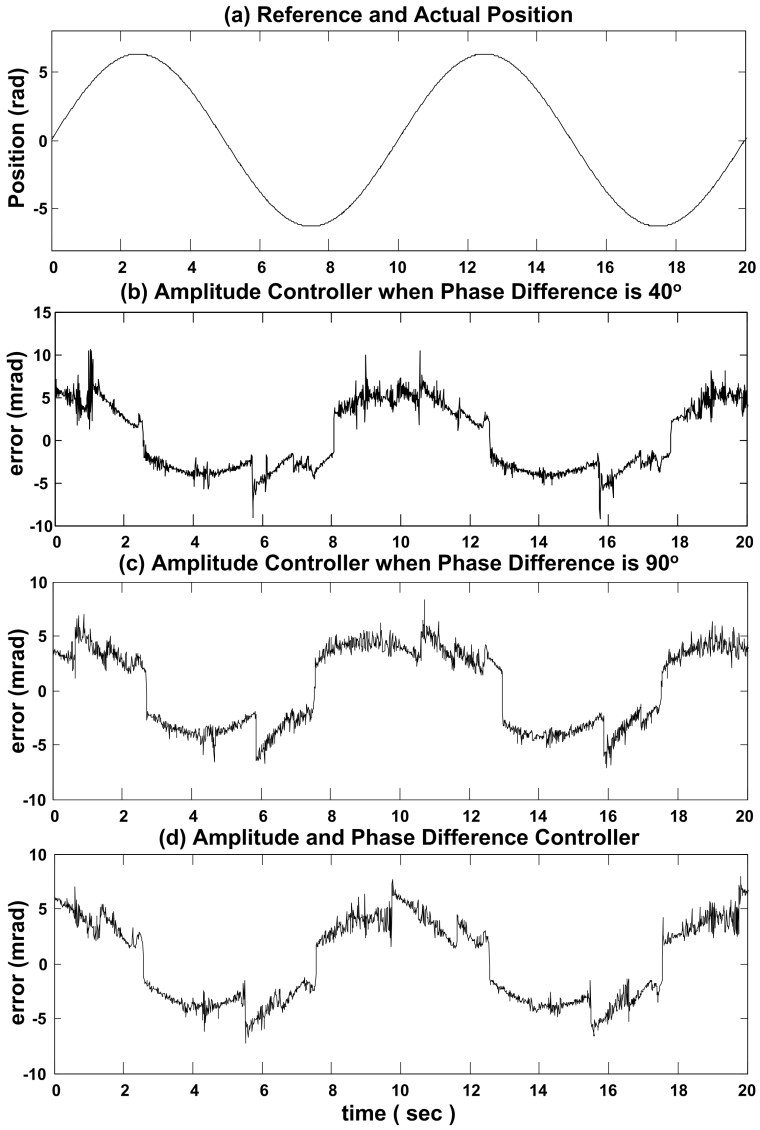

Figure F.12: Tracking position and error when input is a 0.1 Hz, peak value 2π sinusoidal waveform (a) reference and actual position (b) amplitude controller error when phase difference is 40° (c) amplitude controller error when phase difference is 90° (d) amplitude and phase difference controller error.

Fig. F.12 gives the actual position response and error of tracking a 0.1 Hz, peak value 2π sinusoidal position reference when single mode control (amplitude control) at different phase difference and dual mode control (Amplitude and Phase Difference Control) are applied, respectively. It suggests that the performance of

Amplitude and Phase Difference Control is almost same as that of Amplitude and Frequency Control. When using Amplitude and Phase difference control also can achieve high speed operation stably. However, since more ripples exist when phase difference control is applied, it has more oscillations than using Amplitude and Frequency Control.

From all the discussions, we can conclude that amplitude and frequency control is the most suitable control method for the position tracking application.

F.5 Summary

To choose the most suitable control variable for servo applications, namely, speed regulation, speed tracking, position regulation and position tracking, this chapter evaluates the dynamic and steady state position/speed controller performance of the CUSM by using single mode and also dual mode control using the three different control variables. For the single mode control, amplitude control has the best performance for the four different kinds of applications, specially for speed control application. In order to achieve the quick and precise position control, the dual mode control method by using amplitude and frequency control or amplitude and phase difference control is proposed. From the experimental results, it is observed that the dual mode control with amplitude and frequency as control variables is the most suitable strategy for position control of CUSM.

Publications

Published

Conferences

1. X. H. Wu and S. K. Panda, "Position Control of Micro-Cylindrical Ultrasonic Motor," *IEEE IECON 2004*, November, 2004, Korea.

2. X. H. Wu, S. K. Panda, and C. L. Teo, "Servo Control of Micro-Cylindrical Ultrasonic Motor Using Single/Dual Mode Control," *IEEE IECON 2005*, November, 2005, USA.

3. X. H. Wu, S. K. Panda and J. X. Xu, "Development of a New Mathematical Model of Three Phase PWM Boost Rectifier Under Unbalanced Supply Voltage Operating Conditions," *IEEE PESC 2006*, April, 2006, Korea.

4. X. H. Wu, S. K. Panda and J. X. Xu, "Analysis and Control of the Output Instantaneous Power for Three Phase PWM Boost Rectifier Under Unbalanced Supply Voltage Conditions," *IEEE IECON 2006*, November, 2006, France.

5. X. H. Wu, S. K. Panda and J. X. Xu, "Analysis and Experimental Validation of the Output Voltage and Input Current Performances in Three Phase

PWM Boost Rectifiers Under Unbalanced Supply Voltage Conditions," *Invited Paper, CCA 2007*, October, 2007, Singapore.

6. X. H. Wu, S. K. Panda and J. X. Xu, "Effect of Pulse-Width Modulation Schemes on the Performance of the Three-Phase Voltage Source Converter," *IEEE IECON 2007*, November, 2007, Taiwan.

7. X. H. Wu, S. K. Panda and J. X. Xu, "Supply-side Current Harmonics Control of Three Phase PWM Boost Rectifiers under Distorted and Unbalanced Supply Voltage Conditions," *IEEE PEDS 2007*, November, 2007, Thailand.

8. X. H. Wu, S. K. Panda, and J. X. Xu, "Design of a Plug-in Frequency Domain Based Repetitive Current Controller for Three Phase PWM Boost Rectifier Under Distorted and Unbalanced Supply Voltages," *IEEE PESC 2008*, June, 2008, Greece.

9. X. H. Wu, S. K. Panda, and J. X. Xu, "Dual Frame Cascaded Controller Design for Three Phase PWM Boost Rectifier Under Generalized Supply Voltage Conditions Using Singular Perturbation Method," *IEEE PESC 2008*, June, 2008, Greece.

10. X. H. Wu, S. K. Panda, and J. X. Xu, "Dual Frame Control Scheme with a Plug-in Frequency Domain Based Repetitive Controller for Three Phase PWM Boost Rectifier Under Distorted and Unbalanced Supply Voltages," *IEEE ISIE 2008*, June, 2008, UK.

11. X. H. Wu, S. K. Panda, and J. X. Xu, "Frequency Domain Based Repetitive Control of Three Phase Boost PWM Rectifier under Distorted Supply Voltage Conditions," *Invited Paper, IFAC 2008*, July, 2008, Korea.

Transactions

1. X. H. Wu, S. K. Panda, and J. X. Xu, "Analysis of the Instantaneous Power Flow for Three Phase PWM Boost Rectifier under Unbalanced Supply Voltage Conditions," *IEEE Trans. on Power Electronics*, vol. 23, pp. 1679 - 1691, July 2008.

2. X. H. Wu, S. K. Panda, and J. X. Xu, "DC Link Voltage and Supply-side Current Harmonics Minimization of Three Phase PWM Boost Rectifiers Using Frequency Domain Based Repetitive Current Controllers," *IEEE Trans. on Power Electronics*, vol. 23, pp. 1987 - 1997, July 2008.

Accepted

Transactions

1. X. H. Wu, S. K. Panda, and J. X. Xu, "Design of a Plug-in Repetitive Control Scheme for Eliminating Supply-side Current Harmonics of Three Phase PWM Boost Rectifiers under Generalized Supply Voltage Conditions," *IEEE Trans. on Power Electronics*

Submitted for Review

Transactions

1. X. H. Wu, S. K. Panda, and J. X. Xu, "Dynamic Analysis of Control System for Three Phase PWM Boost Rectifier Under Generalized Supply Voltage Conditions by Using Singular Perturbation Method," *IEEE Trans. on Power Electronics*

2. X. H. Wu, and S. K. Panda, "Servo Control of Micro-Cylindrical Ultrasonic Motor," *IEE Proc. Part-B*

Bibliography

[1] N.Mohan, T.M.Undeland and W.P.Robbins, *Power Electronics: Converters, Applications and Design*, Third Edition, John Wiley & Sons, Inc., 2003.

[2] G.Sequier, *Power Electronic Converters AC/DC Conversion*, New York: McGraw-Hill, 1986.

[3] B.K.Bose, *Modern Power Electronics and AC Drives*, NJ: Prentice-Hall, 2002.

[4] R.Rudervall, J.P.Charpentier and R.Sharma, "High voltage direct current (HVDC) transmission systems technology review paper", *ABB and World Bank,*

[5] M.D.Anderson, D.C.Carr and R.Sharma, "Battery energy storage technologies", *Proceedings of the IEEE*, vol. 81, March 1993, pp. 475–479.

[6] J.W.Kolar and H. Ertl, "Status of the techniques of three-phase rectifier systems with low effects on the mains", *INTLEC,* 6-9 June 1999, pp. 16.

[7] IEEE Std 519 IEEE Recommended Practices and Requirements for Harmonics Control in Electric Power Systems, 1992

[8] IEEE Std 1159-1995 IEEE Recommended Practice for Monitoring Electric Power Quality, 2003

[9] European standard EN-50160 Voltage Characteristics of Electricity Supplied by Public Distribution Systems, CENELEC, Brussels, Belgium, 1994

[10] C.K.Duffey and R.P.Stratford, "Update of harmonic standard IEEE-519 IEEE recommended practices and requirements for harmonic control in electric power system," *IEEE IAS Transactions*, Nov./Dec., 1989, pp. 1025-1034.

[11] B.Singh, B.N.Singh, A.Chandra, K.Al-Haddad, A.Pandey and D.P.Kothari, "A review of three-phase improved power quality AC-DC converters," *IEEE Trans. Ind. Electron.*, vol. 51, no. 3, June 2004.

[12] J.R.Rodriguez, J.W.Dixon, J.R.Espinoza, J.Pontt and P.Lezana "PWM regenerative rectifiers: state of the art," *IEEE Trans. Ind. Electron.*, vol. 52, no. 1, Feberuary 2005.

[13] M.H.J.Bollen, *Understanding Power Quality Problems: Voltage Sags and Interruptions*, New York: IEEE Press, 2000.

[14] M.Lindgren and J.Svensson, "Control of a voltage-source converter connected to the grid through an LCL-filter-application to active filtering," *Proc. IEEE-PESC Conf.*, vol. 1, pp. 229-235, 17-22, May, 1998

[15] S.Kim, P.N.Enjeti, P.Packebush, and I.J.Pitel, "A new approach to improve power factor and reduce harmonics in a three-phase diode rectifier type utility interface," *IEEE Trans. Ind. Applicat.*, vol. 30, pp. 1557-1564, Nov./Dec. 1994.

[16] B.S.Lee, P.N.Enjeti, and I.J.Pitel, "A new 24-pulse diode rectifier system for AC motor drives provides clean power utility interface with low kVA components," *Conf. Rec. IEEE-IAS Annu. Meeting*, pp. 1024-1031, 1996.

[17] S.F.Pinto and J.F.Silva, "Voltage control of twelve pulse rectifiers fitted with double LC filters," *Proc. IEEE ISIE'97*, pp. 323-328, 1997.

[18] Y.B.Blauth and I.Barbi, "A phase-controlled 12-pulse rectifier with unity displacement factor without phase shifting transformer," *Proc. IEEE APEC'98*, vol. 2, pp. 970-976, 1998.

[19] M.Villablanca, J.D.Valle, J.Rojas and W.Rojas, "A modified back-to-back HVdc system for 36-pulse operation," *IEEE Trans. Power Delivery*, vol. 15, pp. 641-645, Apr. 2000.

[20] F.C.Lee and D.Boroyevich, "Power factor correction circuits," presented at professional education seminars, *APEC* , 1993.

[21] A.R.Prasad, P.Ziogas and S.Manias, "An active power factor correction technique for three-phase diode rectifiers," *IEEE Trans. Power electron.*, vol. 6, no. 1, pp. 88-92, Jan. 1991.

[22] N.Mohan, M.Rastogi and R.Naik, "Analysis of a new power electronics interface with approximately simusoidal 3-phase utility currents and a regulated dc output," *IEEE Trans. Power Delivery*, pp. 540-546, Apr. 1993.

[23] J.W.Kolar, F.Stogerer, J.Minibock and H.Ertl, "A new concept for reconstruction of the input phase currents of a three-phase/switch/level PWM (VIENNA) rectifier based on neutral point current measurement," *Proc. IEEE-PESC Conf.*, pp. 139-146, 2000.

[24] J.Arrillaga and N.Watson, *Power System Harmonics*, Second Edition, New York: IEEE Press 1996.

[25] W.M.Grady, M.J.Samotyj and A.H.Noyola, "Survey of active power line conditioning methodologies," *IEEE Trans. Power Delivery*, pp. 1536-1542, July 1990.

[26] H.Akagi, "New trends in active filters for power conditioning," *IEEE Trans. Ind. Applicat.*, vol. 32, pp. 1312-1322, Nov./Dec. 1996.

[27] B.Singh, K.A.K.Al.Haddad and A.Chandra "A review of active filters for power quality improvement," *IEEE Trans. Ind. Electron.*, vol. 46, pp. 960-971, Oct. 1999.

[28] M.El-Habrouk, M.K.Darwish and P.Metha, "Active power filter: a review," *Proc. IEE-Elect. Power Applicat.*, vol. 147, pp. 493-413, Sept. 2000.

[29] S.Hiti, D.Boroyevich and C.Cuadros, "Small-signal modeling and control of three-phase PWM converters," *Ind. Applicat. Soc. Annu. Meeting, Conf. Rec.*, vol.2, pp. 1143-1150, Oct. 1994.

[30] M.P.Kazmierkowski, R.Krishinan and F.Blaabjerg, *Control in power electronics selected problems*, Academic press, 2002

[31] P.N.Enjeti, D.Ziogas and M.Ehsani, "Unbalanced PWM converter analysis and corrective measures," *Proc. IEEE-IAS Annual Meeting*, pp. 861-867, 1989.

[32] W.I.Tsai, M.T.Tsai and Y.Y.Sun, "Effects of voltage unbalance and harmonics on three phase SPWM AC-to-DC Converters with instantaneous power feedback," *Proc. IEEE Power Conversion Conference*, pp. 61-66, April, 1993.

[33] X.H.Wu, S.K.Panda and J.X.Xu, "Development of a new mathematical model of three phase PWM boost rectifier under unbalanced supply voltage operating

conditions," *Proc. IEEE Conf. Rec. PESC 2006*, Vol. 2, pp. 1391-1398, April. 2006

[34] X.H.Wu, S.K.Panda and J.X.Xu, "Supply-side current harmonics control of three phase PWM boost rectifier under distorted and unbalanced supply voltage conditions," *The 7th International Conference on Power Electronics and Drive Systems*, Nov. 2007

[35] L.Mihalanche, "A high performance DSP controller for three-phase PWM rectifiers with ultra low input current THD under unbalanced and distorted input voltage," *Proc. IEEE IAS annual meeting 2005.*, vol.1, pp. 138-144, Jan, 2005.

[36] P.Rioual, H.Pouliquen and J.P.Louis, "Control of a PWM rectifier in the unbalanced state by robust voltage regulation," *European Conference on Power Electronics and Applications.*, Vol. 4, pp. 8-14, Sept, 1993.

[37] M.P.Kazmierkowski and H.Tunia, "Automatic Control of Converter-Fed Drives," Elsevier, 1994.

[38] M.Malinowski, M.P.Kazmierkowski and A.M.Trzynadlowski, "A comparatitve study of control techniques for PWM recitifiers in AC adjustable speed drives," *IEEE Trans. Power Electron.*, vol.18, pp. 1390-1396, 2003.

[39] Andrzej M. Trzynadlowski, *Control of Induction Motors*, Academic Press, 2001.

[40] M.P.Kazmierkowski and L.Malesani, "Current control techniques for three-phase voltage source PWM converters: a survey," *IEEE Trans. Ind. Electron.*, vol.45, pp. 691-703, 1998.

[41] R.D.Lorenz and D.B.Lawson, "Performance of feedforward current regulatiors for field oriented induction machine controllers," *IEEE Trans. Ind. Applicat.*, vol.23, pp. 597-602, July, 1987.

[42] L.Moran, P.D.Ziogas and G.Joos, "Design aspects of synchronous PWM rectifier-inverter systems under unbalanced input voltage conditions," *Proc. IEEE-IAS Annual Meeting*, pp. 861-867, 1989.

[43] M.Liserre, A.D.Aquila and F.Blaabjerg "Design and control of a three phase active rectifier under non-ideal operating conditions," *Proc. IEEE-IAS Annual Meeting*, pp. 1181-1188, Oct. 2002.

[44] B.Gerhard, M.D.Manjrekar, J.P.Daniel and P.Maibach "Equal resistance control-a control methodology for line-connected converters that offers balanced resistive load under unbalanced input voltage conditions," *Proc. IEEE-IAS Annual Meeting*, pp. 1592-1598, 2002.

[45] Z.Q.Wu and O.Ojo, "Power factor control of a three phase boost rectifier with specific power factor under asymmetrical conditions," *Proc. IEEE-IAS Annual Meeting*, pp. 161-168, 2005.

[46] P.Verdelho, "Voltage type reversible rectifiers control methods in unbalanced and nonsinusoidal conditions," *Proc. Conf. Rec.IECON'98*, pp. 479-484, 1998.

[47] P.N.Enjeti and S.A.Choudhury, "A new control strategy to improve the performance of a PWM AC to DC Converter under unbalanced operating conditions," *IEEE Trans. Ind. Applicant.*, Vol. 28, pp. 1286-1293, 1992.

[48] P.Rioual, H.Pouliquen and J.P.Louis, "Regulation of a PWM rectifier in the unbalanced network state using a generalized model," *IEEE Trans. Power Electron.*, Vol. 11, pp. 495-502, May, 1996.

[49] H.Song and K.Nam, "Dual current control scheme for PWM converter under unbalanced input voltage conditions," *IEEE Trans. Ind. Electron.*, Vol. 46, pp. 953-959, Oct, 1999.

[50] H.S.Song, I.W.Joo and K.Nam, "Source voltage sensorless estimation scheme for PWM rectifiers under unbalanced conditions," *IEEE Trans. Industrial Electron.*, Vol. 50, pp. 1238-1244, 2003.

[51] Y.Suh, V.Tijeras and T.A.Lipo, "A nonlinear control of the instantaneous power in dq synchronous frame for PWM ac/dc converter under generalized unbalanced operating conditions," *Proc. IEEE-IAS Annual Meeting*, Vol. 2, pp. 1189-1196, 2002.

[52] Y.Suh, V.Tijeras and T.A.Lipo, "A control method in dq synchronous frame for PWM boost rectifier under generalized unbalanced operating conditions," *Proc. IEEE Conf. Rec. PESC 2002*, Vol. 3, pp. 1425-1430, Oct. 2002.

[53] S.C.Ahn and D.S.Hyun, "New control scheme of three phase PWM AC/DC converter without phase angle detection under the unbalanced input voltage conditions," *IEEE Trans. Power Electron.*, Vol. 17, No. 5, pp. 616-622, Sept, 2002.

[54] Y.Suh and T.A.Lipo "Control scheme in hybrid synchronous stationary frame for PWM AC/DC converter under genalized unbalanced operating conditions," *Proc. IEEE-IAS Annual Meeting*, pp. 2244-2251, Oct. 2004.

[55] A.V.Stankovic and T.A.Lipo, "A generalized control method for input output harmonic elemination of the PWM boost rectifier under simultaneous unbalanced input voltages and input impedances," *Proc. IEEE Conf. Rec. PESC 2001*, Vol. 3, pp. 1309-1314, 2001.

[56] A.V.Stankovic and T.A.Lipo, "A novel control method for input output harmonic elemination of the PWM boost type rectifier under unbalanced operating conditions," *IEEE Trans. Power Electron.*, Vol. 16, No. 5, pp. 603-611, 2001.

[57] A.V.Stankovic and T.A.Lipo, "A generalized control method for input simultaneous unbalanced input voltages and input impedances," *Proc. IEEE Conf. Rec. PESC 2001*, Vol. 3, pp. 1309-1314, 2001.

[58] M.Chomat and L.Schreier, "Compensation of unbalanced three phase voltage supply in voltage source inverter," *Proc. IEEE Conf. Rec. IECON 2002*, Vol. 2, pp. 950-955, 2002.

[59] M.Chomat and L.Schreier, "Control method for DC-link voltage ripple cancellation in voltage source inverter under unbalanced three phase voltage supply conditions," *IEE Proc. Electic Power Applications*, Vol. 152, pp. 494-500, 2005.

[60] B.Yin, R.Oruganti, S.K.Panda and A.K.S.Bhat, "A novel instantaneous power control strategy for a PWM rectifier under unbalanced input voltage conditions," *Proc. Conf. Rec. IECON'04*, Vol. 1, pp. 251-256, 2004.

[61] P.Xiao; K.A.Corzine and G.K.Venayagamoorthy;, "Cancellation Predictive Control for Three-Phase PWM Rectifiers under Harmonic and Unbalanced Input Conditions ," *Proc. IEEE Conf. Rec. IECON 2006*, Vol. 2, pp. 1816-1821, Nov. 2006

[62] T.Noguchi, H.Tomiki, S.Kondo and I. Takahashi, "Direct power control of PWM converter without power-source voltage sensors," *IEEE Trans. Ind. Applicant.*, Vol. 34, pp. 473-479, May/June, 1998.

[63] M.Malinowski, M.P.Kazmierkowski, S.Hansen, F.Blaabjerg and G.D.Marques, "Virtual-flux-based direct power control of three-phase PWM rectifiers," *IEEE Trans. Ind. Applicant.*, Vol. 37, pp. 1019-1027, July/Aug, 2001.

[64] T.Ohnishi, "Three phase PWM converter/inverter by means of instantaneous active and reactive power control," *Proc. Int. Conf. Ind. Electron. IECON'91*, Vol. 1, pp. 819-824, 1991.

[65] M.Malinowski and M.P.Kazmierkowski, "Direct power control of three-phase PWM rectifier using space vector modulation-Simulation study," *Proc. IEEE Int. Symp. Ind. Electron. ISIE 2002*, Vol. 4, pp. 1114-1118, 2002.

[66] M.Malinowski, M.Jasinski and M.P.Kazmierkowski, "Simple direct power control of three-phase PWM rectifier using space vector modulation (DPC-SVM)," *IEEE Trans. Ind. Electron.*, Vol. 51, pp. 447-454, April, 2004.

[67] L.A.Serpa, S.D.Round and J.W.Kolar, "A virtual flux decoupling hysteresis current controller for mains connected inverter systems," *Proc. IEEE Conf. Rec. PESC 2002*, pp. 3042-3048, June, 2006.

[68] Y.Komatsu, T.Kawabata "A control method of active power filter in unsymmetrical voltage system," *Proc. IEEE Conf. Rec. PEDS 1997*, Vol. 2, pp. 839-843, May, 1997.

[69] G.Escobar, A.M.Stankovic, J.M.Carrasco, E.Galvan and R.Ortega "Analysis and design of direct power control (DPC) for a three phase synchronous recitifer via output regulation subspaces," *IEEE Trans. Power Electron.*, Vol. 18, pp. 823-830, May, 2003.

[70] M.Cichowlas, M.Malinowski, M.P.Kazmierkowski, D.L.Sobczuk, P.Rodriguez and J.Pou, "Active filtering function of three phase PWM boost rectifier under

different line voltage conditions," *IEEE Trans. Ind. Electron.*, Vol. 52, pp. 410-419, April, 2005.

[71] Yongsug Suh, "Analysis and control of three-phase AC/DC PWM converter under unbalanced operating conditions," Ph.D. dissertation thesis, at the University of Wisconsin-Madison, 2004

[72] J.J.Grainger and W.D.Stevenson, *Power system analysis*, McGraw-Hill, Inc, 1994.

[73] V.Blasko and V.Kaura, "A new mathematical model and control of a three-phase AC-DC voltage source converter," *IEEE Trans. Power Electron.*, vol.12, pp. 116-123, Jan, 1997.

[74] D.Vincenti and H.Jin, "A three-phase regulated PWM rectifier with on-line feedforward input unbalanced correction," *IEEE Trans. Industrial Electron.*, vol.41, pp. 526-532, 1994.

[75] IEEE working group on nonsinusoidal situations "Practical definitions for powers in systems with nonsinusoidal waveforms and unbalanced loads: A Discussion," *IEEE Trans. Power Delivery*, vol.2, pp. 79-101, Jan, 1996.

[76] J.Holtz, "Pulsewidth modulation- a survey," *IEEE Trans. Power Electr.*, Vol.39, no.5. pp.410-420. December 1992

[77] F.M.Gardner *Phaselock Techniques*, New York: Wiley, 1979.

[78] B.Razavi "Monolithic Phase-Locked Loop and Clock Recovery Circuit," New York: IEEE Press, 1996.

[79] V.Blasko, J.C.Moreira and T.A.Lipo "A new field oriented controller utilizing spatial position measurement of rotor end ring current," *Proc. PESC*, vol.1, pp.295 - 300, June, 1989.

[80] F.Nozari, P.A.Mezs, A.L.Julian, C.Sun and T.A.Lipo "Sensorless synchronous motor drive for use on commercial transport airplanes," *IEEE Trans. Ind. Applicat.*, vol.31, pp.850-859, Aug, 1995.

[81] G.C.Hsieh and J.C.Hung "Phase-locked loop techniques–a survey," *IEEE Trans. Ind. electron.*, vol.43, pp.609-615, Dec, 1996.

[82] S.Lee, J.Kang and S.Sul "A new phase detecting method for power conversion systems considering distorted conditions in power system," *IAS Annual Meeting*, vol.4, pp. 2167 - 2172, Oct, 1999.

[83] S.K.Chung "A phase tracking system for three phase utility interface inverters," *IEEE Trans. Power electron.*, vol.15, pp. 431 - 438, May, 2000.

[84] J.Svensson "Synchronisation methods for grid-connected voltage source converters," *IEE Proc. Gener. Transm. Distrib.*, vol.148, pp. 229 - 235, May, 2001.

[85] L.N.Arruda, S.M.Silva and B.J.C.Filho "PLL structure for utility connected systems," *IAS Annual Meeting*, vol.4, pp. 2655 - 2660, Oct, 2001.

[86] K. Ogata, *Modern Control Engineering*, Upper Saddle River, N.J.Prentice-Hall, 2002.

[87] W.D.Stevenson, *Elements of power system analysis*, McGraw-Hill, New York, 1995, 4th Edn.

[88] J.E.Brittain, "Charles L.G. Fortescue and the method of symmetrical components [Scanning the Past]," *Proceedings of the IEEE*, Vol.86, pp. 1020-1021. May 1998

[89] A.G.Phadke, T.Hibka, M.Ibrahim and M.G.Adamiak, "Amicroprecessor based symmetrical component distance relay," *Proc. IEEE Power industry computer applications Conf.,*, pp. 47-55. May 1979

[90] S.R.Kollar, "Block pulse functions based algorithm for symmetrical components calculation," *IEE Proc. C. Gener., Transm. Distrib.,*, vol.135, pp. 487-488. 1988

[91] G.Andria and L.Salvatore, "Inverter drive signal processing via DFT and EKF," *IEE Proc. B., Electr. Power Appl.,*, vol.137, pp. 111-118. 1990

[92] T.Lobos, "Fast estimation of symmetrical components in real time," *IEE Proc. C. Gener., Transm. Distrib.,*, vol.139, pp. 27-30. 1992

[93] A.Campos, G.Joos, P.D.Ziagos and J.F.Lindsay, "A dsp-based real-time digital filter for symmetrical components," *Proc. IEEE/NTUA Power technology Conf.,*, pp. 75-79. 1993

[94] E.Rosolowski and M.Michalik, "Fast identification of symmetrical components by use of a state observer," *IEE Proc. C. Gener., Transm. Distrib.,*, vol.141, pp. 617-622. 1994

[95] D.C.Yu, D.Chen, S.Ramasamy and D.G.Flinn, "A windows based graphical package for symmetrical components analysis," *IEEE Trans. Power Syst.,*, vol.10, pp. 1742-1749. 1995

[96] A.Ghosh and A.Joshi, "A new approach to load balancing and power factor correction in power distribution system," *IEEE Trans. Power Deliv.,*, vol.15. pp. 417-422. 2000

[97] G.C.Paap, "Symmetrical components in the time domain and their application to power network calculations," *IEEE Trans. Power Syst.,*, vol.15. pp. 522-528. 2000

[98] J.S.Hsu, "Instantaneous phasor method for obtaining instantaneous continuous diagnostics," *IEEE Trans. Power Deliv.,*, vol.13. pp. 1494-1500. 1998

[99] A.M.Stankovic and T.Aydin, "Analysis of asymmetrical faults in power systems using dynamic phasors," *IEEE Trans. Power Syst.,*, vol.15. pp. 1062-1068. 2000

[100] C.C.Chen and Y.Y.Hsu, "A novel approach to the design of a shunt active filter for an unbalanced three-phase four-wire system under nonsinusoidal conditions," *IEEE Trans. Power Deliv.,*, vol.15. pp. 1258-1264. 2000

[101] M.R.Iravani and M.K.Ghartemani, "Online estimation of steady state and instantaneous symmetrical components," *IEE Proc. Gener. Transm. Distrib.,*, vol.150. pp. 616-621. 2003

[102] V.D.Yurkevich, "Design of nonlinear control systems with the highest derivative in feedback,", World Scientific, 2004.

[103] A.N.Tikhonov, "Systems of differential equations containing a small parameter multiplying the derivative," *Mathematical Sb.*, vol.31, no. 3, pp. 575-586, 1952.

[104] P.V.Kokotovic, H.K.Khalil and J.O'Reilly, "Singular Pertubation Methods in Control: Analysis and Design, Philadelphia, PA: SIAM" 1999.

[105] D.S.Naidu, "Singular perturbations and time scales in control theory and application: an overview." *Dynamics of Continuous, Discret & Impulsive Systems (DCDIS) Series B: Applications & Algorithms,*, vol.9, no. 2, pp. 233-278, June, 2002.

[106] B.A.Francis and W.M.Wonham, "The internal model principle of control theory," *Automatica*, Vol. 12, pp. 457-465, 1976.

[107] M.Tomizuka, T.Tsao and K.Chew, "Analysis and synthesis of discrete-time repetitive controllers," *Trans. ASME: J. Dyn. Syst. Devices*, Vol. 110, pp. 271-280, Jan, 1988.

[108] K.Zhou and D.Wang, "Digital repetitive controlled three-phase PWM rectifier," *IEEE Trans. Power Electron.*, Vol. 18, pp. 309-316, Jan, 2003.

[109] B.Zhang, K.Zhou Y.Ye and D.Wang, "Design of linear phase lead repetitive control for CVCF PWM DC-AC converters," *American Control Conference 2005*, pp. 1154-1159, June, 2005.

[110] W.Z.Qian, S.K.Panda and J.X.Xu, "Torque ripple minimization in PM synchronous motors using iterative learning control ," *IEEE Trans. Power Electron.*, pp. 272-279, March, 2003.

[111] S.K.Sahoo, S.K.Panda and J.X.Xu, "Iterative learning-based high-performance current controller for switched reluctance motors ," *IEEE Trans. Energy Conversion*, pp. 491-498, Sept, 2004.

[112] M.Ishida, S.Higuchi and T.Hori, "Reduction control of mechanical vibration of an induction motor with fluctuated torque load using repetitive controller," *Industry technology Conference 1994*, pp. 533-537, Dec, 1994.

[113] T.Senjyu, H.Miyazato and K.Uezato "Precise speed control of ultrasonic motors with repetitive control ," *Industrial Automation and Control: Emerging Technologies, 1995*, pp. 165-169, May, 1995.

[114] J.X.Xu and W.J.Cao, "Learning variable structure control approaches for repeatable tracking control tasks," *Automatic.*, Vol. 37, no. 7, pp. 997-1006, July, 2001.

[115] W.Wang, S.K.Panda and J.X.Xu, "Control of high performance DC/AC inverters using frequency domain based repetitive control ," *Proc. IEEE PEDS annual meeting 2006.*, pp. 442-447, Jan, 2006.

[116] C.Luo, H.Banakar, B.Shen and B.T.Ooi, "Strategies to Smooth Wind Power Fluctuations of Wind Turbine Generator ," *IEEE Trans. Energy Conversion*, Vol. 22, pp. 341-349, June, 2007

[117] F.Blaabjerg, J.K.Pedersen, U.Jaeger and P.Thoegersen, "Single current sensor technique in the dc link of three-phase PWM-VS inverters: a review and a novel solution," *IEEE Trans. Indust. Appl.*, Vol. 33, pp. 1241-1253, 1997

[118] K. Ogata, *Discrete-time control systems*, Englewood Cliffs, N.J.Prentice-Hall, c1987.

[119] T. Kenjyo and T. Sashida, *An Introduction of Ultrasonic Motor*, Oxford Science Publications, 1993.

[120] T. Izumi, H. Yasutsune, Y.J. Kim and M. Nakaoka, "New Inverter-Fed Power Ultrasonic Motor for Speed Traking Servo Application and Its Feasible Evaluations", *Proceedings of International Conference on Power Eletronics and Drive Systems*, 1995, pp. 766–733.

[121] T. Senjyu, K. Uezato and H. Miyazato, "Quick and Precise Position Control of Ultrasonic Motors with two control inputs", *Electric Machines and Power Systems*, vol. 25, 1997, pp. 761–781.

[122] T. Senjyu, H. Miyazato, S. Yokoda and K. Uezato, "Position Control of Ultrasonic Motors Using Neural Network", *IEEE Internationl Symposium on Industrial Electron*, June 1996, pp. 254–259.

[123] F.J. Lin, "Fuzzy Adaptive Model-following Position Control for Ultrasonic Motor", *IEEE Trans. Power Electron.*, vol. 12, Mar. 1997, pp. 261–268.

[124] T. Morita, M. Kurosawa and T. Higuchi, "Design of a Cylindrical Ultrasonic Micromotor to Obtain Mechanical Output", *Jpn. J. Appl. Phys.*, Part 1, No. 5B, May 1996.

[125] Xiaopeng Wang, S.K.Panda, C.L.Teo and C.J.Ong "Speed Control of Cylindrical Ultrasonic Motor", Industrial Electronics Society, IEEE 2002 28th Annual Conference vol. 4, 2002, pp. 2739–2744.

[126] Xiaopeng Wang, "Modelling and Control of Cylindrical Ultrasonic Motor", Master Degree Thesis, Dept. of Mech. Engr., National Unviersity of Singapore, 2002.

[127] L. Petit, N. Rizet, R. Briot and P. Gonnard, "Frequency Behaviour and Speed Control of Piezomotors", *Sensors and Actuators*, 80, 2000, pp 45–52.